

Measurement of azimuthal correlations between D-mesons and charged particles in pp collisions at $\sqrt{s} = 13$ TeV with ALICE at the LHC

By

SAMRANGY SADHU

PHYS04201404009

Variable Energy Cyclotron Centre, Kolkata

A thesis submitted to

The Board of Studies in Physical Sciences

In partial fulfillment of requirements

For the Degree of

DOCTOR OF PHILOSOPHY

of

HOMI BHABHA NATIONAL INSTITUTE




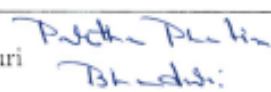

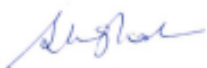


June, 2019

Homi Bhabha National Institute¹

Recommendations of the Viva Voce Committee

As members of the Viva Voce Committee, we certify that we have read the dissertation prepared by Samrangy Sadhu entitled "Measurement of azimuthal correlations between D-mesons and charged particles in pp collisions at $\sqrt{s} = 13$ TeV with ALICE at the LHC" and recommend that it may be accepted as fulfilling the thesis requirement for the award of Degree of Doctor of Philosophy.

Chairman	Jane Alam		Date: 30/8/2017
Guide/Convener	Premomoy Ghosh		Date: 30/08/2019
Examiner	Raghava Varma		Date: 30/08/2019
Member 1	Partha Pratim Bhaduri		Date: 30/08/19
Member 2	Anand Kumar Dubey		Date: 02/09/19
Member 3	Sanjay Ghosh		Date: 30/8/19

Final approval and acceptance of this thesis is contingent upon the candidate's submission of the final copies of the thesis to HBNI.

I hereby certify that I/we have read this thesis prepared under my direction and recommend that it may be accepted as fulfilling the thesis requirement.

Date: 30/08/2019

Place: Kolkata


Guide 

¹This page is to be included only for final submission after successful completion of viva voce.

STATEMENT BY AUTHOR

This dissertation has been submitted in partial fulfillment of requirements for an advanced degree at Homi Bhabha National Institute (HBNI) and is deposited in the Library to be made available to borrowers under rules of the HBNI.

Brief quotations from this dissertation are allowable without special permission, provided that accurate acknowledgement of source is made. Requests for permission for extended quotation from or reproduction of this manuscript in whole or in part may be granted by the Competent Authority of HBNI when in his or her judgment the proposed use of the material is in the interests of scholarship. In all other instances, however, permission must be obtained from the author.

A handwritten signature in blue ink, reading "Samrangy Sadhu". The signature is written in a cursive, flowing style.

Samrangy Sadhu

DECLARATION

I, hereby declare that the investigation presented in the thesis has been carried out by me. The work is original and has not been submitted earlier as a whole or in part for a degree / diploma at this or any other Institution / University.

A handwritten signature in black ink, reading "Samrangy Sadhu". The script is cursive and fluid, with the first name "Samrangy" and the last name "Sadhu" clearly distinguishable.

Samrangy Sadhu

List of Publications

Journal

1. **Samrangy Sadhu** and Premomoy Ghosh, *Anomalous features of particle production in high-multiplicity events of pp collisions at the LHC energies*, *Phys. Rev.* **D99** (2019) 034020.
2. Somnath Kar, Subikash Choudhury, **Samrangy Sadhu** and Premomoy Ghosh, *Centrality dependent long-range angular correlations of intermediate-pT D-mesons and charged particles in pPb collisions at the LHC energy*, *J. Phys. G: Nucl. Part. Phys.* **45** (2018) 125103.

Conference proceedings

1. **Samrangy Sadhu** and Premomoy Ghosh, *Hydro-like features in high-multiplicity pp events at the LHC energies contrasted with EPOS3 hydrodynamic model*, **Proceedings of the DAE Symp. on Nucl. Phys.** **62** (2017).
2. **Samrangy Sadhu** on behalf of the ALICE collaboration, *Azimuthal correlations of D mesons with charged particles in pp collisions $\sqrt{s}=13$ TeV with the ALICE experiment at the LHC*, Sixth Annual Conference on Large Hadron Collider Physics (LHCP2018) 4-9 June 2018 Bologna, Italy, **PoS(LHCP2018)042**.
3. **Samrangy Sadhu** on behalf of the ALICE collaboration, *Study of in-Medium Energy Loss with Heavy-Flavour Correlations in pp and Pb-Pb Collisions with ALICE at the LHC*, Hot Quarks 2018-Workshop for Young Scientists on the Physics of Ultrarelativistic Nucleus-Nucleus Collisions, Texel, The Netherlands, 7-14 September 2018, **Proceedings 2019, 10, 43**.



Samrangy Sadhu

DEDICATION

This thesis is dedicated to

My Mother

for being the one who empowered me with strength and courage to overcome difficulties and fight with any negative situation.

My Father

for being the idol of honesty and simplicity in my life and encouraging me to keep faith on myself.

ACKNOWLEDGEMENTS

I would like to express my gratitude to **the Almighty**, for granting me strength and capability to fight with all the obstacles and negative situations in my life, for encouraging me to work hard and stay focussed in all ups and downs of my life and for giving me blessings to keep faith on myself and stay optimistic.

A handwritten signature in dark blue ink, reading "Samrangy Sadhu". The script is cursive and fluid, with the first name "Samrangy" and the last name "Sadhu" written in a single continuous line.

Samrangy Sadhu

Contents

Synopsis	xxvi
List of Figures	xxxv
List of Tables	xxxvii
1 Introduction	1
1.1 The Standard Model	4
1.2 Quantum Chromodynamics (QCD)	6
1.3 The QCD phase diagram and the Quark-Gluon Plasma	10
1.4 The study of QGP in relativistic heavy-ion collisions	11
1.5 The Signatures of QGP	14
1.5.1 Electromagnetic Probes	15
1.5.2 Energy loss	16
1.5.3 Collective Flow	18
1.5.4 Heavy Quarks	19
1.5.5 Quarkonia Dissociation	19
1.5.6 Role of pp and pA collisions in search of QGP signals	20
1.6 Thesis focus	24
1.6.1 The study of the heavy-flavour jets, in terms of two-particle angular correlations between D-mesons and charged particles	25
1.6.2 Study of high multiplicity events of small systems	25
2 Open heavy-flavour probes in high energy collisions	27
2.1 Introduction to heavy quarks and heavy-flavour Mesons	27
2.2 Heavy flavour production	28
2.3 Open heavy-flavour as a probe in relativistic heavy-ion collisions	29
2.3.1 The effect of QGP medium on heavy flavour	30
2.3.2 Experimental review	33
2.4 Open heavy-flavour in small systems	36
2.4.1 pPb collisions	36
2.4.2 pp collisions	38

3	Experimental Setup	43
3.1	The Large Hadron Collider	43
3.2	The ALICE detector	45
3.2.1	Inner Tracking System	48
3.2.2	Time Projection Chamber	49
3.2.3	Time Of Flight	51
3.2.4	V0 detector	52
3.3	ALICE online data taking framework	53
3.4	ALICE offline computation	54
3.4.1	AliRoot and AliPhysics framework	54
4	Analysis Detail for two-particle azimuthal correlations between D meson and charged particles in pp collisions with ALICE detector	59
4.1	Dataset and event selection	59
4.2	Analysis method	61
4.2.1	Selection of D meson as trigger particle	62
4.2.2	Selection of charged tracks as associated particle	66
4.2.3	Building correlations and background subtraction	70
4.2.4	Corrections	70
5	Systematic studies and results	91
5.1	Systematic studies	91
5.1.1	Uncertainty on D-meson yield extraction	92
5.1.2	Uncertainty on background subtraction	93
5.1.3	Uncertainty on associated track efficiency	95
5.1.4	Uncertainty on D-meson reconstruction and selection efficiency	97
5.1.5	Uncertainty on feed-down subtraction	98
5.1.6	Uncertainty on secondary track contamination	102
5.1.7	Uncertainty on correction for the bias on the b to D decay topology	103
5.1.8	Overall uncertainty	103
5.2	Results	104
5.2.1	Comparison of results from D^0 , D^+ and D^{*+}	104
5.2.2	Fitting of correlation spectra and fit observables	107
5.2.3	Final results	109
6	Study of small systems with hydro-based simulated events	117
6.1	High multiplicity events of small systems: An experimental review	117
6.1.1	pp collisions	117
6.1.2	pPb collisions	123
6.2	Event generation with EPOS3	125
6.3	Analysis in pp collisions	126
6.3.1	Long-range two-particle azimuthal correlations	127

6.3.2	Blast-wave description of identified charged particle yield	131
6.3.3	Mean transverse momentum ($\langle p_T \rangle$) as a function of charged particle multiplicity (N_{ch})	134
6.3.4	Inverse slope parameter of transverse mass (m_T) distribution	137
6.4	Analysis in pPb collisions	138
6.4.1	Centrality dependent invariant yields of identified charged particles	138
6.4.2	Mean transverse momentum ($\langle p_T \rangle$) as a function of charged particle multiplicity	139
6.4.3	Inverse slope parameter of transverse mass (m_T) spectra	140
6.4.4	Long-range two-particle azimuthal correlations	140
7	Summary and Outlook	147
7.1	Azimuthal correlations between D mesons and charged particles in pp collisions at $\sqrt{s} = 13$ TeV measured by ALICE	147
7.1.1	Summary and conclusion	147
7.1.2	Outlook	148
7.2	Simulation studies with hydro-based event generator EPOS3 for high-multiplicity events of pp and pPb collisions at LHC energies	149
7.2.1	Summary and conclusion	149
7.2.2	Outlook	152
	Bibliography	168

Synopsis

Quark-Gluon Plasma (QGP) [1, 2, 3], the thermalized partonic phase of strongly interacting matter, is predicted by the Quantum Chromodynamics (QCD), the theory of strong interactions. Relativistic heavy-ion (AA) collisions are proven means for creating the QGP in the laboratories. While CERN experiment at the Super Proton Synchrotron (SPS) indicated [4, 5] formation of QGP-like medium, experiments at Brookhaven at the Relativistic Heavy-Ion Collider (RHIC) with AuAu collisions at center of mass energy ($\sqrt{s_{NN}}$) = 130 and 200 GeV provided first convincing evidence [6, 7, 8, 9] on formation of QGP in the laboratory. In absence of any unique and “smoking-gun” type of signal of QGP, the discovery of QGP at the RHIC involved confirmation of several predicted signals. The two most prominent signals were i) the azimuthal anisotropic flow of the produced particles exhibiting the collective property of the source of the particles, as was expected from a thermalized medium, and ii) the suppression of high p_T -particles, indicating formation of a dense partonic medium. The suppression of high- p_T particles in AuAu collisions was extracted by normalizing the data with the same energy data of proton-proton (pp) collisions, where one doesn’t expect formation of QGP. The Large Hadron Collider (LHC) at CERN has extended the scope of the QGP study with the collisions of heavier nuclei (PbPb) at higher $\sqrt{s_{NN}} = 2.76, 5.02$ TeV and thus creating hotter partonic matter with increased energy density, volume and the lifetime [10]. The LHC also facilitates the study on properties of the QGP medium with copiously produced unique hard probes, the heavy-flavor (HF) particles. The heavy quarks (c, b) are considered to be an useful tool to study the properties of the partonic medium as these particles, having large masses ($m_c \approx 1.3$ GeV/ c^2 , $m_b \approx 4.2$ GeV/ c^2), are produced at the early stages of the collisions and expected to experience the full evolution of the medium [11]. Heavy quarks are produced via parton-parton hard scattering, the production cross-sections are calculable using perturbative QCD (pQCD).

The LHC provides pp collisions at widely varied center-of-mass collision energy (\sqrt{s}), from 900 GeV up to 13 TeV (planned to reach 14 TeV) and pPb collisions at $\sqrt{s_{NN}} = 5.02$ TeV. While the minimum-bias data of these small collision systems form the baselines for extraction of QGP signals of the AA collisions, the study of these data at varied energy upto the new-heights in the energy-scale at the

LHC is important by itself in understanding the particle production mechanisms, particularly those originated from heavy quarks. The main content of this thesis, as implied in its title, “Measurement of azimuthal correlations between D-mesons and charged particles in pp collisions at $\sqrt{s} = 13$ TeV” pertains to the heavy-flavor particles at the LHC energy. The azimuthal correlations between D-mesons and charged particles, when studied in the short range of rapidity, reveals properties of the jets, originated from charm quarks. The jet formed by a high- p_T particle, a proven tool to study in-medium energy loss, is used in characterizing the medium formed in relativistic AA collisions. So, the jet properties, studied in minimum-bias pp events at 13 TeV, can be used as a baseline in characterizing the medium formed in high-multiplicity pp events in the same energy of collision. It is worth mentioning that, though the multi-particle productions in high-multiplicity events of pp and pPb collisions at the LHC energies have been shown to have exhibited collective properties of hydrodynamic origin [12, 13, 14, 15] in contrast to the understanding on particle production in pp collisions at pre-LHC era, the characterization of the collective medium in these small systems still remains unsolved due to non-observance of suppression of high- p_T particles or any such compelling signal to identify the medium as like the one formed in AA collisions. Also, the non-observance of suppression of high- p_T particles may be attributed to the limitations in measurement of path-length dependent energy-loss in small system, formed in high-multiplicity pp events. In this context, the comparison of the properties of jets formed in high and minimum-bias pp events may throw some light in characterizing the medium formed in high-multiplicity pp events. Due to the lack of sufficient statistics on D-mesons in high-multiplicity events at ALICE, during the work, the study of simulated high-multiplicity events in terms of several observables related to D-mesons as well as to charged particles, in general, has been carried out to understand possible origin of the collective behaviour of high-multiplicity events in small systems.

Following a brief review of related literature, the contents of this thesis has been presented in two parts, 1) Analysis of pp data in $\sqrt{s} = 13$ TeV with ALICE at the LHC and 2) Analysis of simulated events in small systems (pp and pPb) at LHC energies. In the first part, the study of two-particle azimuthal correlations with D mesons and charged particles in minimum-bias pp collisions at $\sqrt{s} = 13$ TeV measured by ALICE detector at the LHC has been presented. The study has been carried out with $|\Delta\eta| < 1$, to extract the short-range correlations, aiming for the characterization of charm-jet properties in pp collisions for the highest available energy in LHC. In the second part, a multiplicity dependent study in pp and pPb collisions at LHC energies on the anomalous features of particle production mechanisms have been compared with the simulated events from a hydro-based Monte Carlo event generator.

First part:

We have organized this part of the thesis with the followings: physics motivation to study heavy quarks, the ALICE experimental setup and reconstruction of D mesons, description of analysis tool i.e., the measurement of two particle azimuthal correlations, several corrections followed by the final results.

The measurement of azimuthal correlations are done by considering D mesons as “trigger” particles and primary charged particles as “associated particles”. The ALICE sub-detectors used in this analysis are Inner Tracking System (ITS), Time Projection Chamber (TPC), Time Of Flight (TOF) and V0 scintillator detectors [16]. The reconstruction of charged particle tracks are done using ITS and TPC. The Particle Identification (PID) is based on the specific energy loss (dE/dx) in TPC and the information on time of flight from the interaction vertex to the TOF detector. The V0 scintillator detectors are used for triggering and multiplicity estimation.

The D-meson (D^0 , D^+ and D^{*+}) invariant mass is reconstructed with the hadronic decay products applying optimized topological cuts which help in reducing combinatorial background during signal extraction [17]. The main topological cuts applied for the reconstruction are the threshold of transverse momentum of the decay daughters, the distance of closest approach (DCA) of the decay tracks from the primary vertex, the minimum distance between the two daughter track helices, the angle between the reconstructed D-meson momentum and the flight line defined by the primary and secondary vertices etc. The reconstructed D-meson candidates are considered as “trigger” and are correlated with primary charged particles in a given kinematic range. The analysis has been performed with three different p_T -intervals of D-mesons ($3 < p_T < 5$, $5 < p_T < 8$, $8 < p_T < 16$ GeV/ c) and associated particles, in the p_T -intervals, $p_T > 0.3$, $1, 0.3 < p_T < 1$ GeV/ c , as a function of $(\Delta\eta, \Delta\varphi)$. A relatively wide p_T intervals are chosen for D mesons in order to reduce statistical fluctuations in the correlation distributions.

The correlation distributions are affected by limited detector acceptance and detector inhomogeneities. The detector effect is neutralized by constructing similar correlation functions with mixed events and proper normalization condition $(\Delta\eta, \Delta\varphi) = (0, 0)$. A “side-band” correction is applied on the correlation distributions to get rid of the background coming under the signal mass peak of the invariant mass spectra.

Genuine D-meson candidates as well as the primary charged tracks may get lost during reconstruction of tracks, primary and secondary vertices and due to the topological cuts. We correct these lost fractions by implementing appropriate weighted efficiency for both D mesons and associated tracks using several Monte-Carlo event generators. After that, we take the one-dimensional projections of

the correlation distributions over $\Delta\varphi$ and apply second round of corrections with Monte Carlo event generators, for removal of the biased B to D decay topologies, subtraction of feed-down D mesons, removal of secondary track contamination from the associated charged particle sample. After implementing all these corrections, we calculate the systematic uncertainties originating from several sources like fitting of the D-meson invariant mass spectra, determination of sideband ranges, cut selections for D mesons and associated charged tracks etc.

In order to characterize the jet properties, we fit the fully corrected correlation distributions with a function consisting two Gaussian and a constant term. The integral and the σ of the Gaussian fits give the per-trigger associated-particle yields for the near-side (NS) peak and the away-side (AS) peak with their widths (σ_{NS}, σ_{AS}) while the constant term describes “baseline”.

The study in small $\Delta\eta < 1$ reveals short-range correlations among D-mesons and charged particles. The results have been compared with the pp collisions at $\sqrt{s} = 7$ TeV and pPb collisions at $\sqrt{s_{NN}} = 5.02$ TeV [18]. The correlation distributions as well as the peak properties for the considered colliding systems match, within the uncertainties, indicating similar charm-jet properties.

Second part:

The remaining part of the thesis presents the motivation for studying high-multiplicity events in small systems followed by a brief description of EPOS3 event generator and the results of analysis of generated pPb and pp events. The aim of this study with EPOS event generator is to access how good this hydro-based event generator reproduces the data. Depending on the goodness of quantitative data matching only, one can conclude if the physics origin of the collective properties of particle production, seen in the data for these small systems, may be explained by the physics of the model, implemented in the Monte-Carlo event generator EPOS3 [19] or not.

The EPOS model works on the parton-based Gribov-Regge theory and a 3+1D viscous hydrodynamical evolution is implemented in the code. We have generated around 10 millions events of pPb collisions at $\sqrt{s_{NN}} = 5.02$ TeV and 40 million events of pp collisions at $\sqrt{s} = 7$ and 13 TeV, each. Suitable subsamples of different multiplicity and centrality classes and different kinematic cuts, to match those for available data, are selected from the simulated minimum-bias event samples for analysis in terms of observables for which data is available.

We analyse the selected simulated pPb events to study the general observables (for which data exist), like p_T spectra for identified particles, mean p_T as a function of event multiplicity for both inclusive and identified particle spectra, the inverse slope parameter of transverse mass (m_T) distribution are performed and compared with data with same kinematic variables. It has been observed that the EPOS3 generator, with hydrodynamic evolution, can describe the data well both qualitatively and

quantitatively. The good matching between the data and the simulated events, thus motivate us to extend this study with the long-range centrality dependent charged particle correlations analysis as well as the D mesons and charged particle correlation analysis (our results could not be matched with data because of non-availability of centrality dependent experimental study). For both the correlation analysis, a “ridge”-like structure is seen in small $|\Delta\varphi|$ and over a wide $|\Delta\eta|$ for most central collisions.

The multiplicity dependent analysis of the charged particles of the simulated pp events have been carried out in terms of experimental observables that exhibit the flow-like behaviour in high-multiplicity events, namely, long-range two-particle azimuthal correlations among charged particles, blast-wave description of identified charged particle yield, mean transverse momentum ($\langle p_T \rangle$) as a function of average charged particle multiplicity and inverse slope parameter of transverse mass (m_T) distribution. The long-range ($|\Delta\eta| \gg 1$) two-particle angular correlations of the charged particles have been constructed in simulated events, keeping the kinematic cuts and multiplicity classes same as chosen for data analysis [20] of pp $\sqrt{s} = 7$ and 13 TeV. The multiplicity dependent analysis of the simulated events, in terms of all these observables, clearly reveal mismatch between particle production in the experiments and that implemented in this model.

This analysis concludes that, though EPOS3 model describes the pPb data both qualitatively and quantitatively, satisfactorily, it has limitations in explaining the features of particle production mechanisms in the pp data. The particle production mechanism in the Monte Carlo code thus need to be modified / further tuned to properly explain the particle production mechanisms in high-multiplicity pp events at the LHC energy range.

Bibliography

- [1] E. V. Shuryak, *Theory of Hadronic Plasma*, *Sov. Phys. JETP* **47** (1978) 212.
- [2] E. V. Shuryak, *Quark-Gluon Plasma and Hadronic Production of Leptons, Photons and Psions*, *Phys. Lett.* **78B** (1978) 150.
- [3] E. V. Shuryak, *Quantum Chromodynamics and the Theory of Superdense Matter*, *Phys. Rept.* **61** (1980) 71.
- [4] U. W. Heinz and M. Jacob, *Evidence for a new state of matter: An Assessment of the results from the CERN lead beam program*, [nucl-th/0002042](#).
- [5] T. Csörgő, *New form of matter at cern sps: Quark matter but not quark gluon plasma*, *Nuclear Physics B - Proceedings Supplements* **92** (2001) 62 .
- [6] BRAHMS collaboration, *Quark gluon plasma and color glass condensate at RHIC? The Perspective from the BRAHMS experiment*, *Nucl. Phys.* **A757** (2005) 1 [[nucl-ex/0410020](#)].
- [7] PHENIX collaboration, *Formation of dense partonic matter in relativistic nucleus-nucleus collisions at RHIC: Experimental evaluation by the PHENIX collaboration*, *Nucl. Phys.* **A757** (2005) 184 [[nucl-ex/0410003](#)].
- [8] B. B. Back et al., *The PHOBOS perspective on discoveries at RHIC*, *Nucl. Phys.* **A757** (2005) 28 [[nucl-ex/0410022](#)].
- [9] STAR collaboration, *Experimental and theoretical challenges in the search for the quark gluon plasma: The STAR Collaboration's critical assessment of the evidence from RHIC collisions*, *Nucl. Phys.* **A757** (2005) 102 [[nucl-ex/0501009](#)].
- [10] B. Müller, J. Schukraft and B. Wysłouch, *First results from pb+pb collisions at the lhc*, *Annual Review of Nuclear and Particle Science* **62** (2012) 361 [<https://doi.org/10.1146/annurev-nucl-102711-094910>].

- [11] P. Braun-Munzinger, *Quarkonium production in ultra-relativistic nuclear collisions: Suppression versus enhancement*, *J. Phys.* **G34** (2007) S471 [[nuc1-th/0701093](#)].
- [12] CMS collaboration, *Observation of Long-Range Near-Side Angular Correlations in Proton-Proton Collisions at the LHC*, *JHEP* **09** (2010) 091 [[1009.4122](#)].
- [13] CMS collaboration, *Evidence for collectivity in pp collisions at the LHC*, *Phys. Lett.* **B765** (2017) 193 [[1606.06198](#)].
- [14] ALICE collaboration, *Long-range angular correlations on the near and away side in p-Pb collisions at $\sqrt{s_{NN}} = 5.02$ TeV*, *Phys. Lett.* **B719** (2013) 29 [[1212.2001](#)].
- [15] CMS collaboration, *Observation of long-range near-side angular correlations in proton-lead collisions at the LHC*, *Phys. Lett.* **B718** (2013) 795 [[1210.5482](#)].
- [16] C. Fabjan and J. Schukraft, *The Story of ALICE: Building the dedicated heavy ion detector at LHC*, in 'The Large Hadron Collider: A marvel technology', EPFL-Press Lausanne, Switzerland, 2009 (Editor: L. Evans), chapter 5.4, 2011, [1101.1257](#).
- [17] ALICE collaboration, *Measurement of charm production at central rapidity in proton-proton collisions at $\sqrt{s} = 7$ TeV*, *JHEP* **01** (2012) 128 [[1111.1553](#)].
- [18] ALICE collaboration, *Measurement of azimuthal correlations of D mesons and charged particles in pp collisions at $\sqrt{s} = 7$ TeV and p-Pb collisions at $\sqrt{s_{NN}} = 5.02$ TeV*, *Eur. Phys. J.* **C77** (2017) 245 [[1605.06963](#)].
- [19] K. Werner, *The hadronic interaction model epos*, *Nuclear Physics B - Proceedings Supplements* **175-176** (2008) 81 .
- [20] CMS collaboration, *Measurement of long-range near-side two-particle angular correlations in pp collisions at $\sqrt{s} = 13$ TeV*, *Phys. Rev. Lett.* **116** (2016) 172302 [[1510.03068](#)].

List of Figures

1.1	Elementary particles in Standard model.	4
1.2	The quark structure of mesons and baryons.	5
1.3	Inseparability of a quark and anti-quark inspite of adding sufficint energy.	8
1.4	Change on field lines on increasing the separation between a pair of electric charges and a quark-antiquark pair.	8
1.5	Measurements of α_s as a function of the energy scale Q with different degrees of QCD perturbation theory used in the extraction of α_s	9
1.6	Potential due to strong interaction.	9
1.7	The QCD phase diagram.	11
1.8	Different stages of a typical relativistic heavy-ion collisions.	13
1.9	The schematic diagram showing the evolution of the fireball produced in relativistic heavy ion collisions in the light cone picture.	14
1.10	Energy loss of the away side jet in the QGP medium.	17
1.11	A typical non-central heavy-ion collision.	19
1.12	The nuclear modification factors of charged particles as a function of transverse mo- mentum in pPb and PbPb collisions measured by ALICE	22
1.13	Inelastic processes in pp collisions: (a) Non-Diffractive, (b) Single-Diffractive and (c) Double-Diffractive.	22
1.14	Illustration of the way used in QCD Monte-Carlo models to simulate a pp collision. . .	23
2.1	Leading Order (LO) Feynman diagrams for the heavy quark production: (a) gluon fusion and (b) pair annihilation.	30
2.2	Few of the Feynman diagrams for the Next to Leading Order (NLO) processes of the heavy quark production: (a) gluon fusion with one final state gluon (b) flavour excitation and (c) gluon splitting.	30
2.3	Collisional and radiative energy loss of a quark with energy E	31

2.4	Collisional energy loss of charm quark in RHIC and LHC energies.	31
2.5	Comparison of collisional and radiative energy loss for charm and bottom quark.	33
2.6	Schematic diagram of dead cone effect in heavy quarks.	33
2.7	Heavy-flavour decay electron nuclear modification factor R_{AA} and elliptic flow v_2 as a function of p_T in AuAu collisions at $\sqrt{s_{NN}} = 200$ GeV measured by PHENIX.	34
2.8	Elliptic flow (v_2) of D^0 meson compared to light-flavour mesons in AuAu collisions at $\sqrt{s_{NN}} = 200$ GeV measured by STAR experiment.	34
2.9	R_{AA} for prompt D^0 , D^+ and D^{*+} in 0 – 20% and 40 – 80% centrality bins measured by ALICE.	35
2.10	Elliptic flow v_2 of prompt D mesons as a function of p_T in PbPb collisions at $\sqrt{s_{NN}} = 5.02$ TeV in 30-50% centrality class compared to the same and v_2 of π^\pm in PbPb collisions at $\sqrt{s_{NN}} = 2.76$ TeV.	35
2.11	Near-side ($0 < \Delta\varphi < 1.25$ rad) I_{AA} for $2.0 < p_T^e < 3.0$ GeV/ c and $3.0 < p_T^e < 4.0$ GeV/ c as a function of the associated hadron p_T for eHF and hadron triggers.	36
2.12	Angular correlations of $c\bar{c}$ pairs in central AuAu collisions.	37
2.13	The nuclear modification factor R_{pPb} of D mesons and heavy-flavour decay electrons in pPb collisions at $\sqrt{s_{NN}} = 5.02$ TeV as compared to different theoretical models.	38
2.14	Electron-hadron correlations in pPb collisions at $\sqrt{s_{NN}} = 5.02$ TeV with three different multiplicity classes compared to minimum bias pp collisions at $\sqrt{s} = 7$ TeV.	39
2.15	Azimuthal correlations between D mesons and charged particles in pPb collisions at $\sqrt{s_{NN}} = 5.02$ TeV with three different multiplicity classes compared to minimum bias pp collisions at $\sqrt{s} = 7$ TeV.	40
2.16	p_T -differential cross-section of D^{*+} (left) and D^0 (right) with $\sqrt{s} = 5$ and 13 TeV respectively measured by ALICE.	41
2.17	p_T -differential cross section of charm jets tagged with D^0 mesons in pp collisions at $\sqrt{s} = 7$ TeV measured by ALICE.	41
3.1	Large Hadron Collider accelerator ring complex.	44
3.2	The schematic view of ALICE detector.	45
3.3	The schematic view of Inner Tracking System.	48
3.4	The schematic view of Time Projection Chamber.	49
3.5	Specific energy loss (dE/dx) of particles as a function of particle momentum in pp collisions at $\sqrt{s}=7$ TeV.	50

3.6	Particle velocity (β) as a function of particle momentum in pp collisions at $\sqrt{s}=5.02$ TeV	51
3.7	Position of the two VZERO arrays within the general layout of the ALICE experiment. Schematic diagram of VZERO-A and VZERO-C arrays showing their segmentation. . .	52
3.8	The ALIROOT framework.	55
4.1	Schematic diagram for D^0 and D^{*+} decaying into a pion and kaon pair.	62
4.2	Schematic diagram for D^0 decaying in D^0 rest frame.	64
4.3	$\cos\theta^*$ distribution for signal and background D^0 candidates.	64
4.4	Sign of product of impact parameters of two daughter tracks coming from D^0 decay. .	65
4.5	Product of impact parameters for D meson candidates.	66
4.6	Invariant mass distribution of D^0 in different p_T region.	67
4.7	Invariant mass distribution of D^+ in different p_T region.	68
4.8	Invariant mass distribution of D^{*+} in different p_T region.	69
4.9	Tracking efficiency for different period as a function of p_T	71
4.10	Efficiency maps for prompt D^0 , D^+ and D^{*+}	73
4.11	Efficiency maps for feed-down D^0 , D^+ and D^{*+}	74
4.12	Schematic diagram for Event mixing in D-hadron azimuthal correlations.	75
4.13	Example of mixed event correlation distribution for D^0 meson with $p_T(\text{trigg})$ 5-8 GeV/c and $p_T(\text{assoc}) > 0.3$ GeV/c.	76
4.14	Example of signal and sideband regions in a D^0 meson invariant mass spectra.	77
4.15	Correlation distributions between D^0 mesons and charged particles for signal+background region and sideband region and the correlation distribution after sideband correction.	78
4.16	Example of azimuthal correlation distributions between D^0 mesons and charged particles: signal+background region, sideband, and signal minus sideband correlation distributions.	78
4.17	Azimuthal correlations between D^0 mesons and charged particles obtained from Monte Carlo, at kinematics and reconstructed step with $3 < p_T(D) < 5$ GeV/c, $5 < p_T(D) < 8$ GeV/c, $8 < p_T(D) < 16$ GeV/c and $p_T(\text{assoc}) > 0.3$ GeV/c.	80
4.18	Azimuthal correlations between D^0 mesons and charged particles obtained from Monte Carlo, at kinematics and reconstructed step with $3 < p_T(D) < 5$ GeV/c, $5 < p_T(D) < 8$ GeV/c, $8 < p_T(D) < 16$ GeV/c and $0.3 < p_T(\text{assoc}) < 1.0$ GeV/c.	81

4.19	Azimuthal correlations between D^0 mesons and charged particles obtained from Monte Carlo, at kinematics and reconstructed step with $3 < p_T(D) < 5$ GeV/c, $5 < p_T(D) < 8$ GeV/c, $8 < p_T(D) < 16$ GeV/c and $p_T(assoc) > 1.0$ GeV/c.	82
4.20	Ratios of fully corrected azimuthal correlation plots at reconstructed level over azimuthal correlation plots at kinematic level, in the three D^0 p_T bins, for the different associated p_T ranges with $3 < p_T(D) < 5$ GeV/c, $5 < p_T(D) < 8$ GeV/c, $8 < p_T(D) < 16$ GeV/c and $p_T(assoc) > 0.3$ GeV/c.	83
4.21	Ratios of fully corrected azimuthal correlation plots at reconstructed level over azimuthal correlation plots at kinematic level, in the three D^0 p_T bins, for the different associated p_T ranges with $3 < p_T(D) < 5$ GeV/c, $5 < p_T(D) < 8$ GeV/c, $8 < p_T(D) < 16$ GeV/c and $0.3 < p_T(assoc) < 1.0$ GeV/c.	83
4.22	Ratios of fully corrected azimuthal correlation plots at reconstructed level over azimuthal correlation plots at kinematic level, in the three D^0 p_T bins, for the different associated p_T ranges with $3 < p_T(D) < 5$ GeV/c, $5 < p_T(D) < 8$ GeV/c, $8 < p_T(D) < 16$ GeV/c and $p_T(assoc) > 1.0$ GeV/c.	84
4.23	The residual contamination from secondary tracks in the correlation distribution as a function of $\Delta\varphi$ for the D-meson p_T ranges: 3-5, 5-8, 8-16 GeV/c respectively in the associated $p_T > 0.3$ GeV/c.	85
4.24	The primary tracks over all tracks (Blue points), primary tracks over all tracks with moving average of three points (Red points), primary tracks over all tracks fitted with a 9th order polynomial (Red line), in the correlation distribution as a function of $\Delta\varphi$ for the D-meson p_T ranges: 3-5, 5-8, 8-16 GeV/c respectively in the associated $p_T > 0.3$ GeV/c.	86
4.25	Azimuthal correlation distribution between D mesons from B hadrons decay and charged particles obtained from Monte Carlo simulations based on different PYTHIA tune for associated track $p_T(assoc) > 0.3$ GeV/c and D meson p_T 5-8 GeV/c.	87
4.26	f_{prompt} as a function of p_T for D^0 (top), D^+ (middle) and D^{*+} (bottom) estimated on the basis of FONLL predictions.	88
5.1	Two-particle azimuthal correlation distributions between D^0 mesons and charged particles obtained by changing signal and background extraction procedure and the ratio of the correlation distributions with modified signal and background extraction procedure over the standard yield extraction procedure for $p_T(\text{trigger})$ 3-5 GeV/c and $p_T(assoc) > 0.3$ GeV/c.	92

5.2	Two-particle azimuthal correlation distributions between D^+ mesons and charged particles obtained by changing signal and background extraction procedure and the ratio of the correlation distributions with modified signal and background extraction procedure over the standard yield extraction procedure for $p_T(\text{trigger})$ 3-5 GeV/ c and $p_T(\text{assoc}) > 0.3$ GeV/ c	93
5.3	Two-particle azimuthal correlation distributions between D^{*+} mesons and charged particles obtained by changing signal and background extraction procedure and the ratio of the correlation distributions with modified signal and background extraction procedure over the standard yield extraction procedure for $p_T(\text{trigger})$ 3-5 GeV/ c and $p_T(\text{assoc}) > 0.3$ GeV/ c	94
5.4	Ratios of correlation distributions between D^0 -mesons and charged particles obtained by changing the sideband ranges over those obtained with standard sideband ranges with $p_T(\text{trigger})$ 3-5, 5-8, 8-16 GeV/ c and $p_T(\text{assoc}) > 0.3$ GeV/ c	95
5.5	Ratios of correlation distributions between D^+ -mesons and charged particles obtained by changing the sideband ranges over those obtained with standard sideband ranges with $p_T(\text{trigger})$ 3-5, 5-8, 8-16 GeV/ c and $p_T(\text{assoc}) > 0.3$ GeV/ c	96
5.6	Ratios of correlation distributions between D^{*+} -mesons and charged particles obtained by changing the sideband ranges over those obtained with standard sideband ranges with $p_T(\text{trigger})$ 3-5, 5-8, 8-16 GeV/ c and $p_T(\text{assoc}) > 0.3$ GeV/ c	96
5.7	Associated track efficiency maps as a function of p_T for different cut variation (left). Ratio of efficiency maps with different cut variations w.r.t. the standard one (right). .	97
5.8	Ratios of correlation plots between D^0 mesons and charged particles obtained with alternate associated track cut sets over those obtained with standard selection with $p_T(\text{trigger})$ 3-5, 5-8, 8-16 GeV/ c and $p_T(\text{assoc}) > 0.3$ GeV/ c	98
5.9	Ratios of correlation plots between D^+ mesons and charged particles obtained with alternate associated track cut sets over those obtained with standard selection with $p_T(\text{trigger})$ 3-5, 5-8, 8-16 GeV/ c and $p_T(\text{assoc}) > 0.3$ GeV/ c	99
5.10	Ratios of correlation plots between D^{*+} mesons and charged particles obtained with alternate associated track cut sets over those obtained with standard selection with $p_T(\text{trigger})$ 3-5, 5-8, 8-16 GeV/ c and $p_T(\text{assoc}) > 0.3$ GeV/ c	99
5.11	Prompt D^0 efficiencies for alternate cut variations and ratio of prompt D^0 efficiencies for different alternate cutset w.r.t. the standard one.	100

5.12	Prompt D^+ efficiencies for alternate cut variations and ratio of prompt D^0 efficiencies for different alternate cutset w.r.t. the standard one.	100
5.13	Ratios of azimuthal correlations between D^0 mesons and charged particles obtained with alternate D-meson cut sets over those obtained with standard selection with $p_T(\text{trigger})$ 3-5, 5-8, 8-16 GeV/ c and $p_T(\text{assoc}) > 0.3$ GeV/ c	100
5.14	Ratios of azimuthal correlations between D^+ mesons and charged particles obtained with alternate D-meson cut sets over those obtained with standard selection with $p_T(\text{trigger})$ 3-5, 5-8, 8-16 GeV/ c and $p_T(\text{assoc}) > 0.3$ GeV/ c	101
5.15	Ratios of azimuthal correlations between D^{*+} mesons and charged particles obtained with alternate D-meson cut sets over those obtained with standard selection with $p_T(\text{trigger})$ 3-5, 5-8, 8-16 GeV/ c and $p_T(\text{assoc}) > 0.3$ GeV/ c	101
5.16	Ratios of azimuthal correlations between D^0 mesons and charged particles obtained with alternate DCA cut over those obtained with standard DCA cut with $p_T(\text{trigger})$ 3-5, 5-8, 8-16 GeV/ c and $p_T(\text{assoc}) > 0.3$ GeV/ c	102
5.17	Comparison of azimuthal correlation distributions between D mesons (D^0 , D^+ and D^{*+}) and charged particles with D-meson p_T 3-5 GeV/ c , 5-8 GeV/ c and 8-16 GeV/ c and associated $p_T > 0.3$ GeV/ c	104
5.18	Average of D^0 , D^+ and D^{*+} azimuthal correlations, from analysis on the data sample, for the different D p_T bins 3-5, 5-8, 8-16 GeV/ c and associated $p_T > 0.3$ GeV/ c	106
5.19	Example of fit to azimuthal correlation distributions and baseline estimation.	108
5.20	Near-side yield $p_T(D)$ trend for the D-meson average, extracted from fit to the azimuthal correlation distributions, for all the analyzed kinematic ranges of associated track p_T	109
5.21	Near-side sigma $p_T(D)$ trend for the D-meson average, extracted from fit to the azimuthal correlation distributions, for all the analyzed kinematic ranges of associated track p_T	110
5.22	Away-side yield $p_T(D)$ trend for the D-meson average, extracted from fit to the azimuthal correlation distributions, for all the analyzed kinematic ranges of associated track p_T	110
5.23	Away-side sigma $p_T(D)$ trend for the D-meson average, extracted from fit to the azimuthal correlation distributions, for all the analyzed kinematic ranges of associated track p_T	111

5.24	Baseline height for the D-meson average, extracted from fit to the azimuthal correlation distributions, for all the analyzed kinematic ranges of associated track p_T	111
5.25	Two-particle azimuthal correlations between D mesons and charged particles: comparison among pp 7 TeV, 13 TeV and pPb 5.02 TeV data.	112
5.26	Near-side physical observables: comparison among pp 7 TeV, 13 TeV and pPb 5.02 TeV data.	113
5.27	Two particle azimuthal correlations between D mesons and charged particles : comparison of pp 13 TeV data with different Monte-Carlo models.	114
5.28	Near-side physical observables : comparison of pp 13 TeV data with different Monte-Carlo models.	115
5.29	Away-side physical observables : comparison of pp 13 TeV data with different Monte-Carlo models.	116
6.1	Two-particle azimuthal correlations as a function of $(\Delta\eta, \Delta\varphi)$ in pp collisions at $\sqrt{s} = 7$ TeV	119
6.2	Near-side long-range associated yield as a function of (a) transverse momentum, (b) multiplicity for pp $\sqrt{s}=7$ TeV and 13 TeV measured by CMS experiment.	120
6.3	The elliptic flow measurement of inclusive charged particles, K_s^0 and $\Lambda/\bar{\Lambda}$ as a function of transverse momentum for pp $\sqrt{s} = 13$ TeV measured by CMS experiment.	121
6.4	The $v_2^{sub}\{2\}$ and $v_3^{sub}\{2\}$ of charged particles as a function of charged particle multiplicity $N_{trk}^{offline}$ in pp collisions at $\sqrt{s} = 5, 7$ and 13 TeV, pPb collisions at $\sqrt{s}_{NN} = 5$ TeV, and PbPb collisions $\sqrt{s}_{NN} = 2.76$ TeV, after correcting for back-to-back jet correlations estimated from low-multiplicity data.	121
6.5	The \sqrt{s} and centrality $(dn_{ch}/d\eta)$ dependence of mean transverse radial velocity ($\langle\beta\rangle$) and kinetic-freezeout temperature (T_{kin}), as obtained by simultaneous fits in the BGBW framework to the published spectra of π^\pm , K^\pm and $p(\bar{p})$ in pp collisions at LHC is compared with results from similar analysis for AuAu collisions at RHIC. . .	123
6.6	The inverse slope parameter $T_{effective}$ as a function of mass of identified particles ($m_{\pi^\pm} = 0.14$, $m_{K^\pm} = 0.495$, $m_{p(\bar{p})} = 0.938$ GeV/ c^2) as obtained from the measured transverse momentum spectra from non-single diffractive events of pp collisions as measured by the CMS experiment at $\sqrt{s} = 7$ TeV. $\langle N_{ch} \rangle$ is the mean multiplicity of the charged particles.	124

6.7	Near-side long-range associated yield as a function of multiplicity for pp $\sqrt{s}=7$ TeV and 13 TeV, pPb $\sqrt{s_{NN}}=5.02$ TeV and PbPb $\sqrt{s_{NN}} = 2.76$ TeV data measured by CMS experiment.	125
6.8	Two-particle azimuthal correlations of $h - \pi$ (left) and h -p (right) of pPb collisions at $\sqrt{s_{NN}}=5.02$ TeV measured by ALICE.	126
6.9	Elliptic flow v_2 as a function of transverse momentum for pPb $\sqrt{s_{NN}}=5.02$ TeV measured by ALICE.	127
6.10	Identified charged particle ratios K/π , p/π and Λ/K_s^0 for pPb and PbPb collisions with $\sqrt{s_{NN}} = 5.02$ TeV and 2.76 TeV respectively for most central and peripheral event classes.	128
6.11	Inclusive charged particles p_T spectra from generated minimum-bias events of pp collisions at $\sqrt{s}= 7$ and 13 TeV from the EPOS3 event generator, with hydrodynamic calculations, are compared with data, as measured by the ALICE and ATLAS. . . .	129
6.12	Two particle $\Delta\eta - \Delta\varphi$ charge particle correlation function for $1 < p_T^{\text{trigger}}, p_T^{\text{associated}} < 2$ GeV/c with unidentified charged particle as trigger, for the hydrodynamic-EPOS3 generated pp collisions at $\sqrt{s} = 7$ TeV and 13 TeV for events of multiplicity-class $N_{ch} > 110$ and $N_{ch} < 35$	130
6.13	One dimensional $\Delta\varphi$ projection for high-multiplicity events for the region of ridge-like correlations obtained from the long-range two-particle azimuthal correlations of charged particles, averaged over $2 < \Delta\eta < 4$, for $1 < p_T^{\text{trigger}}, p_T^{\text{associated}} < 2$ GeV/c, $2 < p_T^{\text{trigger}}, p_T^{\text{associated}} < 3$ GeV/c and $3 < p_T^{\text{trigger}}, p_T^{\text{associated}} < 4$ GeV/c from the data and the EPOS3 generated events of pp collisions at $\sqrt{s} = 7$ and 13 TeV.	131
6.14	The transverse momentum spectra for π^\pm , K^\pm , $p(\bar{p})$ as measured by the CMS experiment at LHC for the event-class of average multiplicity = 131 and 98 in pp collisions at $\sqrt{s} = 7$ TeV, along with BG-blast-wave fits.	133
6.15	Average transverse momentum, $\langle p_T \rangle$, as a function of charged particle multiplicity, N_{ch} , as measured by ALICE and ATLAS.	135
6.16	Average transverse momentum, $\langle p_T \rangle$, as a function of mean charged particle multiplicity, $\langle N_{ch} \rangle$, for the identified charged particles in pp collisions at $\sqrt{s} = 7$ and 13 TeV. The CMS data have been compared with simulated events using EPOS3 event generator with and without hydrodynamics.	136

6.17	The mass ordering of the inverse slope parameter $T_{effective}$ of identified particles ($m_{\pi^\pm} = 0.14$, $m_{K^\pm} = 0.495$, $m_{p(\bar{p})} = 0.938 \text{ GeV}/c^2$) as measured by the CMS experiment at $\sqrt{s} = 7 \text{ TeV}$ and 13 TeV , for a few event classes of high-multiplicity, is compared with those obtained from EPOS3-hydro simulated events.	138
6.18	Centrality dependent invariant yields of identified charged particles in pPb collisions at $\sqrt{s_{NN}} = 5.02 \text{ TeV}$, measured by ALICE compared with the simulated events from the EPOS3 event generator with Hydro calculations.	139
6.19	Average transverse momentum, $\langle p_T \rangle$, as a function of charged particle multiplicity, N_{ch} , as measured by ALICE in pPb collisions at $\sqrt{s_{NN}} = 5.02 \text{ TeV}$ respectively, compared with the simulated events from EPOS3 event generator, with and without Hydro calculations.	140
6.20	Average transverse momentum, $\langle p_T \rangle$, as a function of mean charged particle multiplicity, $\langle N_{ch} \rangle$, as measured by CMS in pPb collisions at $\sqrt{s_{NN}} = 5.02 \text{ TeV}$, compared with EPOS3 generated events.	141
6.21	The mass ordering of the inverse slope parameter $T_{effective}$ of identified particles ($m_{\pi^\pm} = 0.14$, $m_{K^\pm} = 0.495$, $m_{p(\bar{p})} = 0.938 \text{ GeV}/c^2$) in pPb collisions at $\sqrt{s_{NN}} = 5.02 \text{ TeV}$: comparison between CMS data and EPOS3 generated events.	142
6.22	Centrality dependent correlated yield as a function $\Delta\varphi$, as obtained from the long-range two-particle azimuthal correlations between charged particle and between D mesons and charged particles, for EPOS3 generated pPb collisions at $\sqrt{s_{NN}} = 5.02 \text{ TeV}$ in different ranges of $p_T^{trigger}$ and p_T^{assoc}	143
6.23	Centrality dependent correlated yield, as obtained from the long-range two-particle azimuthal correlations of D-mesons and charged particles, averaged over $2 < \Delta\eta < 4$, for $3 < p_T^{trigg} < 5 \text{ GeV}/c$ and $1 < p_T^{assoc} < 3 \text{ GeV}/c$, for the hydrodynamic-EPOS3 generated pPb collisions at $\sqrt{s_{NN}} = 5.02 \text{ TeV}$	144
6.24	Invariant yield of EPOS3 generated D-mesons from two different sources, plasma and non-plasma.	144
6.25	Correlated yield, as obtained from the long-range two-particle azimuthal correlations of D-mesons and charged particles, averaged over $2 < \Delta\eta < 4$, for $3 < p_T^{trigg} < 5 \text{ GeV}/c$ and $1 < p_T^{assoc} < 3 \text{ GeV}/c$, for the hydrodynamic-EPOS3 generated pPb collisions with 0-20% centrality events at $\sqrt{s_{NN}} = 5.02 \text{ TeV}$	145

List of Tables

1.1	Three generations of quarks and leptons and their properties.	5
1.2	The fundamental forces and gauge bosons with their properties	5
2.1	Properties of charm quark containing mesons.	28
4.1	General purpose MC productions.	71
4.2	HF enriched MC sample.	72
5.1	Systematic table for D^0	103
5.2	Systematic table for D^+	103
5.3	Systematic table for D^{*+}	103
6.1	T_{kin} , $\langle\beta\rangle$ and n , the parameters of the the BGBW, obtained from the simultaneous fit to the published spectra of π^\pm , K^\pm and $p(\bar{p})$ and respective $\chi^2/n.d.f$ for pp collisions at $\sqrt{s} = 7$ and 13 TeV for different event classes depending on average multiplicity, $\langle N_{ch} \rangle$, in the range $ \eta < 2.4$	133
6.2	T_{kin} , $\langle\beta\rangle$ and n , the parameters of the the BGBW, obtained from the simultaneous fit to the spectra obtained from simulated EPOS events for π^\pm , K^\pm and $p(\bar{p})$ and respective $\chi^2/n.d.f$ for pp collisions at $\sqrt{s} = 7$ and 13 TeV for different event classes depending on average multiplicity, $\langle N_{ch} \rangle$, in the range $ \eta < 2.4$	134

Chapter 1

Introduction

The Quark-Gluon Plasma (QGP) [1] is a thermalized state of strongly interacting matter with partonic degrees of freedom. In QGP, the quarks and gluons do not remain confined within a hadron and they rather become relatively free to propagate over a volume larger than that of a typical hadron. This state of nuclear matter can exist at an extreme condition of high temperature and/or density. It is believed that the QGP state of matter might have existed immediately after the big-bang for a few microseconds and may exist in the core of the neutron stars. In laboratories, the production of QGP was predicted in relativistic collisions of nuclei [2, 3, 4]. Dedicated efforts to detect possible QGP signals in relativistic heavy-ion collisions in the laboratory were initiated by several experiments at Alternating Gradient Synchrotron (AGS), at Brookhaven National Laboratory (BNL) in late eighties, joined by experiments at Super Proton Synchrotron (SPS), CERN during nineties of the 20th century. Experiments at both the AGS and the SPS were of fixed target type and the centre-of-mass energy of collisions were limited to a few tens of GeV. At SPS, an indication of formation of QGP was observed [5]. Finally, the experimental efforts in search of QGP were culminated at Relativistic Heavy-Ion Collider (RHIC) at the BNL where AuAu collisions at $\sqrt{s_{NN}} = 130$ and 200 GeV provided the first convincing evidence of formation of QGP, as observed through comprehensive analysis of data, recorded by four major experiments, namely, PHENIX, PHOBOS, BRAHMS and STAR [6, 7, 8, 9]. The experiments at the Large Hadron Collider (LHC) at CERN with PbPb collisions at $\sqrt{s_{NN}} = 2.76, 5.02$ TeV aim to study the properties of QGP with increased energy density, volume and lifetime. As the names imply, both RHIC and LHC are collider facilities.

In the theoretical front, the only first principle calculation on thermodynamic properties of QGP is available in the LQCD framework. While the LQCD calculations in vanishing baryon chemical potential (μ_B), corresponding to $\sqrt{s_{NN}}$ at LHC (for $\sqrt{s_{NN}}$ at RHIC, the μ_B is very small) is fairly advanced, in the high μ_B range corresponding to energy of collisions at AGS and SPS, the progress

of LQCD calculations is still hindered by some procedural complications. In any case, however, the LQCD calculations do not suggest any signal of QGP that can be straight away connected to any experimental observable and the interpretation to the observed features of particle productions in relativistic heavy-ion collisions are mostly dependent on several signals proposed by some theoretical/phenomenological models. Apart from the lack of comprehensive theoretical back-up, the experimental study of QGP itself is very challenging because of the very short lifetime and tiny volume of QGP matter that is formed in relativistic heavy-ion collisions. In fact, RHIC discovery on QGP did not come from any “smoking-gun” type of signal, but from the observance of several signals. The two most unambiguous signals had been the azimuthal anisotropic flow of produced particles and suppression of high- p_T particles due to energy loss while traversing the dense partonic medium. In extracting signals of QGP in heavy-ion collisions, the collision data of proton-proton (pp) and proton-nucleus (pA) serve as the baselines. While the pp data is compared to ensure that the signal is not mimicked by superposition of many elementary pp collisions, the pA data help disentangling the effect, if any, of cold nuclear matter and that of the hot nuclear matter (QGP).

The pp and pPb data at LHC, however, revealed some unexpected features. The high-multiplicity events of pp and pPb collisions exhibit features of particle productions which resemble that in ultra-relativistic heavy-ion collisions, where QGP is already established. So, while the minimum-bias pp and pPb data are used as the baseline for heavy-ion collisions, the in-depth study of high-multiplicity events of these small collision systems like pp and pPb at LHC energies are now in the focus of the frontline fields of research in high energy physics. Though the origins of these unexpected features are not yet fully understood, the experimental findings definitely indicate to a new aspect of physics of particle productions in relativistic collisions.

The thesis presents studies addressing different aspects of QGP and related physics. The content of this thesis is broadly classified into two parts. The first part contains the results of analysis of minimum-bias data of pp collisions at 13 TeV, recorded by ALICE at the LHC. The focus of the study has been on the heavy-flavour jets, in terms of two-particle angular correlations between D-mesons and charged particles. The second part contains simulation based phenomenological studies addressing possible hydrodynamic origin of the particle production in high-multiplicity pp and pPb events at the LHC energy. The presentation has been arranged chapter-wise. Following the Introduction in Chapter - 1, the Chapters 2, 3, 4 and 5 pertain to the data analysis part. The Chapter - 6 presents the simulation-based study. The Chapter 7 concludes the thesis. Brief descriptions of different chapters are given below:

- **Chapter1 (Introduction):** This chapter introduces the Quark-Gluon plasma (QGP), its pro-

duction in laboratory, properties and several probes to study this medium. For the convenience of the readers, the discussion is followed by some preliminaries of Standard model, quantum chromodynamics (QCD), QCD phase diagrams etc. Next, a brief discussion is made on the main focus of this thesis.

- **Chapter 2 (Study of open heavy flavours):** This chapter contains an introduction to heavy-flavour mesons, their production mechanism and properties. An experimental overview is presented here for the study of open heavy-flavour as a probe of QGP.
- **Chapter 3 (Experimental Setup):** We have done the analysis of minimum-bias events of pp collisions at $\sqrt{s} = 13$ TeV recorded by ALICE detector. In this chapter, we have described the ALICE detector configuration and the working principle of several sub-detectors. The online and offline data taking procedure as well as the overall ALICE analysis framework is discussed here.
- **Chapter 4 (Analysis detail):** This chapter contains the detail of the analysis tool: the two-particle azimuthal correlation with heavy-flavour hadron trigger and charged particles followed by a discussion on reconstruction of heavy-flavour hadrons, topological cut selection, background subtraction, event-mixing and efficiency corrections etc.
- **Chapter 5 (Systematic study and results):** Here, we have discussed the several sources of systematic uncertainties for the heavy-flavour correlation analysis. We have evaluated the uncertainty values for each sources and obtained the final result by taking the average of three D meson candidates D^0 , D^+ and D^{*+} . We have compared the results of pp $\sqrt{s} = 13$ TeV with the pp $\sqrt{s} = 7$ TeV and pPb $\sqrt{s_{NN}} = 5.02$ TeV. Several Monte-Carlo models are also used to check the compatibility with data.
- **Chapter 6 (Studies in small systems with hydro-based event simulations):** In this chapter, we have studied the high multiplicity events of pp and pPb collisions in LHC energies with EPOS3 hydro-based event generator. We have looked into some of the features of particle production mechanism in small systems win terms of observables which reveal the collective properties of particle production in relativistic heavy-ion collisions. Both the qualitative and quantitative comparisons have been made for the results obtained in EPOS3 event generator to that of the data.
- **Chapter 7 (Summary and outlook):** Finally, we summarize the observations obtained from both the parts of this thesis, i.e. the data analysis part as well the simulation studies. A brief

discussion on the scope of future studies is added.

1.1 The Standard Model

Extensive research activities in the last few decades in high energy physics and particle physics led us to know a lot about the fundamental constituents of matter and the interactions among them. The knowledge thus gathered is put together in Standard Model (SM) [10]. According to the **Standard Model (SM)**, a well tested theoretical framework, the basic constituents of matter are quarks, leptons, gauge bosons, Higgs boson and their anti-particles. Pictorially, the elementary particles of standard model are summarized in figure 1.1.

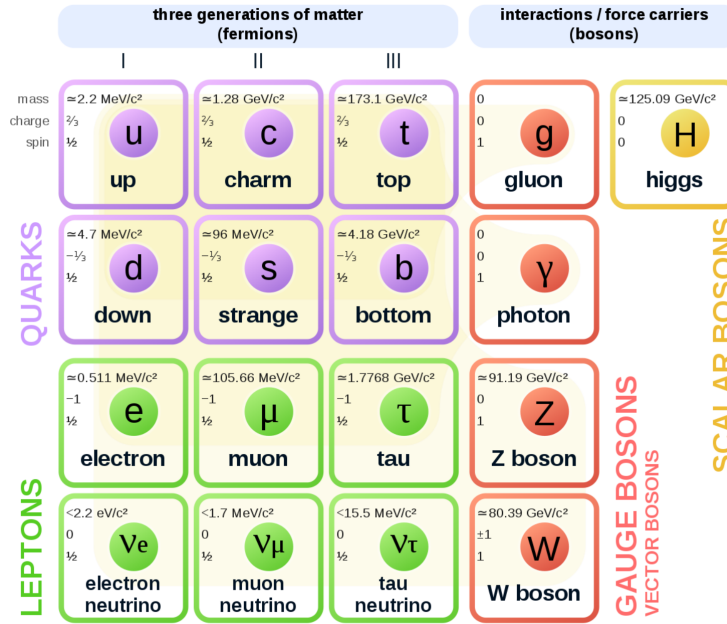


Figure 1.1: Elementary particles in Standard model [11].

A brief description of the basic constituents of matter and the fundamental forces is given below:

- **Quarks and leptons:** Quarks and leptons are the spin- $\frac{1}{2}$ particles, i.e, “fermions”. Standard model is consisted of 6 quarks, 6 leptons and their anti-particles classified into three generations. Table 1.1 shows the names and basic properties of the quarks and leptons belonging to different generations. In normal nuclear matter, the quarks and anti-quarks remain confined in “hadrons”. Hadrons are classified into “Baryons” and “Mesons”. Baryons (anti-baryon) are formed with a combination of three quarks (anti-quarks) and mesons are formed with a pair of quarks and anti-quarks as shown in figure 1.2.

1.1. The Standard Model

generation	particle	symbol	charge	mass (GeV/ c^2)	type
First	up	u	2/3	4×10^{-3}	quark
	down	d	-1/3	7×10^{-3}	quark
	electron	e	-1	5.1×10^{-4}	lepton
	e-neutrino	ν_e	0	$< 7 \times 10^{-9}$	lepton
Second	charm	c	2/3	1.5	quark
	strange	s	-1/3	0.2	quark
	muon	μ	-1	0.106	lepton
	μ -nutrino	ν_μ	0	$< 2.7 \times 10^{-4}$	lepton
Third	top	t	2/3	175	quark
	bottom	b	-1/3	4.7	quark
	tau	τ	-1	1.78	lepton
	τ -neutrino	ν_τ	0	$< 2.7 \times 10^{-2}$	lepton

Table 1.1: Three generations of quarks and leptons and their properties.

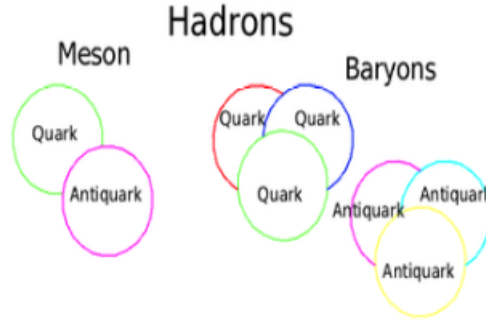


Figure 1.2: The quark structure of mesons and baryons.

- **Gauge bosons:** These are basically the carrier of three fundamental forces of nature which includes strong, weak, electromagnetic. Table 1.2 enlists the fundamental forces and carrier particles along with some of their basic properties.

Force	boson	symbol	charge	mass (GeV/ c^2)	spin
Strong	gluon	g	0	0	1
Electromagnetic	γ	c	0	0	1
Weak	W and Z boson	W^\pm and Z^0	± 1 and 0	81 and 92	1

Table 1.2: The fundamental forces and gauge bosons with their properties

- **Higgs boson:** Higgs boson, considered as a scalar boson, is responsible for providing mass to all other particles in standard model. Though the existence of this particle is theoretically predicted in 1964 by Peter Higgs [12], it was experimentally verified in 2012 by LHC.
- **Fundamental interactions:** There are four fundamental interactions (also known as fundamental forces) existing in nature: gravitational, electromagnetic, strong and weak. Among

these interactions, the gravitational and electromagnetic interactions produce long-range forces which can be observed directly in our daily life, while the weak and strong interactions play a role within subatomic distances. The Standard Model includes the following three fundamental interactions:

- **Electromagnetic force:** This force is carried by the photons and includes the distinct electric and magnetic forces. The electric force acts among the static and/or moving charged particles while the magnetic force acts among moving charges only. This means every charged particle creates an electric field and the moving charged particles create magnetic fields. The electromagnetic interactions are responsible for the attraction among orbital electrons and atomic nuclei through which the atoms are held together, as well as the chemical bonding and electromagnetic waves, including visible light.
- **Strong force:** This force is carried by the gluons that glue the quarks together inside a hadron. As a residual effect, it creates the nuclear force that binds the hadrons to form atomic nuclei. At a distance 1 fm or less, the strength of this force is around 137 times the electromagnetic force, but it dies off with distance much faster than electromagnetic or gravitational force, thus making it impossible to detect outside the nucleus.
- **Weak force:** This force acts inside individual nucleons, which means it is even shorter ranged than the strong force. The weak interaction is carried by W and Z bosons which mediate the radioactive decay.

We elaborate further the strong interaction as it forms the basic physics framework pertaining to the work of the thesis.

1.2 Quantum Chromodynamics (QCD)

The theory of strong interaction of the elementary particles, quarks and gluons, as described in SM is the Quantum Chromodynamics (QCD). The QCD is a non-Abelian gauge theory with symmetry group $SU(3)$. The salient features of QCD can be better presented by comparing the well understood theory of electromagnetic interactions, the Quantum Electrodynamics (QED). While the QED deals with interactions among electric charges, the QCD involves interactions among “colour” charge carrying elementary particles. In contrast to two varieties of electric charges, the colour charge comes in three varieties labeled as red, green and blue. Also, while the mediating photons are charge-less, the mediating gauge bosons of strong interaction are the spin-1 gluons (of eight different

1.2. Quantum Chromodynamics (QCD)

types) of bi-coloured objects. Accordingly, while in QED the photons are not self-interacting, the gluons in the QCD interact among each other and with quarks. The QCD Lagrangian reads [13]

$$\begin{aligned}\mathcal{L}_{\text{QCD}} = & \sum_f \bar{\psi}_f^i (i\gamma^\mu \partial_\mu - m_f) \psi_f^i - \frac{1}{4} (\partial_\mu A_\nu^a - \partial_\nu A_\mu^a) (\partial^\mu A^{a\nu} - \partial^\nu A^{a\mu}) \\ & - \frac{1}{2\xi} (\partial^\mu A_\mu^a) (\partial^\nu A_\nu^a) + (\partial^\mu \phi^{\dagger a}) (\partial_\mu \phi^a) + \sum_f g_s \bar{\psi}_f^i t_{ij}^a \gamma^\mu \psi_f^j A_\mu^a \\ & - g_s f^{abc} (\partial^\mu A_\nu^a) A^{b\mu} A^{c\nu} - \frac{1}{4} g_s^2 f^{abe} f^{cde} A_\mu^a A_\nu^b A^{c\mu} A^{d\nu} - g_s f^{abc} (\partial^\mu \phi^{\dagger a}) \phi^b A_\mu^c \quad (1.1)\end{aligned}$$

where, g_s is the strong coupling, f is the flavour index, i, j are the color indices of the fundamental representation of SU(3), a, b, c etc. are colour indices of the adjoint representation of SU(3) and ξ is the gauge parameter; ψ_f^i ($\bar{\psi}_f^i$) are the quark(anti-quark) fields, A_μ^a are the gluon fields and ϕ^a are the ghost fields. In the above equation, t^a are the generators of SU(3) satisfying the Lie algebra

$$[t^a, t^b] = i f^{abc} t^c \quad (1.2)$$

with f^{abc} being the totally antisymmetric structure functions.

Unlike QED, the QCD coupling constant ($\alpha_s = \frac{g_s^2}{4\pi}$) shows a different kind of behaviour with respect to the momentum transfer involved in the process. The “running coupling constant” of QCD can be obtained from the Renormalization Group (RG) equation by calculating the QCD β -function and is given by [14]

$$\alpha_s(Q^2) \simeq \frac{4\pi}{(11 - \frac{2}{3}N_f) \ln\left(\frac{Q^2}{\lambda_{\text{QCD}}^2}\right)} \quad (1.3)$$

where, N_f is number of quark flavours, Q^2 is momentum transfer in strong interaction and λ_{QCD} is QCD scale parameter. The specific momentum dependence of α_s leads to the following two novel aspects of QCD:

- **Colour Confinement:** The phenomenon that prohibits a colour charge to be isolated is known as colour confinement. It is caused by the mutual interactions of gluons, the mediator of strong interactions. In simple words, if we try to separate a quark-antiquark pair ($q\bar{q}$) by large distance, the energy provided is being utilized in creating a new $q\bar{q}$ pair, which in turn produce two sets of composite systems of $q\bar{q}$. A schematic diagram of this process is shown in figure 1.3. The field lines are collimated into a tube-like shape (called “flux tube”) due to the mutual interactions among gluons. Unlike a pair of electric charges, by increasing the separation between a quark-antiquark pair, the force does not become weak but remains constant as shown

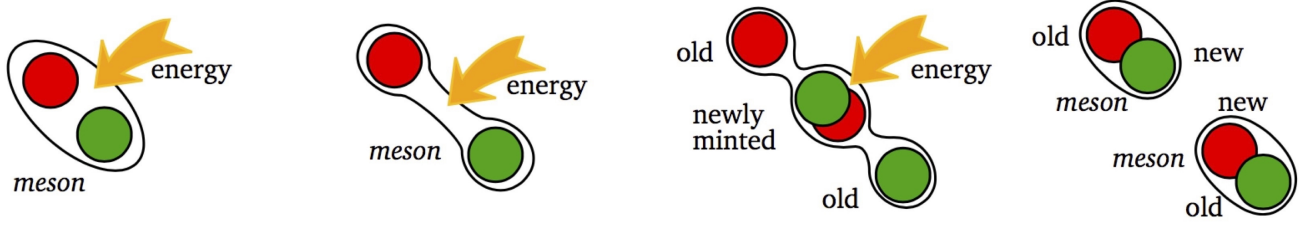


Figure 1.3: Inseparability of a quark and anti-quark inspite of adding sufficient energy.

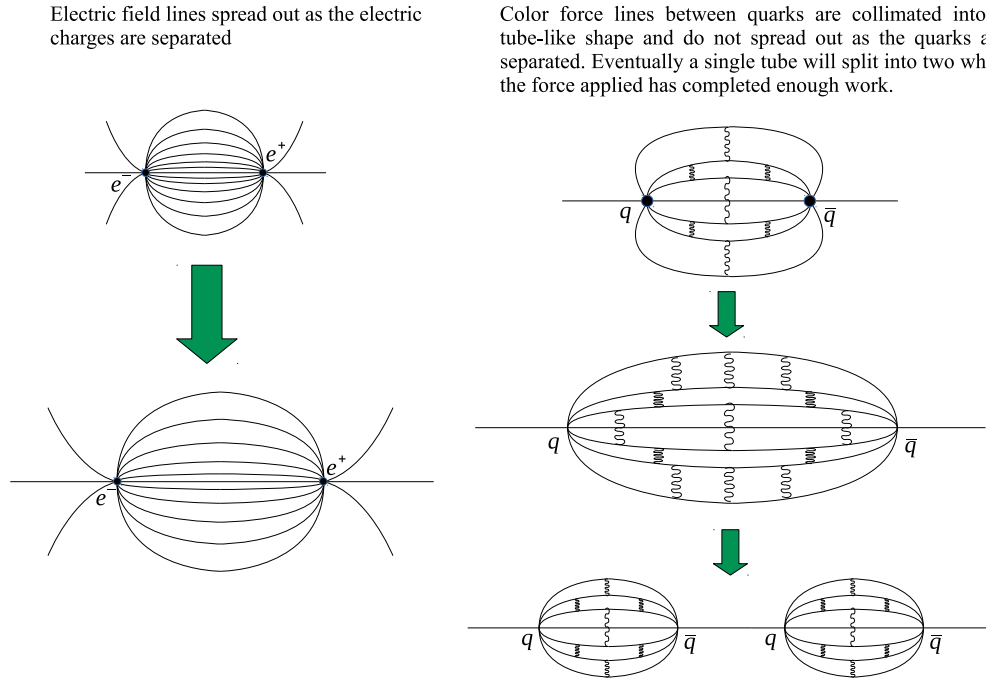


Figure 1.4: Change on field lines on increasing the separation between a pair of electric charges (left) and a quark-antiquark pair (right).

in figure 1.4. Finally one tube breaks into two tubes when sufficient energy is available to create a new quark-antiquark pair and two new mesons. Thus, the colour confinement is the reason why we can not find a single isolated quark in nature.

- **Asymptotic Freedom:** It is a property of the steady reduction in the interaction strength with the increment of the interaction energy scale as well as the decreased length scale. In this regime, we look at high energies (distances ≤ 1 fm) in which the perturbative QCD can be applied as the strong coupling becomes $\alpha_s \ll 1$. In simple word, the quarks and gluon becomes weakly interacting and almost free to roam around. The variation of α_s is shown as a function of energy scale Q in figure 1.5.

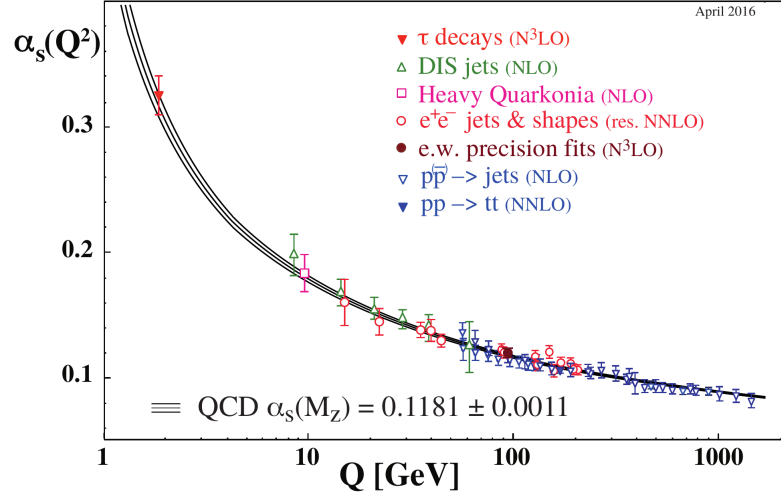


Figure 1.5: Measurements of α_s as a function of the energy scale Q with different degrees of QCD perturbation theory used in the extraction of α_s as indicated in brackets [15].

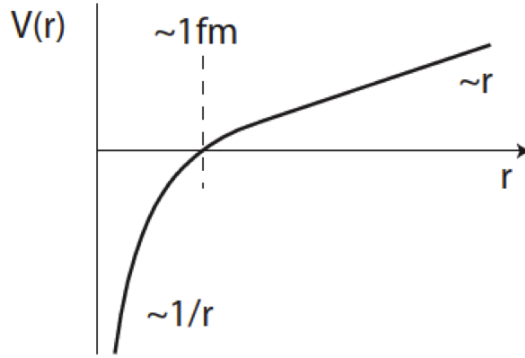


Figure 1.6: Potential due to strong interaction.

The static quark-antiquark potential can be written as

$$V(r) = -\frac{4}{3} \frac{\alpha_s}{r} + kr . \quad (1.4)$$

The potential contains two parts: a Coulomb-like term and a term that rises linearly with the quark-antiquark distance (r) as shown in figure 1.6. The two quarks can be considered that they are bound by a colour string with tension k . The linear part, which becomes relevant at large distances, is responsible for the fact that pulling the quarks apart the energy in the gluon field connecting the quarks becomes larger than the mass of a quark-antiquark pair. So, it becomes favourable energetically for the gluons to produce a new quark-antiquark pair. For this reason, at low energies one can not observe individual quarks, they immediately confine (or hadronize) into hadronic bound states.

1.3 The QCD phase diagram and the Quark-Gluon Plasma

Rolf Hagedorn first gave the idea of de-confinement in one of his early works [16], that predicted a limiting temperature (Hagedorn temperature) for the hadrons beyond which the hadrons could not exist. Later [1, 17, 18, 19], it was realized that, the asymptotically free domain of QCD may lead to the existence of extremely hot and dense form of nuclear matter termed as the Quark-Gluon Plasma (QGP). At very high energy, due to large momentum transfer, the effective coupling between the quarks and gluons becomes very small leading to the asymptotic freedom region where the quarks and gluons behave almost like free particles, within a domain larger than the dimension of a nucleon. This is called “de-confinement” of quarks and gluons. The collisions among the de-confined quarks and gluons in a thermal bath lead to a thermalized partonic matter **Quark-Gluon Plasma** (QGP) [2, 3, 4], a state of asymptotically free thermalized quarks and gluons existing in a volume larger than a typical hadronic volume. This novel state of matter is of great interest in the field of research mainly due to its possible existence in: (1) the microsecond old universe after the Big-Bang where the temperature and density were high enough for the QGP to be existed and (2) the core of the neutron stars where the baryon density could be as high as a few times (5-10 times) more than normal nuclear matter density (0.16 fm^{-3}) and the temperature is almost zero ($T \leq 50 \text{ MeV}$). The heavy-ion collisions at ultra-high relativistic centre-of-mass energy are proven means of formation of QGP in the laboratory.

The formation or the existence of the QGP, the partonic phase, implies phase transition or crossover between the two phases of QCD matter, the hadronic and the partonic. The basic QCD phase diagram and the phase transition or the crossover in the (T, μ_B) -plane is shown in Fig. 1.7. As can be seen in the figure 1.7, the changes between the hadronic phase and the QGP phase can occur at high temperature and/or baryon density. At high temperature and low baryon chemical potential a crossover takes place, while at low temperature and high baryon chemical potential, the changes are believed to occur through the first order phase transition. The experiments in relativistic heavy-ion collisions are performed to create such extreme conditions in the laboratory to probe different regions of the QCD phase diagram as well as to study the hadron-parton phase transitions. As per the present understanding, there exists a critical point in the $T - \mu_B$ plane where the first-order phase transition ends [21, 22, 23].

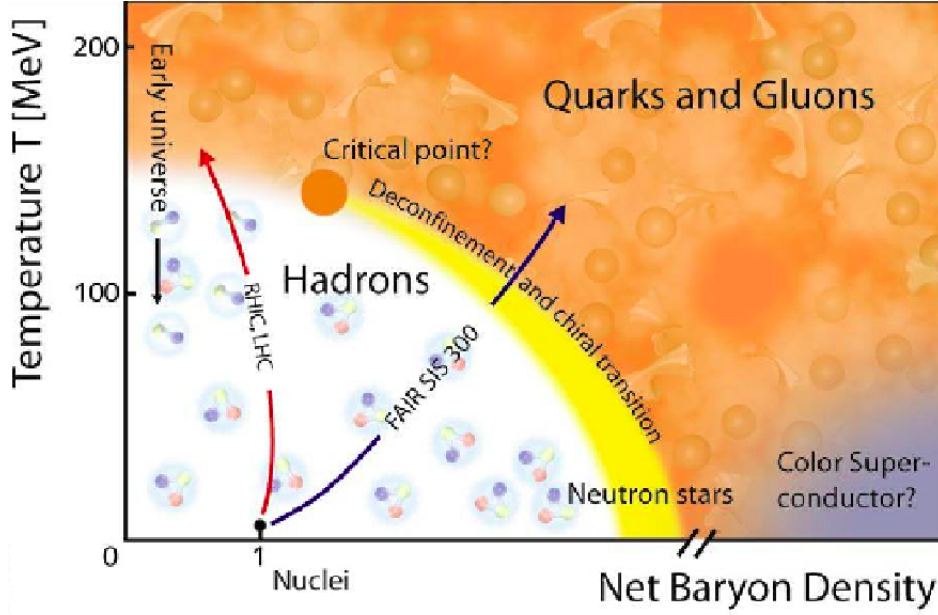


Figure 1.7: The QCD phase diagram [20].

1.4 The study of QGP in relativistic heavy-ion collisions

In high energy physics experiments in the laboratories, the relativistic collisions among heavy-ions are arranged in two ways. In a fixed target type experiment, a beam of accelerated heavy ions are made to collide with a fixed target. In a collider experiment, two beams of accelerated heavy ions are steered to collide at an interaction point. During the collision process, due to deposition of large kinetic energy in the collision zone, a fireball of extremely high energy density (\sim few GeV/fm^3) is created. The temperature (T) of the fireball could be $T \sim$ a few hundreds of MeV. Under such extreme conditions, we expect the de-confinement phase transition to occur, leading to the formation of QGP. The QGP has been formed in experiments at the Relativistic Heavy-ion Collider (RHIC) at Brookhaven in AuAu collisions at center-of-mass energy, $\sqrt{s_{NN}} = 130$ and 200 GeV [6, 7, 8, 9] and at the Large Hadron Collider (LHC) at CERN in PbPb collisions at $\sqrt{s_{NN}} = 2.76$ and 5.02 TeV [24, 25, 26]. The $\sqrt{s_{NN}}$ at RHIC and LHC correspond to small or vanishing value of baryon chemical potential (μ_B) at high temperature (T) in the QCD phase diagram in (T, μ_B) -plane. Theoretically, the first-principle Lattice QCD (LQCD) thermodynamic calculations at vanishing μ_B predict crossover [22, 27] between the QCD-phases as shown in figure 1.7. However, the lattice simulation at finite μ_B to study expected first order parton-hadron phase transition [28, 29, 30] at high μ_B is not yet fully developed, limiting reliable theoretical support. However, several theoretical and phenomenological models, by explaining different experimental observations, help in developing the present physics understanding of relativistic heavy-ion collisions and some basic physics properties

of the QGP.

We briefly discuss the important milestones in search of QGP in laboratory at several facilities.

- **Alternating Gradient Synchrotron (AGS):** It is a fixed target type experiment located at Brookhaven National Laboratory (BNL), New York, USA. In 1960, the AGS became the world's premiere accelerator when it reached energy of 33 billion electron volts (GeV) by accelerating protons. In 1991, the AGS Booster further increased the capabilities of the AGS, enabling it to accelerate more intense proton beams and heavy ions. Now a days, AGS serves as the injector for Brookhaven's Relativistic Heavy Ion Collider (RHIC). The AGS Booster provides particle beams also to the NASA Space Radiation Laboratory.
- **Super Proton Synchrotron (SPS)** The QGP-like new state of matter was first indicated by SPS in PbPb collisions [5]. It is Synchrotron type particle accelerator situated near Geneva, Switzerland. Now a days, SPS plays role of the main injector for the Large Hadron Collider (LHC).
- **Relativistic Heavy Ion Collider (RHIC):** It is a collider experiment situated at Brookhaven National Laboratory (BNL), New York, USA. It performs collisions of AuAu, UU etc. at maximum $\sqrt{s_{NN}} = 200$ GeV. Comprehensive efforts by four major experiments at RHIC, namely, (i) Pioneering High Energy Nuclear Interaction Experiment (PHENIX) (ii) PHOBOS (iii) Broad Range Hadron Magnetic Spectrometers (BRAHMS) and (iv) Solenoidal Tracker at RHIC (STAR) made the discovery on formation of QGP [6, 7, 8, 9] in the laboratory possible.
- **Large Hadron Collider (LHC):** This is a collider experiment and currently, the largest particle accelerator, both in terms of dimension and the energy of the beams, in the world. The LHC is situated at the site of the European Organization for Nuclear Research (CERN) at the border of Switzerland and France. The maximum centre-of-mass energy ($\sqrt{s_{NN}}$) as available on date at LHC for colliding two Pb ions is ~ 5.02 TeV per nucleons and for pp collisions at $\sqrt{s}=13$ TeV (the planned \sqrt{s} is 14 TeV). The ongoing major experiments at the LHC are: (i) A Toroidal LHC Apparatus (ATLAS) [31] (ii) Compact Muon Solenoid (CMS) [32] (iii) Large Hadron Collider beauty (LHCb) [33] and (iv) A Large Ion Collider Experiment (ALICE) [34].
- **Facility of Antiproton and Ion Research (FAIR):** In contrast to experiments at two colliders, the RHIC and the LHC, FAIR, the upcoming accelerator complex at Darmstad in Germany will facilitates fixed-target type Compressed Baryonic Matter (CBM) experiment. In both the RHIC and LHC, the regions of QCD phase diagram that are explored are the ones with

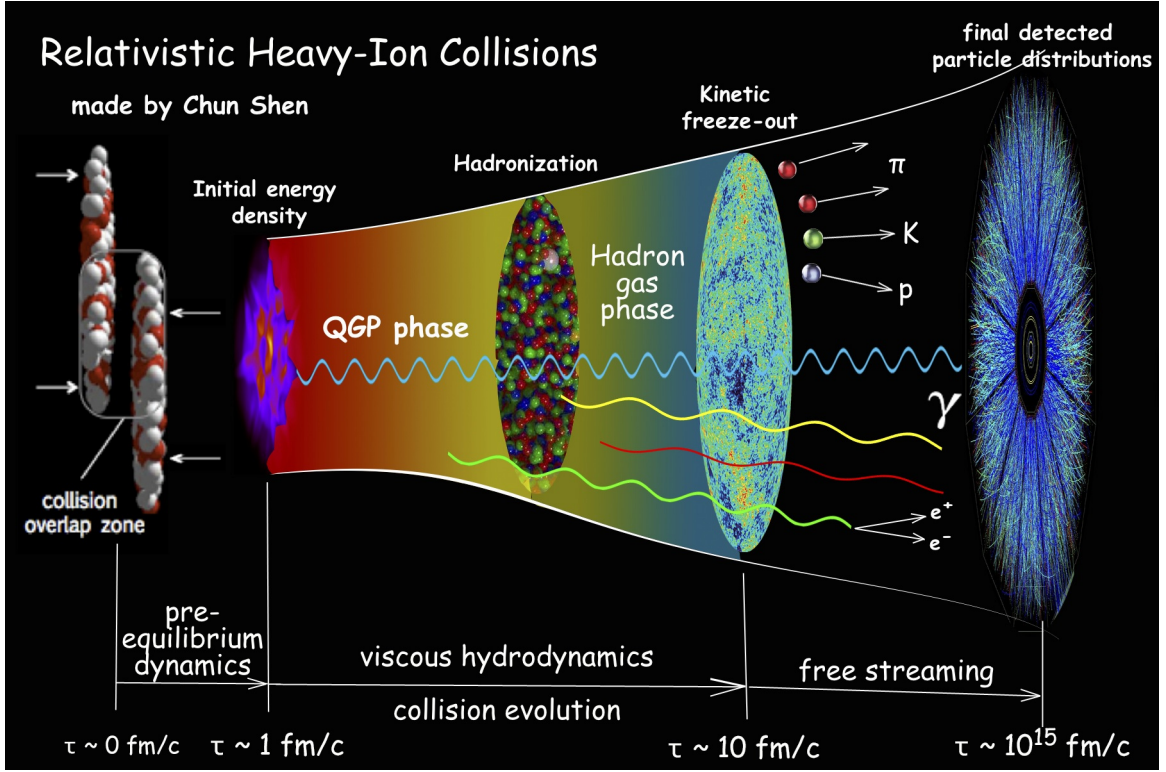


Figure 1.8: Different stages of a typical relativistic heavy-ion collisions [37]

high temperature and low baryon density. In contrast, at the FAIR, the Compressed Baryonic Matter (CBM) experiment will be carried out, which aims to study the low temperature and high baryon density region of the QCD phase diagram [35, 36].

The different stages of a typical relativistic heavy-ion collision is schematically shown in Fig. 1.8 and described below:

1. **Preequilibrium Initial State:** The two Lorentz contracted nuclei moving with ultra relativistic velocities collide with each other with impact parameter b , at $t=0$ and $z=0$, i.e., at the origin. Figure 1.9 shows the space time diagram of relativistic heavy-ion collisions. Depending on b , there is a full or partial overlap of the colliding nuclei and a large fraction of their kinetic energy is dumped in the collision zone due to the inelastic collisions between nucleons. A large number of quarks and gluons are emitted from the overlap zone where the energy has been deposited.
2. **Thermalization:** The quarks and gluons, created from the collision zone, interact among themselves with a characteristic mean free path much smaller than the system size. After sufficient re-interactions, the system is believed to achieve a state of local thermal equilibrium

1.5. The Signatures of QGP

the observables are divided into two categories: (i) soft probes corresponding to the energy scale associated with the temperature of the medium and (ii) hard probes corresponding to the processes involving high energies much greater than the temperature scale of the medium. The examples of soft probes are: electromagnetic probes (thermal photon and dileptons), hadrons with low transverse momenta (p_T) etc. On the other hand, the hard probes include the high energetic particles produced in early stages of a relativistic heavy-ion collision (for example: Drell-Yan dileptons, heavy quarks, quarkonia etc.). The hard probes, being an independent degree of freedom do not participate in the thermalization of the medium and they simply pass through the medium. While propagating, they interact with the medium through different physical processes and thus can reveal the whole history of the medium evolution. There are also various indirect probes for example: collective flow, jet quenching, multi-particle correlation, fluctuations etc. In the following subsections, we elaborate different signatures of QGP.

1.5.1 Electromagnetic Probes

The photons and dileptons are considered as the electromagnetic probes [39, 40, 41, 42, 43, 44, 45, 46, 47] as they only interact with the medium by electromagnetic interaction. The interaction strength is proportional to the QED coupling constant $\alpha = \frac{1}{137}$ which in turn makes their mean free paths large (comparable to size of the medium). Thus, the electromagnetic probes come out of the thermal medium soon after their production undergoing almost zero further collisions. Hence, they carry the precious information about the thermodynamic state of the medium where they are produced. Unlike the hadrons which only emerge from the freezeout hypersurface, the photons and dileptons are emitted from every space-time points throughout the evolution of the medium.

- **Photons:** There are several processes in which photons are produced in a relativistic heavy-ion collision. We are only interested in the ‘direct’ photons which are produced in various collisional processes. The photons coming from decay of various hadrons constitute the background which must be subtracted. In the QGP phase, the dominant contributions come from: (i) quark-anti quark annihilation ($q\bar{q} \rightarrow \gamma\gamma$ and $q\bar{q} \rightarrow g\gamma$) (ii) Compton scattering of gluons producing photon in final state ($qg \rightarrow q\gamma$) and ($\bar{q}g \rightarrow \bar{q}\gamma$) (iii) bremsstrahlung ($qq \rightarrow qq\gamma$). There are various channels of photon production in the hadronic phase as well for example: (i) $\pi\pi \rightarrow \rho\gamma$ (ii) $\pi\rho \rightarrow \pi\gamma$ (iii) $\pi K \rightarrow K^* \gamma$ and so on. Except these, there are photons coming from pre-equilibrium phase (‘prompt photon’) and from the jet conversion in the medium.
- **Dileptons:** Alike photons, the dileptons are also emitted from all the stages of relativistic

heavy-ion collisions. In the QGP phase, the $q\bar{q}$ annihilation to a virtual photon and subsequent decay into lepton pair is the most dominant source of dileptons. There are various hadronic processes which contribute to the dilepton production such as (i) annihilation of the charged hadrons with their antiparticles (for eg: $\pi^+\pi^- \rightarrow l\bar{l}$) (ii) hadronic decays of various mesons like pions, rho mesons, omega mesons etc. (for eg: $\pi^0 \rightarrow l\bar{l}\gamma$, $\omega \rightarrow l\bar{l}$). Another source of dileptons in relativistic heavy-ion collisions is the Drell-Yan processes occurring at the early stages of the collision. The dileptons are classified in various classes depending on their invariant masses (M). The low invariant mass dileptons ($M \leq 1.024$ GeV) mainly originates from the decay of vector mesons; the intermediate invariant mass dileptons ($1.024 < M \leq 3.1$ GeV) come from thermal production in the QGP medium; the high invariant mass dileptons ($M > 3.1$ GeV) have sources from decay of heavy quarkonia, primordial emissions etc.

1.5.2 Energy loss

The study of in-medium energy loss gives insight into the density of the medium and the energy-loss mechanisms, thus becomes an important signature of QGP. The energy loss is studied by means of high- p_T suppression from single particle spectrum, jet quenching is measured by fully reconstructed jets, correlations between high- p_T hadrons etc.

The single-particle p_T spectrum is an important tool to study parton energy-loss in QGP medium produced in relativistic heavy-ion collisions. The high- p_T particles, originated from parton fragmentation, are sensitive to the amount of energy loss that the partons experience traversing the medium. The modification of high- p_T particle production is quantified in terms of nuclear modification factor as given below:

$$R_{AA} = \frac{1}{N_{\text{coll}}} \frac{dN_{AA}}{dyd^2p_T} \bigg/ \frac{dN_{pp}}{dyd^2p_T} \quad (1.5)$$

where, $\frac{dN_{AA}}{dyd^2p_T}$ and $\frac{dN_{pp}}{dyd^2p_T}$ are respectively the differential yields in heavy-ion (AA) collision and pp collisions; N_{coll} is the number of binary collisions among the nucleons. If the AA collision is just the superposition of N_{coll} number of pp collisions, then the above quantity would have been unity. The R_{AA} is being measured in both the RHIC and LHC energies and it is found less than unity [48, 49]. Energy loss is also studied by jets, which are the collimated cluster of high energy hadrons. They are produced due to the fragmentation of energetic partons which are produced through hard scattering. Usually, jets are produced back-to-back due to the conservation of momentum. However, if the jets encounter a thermal medium after their production, they can lose energy while propagating through

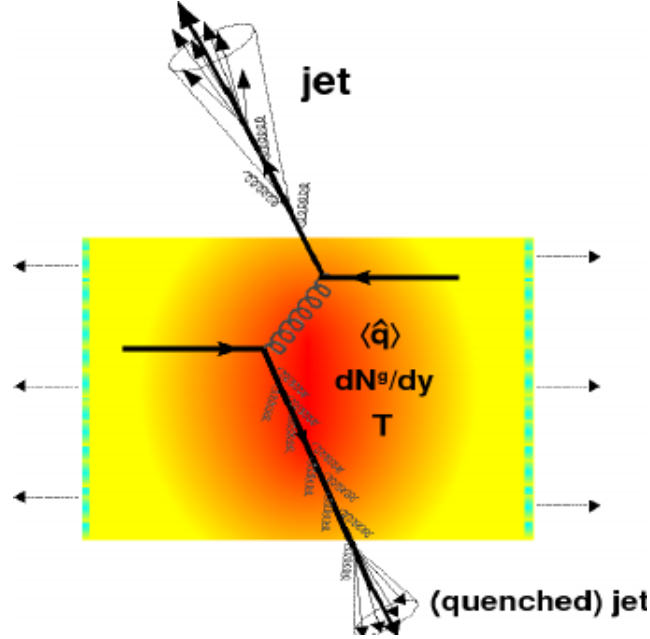


Figure 1.10: Energy loss of the away side jet in the QGP medium. Figure is taken from Ref. [56].

it by means of elastic scattering as well as radiating gluons. In figure 1.10, the back-to-back jets are shown which are created at the edge of the thermal medium. The jet, which is near to the edge (called the near side jet), leaves the QGP medium without suffering much collision, whereas the other jet (called the away side jet) propagates through the medium. Thus, the later will interact with the medium and loose its energy [38, 50]. In other way, the away side jet is expected to have less energy and thus it is ‘quenched’ in the QGP medium [51, 52, 53, 54, 55].

The anti- k_T algorithm [57] is used to identify jet candidates primarily by all experiments, but there are several approaches to remove the large combinatorial background from unrelated processes (underlying events). The energy loss in the medium is quantified as the jet-energy imbalance given by:

$$A_J = \frac{E_{T1} - E_{T2}}{E_{T1} + E_{T2}} \quad (1.6)$$

Here, E_{T1} and E_{T2} are the energies of the jets from opposite hemisphere of the system. The asymmetry A_J deviates largely from zero due to the energy loss inside the medium.

Jets can also be studied by looking at the azimuthal correlations between two hadrons. In this study, a particle from a certain p_T range is chosen as “trigger” particle and “associated” particles are chosen from another p_T range such that $p_T^{trigg} > p_T^{assoc}$. The near-side and away-side peaks arise from back-to-back jets. The per-trigger associated yield is quantified as:

$$Y(\Delta\varphi) = \frac{1}{N_{trigg}} \frac{dN_{assoc}}{d\Delta\varphi} \quad (1.7)$$

At sufficiently high p_T , the collective effects are expected to be very small and jet-like correlations dominate. To determine the effect of in-medium partonic energy loss, a quantity I_{AA} is considered:

$$I_{AA} = \frac{Y_{AA}(\Delta\varphi)}{Y_{pp}(\Delta\varphi)} \quad (1.8)$$

The away-side I_{AA} comes less than unity in heavy-ion collisions revealing the energy-loss due to the presence of the medium [58].

1.5.3 Collective Flow

One of the most promising indications of QGP is its collective behaviour. It can be quantified in terms of the azimuthal distribution of the produced final state particles in the transverse plane [59, 60, 61, 62, 51, 63, 64]. In a non-central collision, the overlap zone of the two participating nuclei resembles the shape of an almond which corresponds to a particular spatial anisotropic distribution of the initial energy deposition as shown in figure 1.11. The initial transverse momentum distribution is expected to be isotropic. If there is no collectivity in the medium, one can expect that the transverse momentum distribution of final state particles should also be isotropic. On contrary, if the overlap zone exhibits collective behaviour, the spatial anisotropy in the initial energy deposition would cause anisotropic pressure gradient. This in turn produces anisotropy in the transverse momentum distribution of the final state particles. The collective flow is analysed by Fourier expansion the azimuthal dependence of the Lorentz invariant particle spectra as:

$$E \frac{d^3N}{d^3p} = \frac{d^3N}{dy d^2p_T} = \frac{1}{2\pi} \frac{d^2N}{dy p_T dp_T} \left[1 + 2 \sum_{n=1}^{\infty} v_n \cos \left\{ n(\phi - \Psi_{RP}) \right\} \right] \quad (1.9)$$

where, Ψ_{RP} is the reaction plane angle (corresponding to the symmetry-plane of the collision zone) and ϕ is the azimuthal angle. The different Fourier coefficients v_n refers to different flow parameters, for example v_1 gives the directed flow, v_2 gives the elliptic flow, v_3 corresponds to triangular flow and so on. Among all these flow parameters, v_2 is being extensively studied and measured. It is worth mentioning that, in hydrodynamic models of relativistic heavy-ion collisions, the calculated v_2 of charged particles has sensitive dependence on the transport coefficients of the medium (mainly the shear viscosity to entropy density ratio η/s). This in turn provides us the opportunity to extract the η/s of the QGP medium and it has been found that the value of η/s of QGP is close to its quantum bound (called the KSS bound $\eta/s \simeq \frac{1}{4\pi}$). This reveals the nearly perfect fluid nature of the QGP.

The study of two-particle azimuthal correlations in long-range ($\Delta\eta > 1$) also provides informa-

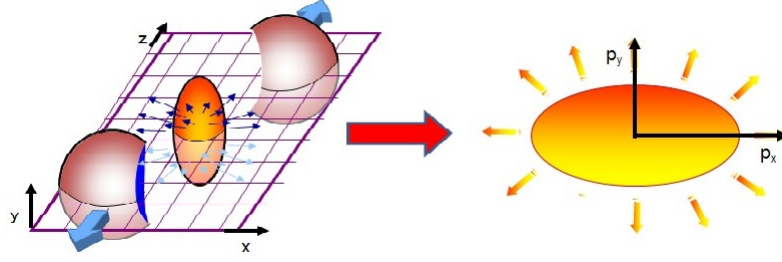


Figure 1.11: A typical non-central heavy-ion collision. The almond shape of initial collision geometry (spatial anisotropy) is translated into the elliptic flow anisotropy in the final state momentum space [65].

tion on collectivity. The ridge-like structures appears for smaller $\Delta\varphi$ and larger $\Delta\eta$ for which the hydrodynamical collective flow of a strongly interacting and expanding medium is expected to be responsible [66, 67, 68].

1.5.4 Heavy Quarks

The heavy quarks refer to charm (c) and beauty (b) quarks. Because of their large masses ($m_c \simeq 1.3 \text{ GeV}/c^2$ and $m_b \simeq 4.2 \text{ GeV}/c^2$), they are produced in very early stages of the relativistic proton-proton or heavy-ion collisions by initial hard scattering among the partons, the production cross-section can be calculated via perturbative QCD (pQCD). At the LHC energy, gluon-gluon fusion $gg \rightarrow Q\bar{Q}$ dominates the heavy-quark production processes. In relativistic heavy-ion collisions, because of production at the very initial stage, the heavy-quarks experience the whole evolution of the medium [69] formed in the collisions. The heavy quarks lose energy while propagating through the medium. Energy loss and elliptic flow of heavy-quark hadrons are sensitive to the dynamics of the medium, such measurements are used to determine the fundamental properties of the QGP, for instance the transport coefficients [69]. Elliptic flow of heavy quarks gives information on possible collective behaviour of the created nuclear matter.

1.5.5 Quarkonia Dissociation

One of the novel characteristics of any kind of plasma is the ‘*Debye screening*’ of the charged particles. For example, in a QED plasma, if one put a static charge inside the medium, then the electric field produced by this static charge will be screened by other charges which constitute the plasma medium. In other words, the electric field or potential $V(r)$ created by the static charge is no longer a Coulombic one like $V(r) \sim \frac{1}{r}$; rather it becomes an Yukawa type $V(r) \sim \frac{e^{-m_D r}}{r}$ where m_D is the Debye mass. The more the Debye mass is, the distance at which the potential dies out will be less.

The quarkonia are the bound states of a heavy quark and antiquark ($Q\bar{Q}$) like charmonium ($c\bar{c}$) and bottomonium ($b\bar{b}$) [70, 71]. Being highly massive objects, they are produced in the early stages of a relativistic heavy-ion collision by hard scattering processes among the partons [72, 73]. After getting produced, the quarkonia finds itself in the QGP medium. The QGP being a plasma of colour charges, also exhibits the Debye screening. It can be shown from perturbative QCD (pQCD) calculations that, the Debye mass increases with the increase in temperature of the QGP medium. Thus at high temperature, the inter-quark potential between the $Q\bar{Q}$ becomes Debye screened. If the Debye radius (inverse of the Debye mass) becomes more than the radius (size) of the $Q\bar{Q}$ bound state, then the quarkonia dissociates in the medium and Q and \bar{Q} moves separately in the QGP medium. There are various excited states of $c\bar{c}$ and $b\bar{b}$ each having different radii (sizes) and binding energy. The loosely bound states (excited states) dissociate first at a lower temperature. The J/ψ and Υ are respectively the ground states of charmonium and bottomonium which are most tightly bound, so that they melt at comparatively higher temperatures. The sequential quarkonia suppression is being one of the efficient probes of the QGP medium [74].

1.5.6 Role of pp and pA collisions in search of QGP signals

The pA collisions: Cold Nuclear Matter effect

The complete understanding of the results from heavy-ion collisions needs a clear concept of proton-nucleus collisions also, as it provides the information on initial state nuclear effect. The presence of additional nuclear matter in pA collisions, relative to pp collisions, can modify incoming wave-function of the nucleus which leads to the modification of final state observables. This is known as Cold Nuclear Matter (CNM) effect. The several sources of CNM effects are modification of nuclear PDFs, k_T broadening or Cronin effect, isospin effect, initial state parton energy loss etc. A brief description of these sources are given below:

- **Modification of nuclear PDFs:** The colliding nuclei are not the merely superposition of their constituent nucleons. In the initial state, the nuclear environment affects the parton distributions, which are modified in bound nucleons depending on the parton fractional momentum x and atomic number A [75, 76]. This phenomenon is known as parton-density shadowing. The term “shadow” can be interpreted like, the nucleons presented on the surface overshadow the nucleons inside the nucleus.
- **k_T broadening or Cronin effect:** It has been observed that the high- p_T hadrons are not suppressed in pA collisions [77], rather produced copiously. The multiple scattering inside the

1.5. The Signatures of QGP

nucleus leads to the broadening of transverse momentum (k_T) for both initial and final state partons. This k_T broadening is responsible for the enhancement of hadron production in pA collisions known as “Cronin effect” [78, 79], demonstrated by James Cronin.

- **Isospin effect:** It can be accounted for on average in the nPDFs for a nucleus with atomic mass A and Z protons via:

$$f_{a/A}(x) = \frac{Z}{A}f_{a/p}(x) + (1 - \frac{Z}{A})f_{a/n}(x) \quad (1.10)$$

where $f_{a/p}(x)$ and $f_{a/n}(x)$ are the PDFs inside a proton and a neutron respectively [80].

- **Initial state parton energy loss:** As the parton from the nucleon undergoes multiple scattering in the nucleus before the hard collisions, it loses energy due to medium-induced gluon bremsstrahlung [81]. This effect can be easily implemented as a momentum fraction shift in the PDFs.

ALICE has studied nuclear modification factor R_{pPb} (as a function of transverse momentum) of charged particles in pPb collisions [82] defined by equation 1.11 which is a similar quantity like R_{AA}

$$R_{pA} = \frac{1}{A} \frac{d\sigma_{pA}/dp_T}{d\sigma_{pp}/dp_T} \quad (1.11)$$

Where $d\sigma/dp_T$ is the cross-section measured in pA/pp collisions. The value of R_{pA} comes unity if there is no CNM effect. In figure 1.12, the R_{pPb} value is consistent with unity after $p_T > 2$ GeV/c. ALICE has shown strong suppression of R_{AA} in most most central PbPb collisions only.

Several other studies with CNM effects have been done like long-range correlations with charged particles in pPb collisions at the LHC [83, 84, 85], nuclear modification factor in dAu collisions at RHIC etc [86].

The elementary pp collisions

Conventionally, the study of properties of particle of production from the medium formed in relativistic heavy-ion collisions are compared with similar data from pp collisions at the same centre-of mass energy, considering the pp collisions as elementary ones, where no medium is formed. The pp collisions are categorized by elastic and non-elastic collisions. In elastic collisions, there is no new particle formation, thus identical initial and final states. There are three different types of inelastic collisions : Non-Diffractive (ND), Single-Diffractive (SD) and Double-Diffractive (DD) as shown in figure 1.13. The diffractive systems are created by the excitation of incoming particles (nucleons),

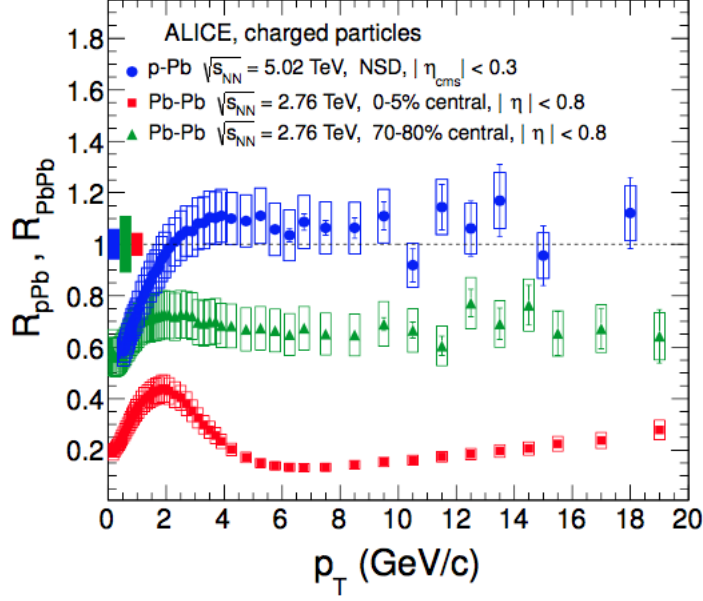


Figure 1.12: The nuclear modification factors of charged particles as a function of transverse momentum in pPb and PbPb collisions measured by ALICE [82].

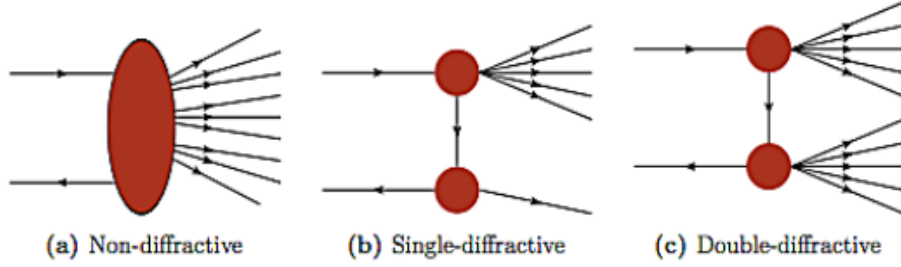


Figure 1.13: Inelastic processes in pp collisions: (a) Non-Diffractive, (b) Single-Diffractive and (c) Double-Diffractive.

which are originated from the gluon-exchange, regarded as “Pomeron” [87]. In SD events, only one of the colliding particles becomes a diffractive and dissociates, whereas both the particles become diffractive systems in of DD events. In ND events, both the particles collide head-on and results complete dissociation. The total cross-section in pp collisions is given by equation 1.12.

$$\sigma_{total}^{pp} = \sigma_{el}^{pp} + \sigma_{ND}^{pp} + \sigma_{SD}^{pp} + \sigma_{DD}^{pp} \quad (1.12)$$

In LHC energies, the main contribution factor is σ_{ND}^{pp} , but ALICE is unable to distinguish ND and DD processes in event-by-event basis, as a result it produces the combined results of ND and DD processes, referred as Non-Single-Diffractive (NSD) events.

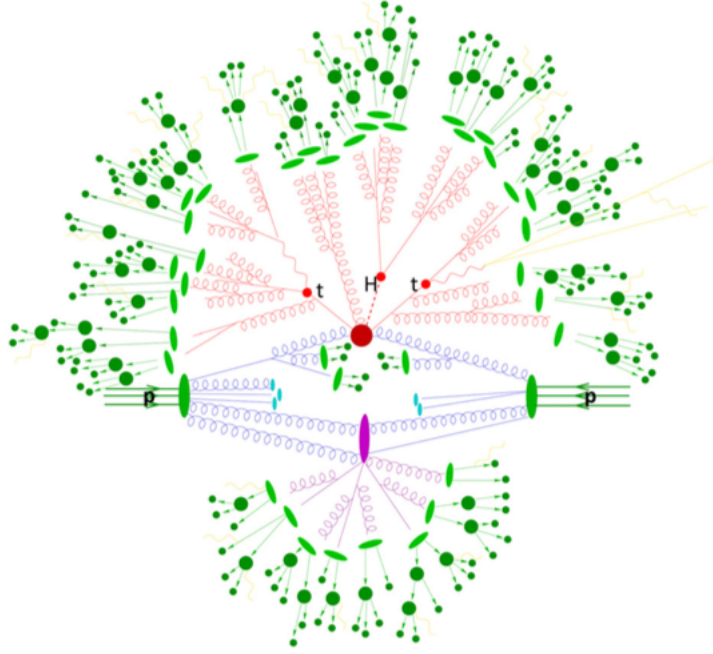


Figure 1.14: Illustration of the way used in QCD Monte-Carlo models to simulate a pp collision: hard interaction between two partons (red blobs), hard QCD radiation (red), underlying events of a secondary interaction (purple blob), proton remnant that hadronize (light blue blobs), final-state partons that hadronize (light green blobs), hadron decay (dark green blobs), photon radiation (yellow) [89].

The elementary pp collisions involves both hard and soft subprocesses depending on the momentum transfer of the partons. The hard processes can be studied by perturbative QCD (pQCD) calculations, while for soft processes these calculations are not valid as the coupling constant α_s approaches to unity. Thus, several QCD Monte Carlo event generators like PYTHIA, HERWIG, Sherpa, POWHEG etc [88] have been developed to study such processes on a phenomenological background. Figure 1.14 describes the way of a QCD MC model to simulate pp collisions in which “hard” parton scattering occurs. The different sub-processes and stages illustrated in the figure are described in the following:

- In the figure 1.14, the two incoming protons are indicated by green ellipse and the green lines indicate the valance quarks. Each proton is consisted of partons whose distribution is given by parton distribution functions (PDFs). A PDF $f_i(x, Q_2)$ is defined as the probability density for finding a particle with a certain longitudinal momentum fraction x at resolution scale Q_2 . The hard scattering in the collision is not actually between two protons, but between two partons. Thus the whole centre-of-mass energy \sqrt{s} of the collision is not available for each of the hard processes, only a partonic centre-of-mass energy $\sqrt{\hat{s}}$ plays the role. The square of the partonic centre-of-mass energy is given by $\hat{s} = x_1 x_2 s$, where x_1, x_2 are the Bjorken-x variable for two

partons.

- Before the physical collision, the incoming particles loose energy and produce additional QCD radiation by gluon splitting ($g \rightarrow gg, g \rightarrow q\bar{q}$) or gluon radiation from quarks ($q \rightarrow qg$). This is known as Initial State Radiation (ISR). This causes the reduction of beam energy prior to the momentum transfer.
- As the two protons collide, a hard interaction occurs between two partons (big red circle) resulting outgoing partons. The products of this scattering emits further QCD radiations repeatedly, known as Final State Radiation (FSR) and a parton shower evolves.
- After the hard scattering between two partons, the left over partons are known as beam remnants which can further collide in the same collision.
- In a single pp collision, there are so many parton-parton interactions. Also, the outgoing partons i.e., the partons produced from initial parton-parton interactions, interact with other partons. This process is called Multiple Parton Interaction (MPI). These multiple interactions produce additional partons throughout the event resulting the increased multiplicity and summed transverse energy [88].
- With the time evolution, the coloured particles produced in parton shower combine into colourless hadrons eventually. This process is known as hadronization and indicated by green blobs in the figure 1.14. The primary hadrons decay into stable particles and jets are formed with the collimated bundles of hadrons.
- The lower part of the figure 1.14 shows a secondary interaction among the beam remnants indicated by a purple ellipse. Here also the parton shower is produced (denoted by purple lines) resulting hadronization. Such soft interactions, typically all interactions except hard processes are considered as Underlying Events (UE), which are the unavoidable background to most of the hadron collider observables. A good understanding of UE provides more precise measurements [89].

1.6 Thesis focus

In this section, we briefly discuss the topics that the thesis addresses.

1.6.1 The study of the heavy-flavour jets, in terms of two-particle angular correlations between D-mesons and charged particles

As already discussed, the heavy-flavour jets, which are copiously produced at the LHC energies, provide unique tools of study the properties of medium formed in ultra-relativistic heavy-ion collisions. Also, the production mechanisms of heavy-flavour hadrons and the associated jets at this new regime of collisional energy in pp collisions need to be understood. The in-medium energy loss by the initially produced high- p_T heavy-flavour hadrons or the jets in a QGP-like medium in heavy-ion collisions is of primary interest. As the pp collision data acts as a base line to find the actual energy loss in heavy-ion collisions, the analysis of heavy-flavour jets in minimum-bias pp data is also important. The energy loss by the jets or the high- p_T particles are studied by means of high- p_T suppression from single particle spectrum, jet quenching measured by fully reconstructed jets, correlations between high- p_T hadrons etc. In this thesis, we have used the two-particle azimuthal correlations as the analysis tool and the correlations are measured between D mesons and primary charged particles in pp collisions at $\sqrt{s} = 13$ TeV. The basic purpose of this study in pp collision is to characterize the charm-jet properties and investigate on several charm production mechanisms. The detail descriptions on charm productions and charm containing mesons are given in chapter 2.

1.6.2 Study of high multiplicity events of small systems

The LHC has reported flow-like behaviour of particle production mechanism in high-multiplicity events of small systems of collisions like pp and pA. The feature cannot be explained with the physics understanding on particle production mechanisms at pre-LHC energies. The most important signature of collectivity found in high-multiplicity events of small systems is the “ridge-like” structure in long-range two-particle azimuthal correlations, reported by CMS experiments in pp collisions at $\sqrt{s} = 7, 13$ TeV [90, 91, 92, 93] and by ALICE experiment in pPb collisions at $\sqrt{s_{NN}} = 5.02$ TeV [94]. The elliptic flow v_2 of charged particles and its p_T dependence has been measured for these systems [95]. The mass ordering of $v_2(p_T)$ of identified charged particles also confirms the formation of collective medium [92], which gives the measure of azimuthal anisotropy in the medium. Further, the collective behaviour of particle production is corroborated with the strong transverse radial flow extracted [96] from identified charged-particle yield using Boltzman Gibbs blast-wave (BGBW) model [97]. Despite all of the studies pointing towards the collective behaviour of particle production in high-multiplicity events of small systems, the anomalous features of particle production can not be connected with the QGP-like thermalized medium, due to the lack of any signal of high- p_T suppres-

sion or any other compelling signal of the formation of the medium. Besides, several models based on different physics considerations, claim to explain the data qualitatively. Thus, it becomes difficult to conclude on the physics origin of the collective behaviour and particle productions in small systems. Therefore, a quantitative comparison of data with the existing theoretical models is important to study collective features in these systems. In this thesis, we have presented a comprehensive study simulated events of pp collisions at $\sqrt{s} = 7$ and 13 TeV and pPb data at $\sqrt{s_{\text{NN}}} = 5.02$ TeV using hydro-based EPOS3 model. An experimental review has been given section 6.1, before presenting the analysis results in sections 6.3 and 6.4.

Chapter 2

Open heavy-flavour probes in high energy collisions

In this chapter, we will give a brief description on the properties of heavy quarks and heavy-flavour mesons, as the main content of the thesis is to study the two-particle azimuthal correlations in heavy-flavour sector. We will mainly focus on the open heavy-flavour and its contribution as a probe in QGP medium. After that, we will give a brief experimental review on several heavy-flavour studies in different collision systems and different centre-of-mass energies.

2.1 Introduction to heavy quarks and heavy-flavour Mesons

As already mentioned in chapter 1, the heavy quarks are considered as efficient probes for the detection and characterization of QGP medium produced in relativistic heavy-ion collisions. The heavy-flavour probes are divided into two categories namely: (i) hidden (ii) open. The bound state of a heavy quark with its antiquark is called the hidden heavy flavour meson (for example J/ψ , Υ etc.). On the other hand, the bound state of a heavy quark with a light quark (up, down or strange) is called the open heavy flavour meson (for example D meson and B meson). In this thesis, we are mainly concerned about the charm (c) quark and the corresponding open heavy-flavour meson (D meson).

The large mass of charm ($\simeq 1.3 \text{ GeV}/c^2$) enforces it to be produced via the initial hard scattering process with large momentum transfer. This in turn provides us the opportunity to calculate the respective production cross section using the pQCD framework since the strong coupling becomes much less than unity at and above the threshold momentum transfer of charm quark production. Also, because of the heavy-quark production at the very early stages in a relativistic heavy-ion

collision, they witness the full evolution of the QGP medium. Soon after the QGP medium is created, the charm quark may form bound state with a light quark (up, down or strange) which are the most abandoned species in the medium. The bound state of a charm quark/antiquark with a light antiquark/quark is referred as D meson. Table 2.1 shows the different charge states of the D mesons along with their key properties (mass, decay modes etc.). For the decay modes in the

Charge State	Quark Content	Mass (MeV)	$I(J^P)$	Decay Modes	Branching Ratio (%)
D^\pm	$c\bar{d}, \bar{c}d$	1869.65 ± 0.05	$\frac{1}{2}(0^-)$	$K^\mp \pi^\pm \pi^\pm$ and leptonic	9.13 ± 0.19
D^0, \bar{D}^0	$c\bar{u}, \bar{c}u$	1864.83 ± 0.05	$\frac{1}{2}(0^-)$	$K^\mp \pi^\pm$ and leptonic	3.87 ± 0.05
D^{*0}, \bar{D}^{*0}	$c\bar{u}, \bar{c}u$	2006.85 ± 0.05	$\frac{1}{2}(1^-)$	$D^0 \pi^0, \bar{D}^0 \pi^0$ $D^0 \gamma, \bar{D}^0 \gamma$	64.7 ± 0.9 35.3 ± 0.9
$D^{*\pm}$	$c\bar{d}, \bar{c}d$	2010.26 ± 0.05	$\frac{1}{2}(1^-)$	$D^0(\bar{D}^0) \pi^\pm$	67.7 ± 0.5
D_s^\pm	$c\bar{s}, \bar{c}s$	1968.34 ± 0.07	$0(0^-)$	$\phi \pi^\pm$ and leptonic	4.5 ± 0.4

Table 2.1: Properties of charm quark containing mesons [15].

hadronic channel, the charmed hadrons are reconstructed analyzed after the identification of decay vertices and decay products. Because of low branching ratio in thses channels, the analysis requires large statistics.

2.2 Heavy flavour production

As already stated, the threshold momentum transfer for the production of charm quark exceeds the typical QCD scale (because of its large bare mass), it is possible to calculate their inclusive production cross section using pQCD framework. This is in contrary to the production of lighter quarks/gluons where the non-perturbative effects play significant role except for the case of very high- p_T partons in which one may still apply pQCD. The cross section for the inclusive heavy-flavour meson can be calculated by applying the “Factorization Theorem” where the calculation is splitted into a convolution of hard scattering cross section with the parton distribution function (PDF) and the fragmentation function. The hard scattering cross section is obtained using pQCD approach

2.3. Open heavy-flavour as a probe in relativistic heavy-ion collisions

however, the fragmentation functions can not be calculated with pQCD. The cross section for the production of a heavy flavour hadron (H_Q) with transverse momentum p_T can be written as

$$\frac{d\sigma^{pp \rightarrow H_Q X}}{dp_T} = \sum_{i,j \in \{q, \bar{q}, g\}} \int \int dx_1 dx_2 f_i(x_1, \mu_F^2) f_j(x_2, \mu_F^2) D_Q^{H_Q}(z, \mu_F^2) \frac{d\hat{\sigma}^{ij \rightarrow Q\bar{Q}}}{dp_T}(\alpha_s, \mu_F^2, \mu_R^2, m_Q, \hat{p}_T) \quad (2.1)$$

where, x_1 and x_2 are the Bjorken- x variables corresponding to the two interacting partons, m_Q is the mass of the heavy quark, μ_R^2 and μ_F^2 respectively the renormalization and factorization scales of QCD. In the above equation \hat{p}_T is the transverse momentum of the parton, $f_i(x_1, \mu_F^2)$ and $f_j(x_2, \mu_F^2)$ are the PDFs and $D_Q^{H_Q}(z, \mu_F^2)$ is the fragmentation function of the heavy quark Q ; $d\hat{\sigma}^{ij \rightarrow Q\bar{Q}}$ denotes the cross section of the elementary process of the scattering of two partons producing a $Q\bar{Q}$ pair in the final state.

The PDFs $f_i(x_1, \mu_F^2)$ and $f_j(x_2, \mu_F^2)$ respectively denotes the probability that a parton i and j respectively carries a fraction of x_1 and x_2 momenta of the parent interacting nucleon. The PDFs are obtained from the Deep Inelastic Scattering experiments. The differential cross section $d\hat{\sigma}^{ij \rightarrow Q\bar{Q}}$ can be calculated using pQCD framework. The Leading Order (LO) contributions mainly come from these two processes (i) $q\bar{q} \rightarrow Q\bar{Q}$ (ii) $gg \rightarrow Q\bar{Q}$ which are shown in Fig. 2.1. However, at the Next to Leading Order (NLO), many more processes contribute for eg. $q\bar{Q} \rightarrow q\bar{Q}$, $g \rightarrow Q\bar{Q}$ etc. as demonstrated in Fig. 2.2. The fragmentation function $D_Q^{H_Q}(z, \mu_F^2)$ corresponds to the probability for the generation of the hadron H_Q carrying fraction of z of the momenta of the quarks. The evaluation of the fragmentation function requires various theoretical modeling such as cluster hadronization model, Lund string model etc. followed by fitting with the experimental data of e^+p , e^+e^- and pp collisions.

2.3 Open heavy-flavour as a probe in relativistic heavy-ion collisions

As already discussed in chapter 1, the study of heavy-flavour particles is an important tool to find the properties of medium formed by heavy-ion collisions. The production time for heavy quark-antiquark pair (0.1 fm/ c for charm and 0.02 fm/ c for beauty) is much lower compared to the expected lifetime of QGP which allows us to study its production mechanism and its propagation through the medium formed in heavy-ion collisions. Heavy quarks are produced through partonic hard scatterings, i.e., with large momentum transfer. Thus the production cross-section can be calculated through perturbative-QCD approach which remains unaffected due to the presence of the medium.

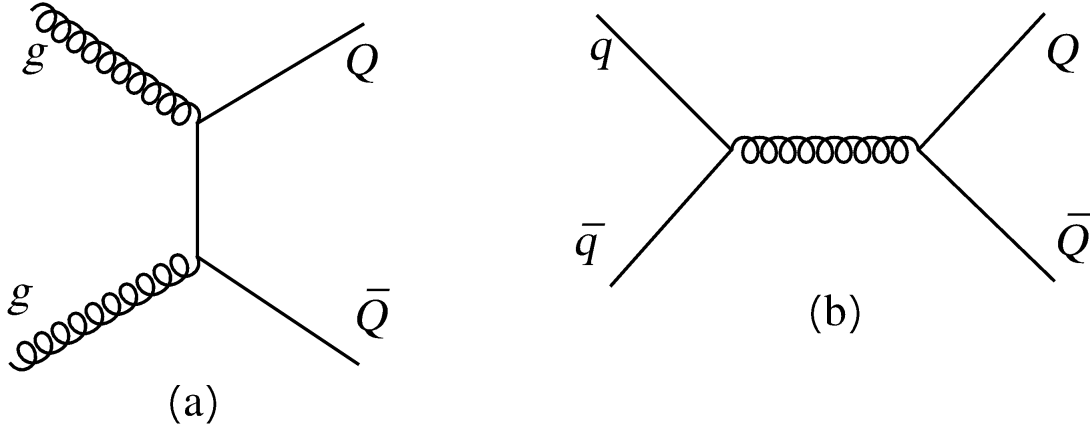


Figure 2.1: Leading Order (LO) Feynman diagrams for the heavy quark production: (a) gluon fusion and (b) pair annihilation.

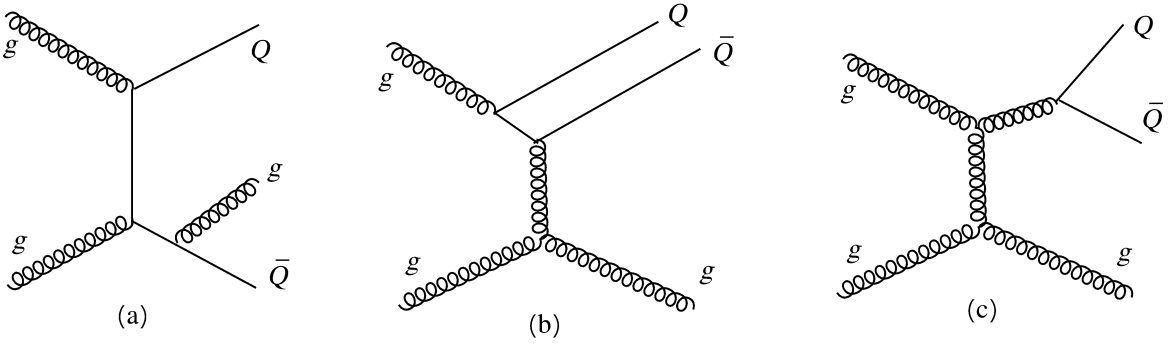


Figure 2.2: Few of the Feynman diagrams for the Next to Leading Order (NLO) processes of the heavy quark production: (a) gluon fusion with one final state gluon (b) flavour excitation and (c) gluon splitting.

2.3.1 The effect of QGP medium on heavy flavour

While traversing through the QGP medium, heavy-quarks interact with the medium constituents resulting an energy loss (ΔE) of partons. This energy loss depends on the medium properties like temperature (T), thickness (L), particle-medium interaction coupling and particle characteristics like energy E , mass m and charge q .

The energy loss takes place via two processes: collisional energy loss and medium-induced radiative energy loss as shown in figure 2.3. The total energy loss given by:

$$\Delta E = \Delta E_{\text{collisional}} + \Delta E_{\text{radiative}} \quad (2.2)$$

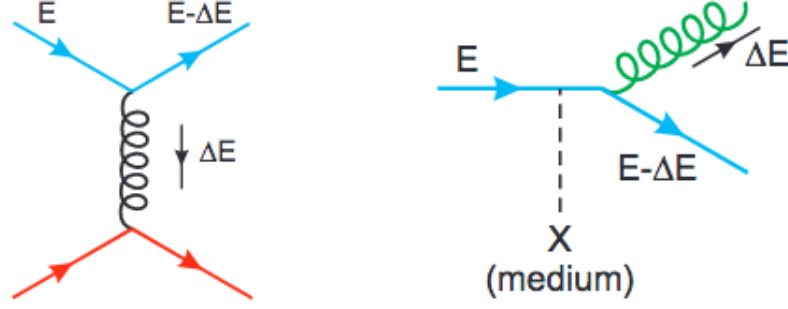


Figure 2.3: Collisional (left) and radiative (right) energy loss of a quark with energy E [98].

Collisional energy loss

This kind of energy loss happens due to the multiple elastic scattering of the parton with the other medium constituents and dominates at low p_T . The amount of energy loss by collisional processes increases linearly with the in-medium path length and has a logarithmic dependence on the initial parton energy. Figure 2.4 shows the collisional energy loss of charm quark obtained from a theoretical calculation in RHIC and LHC energies [99], which reveals the increment of collisional energy loss with centre-of-mass energies.

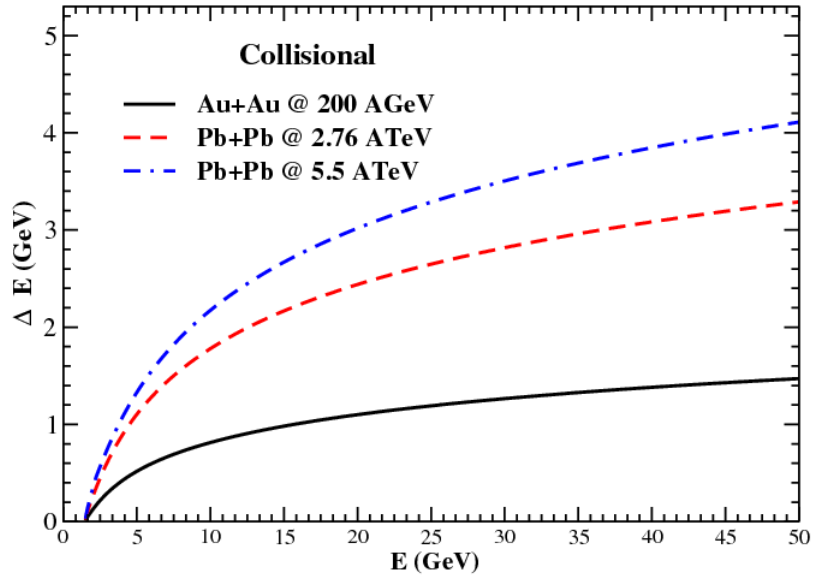


Figure 2.4: Collisional energy loss of charm quark in RHIC and LHC energies [99].

Medium induced radiative energy loss

The radiative energy loss happens due to the inelastic scattering inside the medium and is dominant for high p_T partons. This process, analogous to QED brehmstrahlung, is often regarded as “gluonstrahlung”. A theoretical model of this kind of energy loss was proposed by Baier, Dokshitzer, Muller, Peigne and Schiff (BDMPS model) [100]. According to this model, the partons are produced through hard scattering and undergo a series of multiple scatterings in a Brownian-like motion, with a mean free path that decreases with the increasing medium density. The characteristic energy of the radiated gluons ω_c is given by

$$\omega_c = \hat{q}L^2/2 \quad (2.3)$$

where L is the path length of the gluon inside medium and \hat{q} is its transport coefficient. For a static medium, the energy distribution of the radiated gluons are expressed as:

$$\omega \frac{dI}{d\omega} = \frac{2\alpha_s C_R}{\pi} \sqrt{\frac{\omega_c}{2\omega}} \quad (2.4)$$

for energies $\omega < \omega_c$, C_R i.e. the Casimir factor is equal to 4/3 for qg coupling and to 3 for gg coupling. The average energy loss of the parton can be obtained by integrating the previous equation as:

$$\langle \Delta E \rangle = \int_0^{\omega_c} \omega \frac{dI}{d\omega} d\omega \propto \alpha_s C_R \hat{q} L^2 \quad (2.5)$$

Thus, $\langle \Delta E \rangle$ is proportional to the strong coupling constant α_s , the Casimir factor C_R and square of the path length L but does not depend on the initial energy E of the parton. In general, this feature is present in BDMPS model only, there are several other theoretical calculations which show a logarithmic dependence on E [101, 102, 103].

Figure 2.5 shows an estimate of the average energy loss of charm and bottom quarks as a function of their initial energy separating the collisional and radiative contributions for PbPb collisions at $\sqrt{s_{NN}} = 2.76$ TeV [104].

Dead-cone effect

The radiative energy loss depends on the mass and colour charge of traversing parton with a decreasing order $\langle \Delta E_{heavy-quark} \rangle < \langle \Delta E_{light-quark} \rangle < \langle \Delta E_{gluon} \rangle$. Heavy quarks travelling in vacuum with moderate energy ($m/E \simeq 1$) have a velocity significantly lower than the velocity of light. In this situation, the vacuum gluon radiation inside a front cone with an opening angle $\Theta = m/E$ is expected to be suppressed due to destructive interference [105]. This effect is known as “dead cone

2.3. Open heavy-flavour as a probe in relativistic heavy-ion collisions

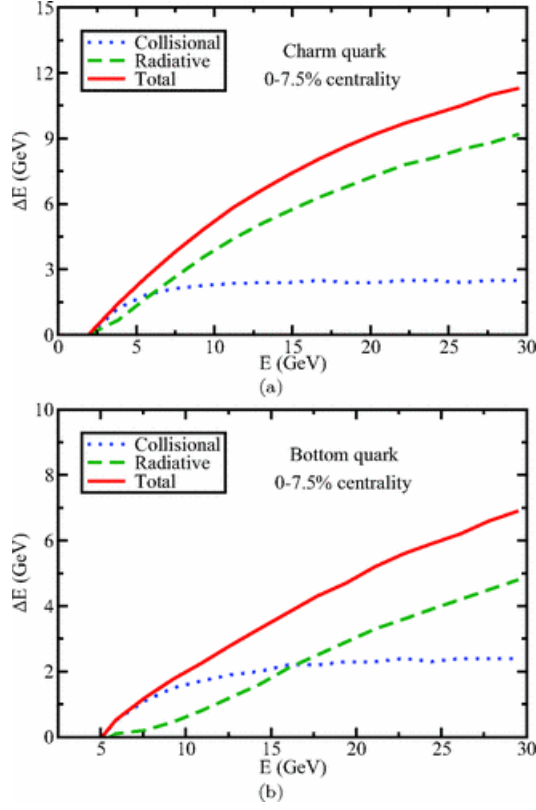


Figure 2.5: Comparison of collisional and radiative energy loss for charm and bottom quark [104].

effect”. If the parton mass is higher, the angular opening of the “dead” cone becomes larger and the energy loss by gluonstrahlung is smaller.

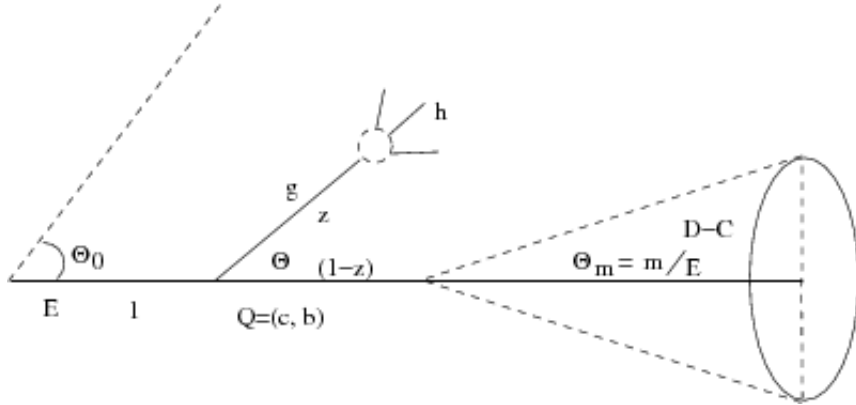


Figure 2.6: Schematic diagram of dead cone effect in heavy quarks [106].

2.3.2 Experimental review

The heavy-flavour studies have been performed in RHIC energies with AuAu $\sqrt{s_{NN}} = 200$ GeV data. Figure 2.7 shows the PHENIX results on nuclear modification factor R_{AA} and elliptic flow v_2 of heavy-flavour decay electron as a function of p_T [107]. In this figure, the large suppression of R_{AA}

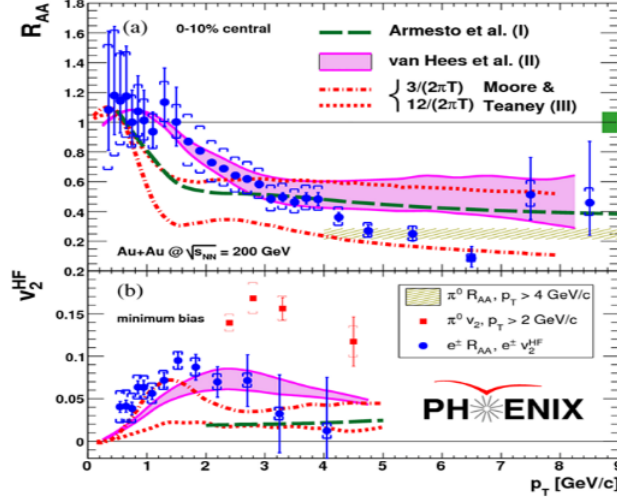


Figure 2.7: Heavy-flavour electron nuclear modification factor R_{AA} and elliptic flow v_2 as a function of p_T in AuAu collisions at $\sqrt{s_{NN}} = 200$ GeV [107] measured by PHENIX.

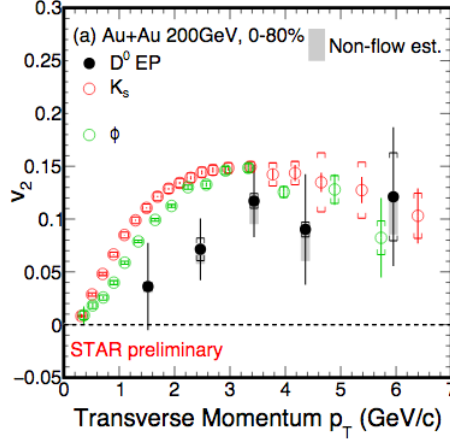


Figure 2.8: Elliptic flow (v_2) of D^0 meson compared to light-flavour mesons in AuAu collisions at $\sqrt{s_{NN}} = 200$ GeV measured by STAR experiment [108].

in high p_T region has indicated the heavy-flavour energy loss while traversing through the medium, also a large v_2 is observed in intermediate- p_T region indicating the thermalization on heavy quarks.

STAR experiment has measured the azimuthal anisotropy of D^0 meson in terms of v_2 for AuAu $\sqrt{s_{NN}} = 200$ GeV as shown in figure 2.8 [108]. This figure shows a v_2 value of D^0 significantly greater than zero for $p_T > 2$ GeV/c.

In LHC energies, the heavy-flavour studies have been carried out with higher precision. Figure 2.9 shows the R_{AA} of three D mesons (D^0 , D^+ , D^{*+}) in PbPb collisions (most central and semi-peripheral) at $\sqrt{s_{NN}} = 2.76$ TeV measured by ALICE [109]. The results show a suppression with a factor 3-4 in central collisions for $p_T > 5$ GeV/c. The azimuthal anisotropy of prompt D mesons has been measured in PbPb collisions at $\sqrt{s_{NN}} = 5.02$ TeV with 30-50% centrality class as shown in figure

2.3. Open heavy-flavour as a probe in relativistic heavy-ion collisions

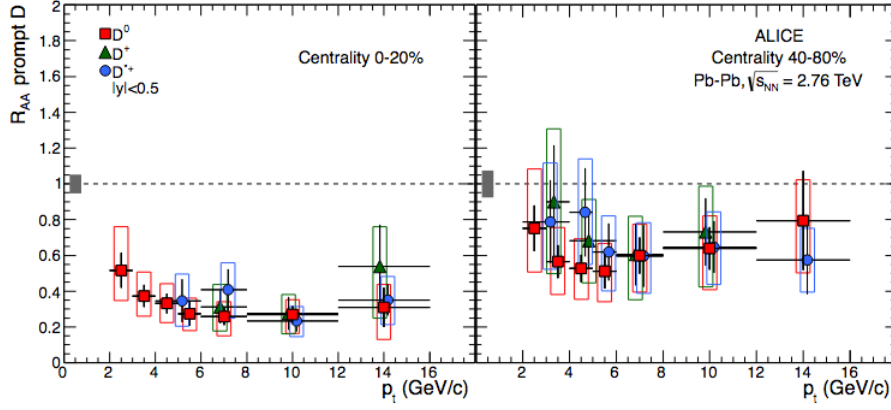


Figure 2.9: R_{AA} for prompt D^0 , D^+ and D^{*+} in 0 – 20% (left) and 40 – 80% (right) centrality bins measured by ALICE [109].

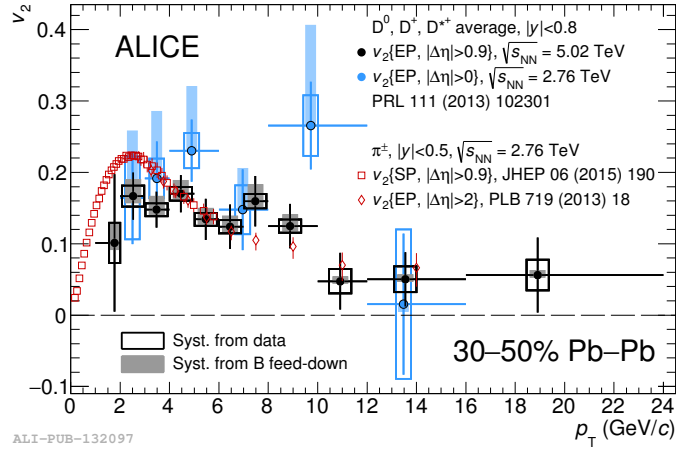


Figure 2.10: Elliptic flow v_2 of prompt D mesons as a function of p_T in PbPb collisions at $\sqrt{s_{NN}} = 5.02$ TeV in 30-50% centrality class compared to the same and v_2 of π^\pm in PbPb collisions at $\sqrt{s_{NN}} = 2.76$ TeV [110].

2.10 [110]. In this figure, the D-meson v_2 is found to be compatible to that measured at $\sqrt{s_{NN}} = 2.76$ TeV and the magnitude is similar to that of charged pions in same centrality class. The study shows positive values in $2 < p_T < 10$ GeV/c that indicates the participation of low and intermediate- p_T charm quarks in the collective expansion of the medium.

One of the important studies in heavy flavour sector is the two-particle azimuthal correlations from which we get further information about the medium effects on heavy quarks. Like the correlation studies in light flavours, heavy quarks also provide further insight into the in-medium energy loss. The first attempt was made by PHENIX experiment to study the heavy-quark energy loss inside the medium with AuAu $\sqrt{s_{NN}} = 200$ GeV data [111]. The measurement of yields from azimuthal correlations between heavy-flavour decay electrons and charged hadrons was made and found to be consistent with hadron-hadron correlations as shown in figure 2.11.

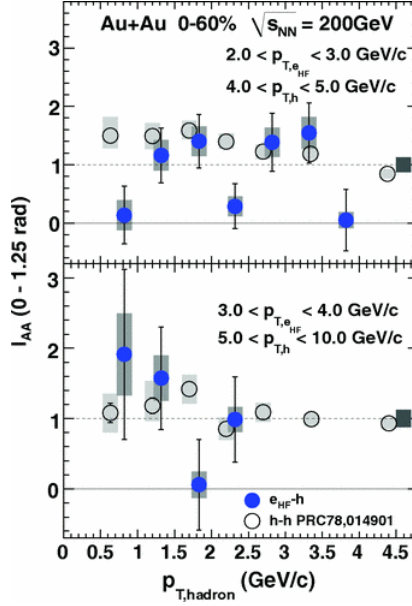


Figure 2.11: Near-side ($0 < \Delta\varphi < 1.25$ rad) I_{AA} for $2.0 < p_T^e < 3.0$ GeV/ c (top panel) and $3.0 < p_T^e < 4.0$ GeV/ c (bottom panel) as a function of the transverse momentum of associated hadrons for heavy-flavour decay electron trigger (solid points). Results are compared with the same using hadron triggers (open points) [111].

A theoretical calculation on azimuthal correlations between $c\bar{c}$ pairs has been done in central AuAu collisions in RHIC energies [112]. In this study, the heavy-quark pair production is initialized by using the leading order pQCD calculation. The $c\bar{c}$ pairs are assumed to be back-to-back with the same magnitudes of transverse momentum. The correlation function of $c\bar{c}$ pair has been calculated as shown in figure 2.12. From this figure, it is clear that different energy-loss mechanism gives different correlation functions of $c\bar{c}$ pairs in final states. It is observed that the angular correlations of final-state $c\bar{c}$ pair give a peak around $\Delta\varphi = \pi$ by considering radiative energy loss only, while the purely collisional energy loss gives a peak around $\Delta\varphi = 0$. This implies that the angular correlation function gives insight into different energy-loss mechanism inside the medium.

2.4 Open heavy-flavour in small systems

2.4.1 pPb collisions

In heavy-flavour sector, pPb collisions are studied not only because it provides reference to PbPb collisions, it has its own importance that allows an assessment of various cold nuclear matter (CNM) effects. It gives information on nuclear shadowing, i.e., the modification of PDFs in bound nucleons as compared to free nucleons, k_T broadening via multiple scattering of partons before hard scattering and energy loss in cold nuclear matter. Except these initial state effects, heavy-flavour hadrons are

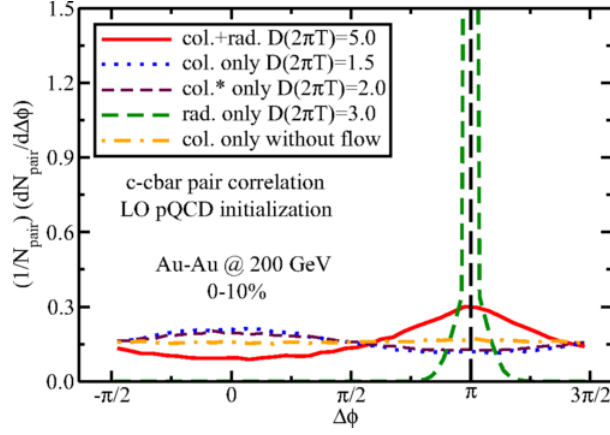


Figure 2.12: Angular correlations of $c\bar{c}$ pairs in central AuAu collisions [112].

also affected by final state effects like collectivity, hydrodynamics etc. The influence of CNM effect is measured by nuclear modification factor R_{pPb} given by:

$$R_{pA} = \frac{1}{A} \frac{d\sigma_{pA}/dp_T}{d\sigma_{pp}/dp_T} \quad (2.6)$$

where, $d\sigma_{pA}/dp_T$ and $d\sigma_{pp}/dp_T$ are the cross-sections measured in pA and pp collisions respectively.

Figure 2.13 shows the nuclear modification factor R_{pPb} of D mesons (left) [113] and electrons from heavy-flavour decay (right) [114] in pPb collisions at $\sqrt{s_{NN}} = 5.02$ TeV as compared to different theoretical models. For both the cases, R_{pPb} comes nearly equal to unity over a certain p_T range indicating that initial-state effects cannot explain the strong suppression alone observed at high- p_T in heavy-ion collisions.

One of the important studies in heavy-flavour sector is the measurements of azimuthal correlations between heavy-flavour hadrons or heavy-flavour decay electrons and the charged particles. Figure 2.14 shows the correlations between heavy-flavour decay electrons and charged particles in pPb collisions at $\sqrt{s_{NN}} = 5.02$ TeV with three different centrality classes: 0 – 20%, 20 – 60%, 60 – 100% [115]. It is observed from this figure that the most central class shows stronger suppressions with respect to the most peripheral class. The correlation studies are carried out further between D mesons and charged particles in pPb collision at $\sqrt{s_{NN}} = 5.02$ TeV by ALICE experiment [116] as shown in figure 2.15. Results are compared with the same analysis in pp $\sqrt{s} = 7$ TeV and found to be similar within uncertainties revealing the absence of CNM effects in LHC energies.

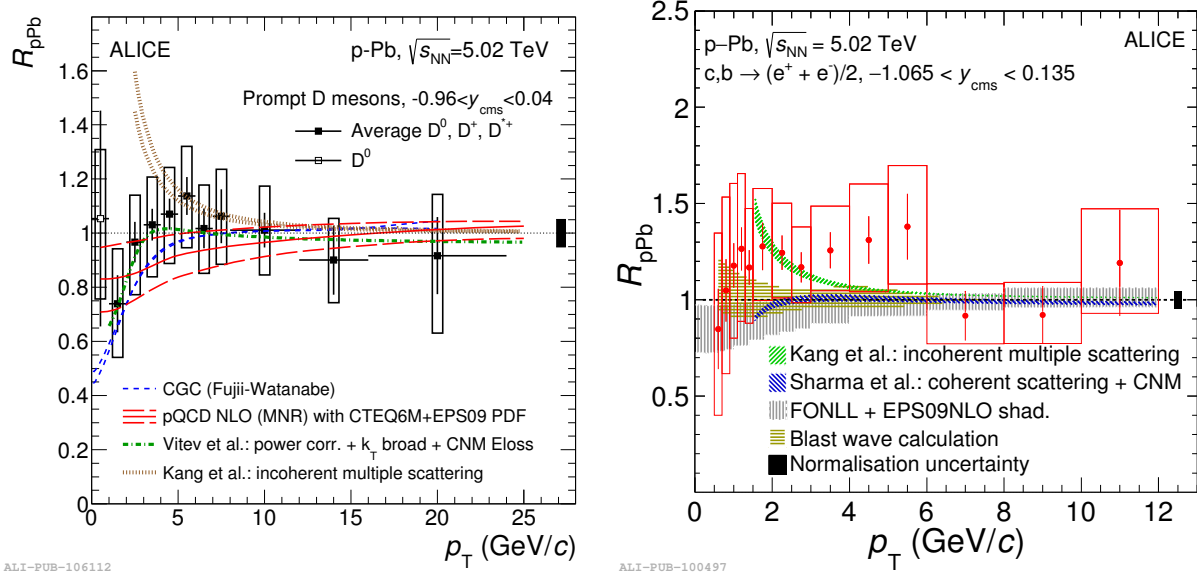


Figure 2.13: The nuclear modification factor R_{pPb} of D mesons (left) [113] and heavy-flavour decay electrons (right) [114] in pPb collisions at $\sqrt{s_{NN}} = 5.02$ TeV as compared to different theoretical models.

2.4.2 pp collisions

The study of heavy-flavours in pp collisions is important not only for being the baseline of AA and pA collisions, but also it allows the study of pQCD calculations. Analytically, the production of heavy-flavour hadrons or their decay products in pp collisions are obtained utilizing FONLL [117] and GM-VFNS [118]. Both the model are implemented in way of collinear factorization approach at Next-to-Leading order (NLO). Alternatively, some calculations based on k_T -factorization at Leading-Order (LO), including real part of higher order corrections are also done. Some more informations are obtained from the heavy-flavour study in pp collisions, namely, the parton distribution functions (PDF), the partonic hard scatterings and the fragmentation functions (FF). For example, the production cross sections of different species allow us to study the fragmentation functions. Similarly, by comparing the heavy-flavour productions with different rapidity and/or energy, the pQCD models get sensitive to gluon PDF.

The p_T -differential production cross sections for different prompt D-meson species (D^0, D^+, D^{*+}, D_s^+) have been measured by ALICE experiment with different $\sqrt{s} = 2.76, 7, 8$ TeV [119, 120, 121] from LHC run 1 and $\sqrt{s} = 5, 13$ TeV [122] from LHC run 2. Figure 2.16 shows the production cross-section of D^{*+} (left) and D^0 (right) with $\sqrt{s} = 5$ and 13 TeV respectively compared with FONLL. The results are found compatible with model within uncertainties.

A study of D-meson tagged jets are performed by ALICE collaboration in pp collisions which will be important a baseline to study the heavy-flavour jets in PbPb and pPb collisions [123]. Figure

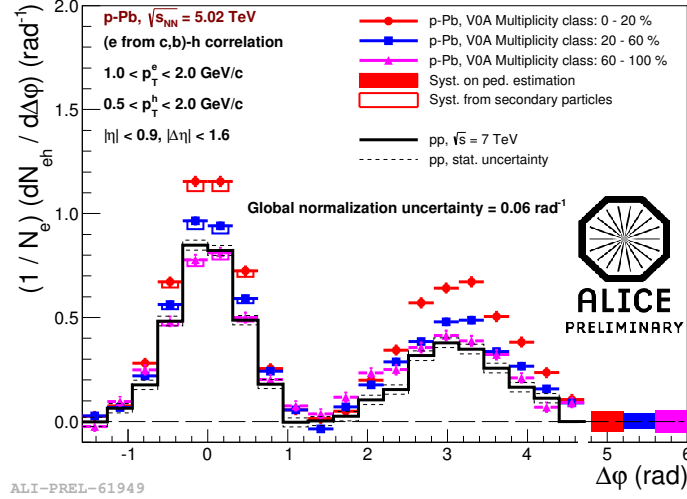


Figure 2.14: Electron-hadron correlations in pPb collisions at $\sqrt{s_{NN}} = 5.02$ TeV with three different multiplicity classes compared to minimum bias pp collisions at $\sqrt{s} = 7$ TeV [115].

2.17 shows the p_T -differential cross section of D^0 mesons tagged jets in pp collisions at $\sqrt{s} = 7$ TeV with $5 < p_{T,jets}^{ch}$ compared to different tunes of PYTHIA and HERWIG event generators.

The study of two-particle azimuthal correlations in heavy-flavour sector is also an important study to understand the charm production and fragmentation mechanisms. This study allows for validation of different Monte-Carlo event generators. Figure 2.15 shows the ALICE results of two-particle correlation between D mesons and charged particles [116]. Correlations have been measured between D mesons by LHCb experiments in pp collisions at $\sqrt{s} = 7$ TeV [124] which has provided the information on charm production mechanisms and event-properties containing heavy flavour. ATLAS has measured the production cross-section of D^{*+} mesons in jets in pp collisions at $\sqrt{s}=7$ TeV for jets with a range $25 < p_T < 70$ GeV/c. The study shows that the production of charm-quark jets or charm-quark fragmentation into D^{*+} mesons is not properly introduced in Monte-Carlo generators [125]. The correlations between heavy-flavour decay electrons and charged particles are also exploited to study in pp collisions both at RHIC and the LHC [126, 127].

Several studies in heavy-flavour sector in pp collisions with different centre-of mass energies motivates us to extend this study in $\sqrt{s} = 13$ TeV, the highest available energy in LHC till date. In this thesis, we have presented the results of two-particle azimuthal correlations between D mesons and charged particles in minimum-bias events of pp collisions at $\sqrt{s} = 13$ TeV. The results have been compared with the same analysis in pp collisions at $\sqrt{s} = 7$ TeV and pPb collisions at $\sqrt{s_{NN}} = 5.02$ TeV to compare the charm-jet properties among different centre-of-mass energies and different collision systems. This study will also become useful as a reference for further multiplicity dependent

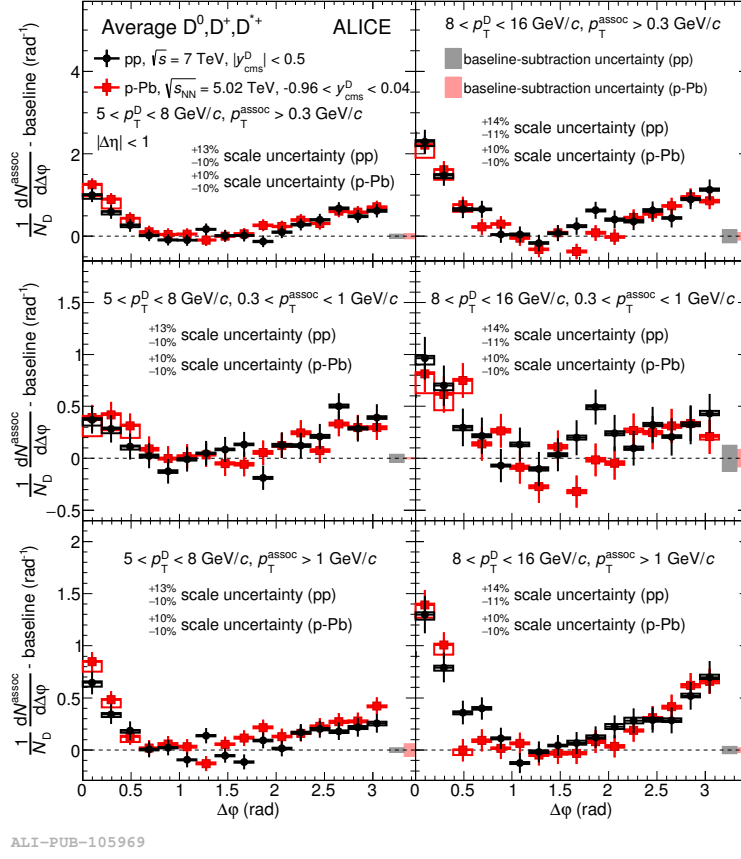


Figure 2.15: Azimuthal correlations between D mesons and charged particles in pPb collisions at $\sqrt{s_{NN}} = 5.02$ TeV with three different multiplicity classes compared to minimum bias pp collisions at $\sqrt{s} = 7$ TeV [116].

correlation analysis.

2.4. Open heavy-flavour in small systems

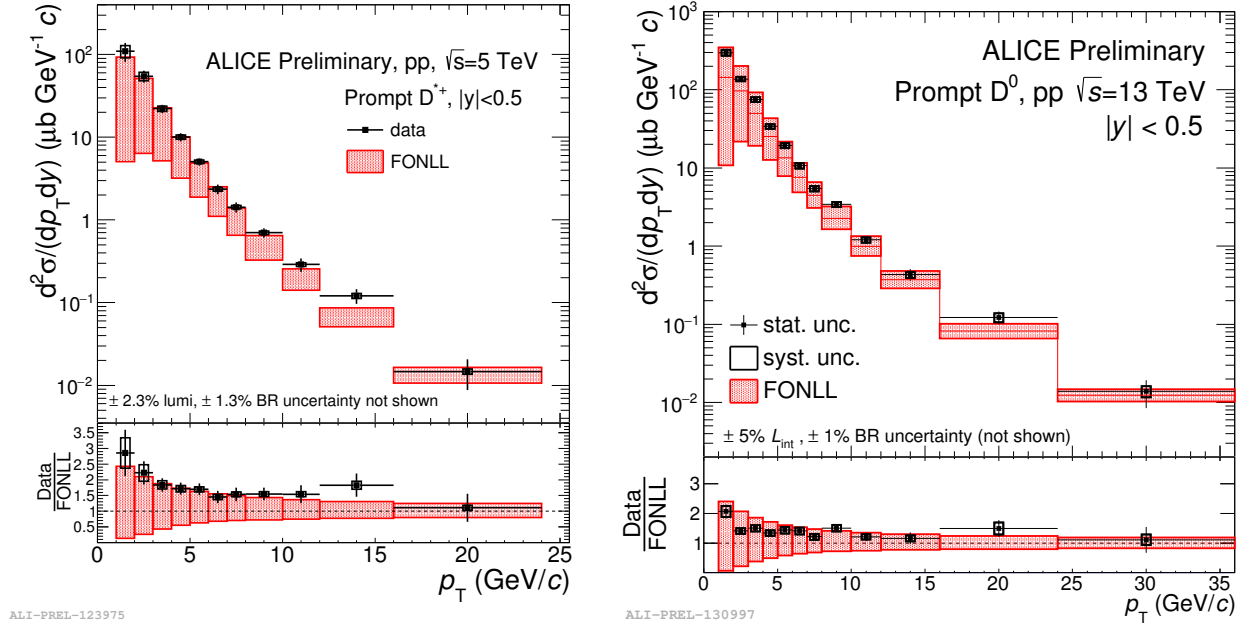


Figure 2.16: p_T -differential cross-section of D^{*+} (left) and D^0 (right) with $\sqrt{s} = 5$ and 13 TeV respectively measured by ALICE [122].

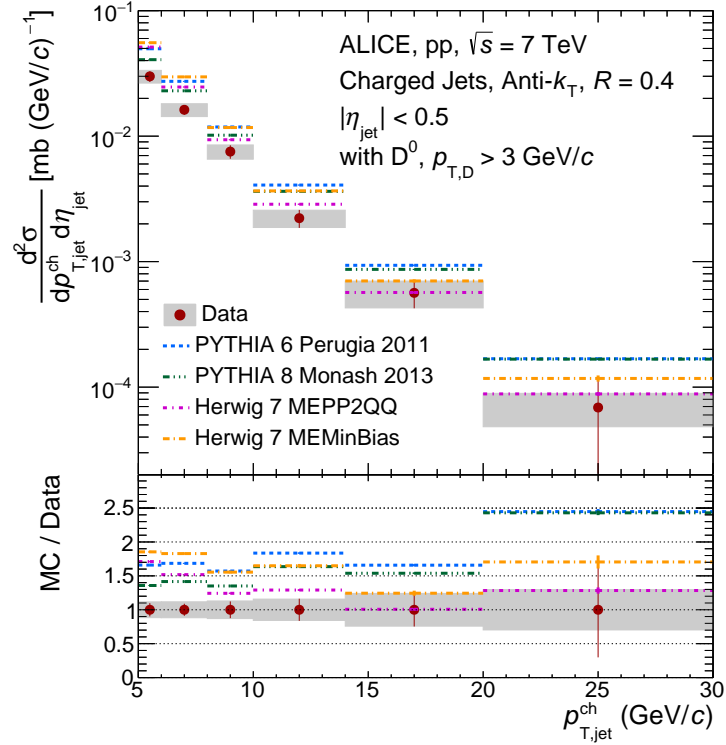


Figure 2.17: p_T -differential cross section of charm jets tagged with D^0 mesons in pp collisions at $\sqrt{s} = 7$ TeV measured by ALICE [123].

Chapter 3

Experimental Setup

In this chapter, we will give a brief description of the Large Hadron Collider (LHC) accelerator and the ALICE detector system along with its subsystems. The online data taking by ALICE and several offline techniques like clustering, track and vertex reconstruction etc have been described followed by an overview of ALICE computing system for several data analysis.

3.1 The Large Hadron Collider

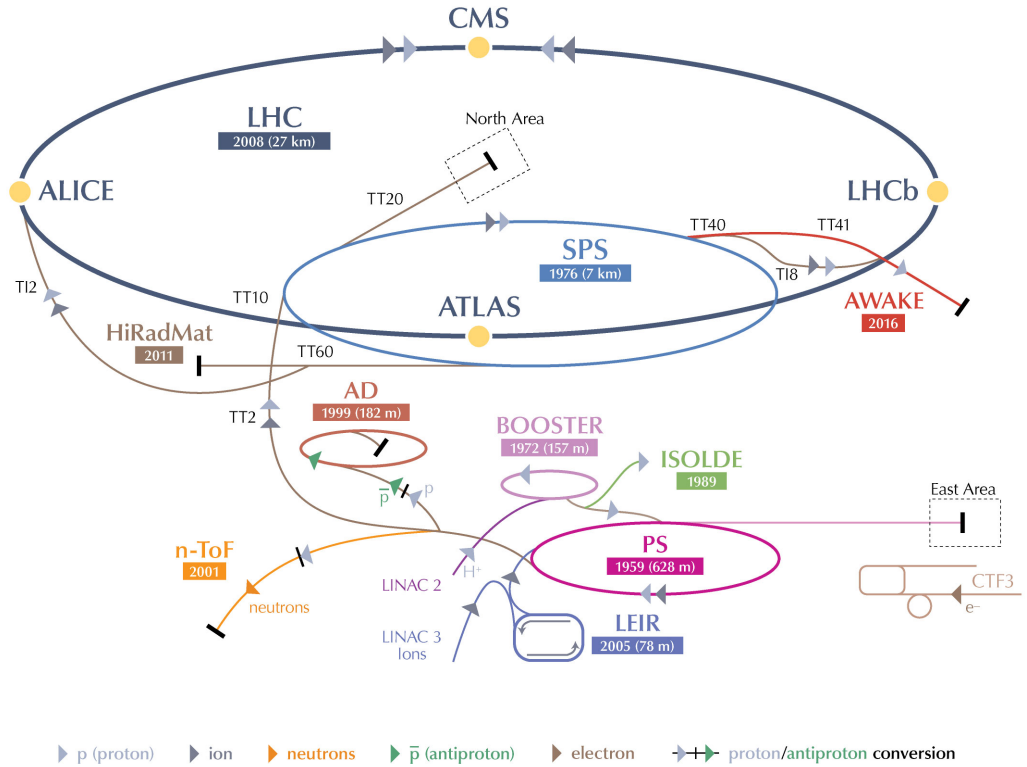
The Large Hadron Collider (LHC), built and operated by the European Organization for Nuclear Research (CERN) in Geneva, Switzerland, is the World's largest and most powerful particle accelerator till date. It is consisted of a 26.7 km double ring of superconducting magnets, buried 50-175 m underground, at the Swiss-French border [128]. The LHC is designed to collide particle beams circulating in opposite directions in separate beam pipes, kept at ultra-high vacuum, at a speed close to the speed of light in vacuum. Both beams are bent by the association of total of 1232 common dipole magnets that provide a strong magnetic field of strength 8.33 T. The magnetic field is generated by a current of 12000 A in the superconducting magnets, cooled by super fluid helium to 1.9 K - a temperature colder than outer space. Along with this, 858 quadrupole and 6000 corrector magnets are used additionally to control and shape the beam. The basic experimental structure of LHC is shown in figure 3.1. There are six detectors at the LHC's interaction points: ATLAS, ALICE, CMS, LHCb, LHCf, TOTEM. Each detectors are focussed with their particular physics goal.

The two large experiments are: A Torroidal LHC Apparatus (ATLAS) [31] and the Compact Muon Solenoid (CMS) [32]. These two detectors are general purpose particle detectors built to explore a wide range of physics from the search for the Higgs boson to the physics of extra dimensions and dark matter. The Large Hadron Collider beauty (LHCb) experiment [33] is specialized to investigate

the differences between matter and antimatter with high precision by studying the beauty quarks. A Large Ion Collider Experiment (ALICE) [34], a detector designed to study the heavy-ion collisions mainly, is dedicated to study the physics of strongly interacting matter at extreme energy densities. The TOTEM [129] and LHCf [130] are much smaller experiments and are intended for very specialized research like forward physics.

The LHC is designed to produce collisions upto a maximum energy $\sqrt{s} = 14$ TeV (for proton-proton) and $\sqrt{s_{NN}} = 5.5$ TeV (for heavy-ion). In run 1, it has provided proton-proton collisions with $\sqrt{s} = 900$ GeV, 2.76 TeV, 7 TeV, 8 TeV, PbPb collisions with $\sqrt{s_{NN}} = 2.76$ TeV and pPb collisions with $\sqrt{s_{NN}} = 5.02$ TeV. After the long shutdown (LS1) of 2 years, LHC started providing run 2 collisions with pp $\sqrt{s} = 5$ TeV, 7 TeV, pPb $\sqrt{s_{NN}} = 5.02$ TeV, PbPb $\sqrt{s_{NN}} = 5.02$ TeV and Xe-Xe $\sqrt{s_{NN}} = 5.44$ TeV. The run 2 operation has been ended in 2018. LHC will not perform any physics

CERN's Accelerator Complex



LHC Large Hadron Collider SPS Super Proton Synchrotron PS Proton Synchrotron
 AD Antiproton Decelerator CTF3 Clic Test Facility AWAKE Advanced WAKEfield Experiment ISOLDE Isotope Separator OnLine DEvice
 LEIR Low Energy Ion Ring LINAC LINear ACcelerator n-ToF Neutrons Time Of Flight HiRadMat High-Radiation to Materials

Figure 3.1: Large Hadron Collider accelerator ring complex [131].

run for the next 2 years. CERN accelerator complex will be upgraded during the long shutdown and again become operational in 2021.

3.2 The ALICE detector

A Large Ion Collider Experiment (**ALICE**), is one of the four major experiments at LHC, dedicated to study the heavy-ion collisions [132]. The primary goal of this detector setup is to study the properties of nuclear matter at ultra-high temperature and energy density, where the formation of Quark-Gluon Plasma (QGP) is expected. It also takes data for proton-nucleus asymmetric collisions and proton-proton collisions and study several QCD related physics problems. The schematic diagram of ALICE apparatus is shown in figure 3.2. It has the dimension of $16 \times 16 \times 26 \text{ m}^3$ and approximate weight around 10000 t. A right-handed orthogonal Cartesian system is used as the ALICE coordinate system. The origin this system is fixed at the LHC Interaction Point 2 (IP2), the z axis is parallel to the mean beam direction at the IP2, the x axis is horizontal pointing towards the centre of the LHC approximately, the y axis is vertical consequently and points upwards. It is composed of seventeen detector systems that can be classified as the group of central barrel and forward-backward detectors based on their pseudorapidity (η) coverage.

Central Barrel Detectors: The detectors in this region are mainly used for tracking and identi-

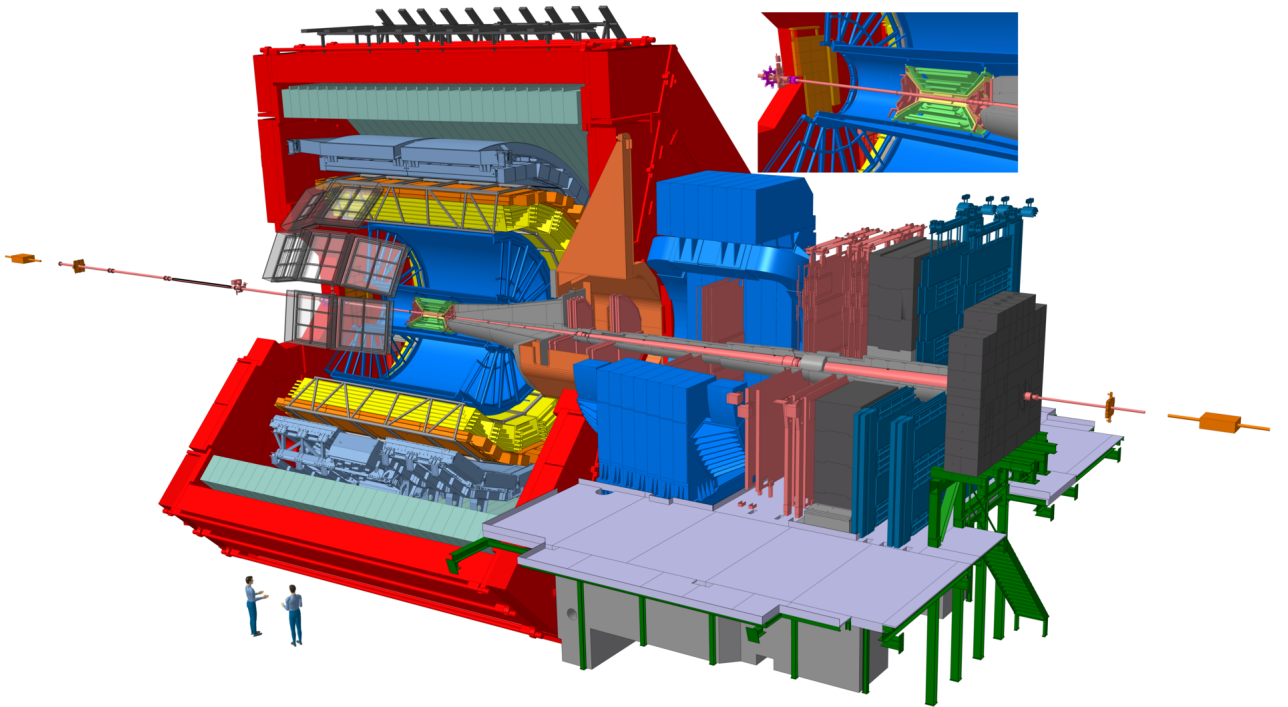


Figure 3.2: The schematic view of ALICE detector.

fication of charged particles and photons. They are embedded in magnetic field $B \leq 0.5$ T, which is generated by the large L3 solenoid magnet. Main detectors in this region are:

- **Inner Tracking System (ITS):** It is consisted of high precision silicon detectors mainly used for vertexing and the tracking of charged particles [133].
- **Time Projection Chamber (TPC):** It is a cylindrical shaped gas detector [134], which takes main role for the tracking of charged particles supported by ITS. It is also used for particle identification via energy loss (dE/dx) mechanism.
- **Time-Of-Flight (TOF):** It consists of Resistive Plate Chambers (MWPC) with excellent intrinsic time resolution to provide high-precision time measurements. It is used for particle identification and capable of separating particles via ratios such as π/K ratio up to 2.2 GeV/ c and K/p ratio up to 4 GeV/ c [135].
- **Transition Radiation Detector (TRD):** It is used for electron identification at high momentum region (>1 GeV/ c) [136], where the rejection of pions via TPC energy loss measurement is not sufficient.
- **Photon Spectrometer (PHOS):** It is a high resolution electromagnetic calorimeter based on lead-tungstate crystals (PWO) and optimized for measuring photons in p_T range 0.5-10 GeV/ c , neutral pions in p_T range 1-10 GeV/ c , and η mesons in p_T range 2-10 GeV/ c [137].
- **Electromagnetic Calorimeter(EMCal):** It is mainly used in the measurements of jet quenching and high- p_T photons and electron identifications [138]. EMCal is a lead scintillator sampling cylindrical calorimeter having coverage $-0.7 < \eta < 0.7$.
- **High Momentum Particle Identification Detector (HMPID):** It is specialized to extend ALICE particle identification feature in higher momentum region (up to 3 GeV/ c for the $\pi(K)$ and up to 5 GeV/ c for the protons) [139], i.e. beyond the momentum range allowed by the energy loss measurements by the ITS + TPC and the TOF.
- **ALICE COsmic Ray DETector (ACORDE):** It is an array of plastic scintillators placed on top of the L3 magnet with a radial distance of 8.5 m ($\eta < 1.3$) over the azimuthal angle $\pm 60^\circ$. In combination with the TPC, TRD and TOF, it is used for detecting the atmospheric muons and multi-muon events (cosmic rays) [140].

Forward and Backward Detectors: In this region, detectors can be characterized into two categories; the first is muon spectrometer and second contains general purpose detectors for event characterization and triggering.

- **Muon Spectrometer:** This detector is used to detect the particles with heavy-quark resonances i.e. the charmonium and bottomonium states via their muonic decay channel ($\mu^+\mu^-$). This detector is located at negative z direction covering a range $-4 < \eta < 2.5$. It is consisted of a complex arrangement of absorbers, dipole magnets, and fourteen planes of the tracking and triggering chambers [141].
- **Zero Degree Calorimeter (ZDC):** The primary role of ZDC is to measure the number of spectator nucleons i.e., to measure the centrality in heavy-ion collisions. Two identical sets of calorimeters are placed 116m away from the IP. Each set is consisted of three calorimeters: the neutron calorimeter (ZN), proton calorimeter (ZP) and electromagnetic calorimeter (ZEP). ZDC works on the detection of Cherenkov light produced by the charged particles shower [142].
- **Photon Multiplicity Detector (PMD):** It is a gas proportional counter, measures event-by-event photon multiplicity and spatial (η, φ) distributions of photons. PMD is kept 3.67 m away from IP with a coverage $2.3 < \eta < 3.9$ [143].
- **Forward Multiplicity Detector (FMD):** FMD provides charged particle multiplicity in wider pseudorapidity coverage $-3.4 < \eta < 5.1$, along with ITS at mid rapidity [144].
- **V0 Detector:** It consists of two arrays of scintillator counters (V0A and V0C). The V0A is located at 330 cm away from the IP while the V0C is installed at the front face of the hadronic absorber at a distance 90 cm from the IP. The V0 detectors are involved in fast triggering and centrality determination tasks [144].
- **T0 Detector:** It is consisted of two arrays of Cherenkov Counters (T0A and T0C) installed at either side of IP with distances -70 cm and 370 cm. Main task of T0 is to measure the collision time and also to provides an early “wake-up” signal to the TRD [144].

The sub-detectors of ALICE detector, used in the correlation analysis of D meson and charged particles are ITS, TPC, TOF and V0. The detail description and working principle of these sub-detectors are elaborated in the next sections.

3.2.1 Inner Tracking System

The Inner Tracking System (ITS) is an important detector in ALICE experiment mainly used for reconstruction of primary and secondary vertices, tracking and identification of charged particles with low momentum cut-off and to improve the momentum resolution at high p_T . This detector is made up of six layers of silicon detectors using three different technologies: pixel, drift and strip [133]. It covers the central pseudorapidity range of $|\eta| < 0.9$ and its distance from the beam line ranges from $r = 3.9$ cm (for the innermost pixel layer) to $r = 43$ cm (for the outermost strip layer) as shown in figure 3.3. A brief description of ITS layers is given below:

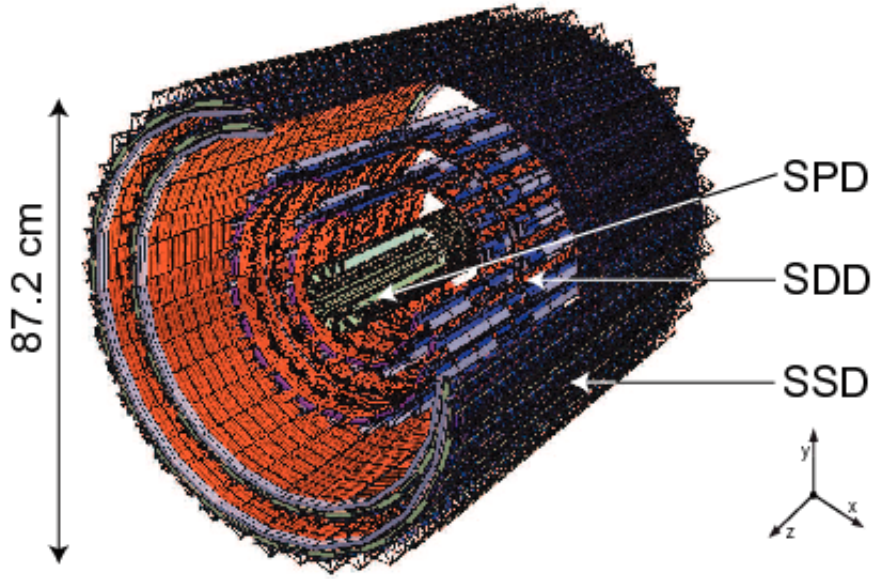


Figure 3.3: The schematic view of Inner Tracking System [145].

- **The Silicon Pixel Detector (SPD):** SPD is consisted of two innermost layers of ITS located at 3.9 cm and 7.6 cm from the beam-pipe and equipped with hybrid silicon pixel detectors. The basic detector module is known as half-stave and each of them contains two pixel detectors, called ladders, which are made of 5 readout chips. The readout chips are arranged in a matrix form containing 32 columns and 256 rows of pixels. Each pixel has the area of $50 \times 425 \mu\text{m}^2$ and they detects the passage of charged particles by giving a binary output when the signal crosses a set threshold. The main purpose of SPD is to provide a good secondary vertexing capability for heavy-flavour (charm and beauty) detection in a high multiplicity environment. It also provides a first level (L0) trigger signal, which is used to define minimum-bias events..
- **Silicon Drift Detector (SDD):** SDD consists the two intermediate layers, with average radii of 15.0 cm and 23.9 cm, equipped with Silicon Drift Detectors. This increases the tracking

3.2. The ALICE detector

resolution as well as the multi-track capability with higher multiplicity events. Therefore, it can give position information with high precision and energy loss (dE/dx) of the tracks which helps in particle identification.

- **The Silicon Strip Detector (SSD):** SSD consists the two outermost layers of ITS. It plays a vital role in the tracking of the particles produced in the collisions by connecting the tracks from TPC to ITS. The SSD also plays a role to the particle identification through the measurement of their energy loss.

The performance of ITS is important to measure the secondary vertices originated from the weak decays of strange, charm and beauty particles, which are located close to the collision vertex. Secondary vertices, separated by at least $100\ \mu\text{m}$ from the primary vertex can be distinguished with the help of ITS.

3.2.2 Time Projection Chamber

The Time Projection Chamber (TPC) is the main tracking detector in the central barrel of the ALICE experiment at the LHC [134]. Its function is to provide track finding, charged particle momentum measurement, particle identification and track separation.

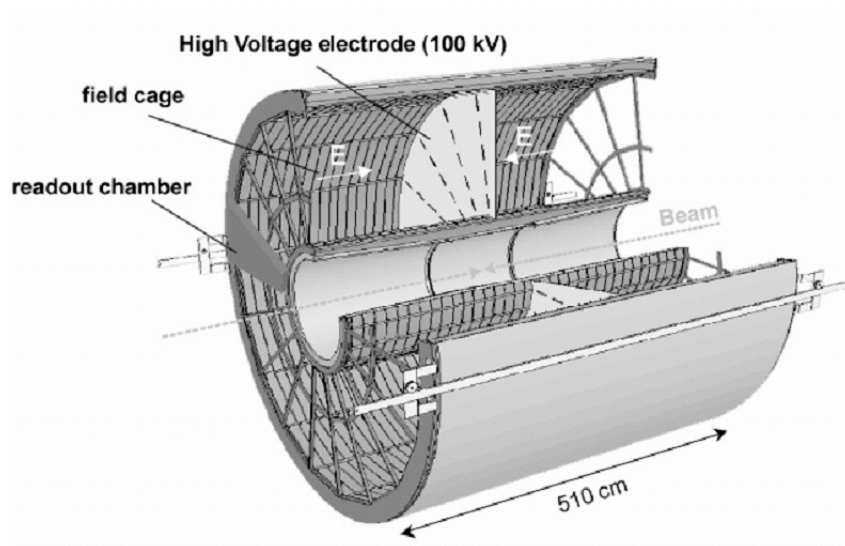


Figure 3.4: The schematic view of Time Projection Chamber [146].

The TPC is a cylindrical shaped detector with $88\ \text{m}^3$ volume. The schematic diagram of ALICE TPC is shown in figure 3.4. A high voltage (HV) electrode is located at its axial centre, which divides the gas volume into two symmetric drift regions. The HV electrode and two opposite axial potential

degraders create an uniform electrostatic field in the two drift regions. TPC contains a gas mixture of $Ne - CO_2$ (90:10) with an addition of N_2 (around 5%) for a better stability.

Charged particles traversing the TPC gas volume ionize the gas creating ion-electron pairs along their paths. The liberated electrons drift towards the end plates of the cylinder where the multi-wire proportional chambers (MWPC) are located for the signal measurements. The MWPC with cathode pad readout are mounted into 18 trapezoidal sectors at each end plate of TPC covering an active area 32.5 m^2 . There are 560,000 readout pads in 3 different sizes at the inner and outer radius, used in trapezoidal sectors to keep low occupancy, which is necessary requirement for getting better dE/dx and position resolution.

TPC gives the particle identification through specific energy-loss (dE/dx), charge and momentum of the particle. The specific energy loss is described by the Bethe-Bloch formula and parametrized by a functional form given in equation 3.1, originally proposed by ALEPH collaboration [147].

$$f(\beta\gamma) = \frac{P_1}{\beta^{P_4}} (P_2 - \beta^{P_4} - \ln(P_3 + \frac{1}{(\beta\gamma)^{P_5}})) \quad (3.1)$$

where β is the particle velocity, γ the relativistic factor and $P_1 - P_5$ are fit parameters.

Figure 3.5 shows specific energy loss dE/dx as a function of particle momentum (p), from which a clear separation is observed among different particle bands.

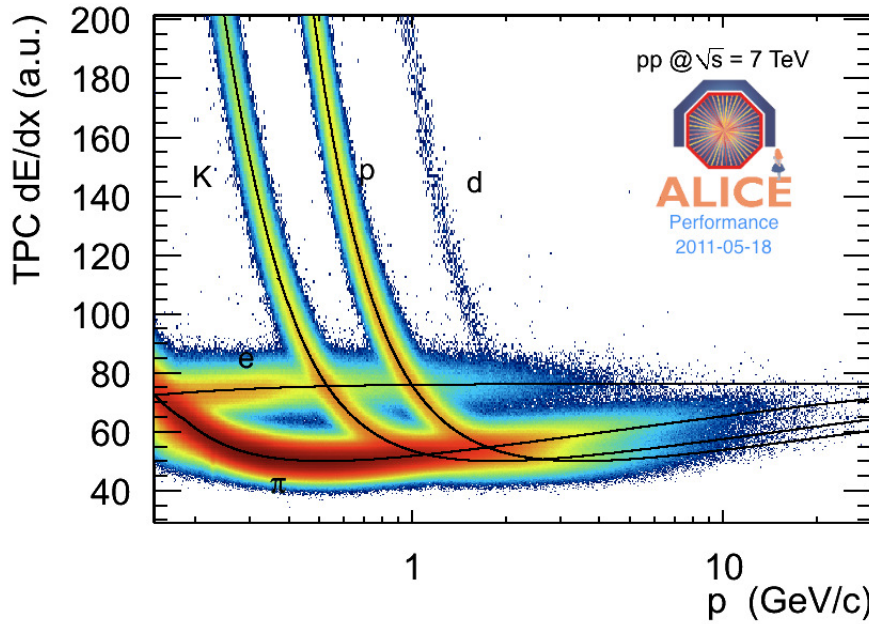


Figure 3.5: Specific energy loss (dE/dx) of particles as a function of particle momentum in pp collisions at $\sqrt{s}=7 \text{ TeV}$.

3.2.3 Time Of Flight

Time Of Flight (TOF) is the detector that identifies the charged particles in intermediate momentum range. A time resolution of 100 ps provides 3σ π /K separation up to 2.2 GeV/ c and K/p separation up to 4 GeV/ c [135]. The main purpose of TOF is to study the QCD thermodynamics via measuring the p_T distributions of π , K and p and particle ratios on an Event-by-Event basis and signatures of QGP formation via open charm and ϕ meson production.

The TOF detector is cylindrical in shape and covers polar angles between 45° to 135° over the full azimuth. It has a modular structure with 18 sectors in φ ; each of these sectors is divided into 5 modules along the beam direction. The modules contain a total of 1638 detector elements (MRPC strips), covering an area of 160 m² with 157248 readout channels (pads).

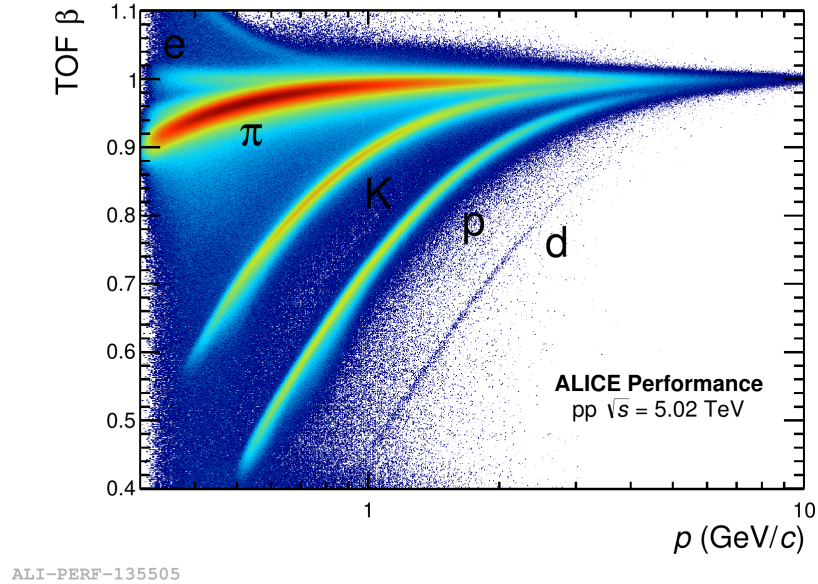


Figure 3.6: Particle velocity (β) as a function of particle momentum in pp collisions at $\sqrt{s}=5.02$ TeV

The particle mass is measured with TOF in conjunction with the momentum and track length measured by the tracking detectors given in equation 3.2.

$$m^2 = p^2 \left(\frac{t^2}{L^2} - 1 \right) \quad (3.2)$$

where m , p , t , L are mass, momentum, time-of-flight and track length respectively. For two particles with masses m_1 and m_2 having same momentum and track length, the time-of-flight difference is given by equation 3.3.

$$t_1 - t_2 = \frac{L}{2} \frac{m_1^2 - m_2^2}{p^2} \quad (3.3)$$

Figure 3.6 represents the particle velocity (β) as a function of particle momentum in pp collisions at $\sqrt{s} = 5.02$ TeV. To improve the precision in particle identification in an extended momentum range, the combination of TPC and TOF is used.

3.2.4 V0 detector

The V0 detector is a small angle detector which is consisted of two arrays of 32 scintillating counters [144, 148]. The two arrays are known as V0A and V0C, which are installed on either side of the IP. The main function of this detector is the estimation of Minimum Bias and Centrality triggers for the central barrel detectors in pp, pA, AA collisions. It also measures multiplicity/centrality and provides information on luminosity. The V0A is located 330 cm away from the IP and V0C is placed at the front face of the hadronic absorber, 90 cm away from the IP. They have the pseudorapidity coverage $2.8 < \eta < 5.1$ (V0A) and $-3.7 < \eta < -1.7$ (V0C) for collision vertex at the central position. A schematic diagram of V0 detector is shown in figure 3.7.

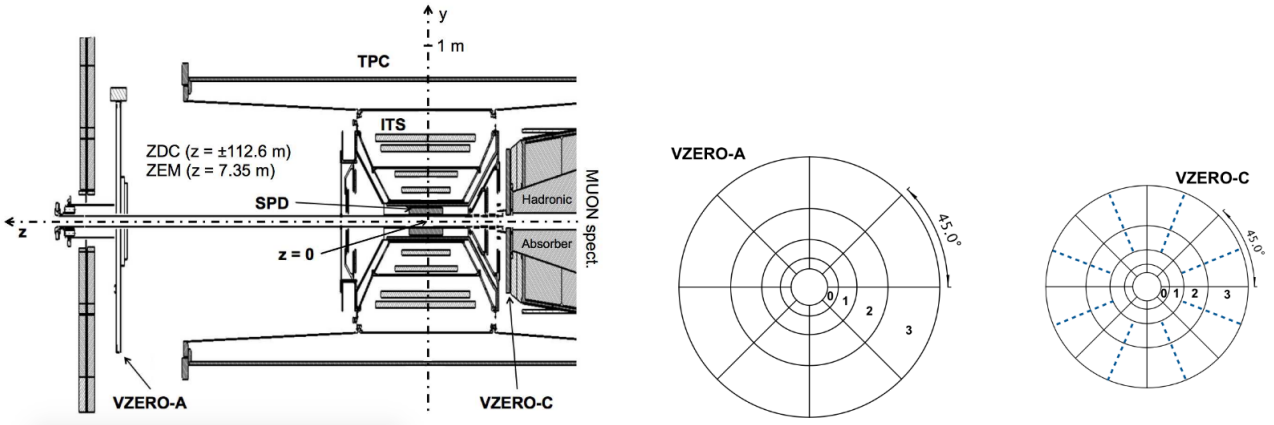


Figure 3.7: Position of the two VZERO arrays within the general layout of the ALICE experiment (left). Schematic diagram of VZERO-A and VZERO-C arrays showing their segmentation (right) [148].

The role of V0 in ALICE experiment is given below:

- **Triggering:** In practice and during operational mode, both V0A and V0C are required (AND mode) to give triggers, namely, Minimum Bias trigger (MB), Multiplicity Trigger (MT), semi-Central (CT1) and Central Trigger (CT2).
- **Multiplicity/Centrality determination:** V0 determines the centrality/multiplicity of the event by measuring the energy deposition on the scintillators.

- **Luminosity measurement:** The online monitoring of luminosity uses a time coincidence between the two V0 arrays. The rate of coincidence is given by:

$$R = A.\epsilon.\sigma.L \quad (3.4)$$

The luminosity measurements are done by van der Meer scan method [149].

3.3 ALICE online data taking framework

A set of activities is done to run the ALICE experiment in order to control the sub-detectors and acquire raw data. The Experiment Control System (ECS) takes the lead role to control the whole detector system as well as the overall data taking. The data taking activities are divided into four major categories:

- **Detector Control System (DCS):** It controls the detectors remotely from the ALICE Run Control (ARC) room. Mainly the DCS takes care of several detector services like cooling, ventilation, magnetic field, power supplies etc.
- **Data Acquisition (DAQ):** It handles the data-flow from the sub-detector electronics to the data storage [150]. A first layer of computers, the Local Data Concentrators (LDCs), reads out the event fragments from the optical Detector Data Links (DDLs). The event fragments aggregated in sub-events are then transferred to a second layer of computers, the Global Data Collectors (GDCs), in charge of performing the event building. The same GDC receives all the fragments of a given event, and assembles them in a full event. The event is recorded to a Transient Data Storage (TDS), migrated to the Permanent Data Storage (PDS) and published via the Grid. The DAQ system also includes software packages to monitor the data quality and the system performance.
- **Trigger (TRG):** It consists of the Central Trigger Processor (CTP) and 24 Local Trigger Units (LTU). The CTP generates three levels of hardware triggers - L0, L1 and L2. Trigger selection includes the past-future protection - a fully programmable hardware mechanism of controlling the event pile-up [151].
- **High Level Trigger (HLT):** It reduces the volume of physics data by selection and compression of the data [152].

3.4 ALICE offline computation

ALICE requires a good offline computation to handle the huge amount of data collected during active runs. The main task of the ALICE offline project is to develop and operate the framework for data processing [153, 154]. The framework is consisted of three main areas:

- **Distributed computing:** It is not possible to concentrate the huge amount of ALICE data in a single computing centre. Thus, the data processing is distributed onto several computing centres worldwide. The “ALICE-grid” handles the treatment of this heterogeneous collection of distributed computing resources as an integrated computing centre. The ALICE VO (Virtual Organization) is spread over more than 80 sites all over the world.
- **Offline data processing:** It includes several tasks like simulation, reconstruction, calibration, alignment, visualization and physics analysis. Typically, the distributed computing facility is used for offline data processing.
- **Quasi-online operations:** It is mainly used for data reconstruction and analysis during pp collisions. The idea of this operation is to provide calibration information available immediately at the end of each run for the first reconstruction pass. The information comes from DAQ, DCS, HLT and trigger.

3.4.1 AliRoot and AliPhysics framework

The offline framework of ALICE known as ALiROOT and AliPhysics is based on ROOT [155] which follows object-oriented programming. The whole framework is mostly written in C++. It is used for simulation, alignment, calibration, reconstruction, visualization and analysis of the experimental data. A schematic diagram of this framework is shown in figure 3.8.

- **Event simulation:** The simulation of proton-proton, proton-nucleus and nucleus-nucleus is done via several events generators like PYTHIA [156, 157], HIJING [158] etc. The simulated events store the information of produced primary particles and their decay products as a function of momentum, charge, rapidity etc. This framework also helps to provide a predictive and precise detector response simulation.
- **Detector response simulation:** For the detector response simulations, different transport Monte-Carlo packages are used like GEANT 3 [159], GEANT 4 [160] and FLUKA [161]. Here, the particles are transported through detectors considering the real detector geometry, alignment and other conditions.

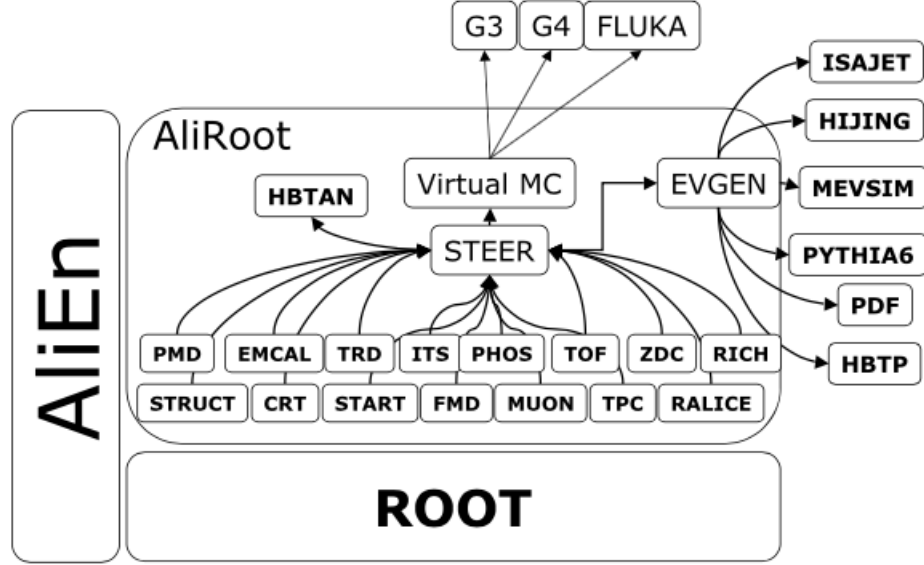


Figure 3.8: The ALIROOT framework.

- **Alignment framework:** The parts of the detector that are subject to relative positioning different from the ideal one, are known as ‘alignable volumes’. When the simulation program is started, the ideal geometry is generated or take the information from the previous run. After that, it finds the objects marked as ‘alignable’, accepts the modification and then the particles are transported through the modified geometry.
- **Calibration framework:** This framework is very similar to the alignment framework. The initial calibration constants are obtained either from the detector properties measured during construction, or from algorithms running online during data-taking. During the reconstruction itself, better calibration constants can be calculated.
- **Reconstruction framework:** This framework provides a simple user interface that allows the users to configure the reconstruction procedure as discussed below:
 - **Cluster finding:** Cluster is defined as a set of adjacent points (in space and/or time) generated by a particle after passing through the sensitive material of the detector. This reconstruction step is executed for each detector separately.
 - **Primary vertex reconstruction:** The information provided by the Silicon Pixel Detectors (SPD) helps in reconstructing the primary vertex. The pairs of reconstructed points are selected in the two layers, which are close in azimuthal angle in the transverse plane. Then, the z-position of the primary vertex is determined from their z-coordinates. The

same procedure is performed for transverse plane also. For well focused and stable beams, the transverse position of the interaction point is determined by averaging over many events. The resolution of the primary vertex position depends on the track multiplicity given by equation 3.5.

$$\sigma_z = \frac{A}{\sqrt{dN_{ch}/d\eta}} + B \quad (3.5)$$

where σ_z is the resolution of z-coordinate of primary vertex, $A = 290 \mu\text{m}$ and B is a few microns typically, depending on the residual mis-alignment of the SPD layers. The vertex position resolution is obtained as $10 \mu\text{m}$ for heavy ion, while it comes out to be $150 \mu\text{m}$ for pp. The primary-vertex position is used as an input for the tracking. After track reconstruction, the position of the primary vertex is recalculated using the measured track parameters and the resolution gets improved.

- **Track reconstruction and PID:** The track finding and fitting is based on Kalman Filter method introduced by P. Billoir [162, 163]. In this method, first the space-point are determined considering the centre-of-gravity of each cluster, then the tracking is done using those space-points reconstructed in TPC. The tracking is done two times: (1) assuming the track originated from the primary vertex and (2) assuming that the track originated elsewhere (decay, secondary interaction, etc.). The tracking output that contains the information from TPC only are known as “TPC-only tracks”. In the next step, the tracks are then propagated to the outer layer of ITS. All the reconstructed points on this outermost layer that are associated with the TPC tracks, are propagated to the next ITS layer inwards. This process is subsequently repeated for all the TPC tracks. For the very low momentum, tracking is repeated inside ITS only. Once the ITS inward tracking is completed, the Kalman filter algorithm is repeated again in the opposite direction, starting from the vertex and going outwards from ITS to TPC. Tracks beyond TPC are followed by assigning space points in the TRD, and matching the tracks with hits in the TOF, minimum-ionizing clusters in the HMPID and space points in the CPV (Charged-Particle Veto detector).
- **Secondary vertex reconstruction:** Secondary vertices i.e. the vertices from the decay of long-lived particles are reconstructed at this level. Opposite-sign tracks that originate sufficiently far away from the primary vertex are combined and their distance of closest approach is calculated. If the distance comes below some predetermined value and the point of the closest approach is located before the first measured points on both tracks, the pair is considered as a candidate for a secondary decay vertex. In addition, topological

cuts are implemented for different physics analysis.

- **Analysis:** Analysis is the final stage performed on the data to extract the physics information. The output obtained from the reconstruction is stored in ESD (Event Summary Data) format. As the ESDs are very large in size, they are further reduced to AOD (Analysis Object Data) format which contains the information to perform physics oriented analysis. These AODs are further used for analysis using a common interface ‘AliAnalysis’ scheduled for the user-end.
- **CERN Analysis Facility (CAF):** It allows to perform various operations very rapidly on acquired data with full offline framework and provides information on the data quality and calibration algorithms.

Chapter 4

Analysis Detail for two-particle azimuthal correlations between D meson and charged particles in pp collisions with ALICE detector

In this chapter, we will give a detail description on the ALICE analysis method of two-particle azimuthal correlations between D mesons and charged particles. First, we will discuss on the data set used and the selected events for this analysis. After that, we will describe the detail analysis steps including the whole correction framework.

4.1 Dataset and event selection

The analysis has been performed on data on pp data at $\sqrt{s} = 13$ TeV collected in 2016 during LHC run 2. The list of runs used in this analysis is given below:

- **LHC16d:** 252330, 252326, 252325, 252322, 252319, 252317, 252310, 252271, 252248, 252235;
- **LHC16e:** 253591, 253589, 253563, 253530, 253529, 253517, 253488, 253482, 253481, 253478, 253437;
- **LHC16g:** 254332, 254331, 254330, 254304, 254303, 254302, 254293, 254205, 254204, 254199, 254193, 254178, 254175, 254174, 254149, 254147, 254128;
- **LHC16h:** 255467, 255466, 255465, 255463, 255447, 255442, 255440, 255421, 255420, 255419, 255418, 255415, 255407, 255402, 255398, 255352, 255351, 255350, 255283, 255280, 255276,

255275, 255256, 255255, 255253, 255252, 255251, 255249, 255248, 255247, 255242, 255240, 255182, 255181, 255180, 255177, 255176, 255174, 255173, 255171, 255167, 255162, 255159, 255154, 255111, 255091, 255086, 255085, 255082, 255079, 254984, 254983, 254654, 254653, 254652, 254651, 254649, 254648, 254646, 254644, 254640, 254632, 254630, 254629, 254621, 254606, 254604;

- **LHC16j:** 256418, 256417, 256415, 256373, 256372, 256371, 256368, 256366, 256365, 256364, 256363, 256362, 256361, 256356, 256311, 256309, 256307, 256302, 256299, 256297, 256295, 256292, 256290, 256289, 256287, 256284, 256283, 256282, 256281, 256231, 256228, 256227, 256223, 256219;

- **LHC16k:** 258537, 258499, 258477, 258456, 258454, 258452, 258426, 258393, 258391, 258387, 258359, 258336, 258332, 258307, 258306, 258303, 258302, 258301, 258299, 258278, 258274, 258273, 258271, 258270, 258258, 258257, 258256, 258204, 258203, 258202, 258198, 258197, 258178, 258117, 258114, 258113, 258109, 258108, 258107, 258063, 258062, 258060, 258059, 258053, 258049, 258045, 258042, 258041, 258039, 258019, 258017, 258014, 258012, 258008, 258003, 257992, 257989, 257986, 257979, 257963, 257960, 257957, 257939, 257937, 257936, 257892, 257855, 257853, 257851, 257850, 257804, 257803, 257800, 257799, 257798, 257797, 257773, 257765, 257757, 257754, 257737, 257735, 257734, 257733, 257727, 257725, 257724, 257697, 257694, 257692, 257691, 257689, 257688, 257687, 257685, 257684, 257682, 257644, 257642, 257636, 257635, 257632, 257630, 257606, 257605, 257604, 257601, 257595, 257594, 257592, 257590, 257588, 257587, 257566, 257562, 257561, 257560, 257541, 257540, 257539, 257537, 257531, 257530, 257492, 257491, 257490, 257488, 257487, 257474, 257468, 257457, 257433, 257364, 257358, 257330, 257322, 257320, 257318, 257260, 257224, 257209, 257206, 257204, 257144, 257141, 257139, 257138, 257137, 257136, 257100, 257095, 257092, 257086, 257084, 257082, 257080, 257077, 257028, 257026, 257021, 257012, 257011, 256944, 256942, 256941, 256697, 256695, 256694, 256692, 256691, 256684, 256681, 256677, 256676, 256658, 256620, 256619, 256592, 256591, 256589, 256567, 256565, 256564, 256562, 256560, 256557, 256556, 256554, 256552, 256514, 256512, 256510, 256506, 256504;

- **LHC16l:** 259888, 259868, 259867, 259866, 259860, 259842, 259841, 259822, 259789, 259788, 259781, 259756, 259752, 259751, 259750, 259748, 259747, 259713, 259711, 259705, 259704, 259703, 259700, 259697, 259668, 259650, 259649, 259477, 259473, 259396, 259395, 259394, 259389, 259388, 259382, 259378, 259342, 259341, 259340, 259339, 259336, 259334, 259307, 259305, 259303, 259302, 259274, 259273, 259272, 259271, 259270, 259269, 259264, 259263,

4.2. Analysis method

259261, 259257, 259204, 259164, 259162, 259118, 259117, 259099, 259096, 259091, 259090, 259088, 258964, 258962, 258923, 258919;

- **LHC16o**: 264035, 264033, 263985, 263984, 263981, 263978, 263977, 263923, 263920, 263917, 263916, 263905, 263866, 263863, 263810, 263803, 263793, 263792, 263790, 263787, 263786, 263785, 263784, 263744, 263743, 263741, 263739, 263738, 263737, 263691, 263690, 263682, 263663, 263662, 263657, 263654, 263652, 263647, 263529, 263497, 263496, 263490, 263487, 263332, 263331, 262858, 262855, 262853, 262849, 262847, 262844, 262842, 262841, 262778, 262777, 262776, 262768, 262760, 262727, 262725, 262723, 262719, 262717, 262713, 262708, 262706, 262705, 262428, 262426, 262425, 262424;
- **LHC16p**: 264347, 264346, 264345, 264341, 264336, 264312, 264306, 264305, 264281, 264279, 264277, 264273, 264267, 264266, 264265, 264264, 264262, 264261, 264260, 264259, 264238, 264235, 264233, 264232, 264198, 264197, 264194, 264190, 264188, 264168, 264164, 264139, 264138, 264137, 264129, 264110, 264109, 264086, 264085, 264082, 264078, 264076;

For event selection, we put a minimum bias (MB) trigger which is defined by a hit on SPD detector or a hit on either of the V0A and V0C detector. The events with a reconstructed primary vertex within 10 cm from the centre of the detector along the beam line have been considered for this analysis. This selection maximizes the detector coverage of selected events, considering the longitudinal size of the interaction diamond and the detector pseudorapidity acceptance. Beam-gas events are removed by offline selections based on the timing information provided by the V0 and the Zero Degree Calorimeters and the correlation between the number of hits and track segments in the SPD detector. The pile-up events i.e. the events with more than one reconstructed vertex are removed from the analysis by applying a cut on two vertices at a minimum distance of 0.8 cm obtained by the SPD vertexer.

4.2 Analysis method

This analysis mostly follows the similar strategy used in 2013 pPb data analysis $\sqrt{s_{NN}} = 5.02$ TeV and 2010 pp data analysis at $\sqrt{s} = 7$ TeV [164]. In the usual method of data analysis of two-particle azimuthal correlation, the pairs of particles of the same collision event are built, where the particle pairs are formed by trigger particles defined by the transverse momentum threshold $p_T > p_T^{\text{trigg}}$ and associated particles defined by $p_T > p_T^{\text{assoc}}$. Each pair of particles is considered only once by requiring $p_T^{\text{assoc}} < p_T^{\text{trigg}}$. But in the correlation analysis of D meson and charged particles, it is the particle

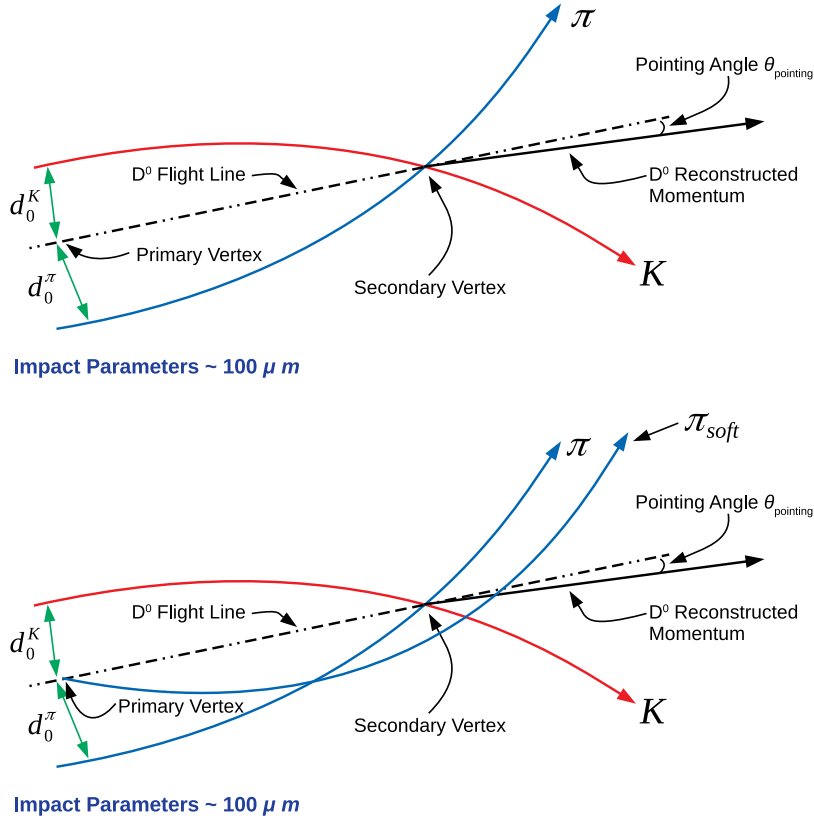


Figure 4.1: Schematic diagram for D^0 and D^{*+} decaying into a pion and kaon pair.

identity to define the trigger particle rather than a momentum cut and therefore the momentum range of the associated particles is not constrained by that of the trigger particle. Correlation pairs are formed by considering D meson (trigger particle) within different $p_T > p_T^{\text{trigg}}$ ranges like $3 - 5 \text{ GeV}/c$, $5 - 8 \text{ GeV}/c$, $8 - 16 \text{ GeV}/c$ and charged tracks (associated particles) within different $p_T > p_T^{\text{assoc}}$ ranges like $> 0.3 \text{ GeV}/c$, $> 1.0 \text{ GeV}/c$, $0.3 - 1.0 \text{ GeV}/c$. The analysis procedure is discussed step by step in the following sections:

4.2.1 Selection of D meson as trigger particle

We define “trigger” particles as the selected D meson candidates (D^0 , D^+ , D^{*+}) within a given p_T^{trigg} range for each single event. The reconstruction of D meson is done from their hadronic decay channels as discussed in chapter 2 and it is mainly based on the selection of displaced-vertex topologies. Figure 4.1 shows a schematic diagrams of D^0 and D^{*+} decays. The reconstruction procedure is done following the main three steps:

Reconstruction of secondary vertex

The secondary vertex i.e. the decay vertex of D meson is reconstructed from the decay tracks using the same procedure used for primary vertex reconstruction as described in [120]. The pair of decay products are matched using ITS+TPC tracks with $\eta < 0.8$ and $p_T > 0.3$ GeV/c. The tracks are also chosen in such way so that it have at least 70 clusters in TPC with $\chi^2/ndf < 2$ and refitted from TPC to ITS.

Topological cuts

The reconstruction of D meson candidates is done by combining all the identified tracks (which may be the decay products) instead of recognizing the the actual decay product. This generates a large amount of combinatorial background D meson candidate, so we need to put some topological selection criteria to get a good signal over background ratio. It is determined by a parameter call “significance value” which is defined by $S = \frac{S}{\sqrt{S+B}}$, where S is the signal and B is background calculated from invariant mass spectra. There is a set of a few single and pair variable tracks optimized for this purpose:

- **Momentum cuts (p_T^K, p_T^π):** A threshold p_T cut on the tracks are applied to remove the tracks coming directly from the primary vertex rejecting some low momentum background candidate effectively.
- **Impact parameter cuts (d_0^K, d_0^π):** The impact parameter d_0 is defined as the closest distance of a particle trajectory from the primary vertex. A lower cut of d_0 is applied to remove the background coming from primary vertex and a upper cut is applied to remove the decay products from strange and bottom hadrons. Though this cut is not applied for the D^+ analysis due the complication arising by the third decay product, this is important for the two-body decay system like D^0 .
- **DCA between the decay tracks:** The distance of closest approach (DCA) is the minimum distance between the two track helices. It is important to set a minimum distance when the secondary vertex is reconstructed. Ideally, it should be zero, but it gives a finite value because of the spatial resolution of the detector. Thus, we set a maximum DCA value above which tracks are rejected. This cut helps to reduce the background coming from primary vertex.
- **Cosine of decay angle ($\cos\theta^*$):** The decay angle is defined as the angle between Kaon momentum in D^0 rest frame and the boost direction as shown in figure 4.2. The daughters

decay isotropically in D^0 reference frame, the $\cos\theta^*$ distribution should come flat ideally for signal while for background it peaks at $|\cos\theta^*| = 1$ as shown in figure 4.3. The occurrence of peaks is due to cuts applied during reconstruction and detector effects. Thus we put a cut $|\cos\theta^*| < 0.8$ to get a better significance value.

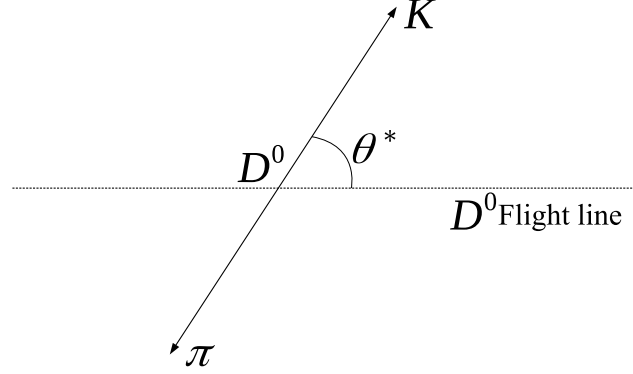


Figure 4.2: Schematic diagram for D^0 decaying in D^0 rest frame.

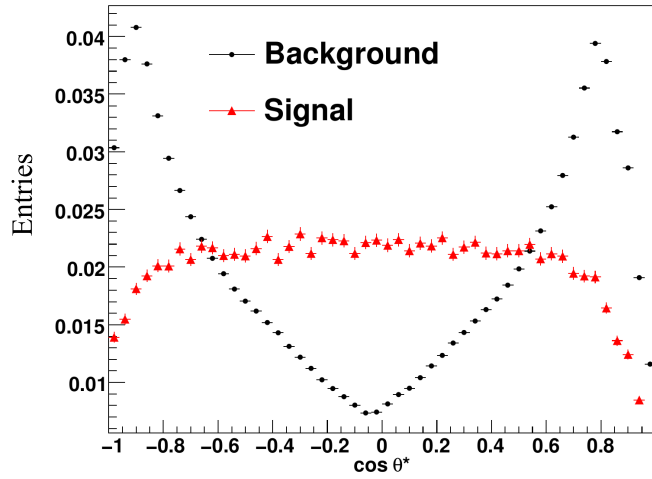


Figure 4.3: $\cos\theta^*$ distribution for signal and background D^0 candidates.

- **Cosine of pointing angle ($\cos\theta_p$):** The pointing angle is defined as the angle between D meson flight line and the total momentum of daughter tracks. Ideally $\cos\theta_p$ should come unity for signal candidates, but a deviation comes for background candidates as there is no correlation between the momentum direction and D meson flight line. This distribution has a mild p_T dependence on D meson candidates, thus a p_T dependent cut set is prepared to reduce background.
- **Product of impact parameters of the decay tracks ($d_0^K \times d_0^\pi$):** As the daughter tracks have impact parameters with opposite signs, the product is to be negative ideally, but due to

4.2. Analysis method

detector resolution it gives positive values too (figure 4.4). The distribution of the product of impact parameters comes asymmetric for signal as the entries in positive side is low as shown in figure 4.5. For background, the distribution is symmetric as they are made up of randomly associated primary tracks. Thus we set an upper cut of this product value to reduce the background fraction.

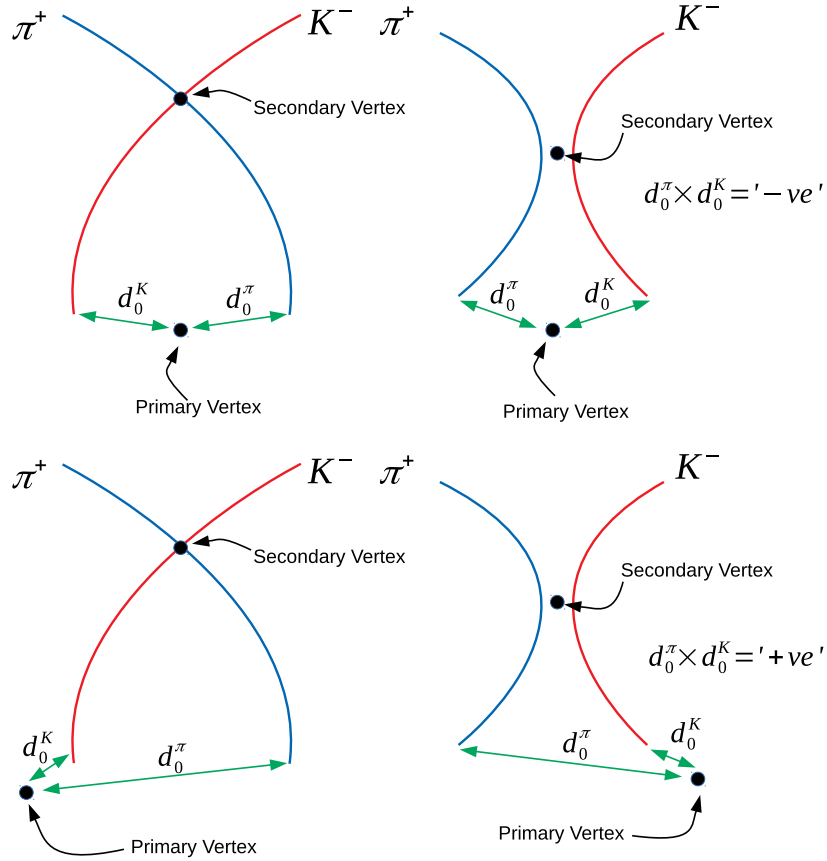


Figure 4.4: Sign of product of impact parameters of two daughter tracks coming from D^0 decay.

- **Soft pions:** The pions coming from $D^{*+} \rightarrow D^0 \pi^+$ decay are known as “soft pions” due to their small transverse momentum. Basically, the momentum of this particles is the small difference between D^{*+} and D^0 mesons. The tracking of soft pions are done by ITS only as they are unable to reach TPC. For D^{*+} analysis, a cut is applied in soft pions also, but this is kept loose as much as possible due to poor reconstruction efficiency.

A fiducial acceptance cut is also applied which excludes D meson candidates with $|y_D| < y(p_T)$.

Particle identification

PID is an important technique to reduce combinatorial background. The identification of daughter tracks is mainly done with dE/dx measurement in TPC. TOF is also used in combination with TPC

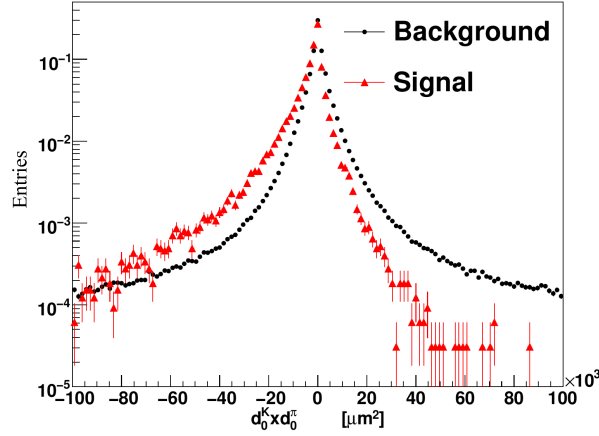


Figure 4.5: Product of impact parameters for D meson candidates.

for separation pion and kaon upto $p_T = 1.5 \text{ GeV}/c$. Basically, PID gives a check for D meson decay products if there is compatibility with pion and kaon hypothesis. A similar procedure is applied for PID selection of D^0 and D^+ that checks the compatibility of daughter tracks to that of final states while for D^{*+} , PID selection is not applied on the soft pion tracks.

Raw signal extraction

The raw yield for D meson is extracted by an invariant mass analysis. For D^0 and D^+ , the invariant mass spectra is fitted with a function which is the sum of a Gaussian and exponential function reproducing the signal peak and background respectively. Figures 4.6 and 4.7 show the invariant mass spectra for D^0 and D^+ respectively in different p_T intervals. For D^{*+} meson the fit is applied on a mass difference of $K\pi\pi - K\pi$ (figure 4.8) with a Gaussian function (for signal peak) and a product of exponential and square root function (for background). The signal (S) value is determined in a 3σ range around the mean of the Gaussian fit.

4.2.2 Selection of charged tracks as associated particle

A set of selections is imposed on the charged particle tracks to be considered as associated particles for building the correlations. These selections are important as they remove the poorly reconstructed tracks and secondary tracks and accept the tracks within a finite pseudorapidity range. The track quality cuts used in this analysis is given below:

- The minimum cluster requirement for ITS is 3.
- The minimum no. of TPC crossed-rows is 80.

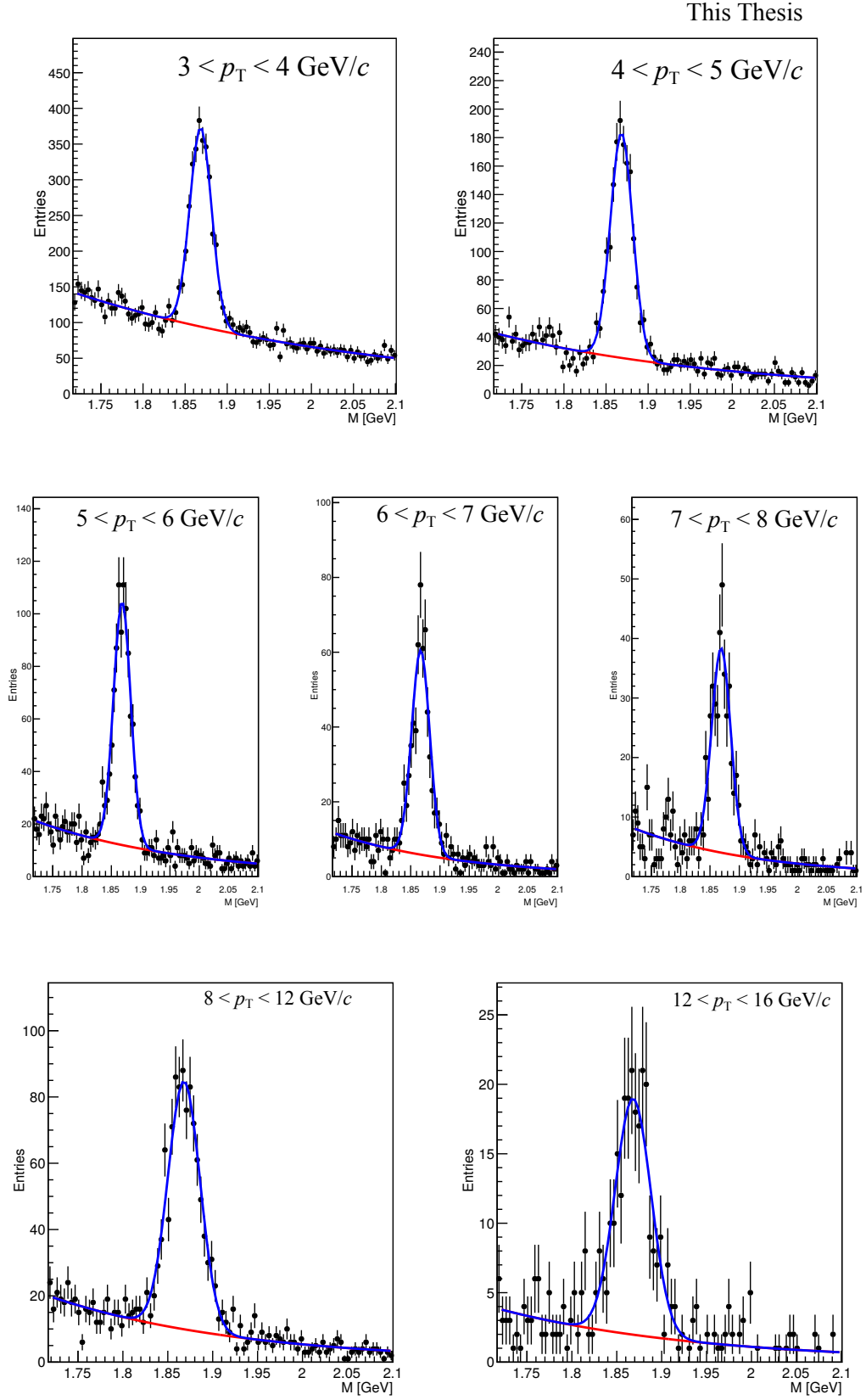


Figure 4.6: Invariant mass distribution of D^0 in different p_T region. Top row: $3 < p_T < 4 \text{ GeV}/c$ (left), $4 < p_T < 5 \text{ GeV}/c$ (right). Middle row: $5 < p_T < 6 \text{ GeV}/c$ (left), $6 < p_T < 7 \text{ GeV}/c$ (middle), $7 < p_T < 8 \text{ GeV}/c$ (right). Bottom row: $8 < p_T < 12 \text{ GeV}/c$ (left), $12 < p_T < 16 \text{ GeV}/c$ (right).

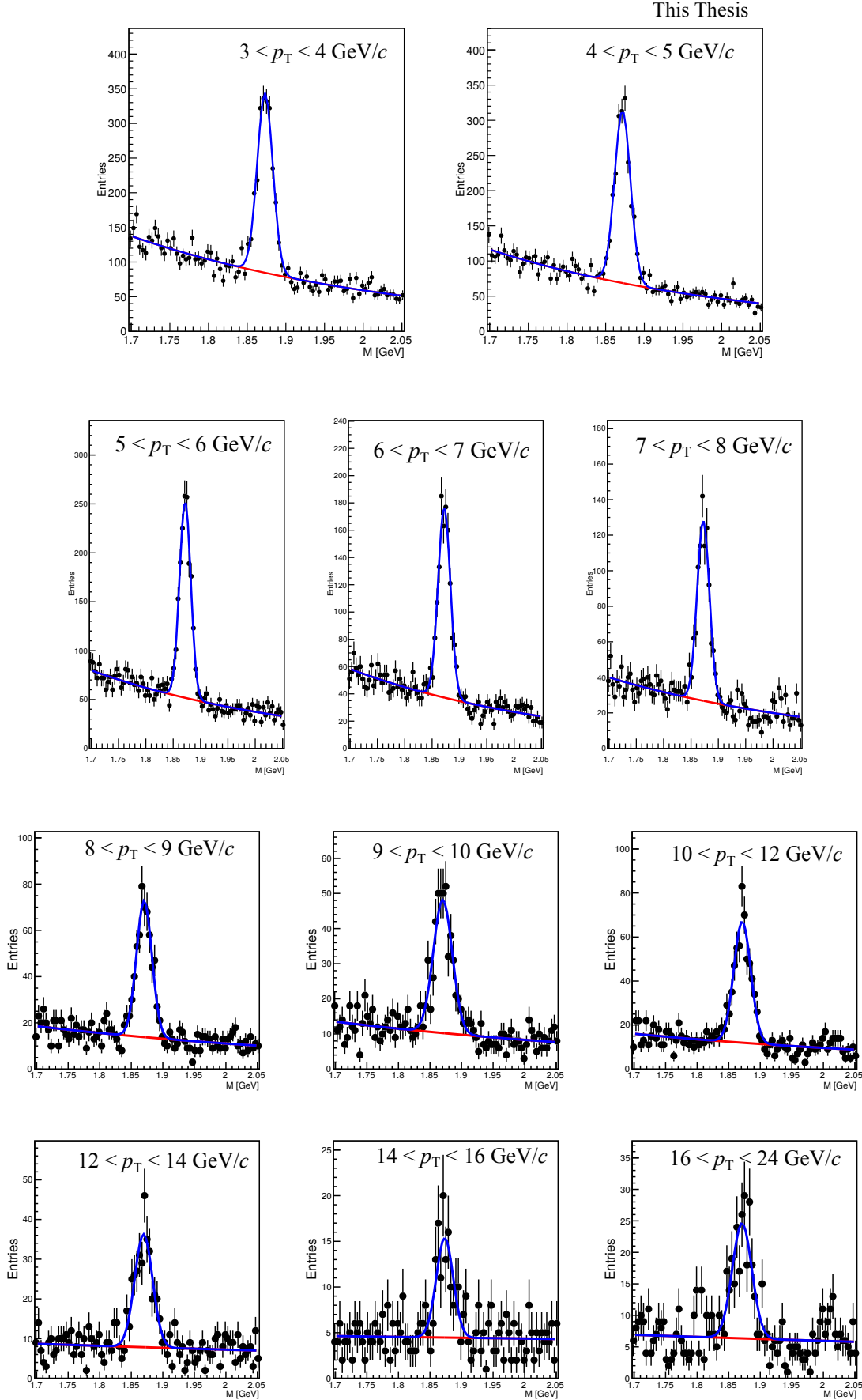


Figure 4.7: Invariant mass distribution of D^+ in different p_T region. 1st row: $3 < p_T < 4$ GeV/c (left), $4 < p_T < 5$ GeV/c (right). 2nd row : $5 < p_T < 6$ GeV/c (left), $6 < p_T < 7$ GeV/c (middle), $7 < p_T < 8$ GeV/c (right). 3rd row: $8 < p_T < 9$ GeV/c (left), $9 < p_T < 10$ GeV/c (middle), $10 < p_T < 12$ GeV/c (right). 4th row: $12 < p_T < 14$ GeV/c (left), $14 < p_T < 16$ GeV/c (middle), $16 < p_T < 24$ GeV/c

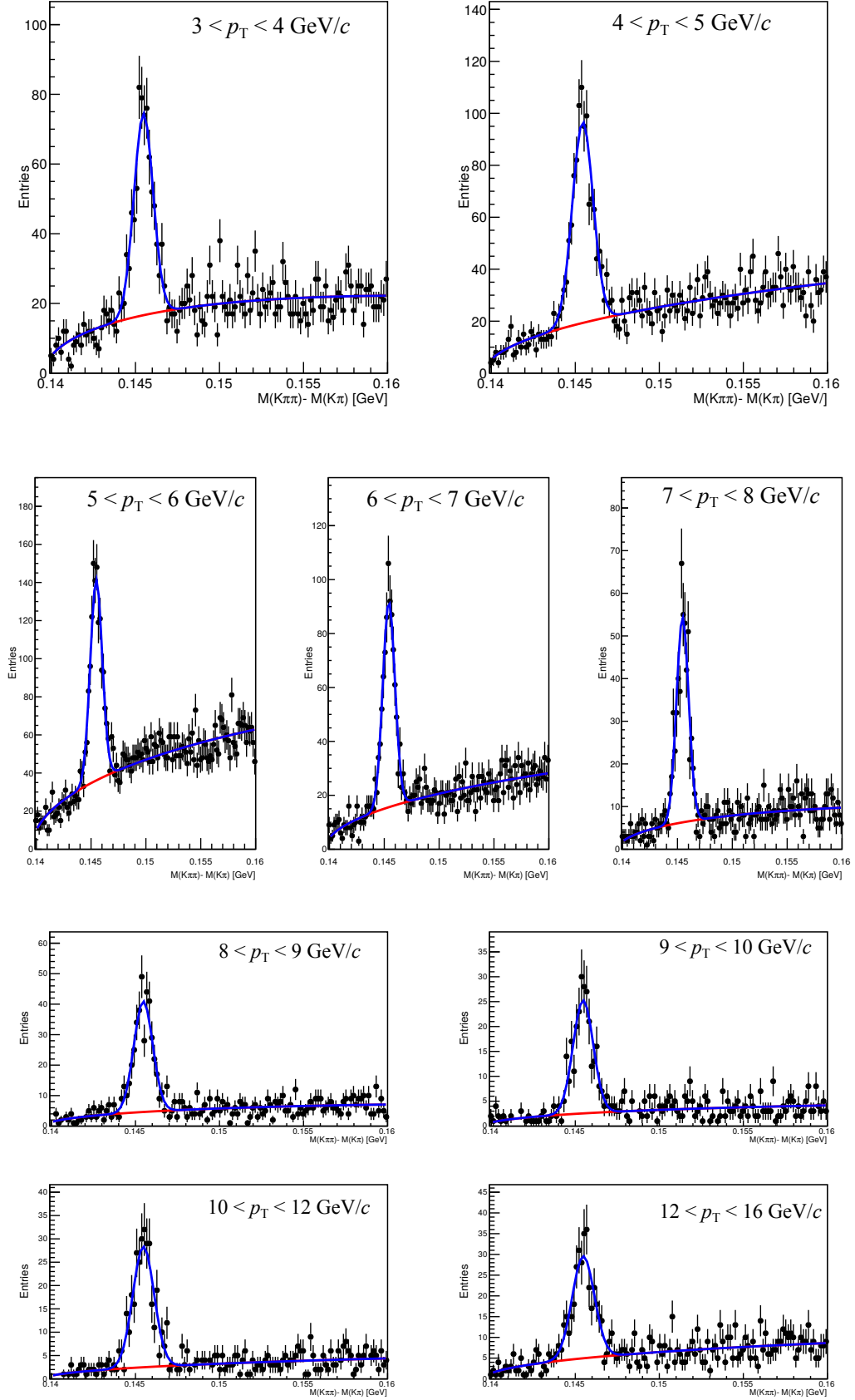


Figure 4.8: Invariant mass distribution of D^{*+} in different p_T region. 1st row: $3 < p_T < 4$ GeV/ c (left), $4 < p_T < 5$ GeV/ c (right), 2nd row : $5 < p_T < 6$ GeV/ c (left), $6 < p_T < 7$ GeV/ c (middle), $7 < p_T < 8$ GeV/ c (right). 3rd row: $8 < p_T < 9$ GeV/ c (left), $9 < p_T < 10$ GeV/ c (right), 4th row: $10 < p_T < 12$ GeV/ c (left), $12 < p_T < 16$ GeV/ c (right).

- The maximum χ^2 per TPC cluster is taken as 4.
- A successful fit of the track using Kalman filter process [165] during the last inward tracking step in the TPC is required (TPC refit).
- DCA to primary vertex along z direction: $\text{DCA}_z < 1$ cm.
- DCA to primary vertex along xy direction: $\text{DCA}_{xy} < 0.25$ cm.
- Pseudorapidity coverage: $|\eta| < 0.8$.

The D^0 and D^+ daughter tracks are excluded for that particular D candidate. The contribution from soft pions are also removed by applying an invariant mass selection on ΔM ($M(K\pi\pi) - M(K\pi)$) value.

4.2.3 Building correlations and background subtraction

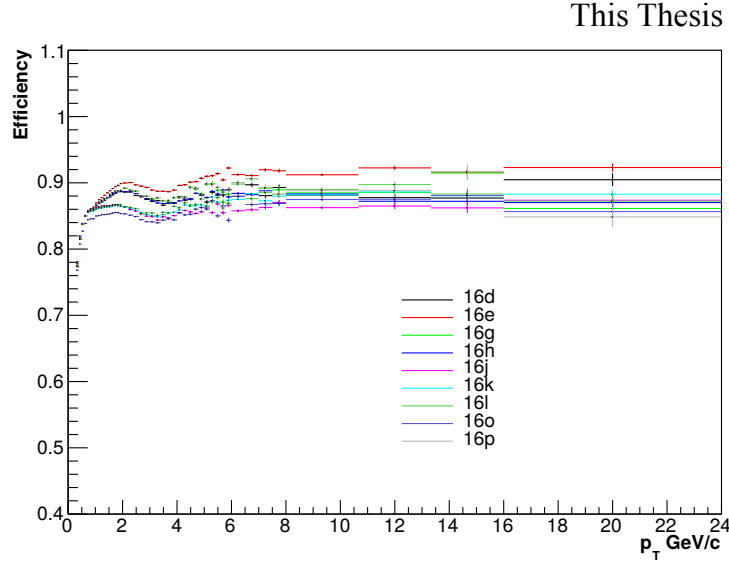
After reconstructing D meson candidates, pairs are formed in each event for each selected D meson with the primary charged particles which pass through all the track selection criteria. For each obtained pair, we calculate the differences in pseudorapidity $\Delta\eta = \eta_{trigg} - \eta_{assoc}$ and azimuthal angle $\Delta\varphi = \varphi_{trigg} - \varphi_{assoc}$ and build the two-dimensional $(\Delta\eta, \Delta\varphi)$ correlations. $\Delta\varphi$ varies from 0 to 2π , but for a good visibility this range is chosen to be $-\pi/2$ to $3\pi/2$ which gives peak around 0 and π . $\Delta\eta$ is taken to be -1 to +1 to avoid the “wing-effect” and statistical fluctuations near edges. Correlation entries are then weighted by trigger selection and reconstruction efficiency and associated track selection efficiency (discussed in section 4.2.4).

4.2.4 Corrections

Several corrections have been implemented in this analysis to take care of the D mesons and charged particles reconstruction efficiency, to remove the detector effects, secondary track contamination and D-meson contribution from beauty hadron decay etc. The corrections are discussed in the following sections.

Tracking efficiency correction

All the charged tracks presented in an event are not reconstructed or unable to pass the selection criteria due to poor reconstruction efficiency. This can be well understood from figure 4.13 (will be explained later), from which it is clear that the yield value is always < 1 revealing the fact that some

Figure 4.9: Tracking efficiency for different period as a function of p_T .

of the charged tracks are lost. In correlation analysis, we need to take care of all these lost tracks and put an efficiency correction using general-purpose Monte-Carlo sample listed in table 4.1.

3-dimensional efficiency maps are prepared as a function of p_T , η and z-coordinate of primary

MC Production	Anchored to
LHC17f6	LHC16d
LCH17f9	LHC16e
LCH17d17	LHC16g
LCH17f5	LHC16h
LCH17e5	LHC16j
LCH17d20a1	LHC16k
LCH17d20a2	LHC16l
LCH17d16	LHC16o
LCH17d18	LHC16p

Table 4.1: General purpose MC productions.

vertex, which are used directly in the online same-event (SE) and mixed (ME) correlation analysis. In same-event correlation analysis, we take the trigger and associated particles from a single event, in mixed-event correlation analysis, the trigger particle is selected from an event and associated particles are taken from rest of the events based on some selection criteria.

The efficiency values are extracted from the maps and the correlation entries are weighted with the inverse of the efficiency values. Figure 4.9 shows the 1D projection of efficiency maps as a function of p_T for different periods from 2016 pp run. From this figure, we can find a strong p_T dependence of efficiency value at $p_T < 2$ GeV/c, otherwise it gives a flat trend in high- p_T region.

D-meson efficiency correction

Similar to the track reconstruction efficiency, correlation distributions are also influenced by D-meson selection and reconstruction efficiency. We need to apply this correction to take care of the D mesons lost due to limited detector acceptance, primary vertex and track reconstruction efficiency and topological cuts. Since charm production has a very low cross-section, we use charm enriched Monte-Carlo sample (table 4.2) where the charm production is enhanced and D mesons are forced to decay through desired channel.

Unlike tracking efficiency maps, 2-dimensional maps are prepared for trigger efficiency correction

MC Production	Anchored to
LHC17c3a1	LHC16k
LHC17c3a2	LHC16l
LHC17h8a	LHC16others

Table 4.2: HF enriched MC sample.

as a function of p_T and event multiplicity. η and z-coordinate of primary vertex are excluded from the trigger efficiency calculation due to limited statistics of trigger particle and absence of strong dependency of these two variables. Efficiency maps for prompt and feed-down D mesons are shown in figures 4.10 and 4.11 respectively. As the figures show a strong dependence of efficiency values on p_T , the binning of this variable is kept narrow in low- p_T region, but we have to keep it broader in high- p_T region to avoid statistical fluctuations.

The process of evaluation and application of efficiency values is same like tracking efficiency correction. So, obtaining the trigger (ϵ_{trigg}) and tracking (ϵ_{track}) efficiency values, the correlation entries are finally weighed by $(\epsilon_{trigg} \times \epsilon_{track})^{-1}$.

Event mixing correction

Structures in the angular correlation distributions may be affected even for uncorrelated pair of particles from the limited detector acceptance or angular inhomogeneities in the trigger and track reconstruction efficiency. We remove these effects using “Event mixing” technique. In this technique, the analysis is executed by taking the trigger particles from one event and they are correlated with the charged particles reconstructed in different events (known as “Mixed Events” analysis, ME) with similar characteristic, in particular concerning the event multiplicity and z position of the primary vertex.

In this technique, the first step is to create an event pool, where events preceding the one containing

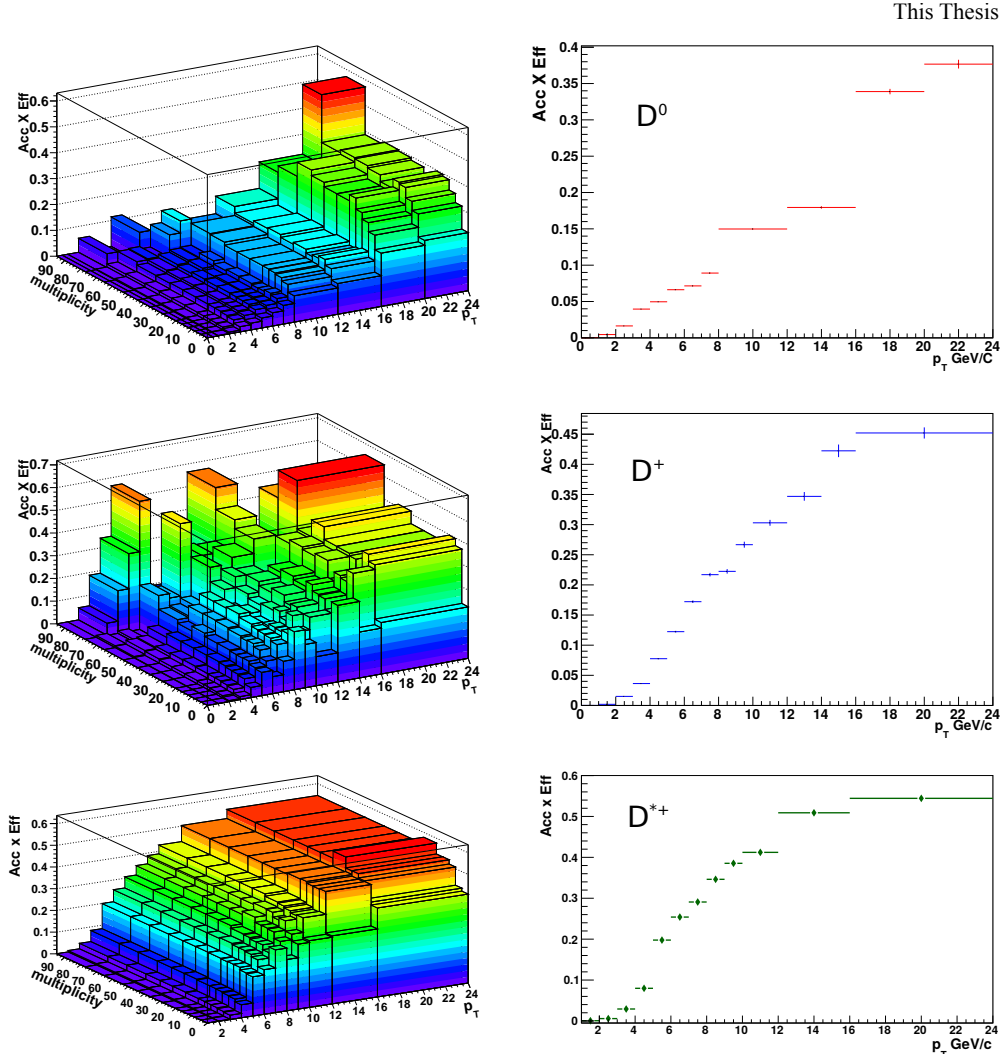


Figure 4.10: Top: prompt D^0 meson efficiency as a function of (p_T , multiplicity) (left) and p_T (right). Middle: prompt D^+ meson efficiency as a function of (p_T , multiplicity) (left) and p_T (right). Bottom: prompt D^{*+} meson efficiency as a function of (p_T , multiplicity) (left) and p_T (right).

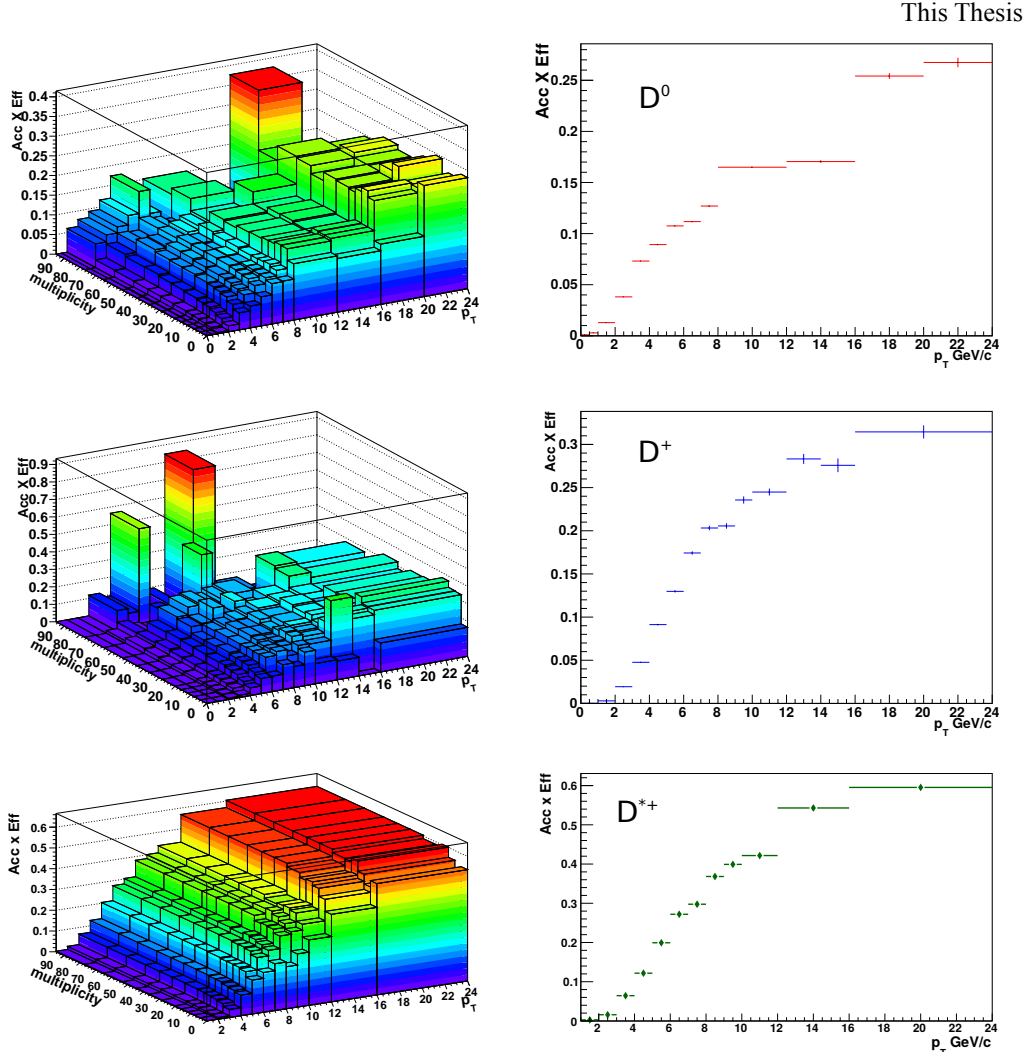


Figure 4.11: Top: feed-down D^0 meson efficiency as a function of (p_T , multiplicity) (left) and p_T (right). Middle: feed-down D^+ meson efficiency as a function of (p_T , multiplicity) (left) and p_T (right). Bottom: feed-down D^{*+} meson efficiency as a function of (p_T , multiplicity) (left) and p_T (right).

4.2. Analysis method

a D candidate are stored based on their properties (position of the vertex along the z axis and multiplicity). Each time a D meson candidate is found, the correlation analysis on the mixed events is performed if the pool satisfies the conditions defined at its creation, i.e:

- Minimum number of events in the pools: 1
- Minimum number of tracks in the pool: 25

The definition of the bins for multiplicity and z vertex dependencies is the following:

- Multiplicity bins for the pools: $(0 - 20)$, $(20 - 35)$, $(35 - +\infty)$
- Binning of pools for z-position of primary vertex: $(-10, -2.5)$, $(-2.5, 2.5)$, $(2.5, 10)$

During the analysis, the pools start to be refreshed (i.e. the tracks from the first inserted event are removed, to make room for the tracks from the last analyzed event) after they contain a minimum of 10000 tracks. The drawback of having a lower refresh of pool tracks is more than compensated by the large increase in the statistics, especially for high- p_T bins.

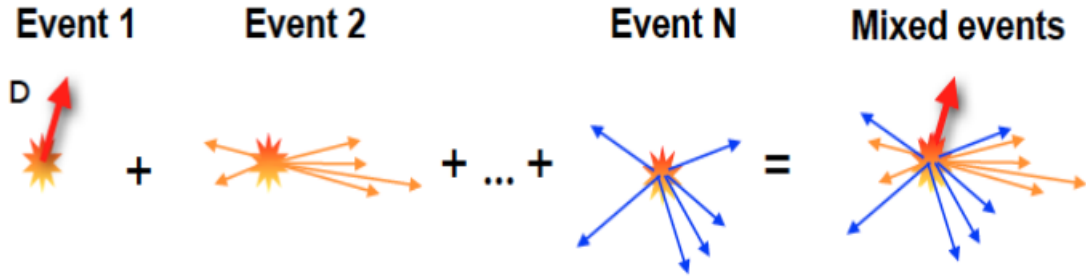


Figure 4.12: Schematic diagram for Event mixing in D-hadron azimuthal correlations.

In an ideal case, the mixed event distribution is expected to have a constant flat distribution as function of $\Delta\varphi$ and a triangular shaped distribution in $\Delta\eta$ deriving from the limited η acceptance of the detector. The obtained distribution is used as a weight in each correlation bin, i.e, the corrected correlation distribution is calculated as follows:

$$\frac{d^2 N^{corr}(\Delta\varphi\Delta\eta)}{d\Delta\varphi d\Delta\eta} = \frac{\frac{d^2 N^{SE}(\Delta\varphi\Delta\eta)}{d\Delta\varphi d\Delta\eta}}{\frac{d^2 N^{ME}(\Delta\varphi\Delta\eta)}{d\Delta\varphi d\Delta\eta}} \frac{d^2 N^{ME}(0,0)}{d\Delta\varphi d\Delta\eta} \quad (4.1)$$

In equation 4.1, the last term stands for the mixed-event correlation in $(\Delta\eta, \Delta\varphi) = (0,0)$ where the trigger and associated particle experience same detector effect. But in practice, we take average of the bins in the region $-0.2 < \Delta\eta < 0.2$, $-0.2 < \Delta\varphi < 0.2$ (multiple bins are used to minimize the effect of statistical fluctuations on the normalization of the mixed-event plots).

The mixed-event correlation distribution is obtained for both the D meson and the sideband candidates. Both are corrected with the relative distributions. An example of the mixed event distribution is shown in Figure 4.13. The expected triangular shape in $\Delta\eta$ addresses the effect of the limited detector pseudo-rapidity acceptance. Note that the mixed-event distribution is limited to the interval $|\Delta\eta| < 1$: the decision to limit the distributions to this range was taken in order to avoid the so-called “wing effect”, i.e. the wing-like structures arising in the correlation distribution at large $\Delta\eta$ due to the limited filling of the correlation bins in that region.

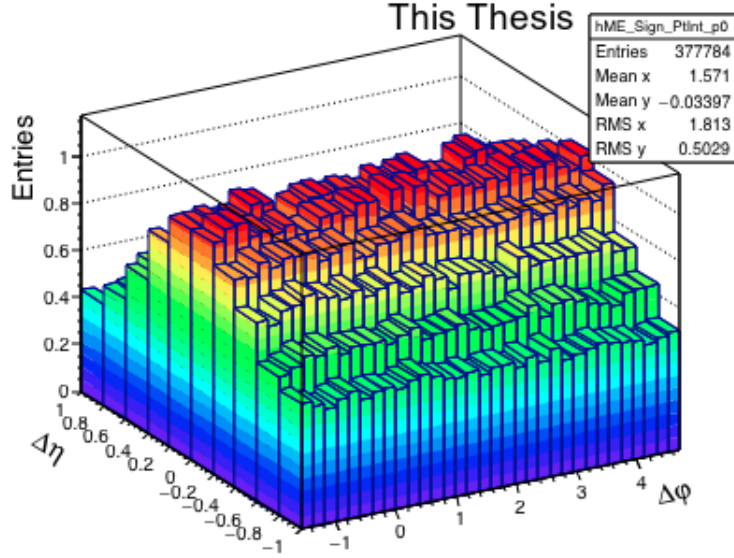


Figure 4.13: Example of mixed event correlation distribution for D^0 meson with $p_T(\text{trigg})$ 5-8 GeV/ c and $p_T(\text{assoc}) > 0.3$ GeV/ c .

sideband subtraction

The same-event and mixed-event correlations are built in three regions classified in the invariant mass spectra:

- signal+background region: $\pm 2\sigma$ (obtained from Gaussian fit) region around mass peak.
- Left sideband region: 4σ region on left side of the signal peak.
- Right sideband region: 4σ region on right side of the signal peak.

These regions are shown in different colours in figure 4.14. After obtaining the correlations from signal+background region ($C^{\text{peak}}(\Delta\eta, \Delta\varphi)$) and left+right sideband region ($C^{\text{SB}}(\Delta\eta, \Delta\varphi)$), we subtract the background contribution and separate out the signal correlation ($C^{\text{signal}}(\Delta\eta, \Delta\varphi)$) using

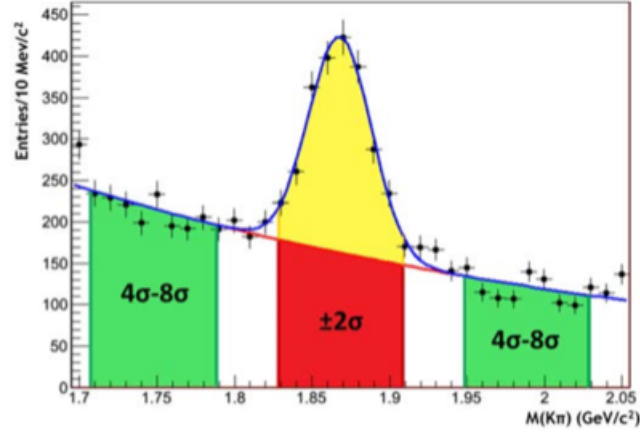


Figure 4.14: Example of signal (red+yellow) and sideband regions (green) in a D^0 meson invariant mass spectra.

equation 4.2.

$$C^{signal}(\Delta\eta, \Delta\varphi) = C^{peak}(\Delta\eta, \Delta\varphi) - \frac{B^{peak}}{B^{sidebands}} \times C^{SB}(\Delta\eta, \Delta\varphi) \quad (4.2)$$

The contributions from sideband correlations are normalized by “sideband-factor” defined as the ratio of the background integral in signal+background region (B^{peak}) over the integral of sidebands ($B^{sidebands}$). This correction is applied after event-mixing correction along with the efficiency weighting.

The example plots for mixed event corrected correlation distributions as a function of $(\Delta\eta, \Delta\varphi)$ are shown in figure 4.15 with the standard $|\Delta\eta| < 1$ range. The upper panel of figure 4.15 shows the correlation distributions for signal+background region and total sideband region and the lower panel shows the same after sideband subtraction.

Due to the statistical limitations, correlation distributions are considered as a projection over $\Delta\varphi$ and integration over $\Delta\eta$. This projection is performed after efficiency weighting, event mixing correction and background subtraction. After taking this projection, the several D-meson p_T bins are merged and classified into three p_T intervals 3-5, 5-8, 8-16 GeV/ c to reduce statistical fluctuations. Figure 4.16 shows an example of sideband subtraction on the one-dimensional $\Delta\varphi$ projection of D^0 - charged particle correlations.

Correction for bias on b to D topologies

A Monte Carlo closure test has been performed on D^0 sample in order to verify the consistency of the corrections applied on the correlation distributions. Charm and beauty enriched MC sample is used for this test and we perform the usual correlation analysis at both kinematic and reconstructed

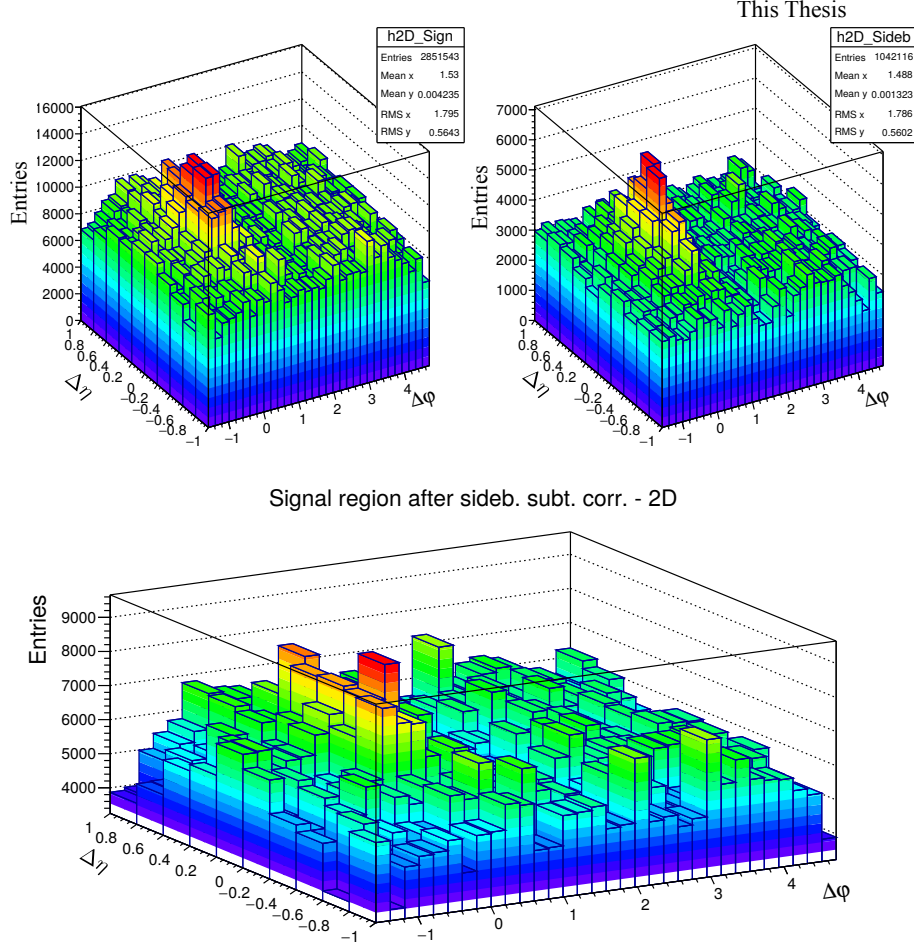


Figure 4.15: D^0 meson ($\Delta\eta, \Delta\phi$) SE/ME correlation distribution at ($|\Delta\eta| < 1$) with $p_T(\text{assoc}) > 0.3$ GeV/ c and D^0 -meson p_T 3-5 GeV/ c . Top panel: correlation distribution in signal+background (left) and sideband (right) region. Bottom panel: correlation distribution after sideband subtraction.

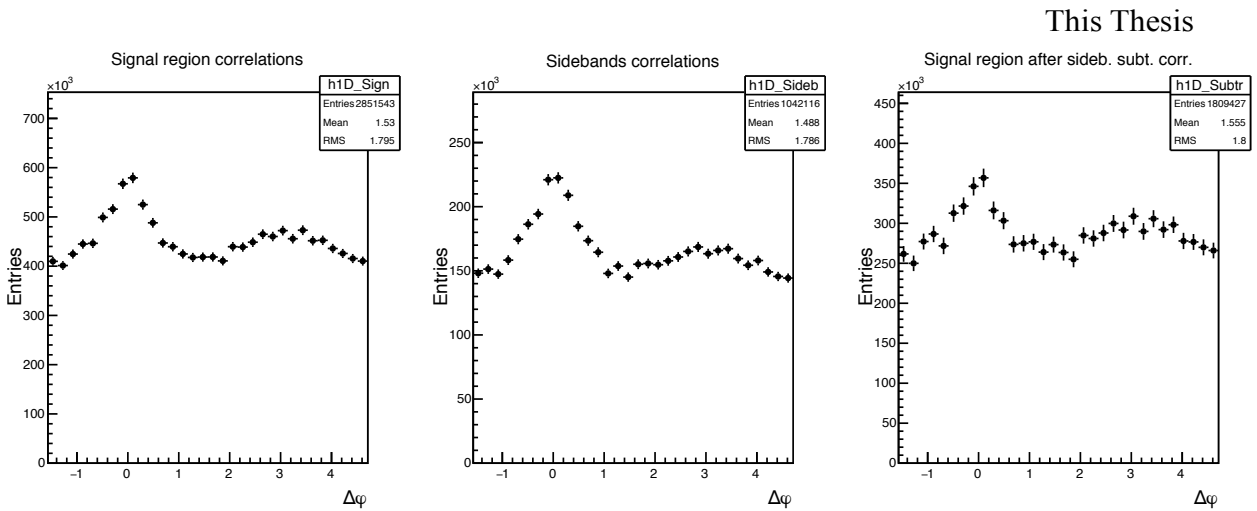


Figure 4.16: Example of azimuthal correlation distributions between D^0 mesons and charged particles: signal+background region (left), sideband (middle), and signal minus sideband (right) correlation distributions.

4.2. Analysis method

level.

At kinematic level, only acceptance cuts are applied on the D mesons and the associated particles, using the Monte Carlo information for the identification of the D mesons and the hadrons in the event and rejecting the non-primary particles. At reconstructed level, the analysis is performed as if it is executed on data, applying the event selection, the acceptance cuts for D mesons and the associated particles, selecting the D meson candidates with filtering cuts on their daughters, topological cuts and PID selection, and then keeping only the true D mesons by matching with the Monte Carlo truth; non-primary particles are rejected by means of the DCA selection. Event mixing correction was applied both at reconstructed and at kinematic level, where it takes into account just the effects of the acceptance cuts. In addition, at reconstructed level, the efficiency corrections for D mesons and associated tracks are also applied. Figures 4.17, 4.17 and 4.19 show the kinematic and reconstructed plots with three different $p_T(D)$ regions: 3-5, 5-8, 8-16 GeV/ c and three different $p_T(assoc)$ regions: > 0.3 , 0.3-1.0, > 1.0 GeV/ C .

We perform this MC closure test to check the compatibility of the correlation plots at reconstructed level (i.e. after the application of several correction factors) to that of the plots at kinematic level. Hence we take the ratios of reconstructed over kinematic plots in all D^0 p_T bins with different p_T for the associated tracks as shown in figures 4.20, 4.21, 4.22.

From the ratio plots, we find a good compatibility with 1, within the uncertainties, with the only exception being due to some structures in the near side region for the beauty origin case. These structures are already found in the pp 2010, pPb 2013 and pPb 2016 analysis, and it has been verified that they are induced by our topological selection for the D mesons. Indeed, in cases in which the D meson triggers come from B hadrons, applying the topological cuts (especially the cosine of the pointing angle) tends to favour cases with a small angular opening between the products of the B hadron decay (i.e. the D meson trigger itself and other particles), with respect to cases where the B decay particles are less collinear. This situation appears only at the reconstructed level where we apply the topological cut selection. Hence, the reconstructed/kinematic ratio plots show an excess at $\Delta\varphi = 0$ (corresponding to B decays with larger angles, which are not favoured). These structures are prominent at low D^0 p_T , where the topological cuts are tighter, and tend to disappear at higher p_T , where the selections are released. They are also larger in the higher associated track p_T ranges, where the fraction of B-hadron decay tracks dominate the overall correlation distributions.

The correlation distribution from data need to be corrected for this bias, and in particular for the enhancement of b-origin correlation pairs at the centre of the near side region, which would influence

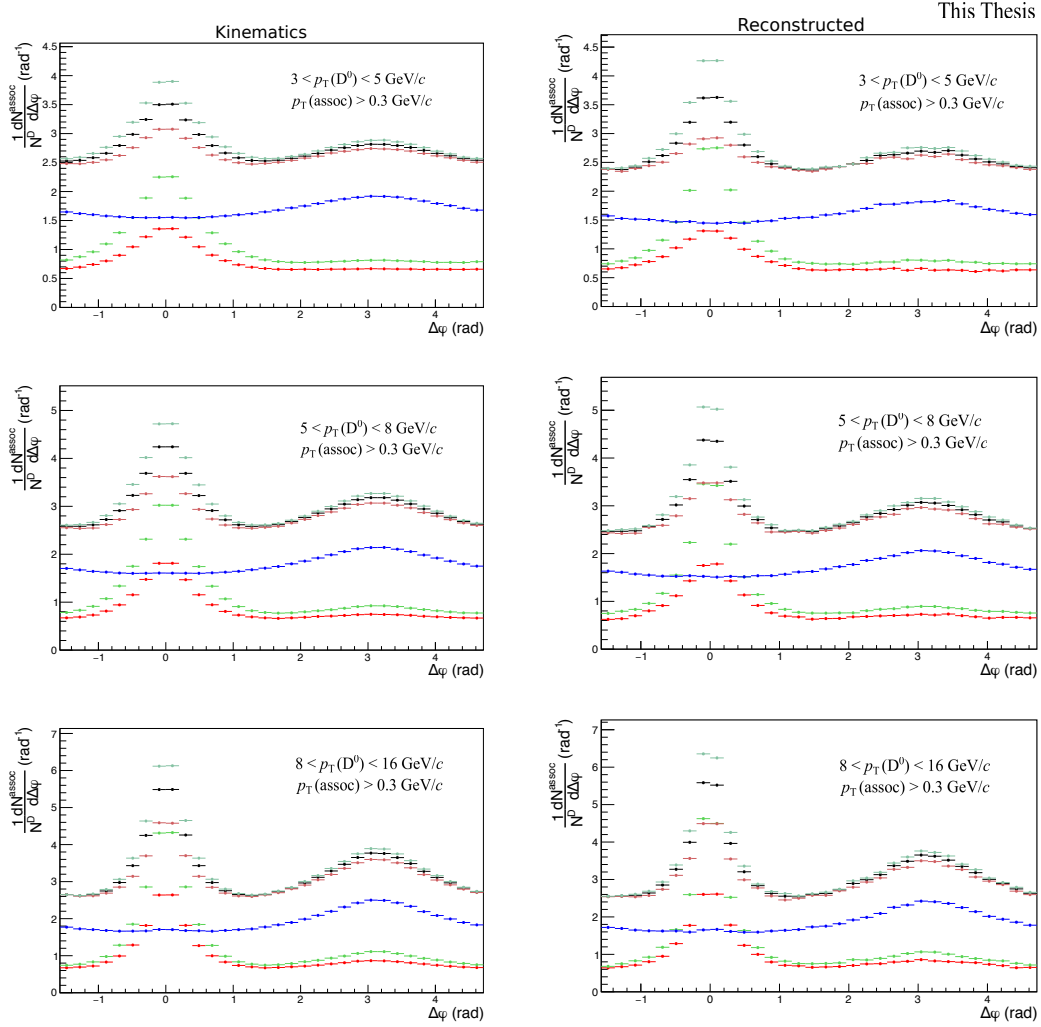


Figure 4.17: Azimuthal correlations between D^0 mesons and charged particles obtained from Monte Carlo, at kinematics (left column) and reconstructed (right column) step. Black points: All D^0 -all hadrons, normalized by all D^0 triggers; light red points: D^0 from c-hadrons from c, normalized by c- D^0 triggers; dark red points: D^0 from c-all hadrons, normalized by c- D^0 triggers; light green points: D^0 from b-hadrons from b, normalized by b- D^0 triggers; dark green points: D^0 from b-all hadrons, normalized by b- D^0 triggers; blue points: All D^0 hadrons from light quarks, normalized by all D^0 triggers. The panels show the ranges: top row: $3 < p_T(D) < 5$ GeV/c, middle row: $5 < p_T(D) < 8$ GeV/c, bottom row: $8 < p_T(D) < 16$ GeV/c, $p_T(assoc) > 0.3$ GeV/c.

4.2. Analysis method

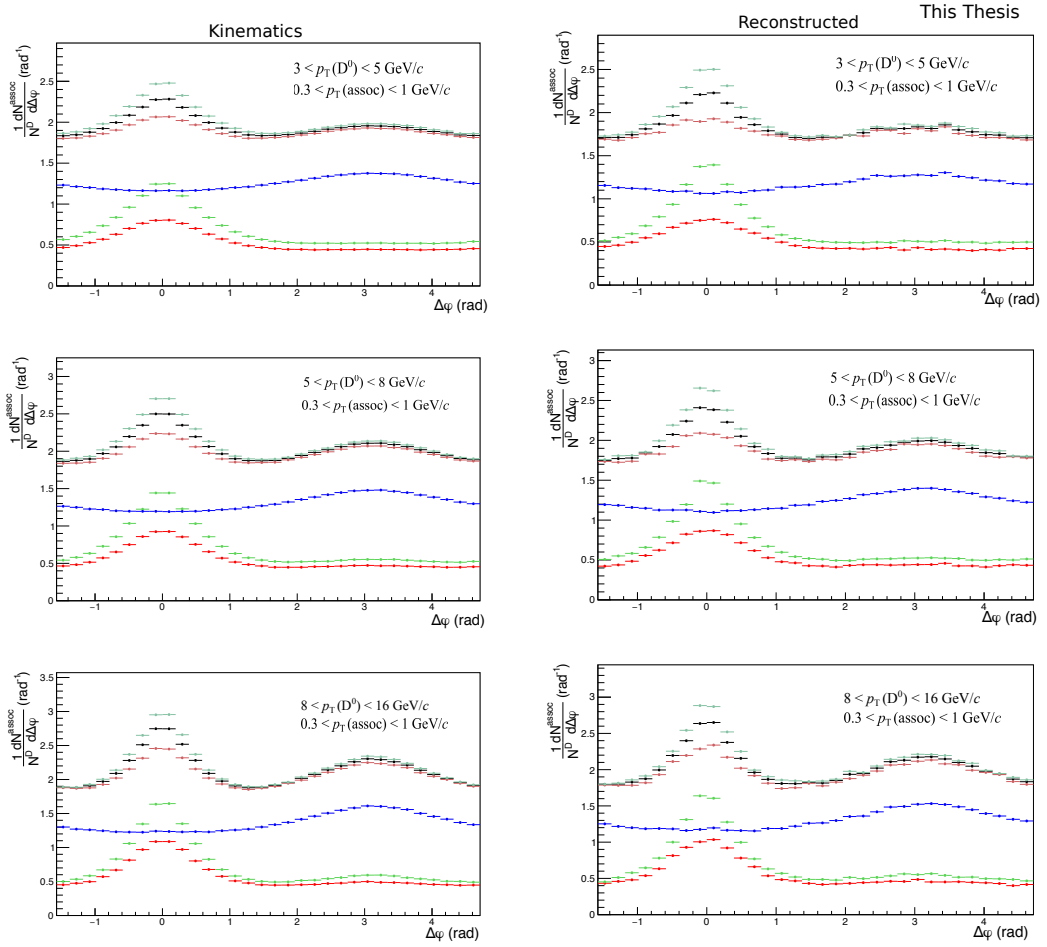


Figure 4.18: Same as figure 4.17, with $0.3 < p_T(\text{assoc}) < 1.0 \text{ GeV}/c$.

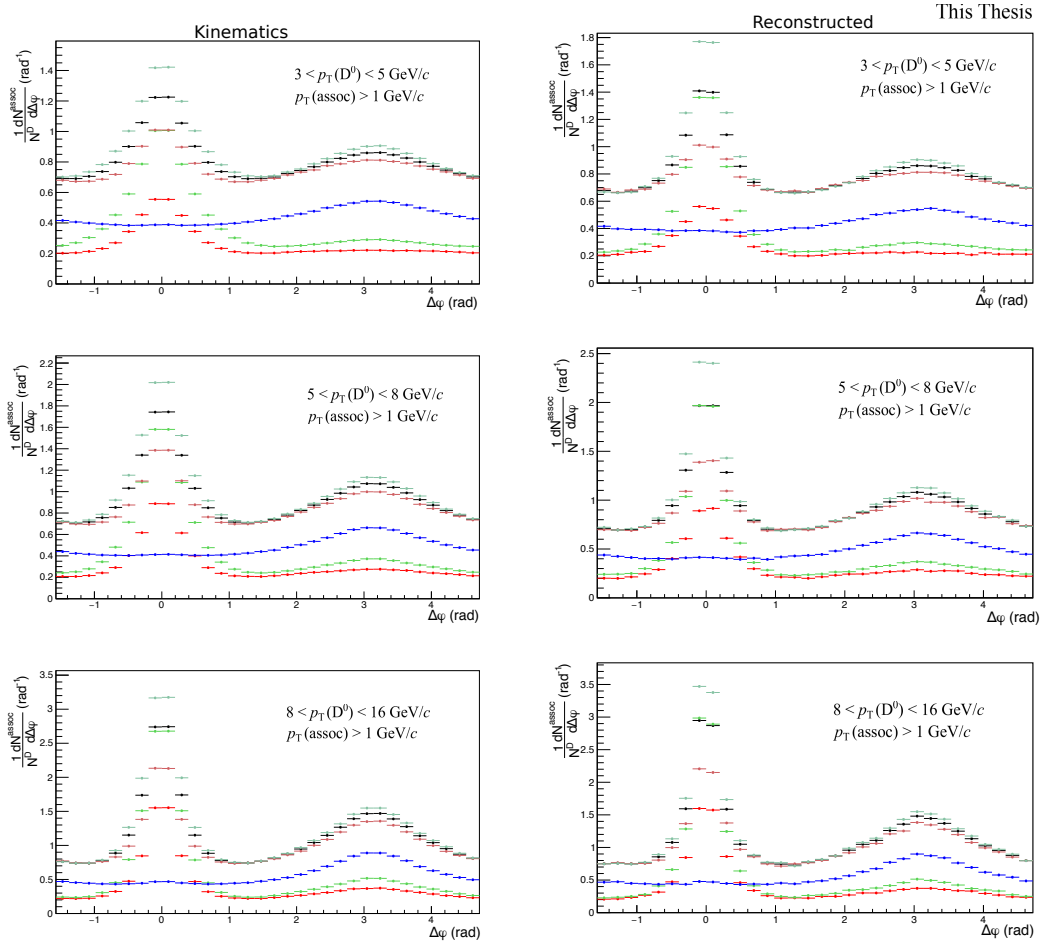


Figure 4.19: Same as figure 4.17, with $p_T(\text{assoc}) > 1.0 \text{ GeV}/c$.

4.2. Analysis method

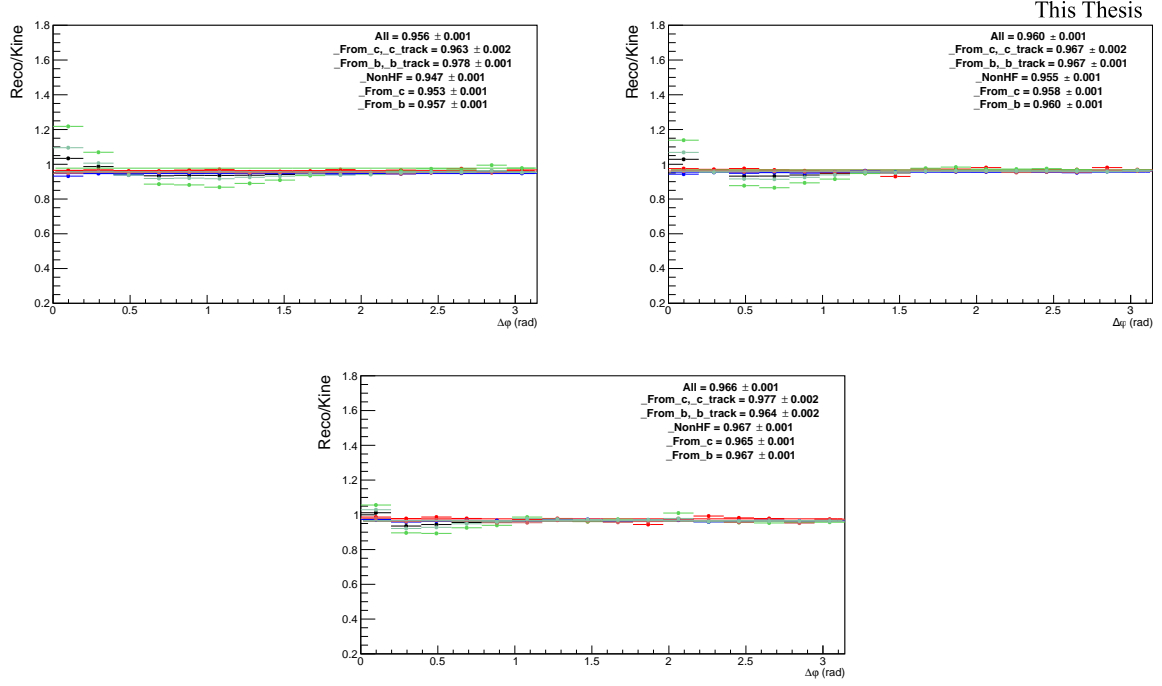


Figure 4.20: Ratios of fully corrected azimuthal correlation plots at reconstructed level over azimuthal correlation plots at kinematic level, in the three D^0 p_T bins, for the different associated p_T ranges. Black points: All D^0 -all hadrons, normalized by all D^0 triggers; light red points: D^0 from c -hadrons from c , normalized by c - D^0 triggers; dark red points: D^0 from c -all hadrons, normalized by c - D^0 triggers; light green points: D^0 from b -hadrons from b , normalized by b - D^0 triggers; dark green points: D^0 from b -all hadrons, normalized by b - D^0 triggers; blue points: All D^0 hadrons from light quarks, normalized by all D^0 triggers. The panels show the ranges: $3 < p_T(D) < 5$ GeV/ c (top left), $5 < p_T(D) < 8$ GeV/ c (top right), $8 < p_T(D) < 16$ GeV/ c (top left) with $p_T(assoc) > 0.3$ GeV/ c .

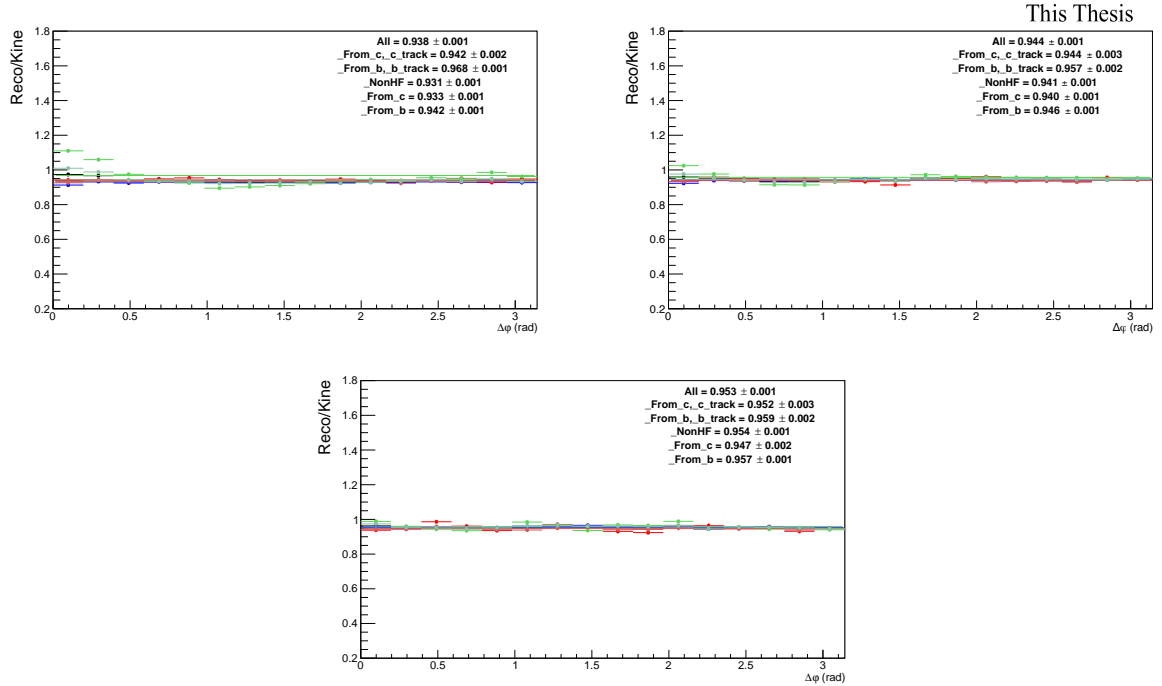


Figure 4.21: Same as figure 4.20, with $0.3 < p_T(assoc) < 1.0$ GeV/ c .

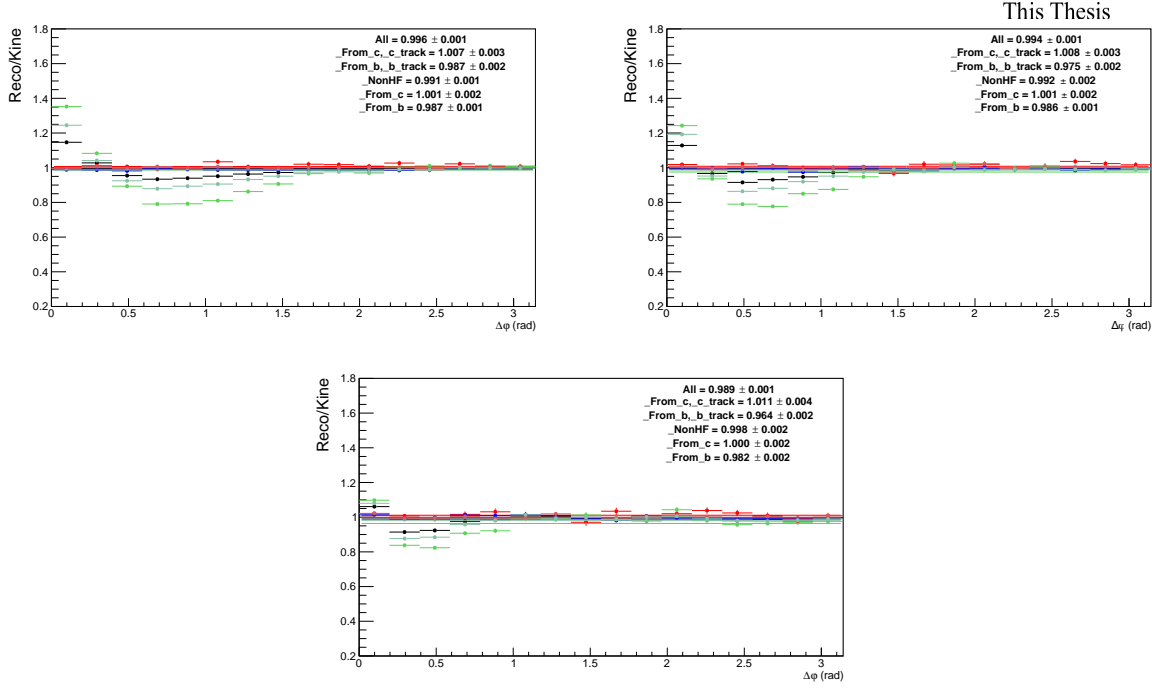


Figure 4.22: Same as figure 4.20, with $p_T(\text{assoc}) > 1.0$ GeV/c

the near-side peak features. In order to do this, the amount of the b-origin excess is evaluated from the Reco/Kine ratio, by considering the b- D^0 -all tracks case (dark green points). The excess at Reco level (affecting data) is quantified as a $\Delta\phi = 0$ modulation **modul** for the few points on each side of the value or, equivalently, on the first five points of the reflected distributions, which start from $\Delta\phi = 0$. This is done separately in each p_T range. Then, the correction is done by applying this modulation to the data correlation distributions, but taking into account that only the correlation entries from $B \rightarrow D$ are affected, while the $c \rightarrow D$ correlations need to be left unaltered. In particular, it has to be considered that, on data, $B \rightarrow D$ correlation pairs are only a fraction $(1 - f_{\text{prompt}})$ of the total and the amplitude of $(B) \rightarrow D|_{\text{amplit}}$ correlation pattern is greater than $(c) \rightarrow D|_{\text{amplit}}$ correlation pattern. Thus we apply the following equation to get the corrected correlation plots.

$$C(\Delta\phi)_{\text{corr}} = C(\Delta\phi)_{\text{raw}} \cdot \left[\frac{c \rightarrow D|_{\text{amplit}}}{(B + c) \rightarrow D|_{\text{amplit}}} \cdot f_{\text{prompt}} + \frac{B \rightarrow D|_{\text{amplit}}}{(B + c) \rightarrow D|_{\text{amplit}}} \cdot (1 - f_{\text{prompt}}) \cdot \frac{1}{\text{modul}} \right] \quad (4.3)$$

Applying the **modul** factor to the beauty part of the data correlation distributions brings its value back to the generated level case, effectively removing the bias. The effect of the correction is a shift of the data points in the near-side region (in general, downward in the first and second points, the upward in the others). To take into account for possible inaccuracies in the definition of the modulations, or in their rescaling, a systematic uncertainty is applied on the corrected data points,

4.2. Analysis method

with value $|C(\Delta\varphi)_{\text{corr}} - C(\Delta\varphi)_{\text{raw}}|/\sqrt{12}$, on each side of the data points affected by the bias.

Removal of secondary track contribution

The secondary particles come from the strange hadron decay or from the interaction of particles with the detector material. The DCA cut is applied in the associated track selection to remove the secondary particles. However, a small fraction of secondary tracks survive event after applying this cut. To remove this residual contamination, the data correlation distribution needs to be corrected. The number of primary and secondary tracks are evaluated from the study of Monte Carlo data sample. The fraction of secondary tracks accepted is calculated as the ratio of amount of secondary tracks accepted over all accepted tracks. If the fraction of residual secondary track is flat along the $\Delta\varphi$ axis, we can scale the data correlation distributions by their purity values (1 - secondary contamination). But, for our case the plot which is showing the residual contamination from secondary tracks in the correlation distribution as a function of $\Delta\varphi$ is not flat along the $\Delta\varphi$ axis as shown in figure 4.23. The inhomogeneities is more than 1%. So, to remove this inhomogeneities the data correlation distribution is corrected by other approach.

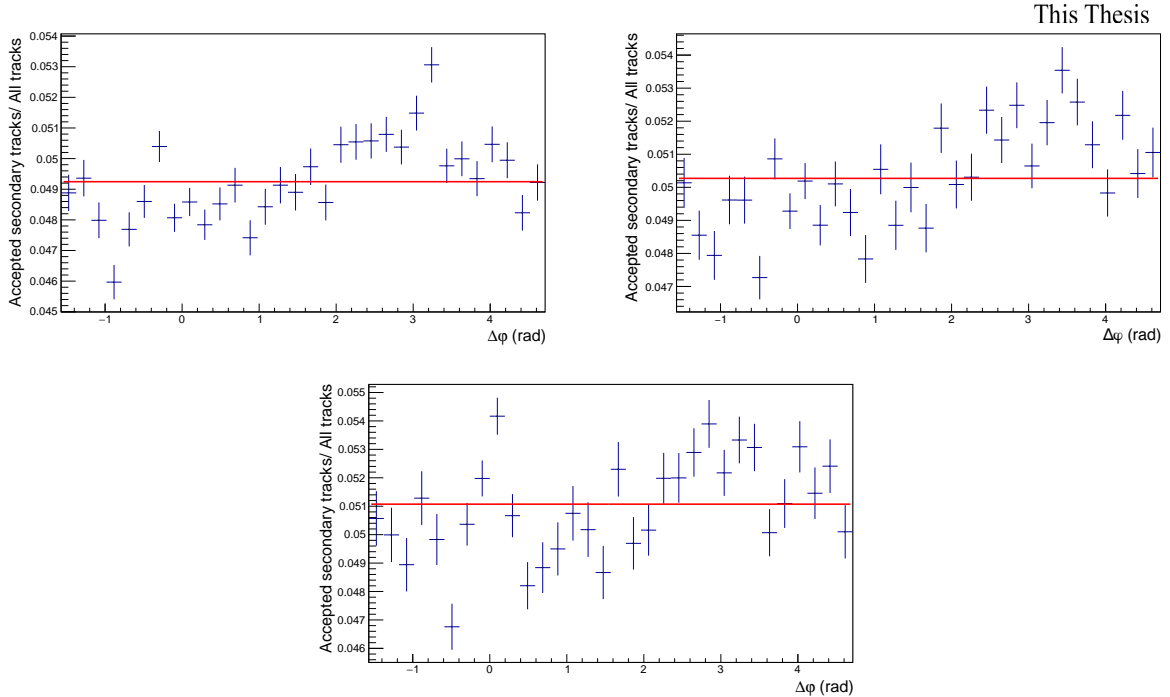


Figure 4.23: The residual contamination from secondary tracks in the correlation distribution as a function of $\Delta\varphi$ for the D-meson p_T ranges: 3-5, 5-8, 8-16 GeV/ c respectively in the associated $p_T > 0.3$ GeV/ c .

The three possible approaches to correct the data correlation distribution:

→ **Approach-I** : The ratio of $\Delta\varphi$ distribution of primary track accepted over all tracks is multiplied

to the data $\Delta\varphi$ correlation distributions.

- **Approach-II** : The ratio of $\Delta\varphi$ distribution of primary track accepted over all tracks distribution is fitted with a 9th order polynomial function and this function is used for to correct the data $\Delta\varphi$ correlation distributions.
- **Approach-III** : The average of the ratio of $\Delta\varphi$ distribution of primary track accepted over all tracks distribution is moving by three points and this distribution is multiplied to the data $\Delta\varphi$ correlation distributions.

The $\Delta\varphi$ distribution of fraction of primary tracks over all tracks for three different approaches is shown in figure 4.24, where the blue color markers are the the $\Delta\varphi$ distribution of primary tracks over all tracks, the red colour markers are the moving average of three points of the same $\Delta\varphi$ distribution of primary tracks over all tracks and the red line is the 9th order polynomial fitting line of same $\Delta\varphi$ distribution of primary tracks over all tracks.

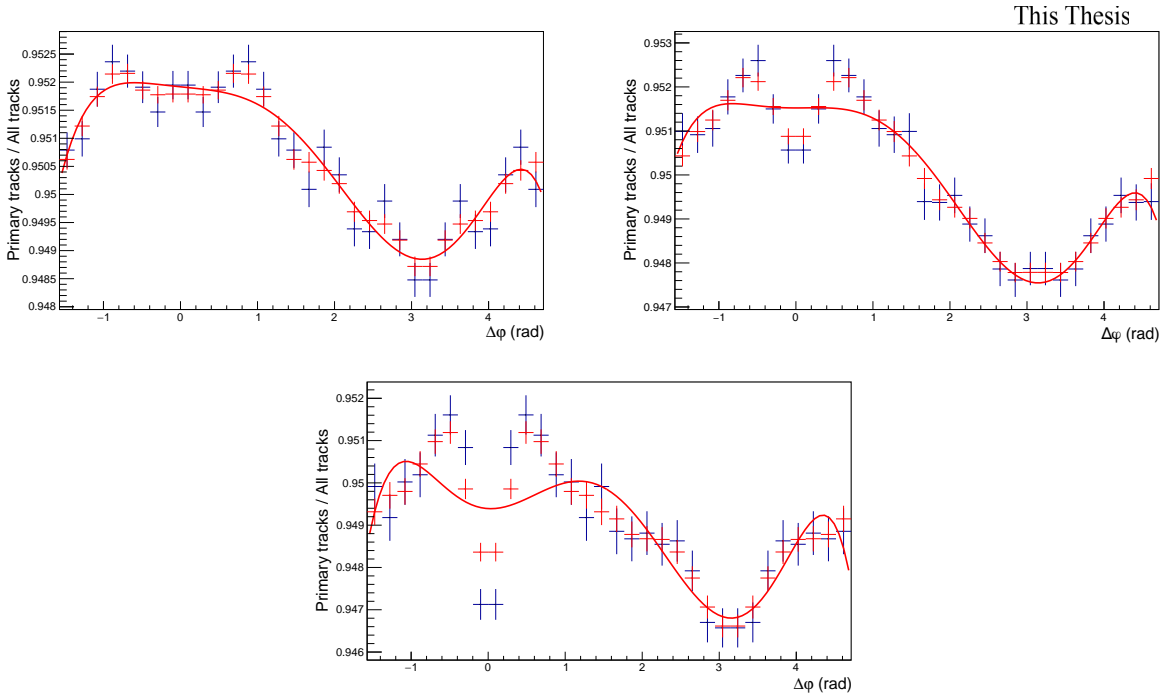


Figure 4.24: The primary tracks over all tracks (Blue points), primary tracks over all tracks with moving average of three points (Red points), primary tracks over all tracks fitted with a 9th order polynomial (Red line), in the correlation distribution as a function of $\Delta\varphi$ for the D -meson p_T ranges: 3-5, 5-8, 8-16 GeV/ c respectively in the associated $p_T > 0.3$ GeV/ c .

Feed-down subtraction

As the selected and reconstructed D mesons are composed of both prompt and feed-down D meson (later is the decay from beauty hadron), the correlation distributions are the mixed up results from these two. Thus, the feed-down contributions is needed to be subtracted and this correction is done after taking the 1-dimensional $\Delta\varphi$ projection of correlation distributions and merging the p_T bins.

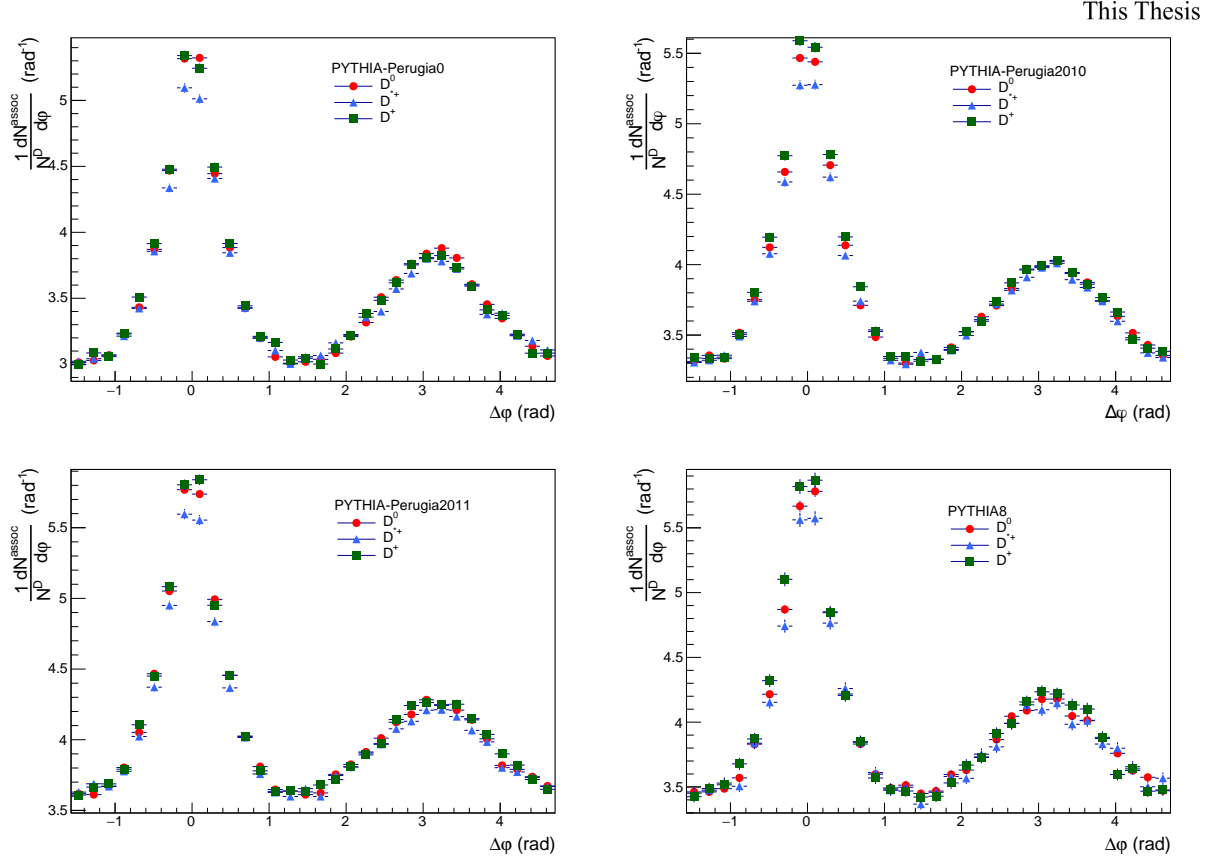


Figure 4.25: Azimuthal correlation distribution between D mesons from B hadrons decay and charged particles obtained from Monte Carlo simulations based on different PYTHIA tune for associated track $p_T(\text{assoc}) > 0.3 \text{ GeV}/c$ and D meson p_T 5-8 GeV/c .

The contribution of correlations of D meson from b-hadron decay is subtracted from the uncorrected as:

$$\tilde{C}_{\text{prompt D}}(\Delta\varphi) = \frac{1}{f_{\text{prompt}}} \left(\tilde{C}_{\text{inclusive}}(\Delta\varphi) - (1 - f_{\text{prompt}}) \tilde{C}_{\text{feed-down}}^{\text{MC templ}}(\Delta\varphi) \right). \quad (4.4)$$

In the above equation, $\tilde{C}_{\text{inclusive}}(\Delta\varphi)$ and $\tilde{C}_{\text{prompt D}}(\Delta\varphi)$ are per-trigger azimuthal correlation distributions before and after feed-down subtraction, f_{prompt} is the fraction of prompt D meson defined by equation 4.5 and $\tilde{C}_{\text{feed-down}}^{\text{MC templ}}$ is a template of the azimuthal correlation distribution of the feed-down component obtained from Monte Carlo simulation.

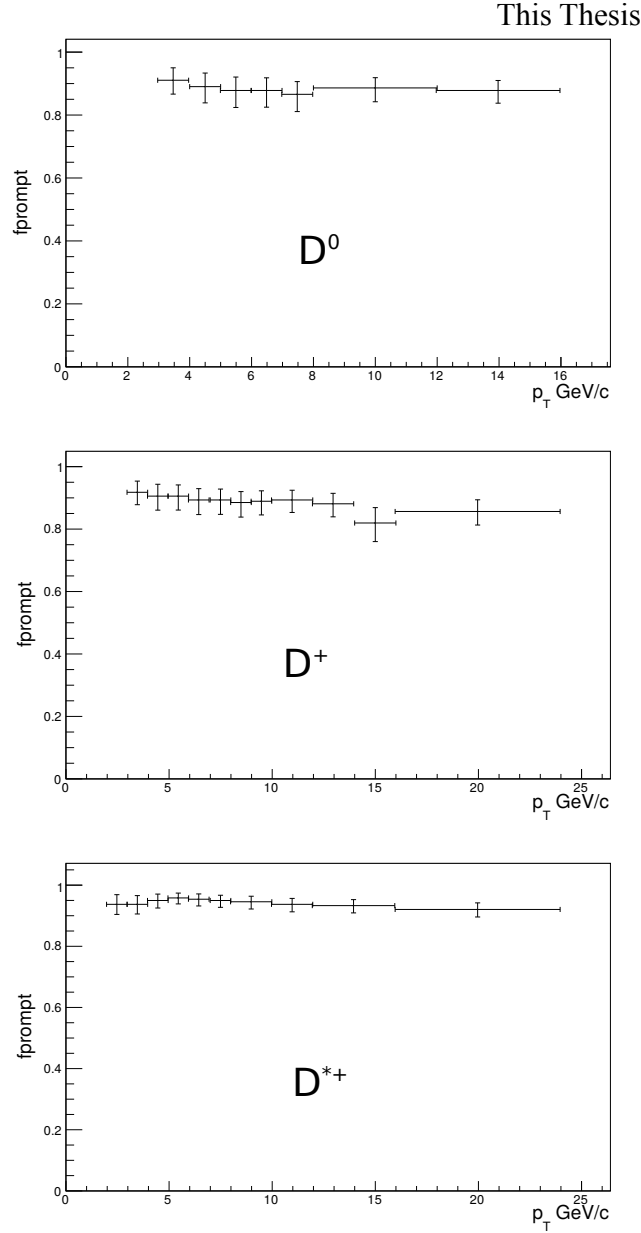


Figure 4.26: f_{prompt} as a function of p_T for D^0 (top), D^+ (middle) and D^{*+} (bottom) estimated on the basis of FONLL predictions.

$$f_{\text{prompt}} = 1 - \frac{N_{\text{feed-down}}^D}{N_{\text{all}}^D} \quad (4.5)$$

$N_{\text{feed-down}}^D$ and N_{all}^D are the no. of D mesons originating from decay of beauty hadron and all sources respectively and are estimated on the basis of FONLL predictions and using the reconstruction efficiency of prompt and feed-down D mesons [166] as given in equation 4.6.

$$N_{\text{feed-down}}^D|_{|y| < y_{\text{acceptance}}} = \frac{d\sigma_{\text{FONLL}}^{D \text{ from } B}}{dp_T}|_{|y| < 0.5} \Delta y \Delta p_T (\text{Acceptance} \times \text{efficiency})_{\text{feed-down}} \cdot \text{BR} \cdot L_{\text{int}} \quad (4.6)$$

Here, BR is the branching ratio of the D -meson species in a particular decay channel and L_{int}

4.2. Analysis method

is the integrated luminosity of that collision. Different Pythia versions and tunes are used for these simulations (Pythia6 with Perugia0, Perugia2010, Perugia2011 and Pythia8 [156, 157]). Figure 4.25 shows example plots for different PYTHIA tunes for azimuthal correlations of D mesons coming from B-hadron decay with charged particles. The value of f_{prompt} depends on D meson species and varies as a function of p_T as shown in figure 4.26.

After implementing all these corrections, we move to the final results followed by a set of systematic studies as described in chapter 5.

Chapter 5

Systematic studies and results

In this chapter, we will discuss several sources of systematic uncertainties in the correlation analysis between D mesons and charged particles. After assigning the values of uncertainties, we will show the final results i.e. the correlation distributions between D mesons and charged particles for pp $\sqrt{s}=13$ TeV. The near-side and away-side peak properties are extracted by fitting the correlation spectra. Results are compared with pp $\sqrt{s}=7$ TeV and pPb $\sqrt{s_{NN}}=5.02$ TeV results. Several Monte-Carlo models are used to check their compatibility with data.

5.1 Systematic studies

The results of the correlation analysis are affected by several sources of systematic uncertainties. The whole analysis procedure is repeated for each of the sources and compared with the standard one to obtain the values of corresponding uncertainty. The origins of systematic uncertainties are as follows:

- D-meson yield extraction
- Background subtraction
- Associated track efficiency
- D-meson reconstruction and selection efficiency
- Feed-down subtraction
- Secondary track contamination
- Bias on b to D decay topology

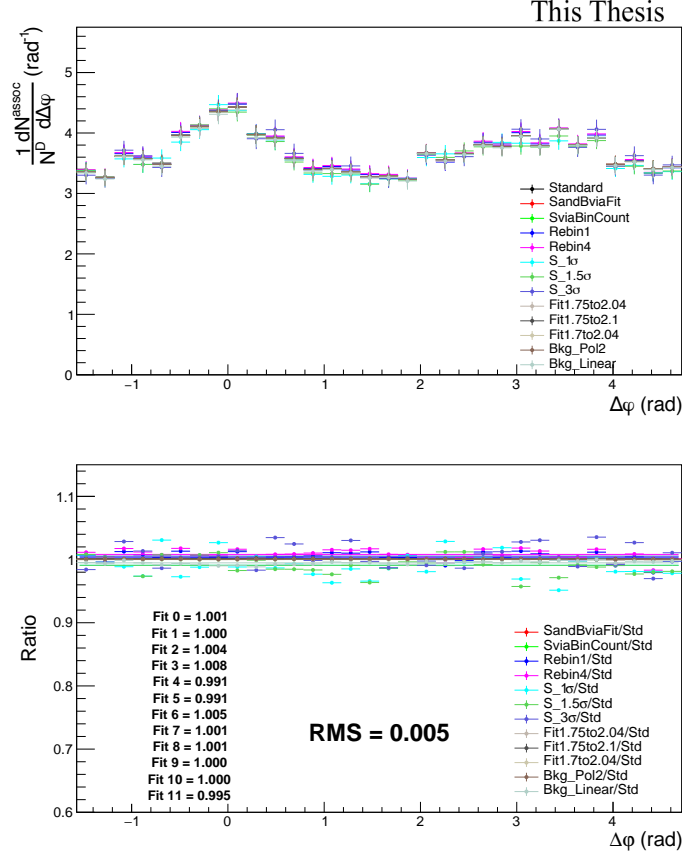


Figure 5.1: Top: Two-particle azimuthal correlation distributions between D^0 mesons and charged particles obtained by changing signal and background extraction procedure. Bottom: Ratio of the correlation distributions with modified signal and background extraction procedure over the standard yield extraction procedure for $p_T(\text{trigger})3 - 5 \text{ GeV}/c$ and $p_T(\text{assoc}) > 0.3 \text{ GeV}/c$.

5.1.1 Uncertainty on D-meson yield extraction

Systematic uncertainty comes for the D meson yield extraction and is determined for all the D mesons separately. The standard method to extract yield is to integrate the Gaussian component from the invariant mass spectra fit. To obtain the systematic uncertainty originated from this source we modify the signal extraction procedure as follows:

- Changing the background fit function as linear and polynomial (not performed on D^{*+})
- Changing the range in which the signal is extracted from the Gaussian fit
- Reducing the range of invariant mass in which the signal region is defined (and S and B are extracted);
- Rebinning the invariant mass distributions before the fitting
- Extracting yield via bin count method instead of integrating fit function

5.1. Systematic studies

- Extracting signal and background both via integral of the fit functions

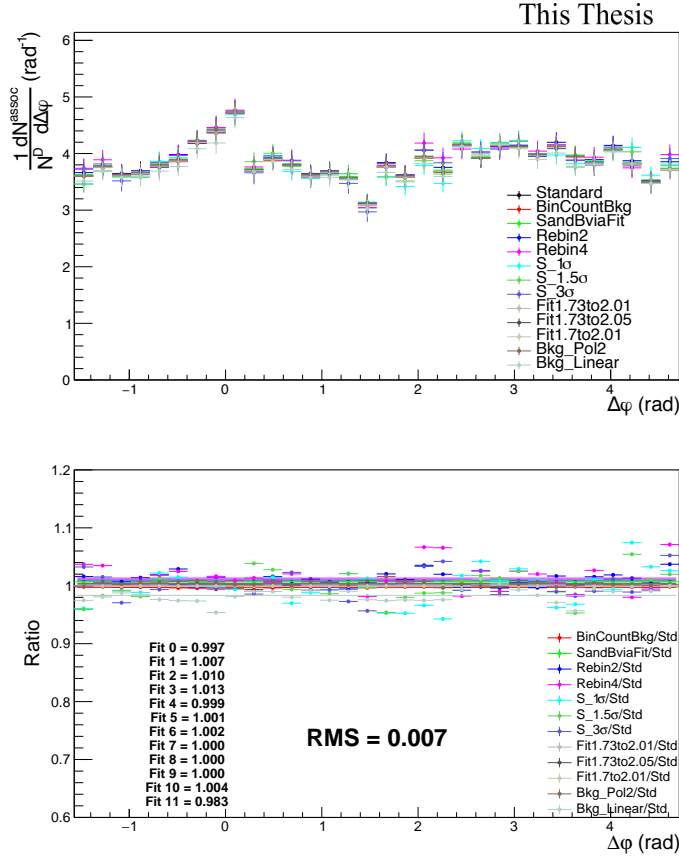


Figure 5.2: Same as figure 5.1 for the two-particle azimuthal correlations between D^+ -mesons and charged particles.

Both the value of the yield and the sideband correlations normalization factor are affected by changing the yield extraction approach, while the rest of the procedure to extract the azimuthal correlation distribution is the same as in the standard analysis. The fully corrected azimuthal correlation plots are evaluated, for each of these approaches, in the various D p_T bins and for each value of associated tracks p_T threshold. The ratios of the correlation distributions obtained with the standard yield extraction procedure and by differentiating the approach are evaluated. The results of the check are shown in figures 5.1, 5.2 and 5.3 for D^0 , D^+ and D^{*+} respectively. From the average of the ratios a systematic uncertainty can be extracted.

5.1.2 Uncertainty on background subtraction

The systematic uncertainty for the subtraction of the background correlations includes the effects due to the subtraction of the sidebands correlations from the signal correlations, after the sidebands normalization. To estimate this uncertainty the invariant mass range of the sidebands definitions is varied with respect to the default values. For the D^0 and D^+ mesons, the usual range of the sidebands

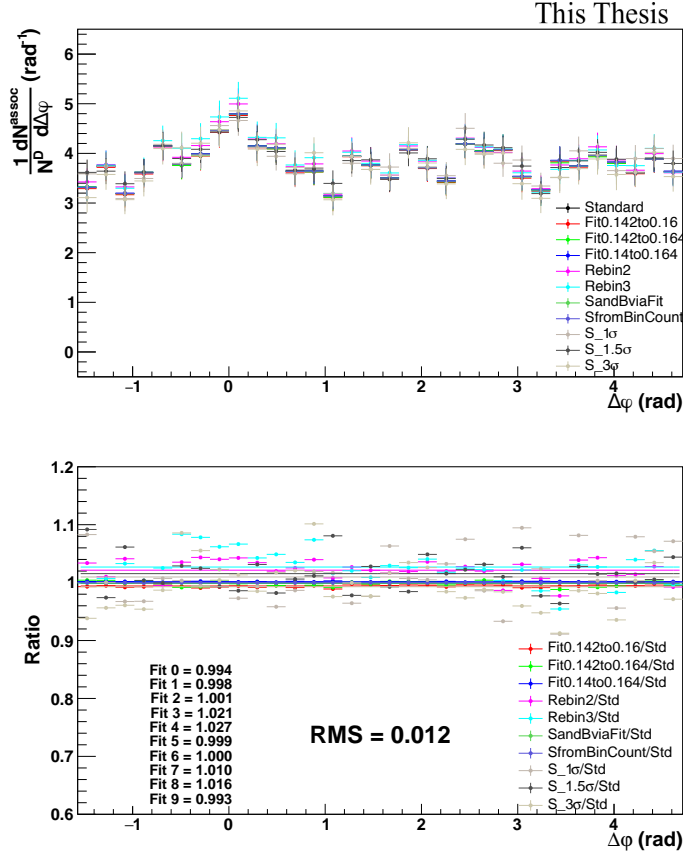


Figure 5.3: Same as figure 5.1 for the two-particle azimuthal correlations between D^{*+} -mesons and charged particles.

is 4 to 8 σ from the centre of the peak of the Gaussian fit of the invariant mass spectra, and it is modified to:

- For D^0
 - 4 to 6 σ from the centre of the peak
 - 6 to 8 σ from the centre of the peak
 - 3 to 9 σ from the centre of the peak
- For D^+
 - 4.5 to 7.5 σ from the centre of the peak
 - 5 to 7 σ from the centre of the peak
 - 3 to 9 σ from the centre of the peak

Due to the quickly decreasing trend of the background distribution on the left-hand side of the invariant mass distribution of the D^{*+} the background subtraction has been repeated selecting the sideband candidates in the following invariant mass regions:

5.1. Systematic studies

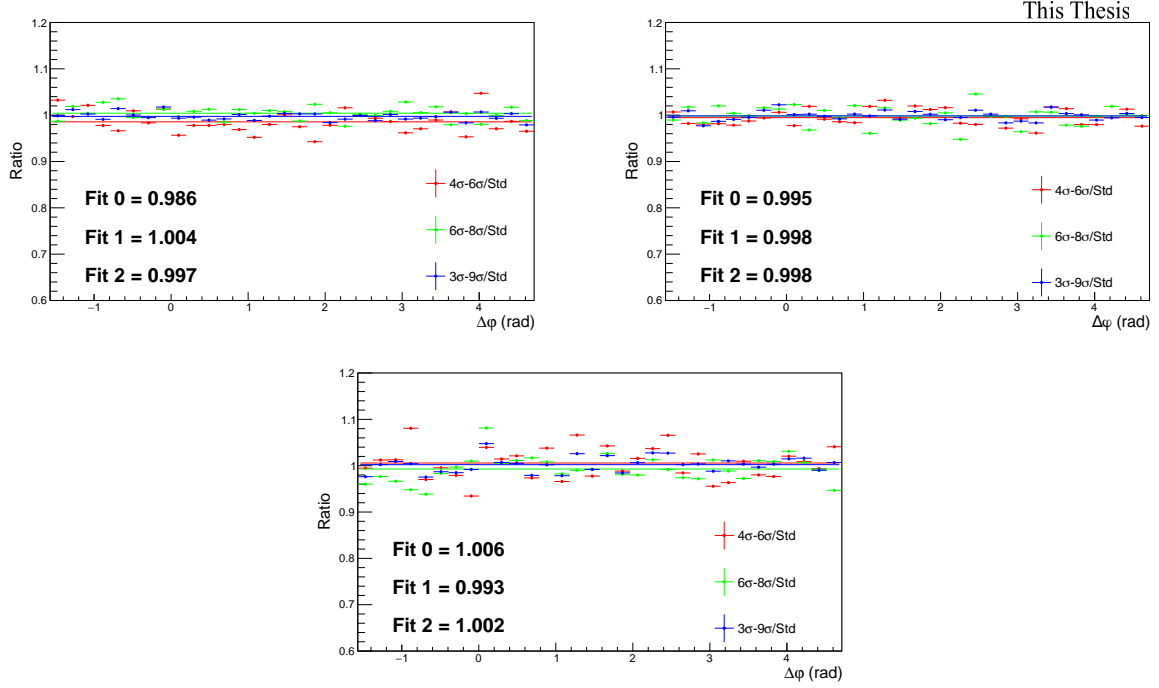


Figure 5.4: Ratios of correlation distributions between D^0 -mesons and charged particles obtained by changing the sideband ranges over those obtained with standard sideband ranges with $p_T(\text{trigger})$ 3-5 (top-left), 5-8 (top-right), 8-16 (bottom) GeV/c and $p_T(\text{assoc}) > 0.3 \text{ GeV}/c$.

- 8 to 15 σ at the right of the peak;
- 5 to 15 σ (the full available sideband region).

The rest of the procedure to find the azimuthal correlation distributions is unchanged and the ratios of the fully corrected azimuthal correlation plots obtained with the standard sidebands range and the correlation plots extracted with different sidebands definitions are evaluated for each D meson p_T bin and associated tracks p_T threshold. The ratios are shown in figures 5.4, 5.5 and 5.6 for D^0 , D^+ and D^{*+} respectively.

The ratio plots for all the three D mesons don't show any specific structure along $\Delta\varphi$ which implies that this kind of uncertainty does not have any effect on correlation shape, it only affects the normalization value.

5.1.3 Uncertainty on associated track efficiency

The systematic uncertainty coming from associated track cut selection is determined by varying the following cuts one by one:

- Minimum ITS cluster: 0

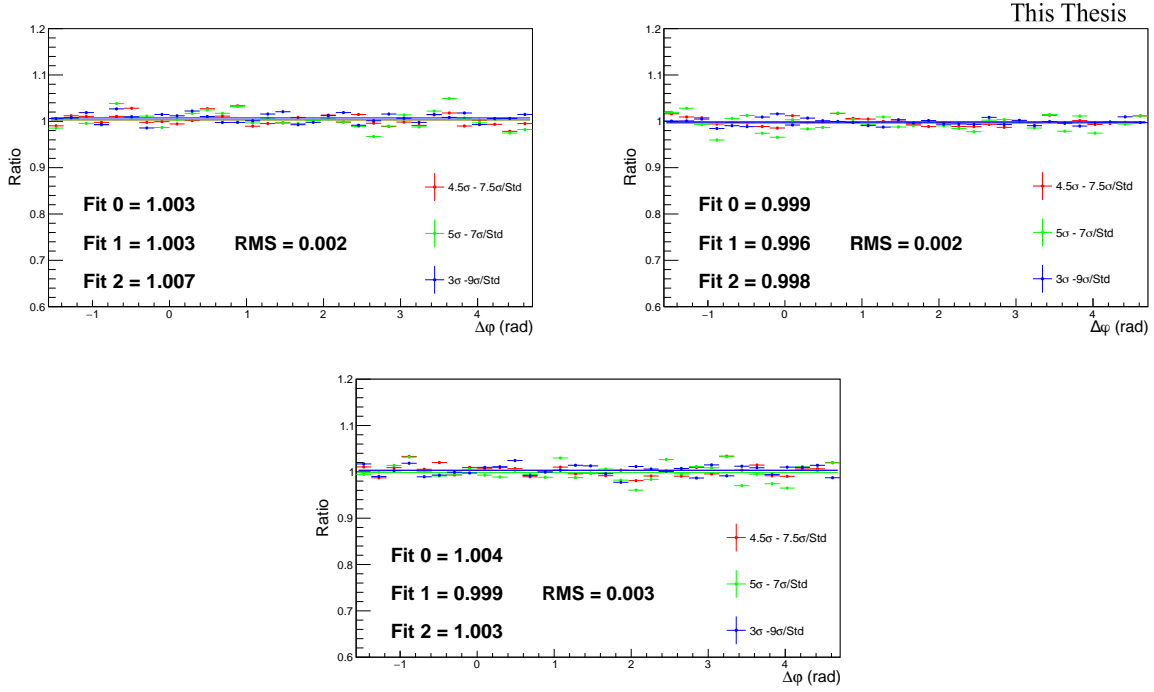


Figure 5.5: Ratios of correlation distributions between D^+ -mesons and charged particles obtained by changing the sideband ranges over those obtained with standard sideband ranges with $p_T(\text{trigger})$ 3-5 (top-left), 5-8 (top-right), 8-16 (bottom) GeV/c and $p_T(\text{assoc}) > 0.3$ GeV/c.

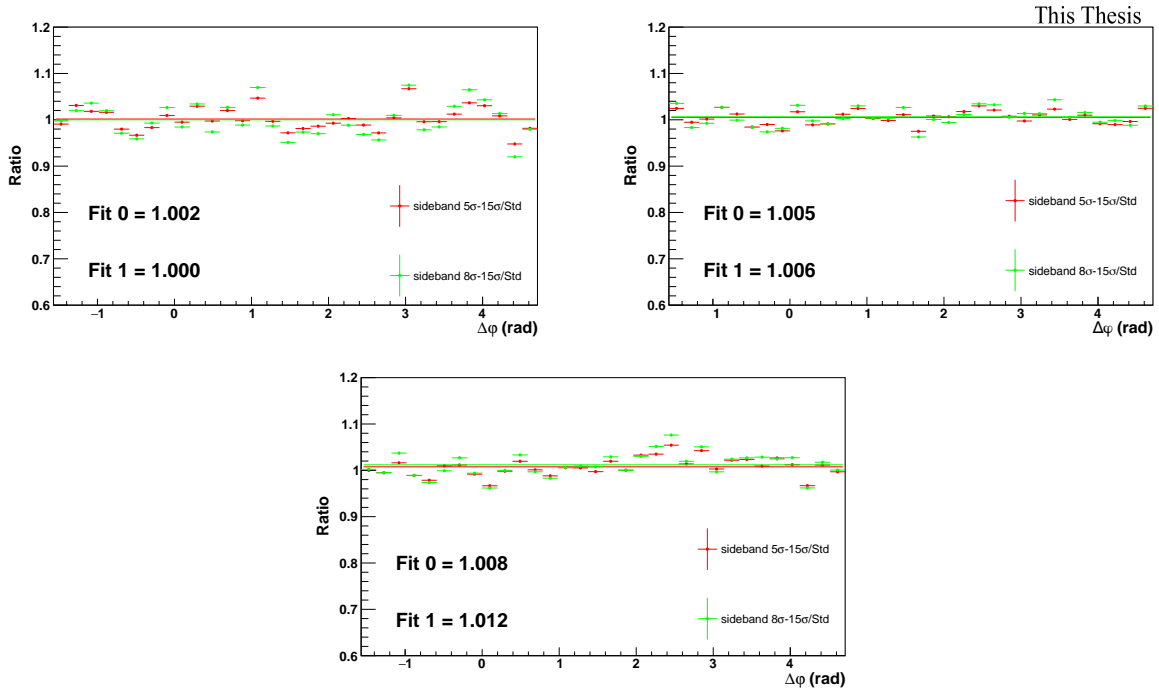


Figure 5.6: Ratios of correlation distributions between D^{*+} -mesons and charged particles obtained by changing the sideband ranges over those obtained with standard sideband ranges with $p_T(\text{trigger})$ 3-5 (top-left), 5-8 (top-right), 8-16 (bottom) GeV/c and $p_T(\text{assoc}) > 0.3$ GeV/c.

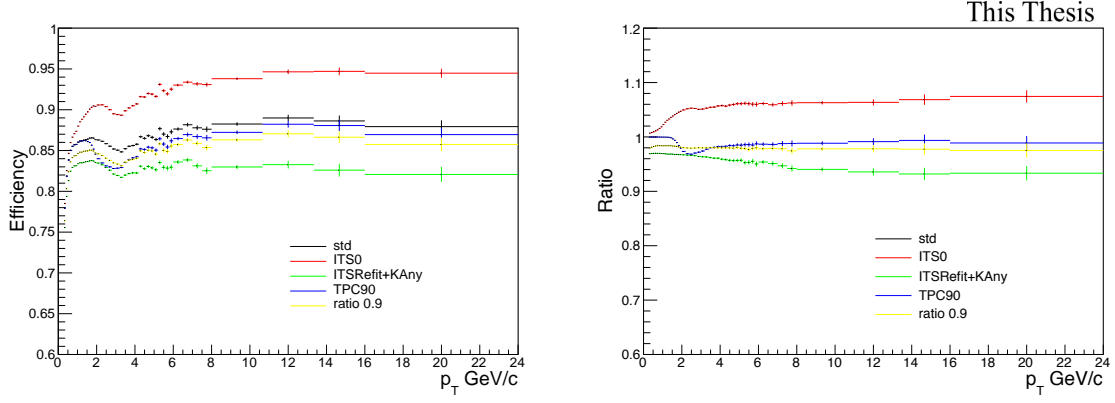


Figure 5.7: Associated track efficiency maps as a function of p_T for different cut variation (left). Ratio of efficiency maps with different cut variations w.r.t. the standard one (right).

- No ITS refit
- Number of TPC crossed rows: 90
- Minimum of ratio of TPC cross rows over findable cluster: 0.9

Considering these modification of the cuts one by one, we prepare tracking efficiency maps as shown in figure 5.7. Next, we repeat the whole analysis considering the different modified cut set and their corresponding tracking efficiency maps. We evaluate the systematic uncertainty values by taking ratios of these modified correlation distributions over the standard one as shown in figures 5.8, 5.9 and 5.10 for D^0 , D^+ and D^{*+} respectively.

Since these ratio plots don't show any structure along $\Delta\varphi$, those are fitted with a constant to determine the systematic uncertainty values.

5.1.4 Uncertainty on D-meson reconstruction and selection efficiency

A systematic uncertainty arises on data and Monte-Carlo simulations for the cut variables used in D-meson selection. To evaluate the uncertainty values, we prepare the D-meson topological cut set by making it tight and loose in various combinations such that we can get sufficient yield even after applying alternate cut selections. Six sets of tight and loose cut set has been prepared for for all the three D mesons like:

- 5%, 10% and 15% tight and loose cut set for D^0
- 5%, 10% and 15% tight and loose cut set for D^+
- 15%, 20% and 30% tight and loose cut set for D^{*+}

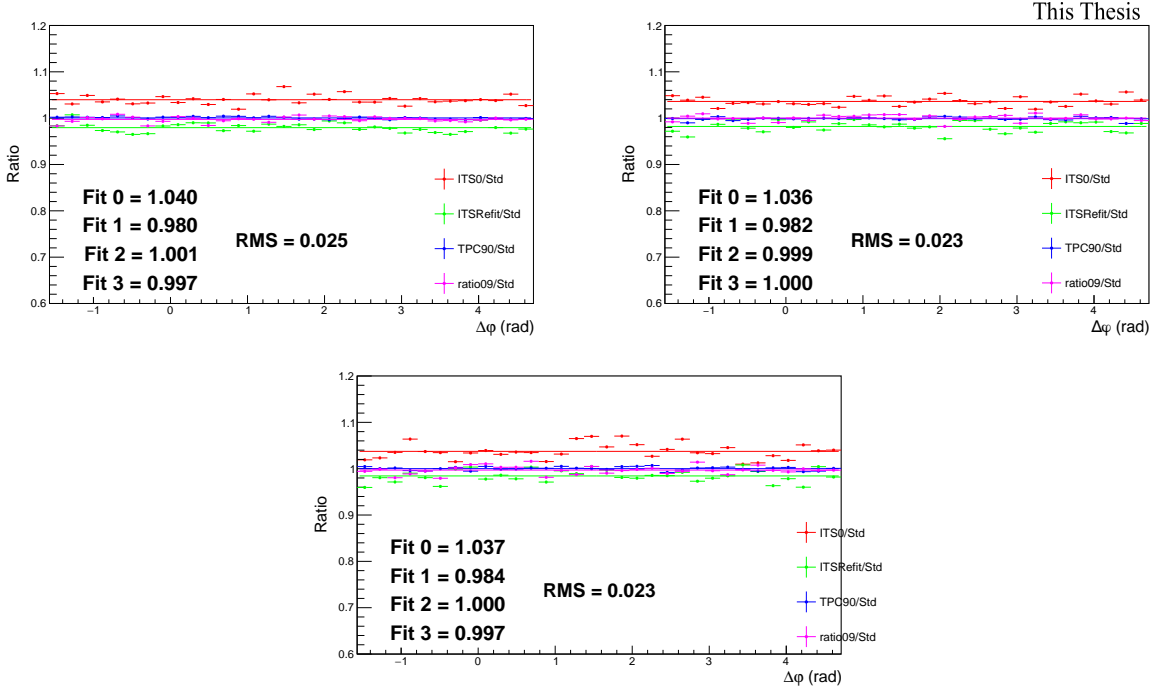


Figure 5.8: Ratios of correlation plots between D^0 mesons and charged particles obtained with alternate associated track cut sets over those obtained with standard selection with $p_T(\text{trigger})$ 3-5 (top-left), 5-8 (top-right), 8-16 (bottom) GeV/ c and $p_T(\text{assoc}) > 0.3$ GeV/ c .

We prepare the trigger efficiency maps using these various cut sets. The p_T dependence of these efficiency maps are shown in figures 5.11 and 5.12 which reveals that the cuts are more sensitive in low- p_T region with respect to high- p_T region.

Figures 5.13, 5.14 and 5.15 show the ratio of the correlation distributions with alternate cut sets over those with the standard approach, for D^0 , D^+ and D^{*+} mesons respectively, for exemplary p_T ranges covering the full kinematic region of interest for the analyses. The ratios are reasonably flat in $\Delta\phi$, hence a flat systematic is evaluated as systematic uncertainty from D-meson the cut variations.

5.1.5 Uncertainty on feed-down subtraction

As described before, the feed-down subtraction from the data distributions is performed by means of simulation templates of correlation distributions between D mesons (from B hadron decay) and charged particles from PYTHIA6 generator, and considering the central value of f_{prompt} to extract the feed-down D-meson contribution. In order to evaluate a systematic uncertainty on this procedure, the feed-down subtraction procedure is repeated considering, together with PYTHIA6+Perugia2011 templates, also PYTHIA6+Perugia2010 and PYTHIA8 simulations. In each case, not only the central value of the measured f_{prompt} is considered to rescale the distributions, but also the maximum and minimum values of its total uncertainty. Then, the envelope of nine the different cases obtained

5.1. Systematic studies

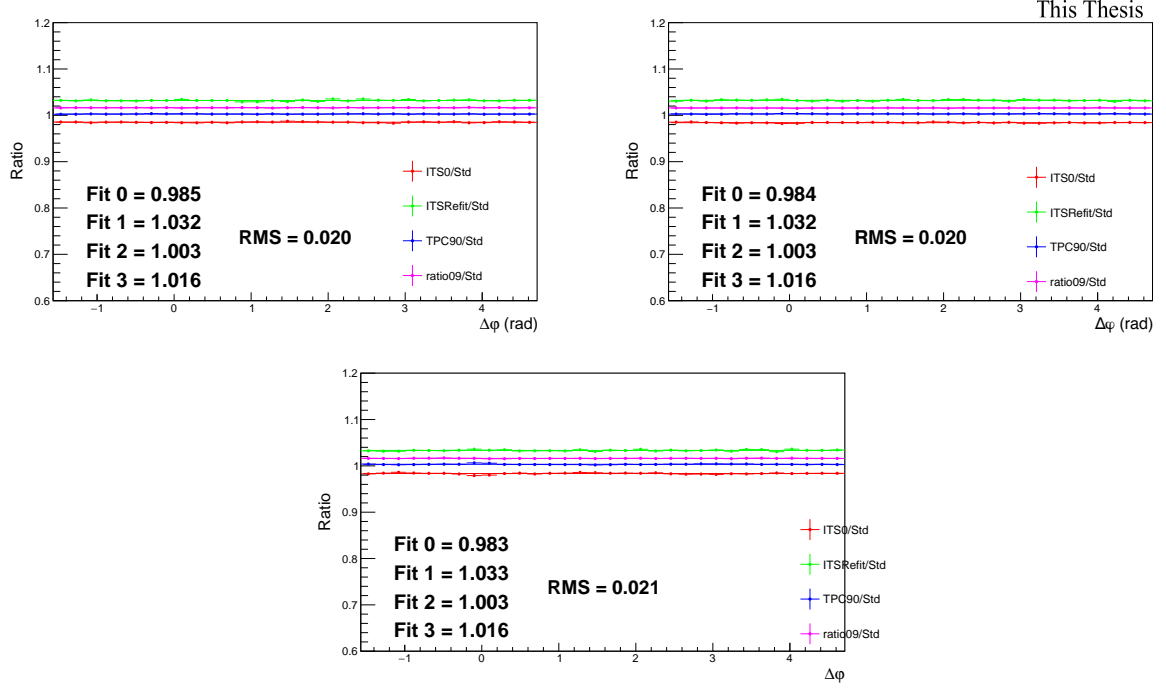


Figure 5.9: Ratios of correlation plots between D^+ mesons and charged particles obtained with alternate associated track cut sets over those obtained with standard selection with $p_T(\text{trigger})$ 3-5 (top-left), 5-8 (top-right), 8-16 (bottom) GeV/c and $p_T(\text{assoc}) > 0.3$ GeV/c.

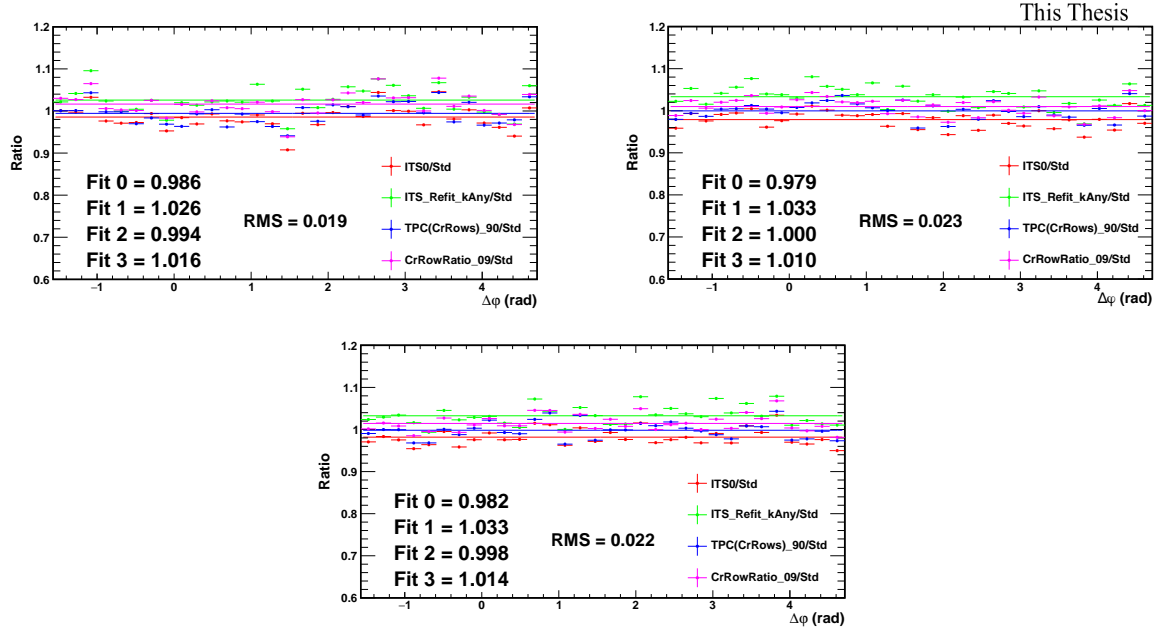


Figure 5.10: Ratios of correlation plots between D^{*+} mesons and charged particles obtained with alternate associated track cut sets over those obtained with standard selection with $p_T(\text{trigger})$ 3-5 (top-left), 5-8 (top-right), 8-16 (bottom) GeV/c and $p_T(\text{assoc}) > 0.3$ GeV/c.

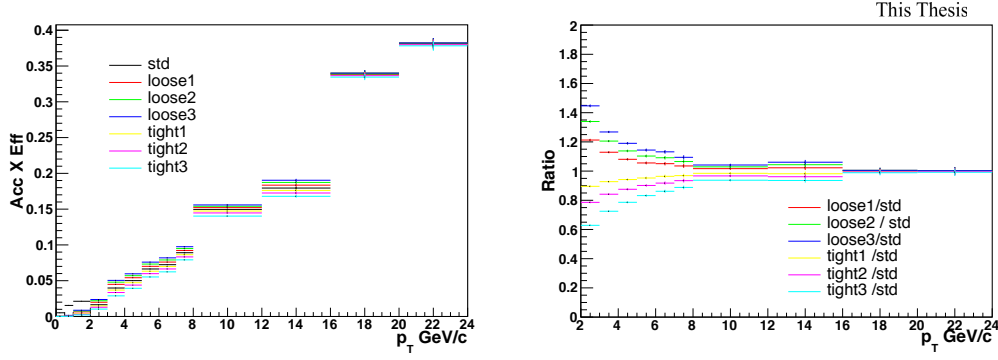


Figure 5.11: Prompt D^0 efficiencies for alternate cut variations (left). Ratio of prompt D^0 efficiencies for different alternate cutset w.r.t. the standard one (right).

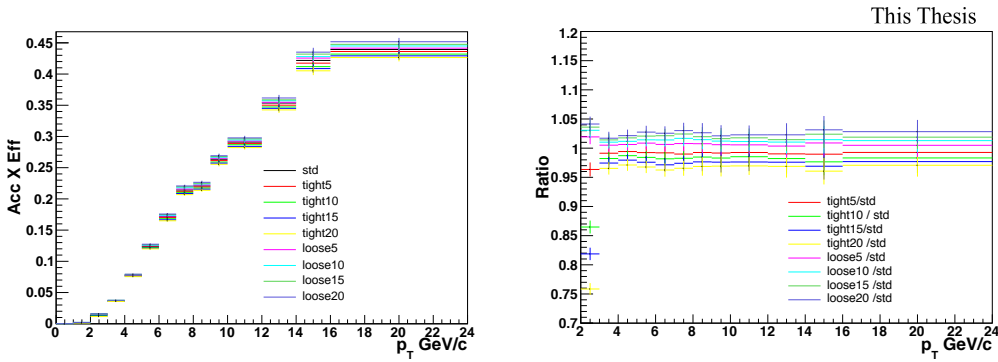


Figure 5.12: Prompt D^+ efficiencies for alternate cut variations (left). Ratio of prompt D^+ efficiencies for different alternate cutset w.r.t. the standard one (right).

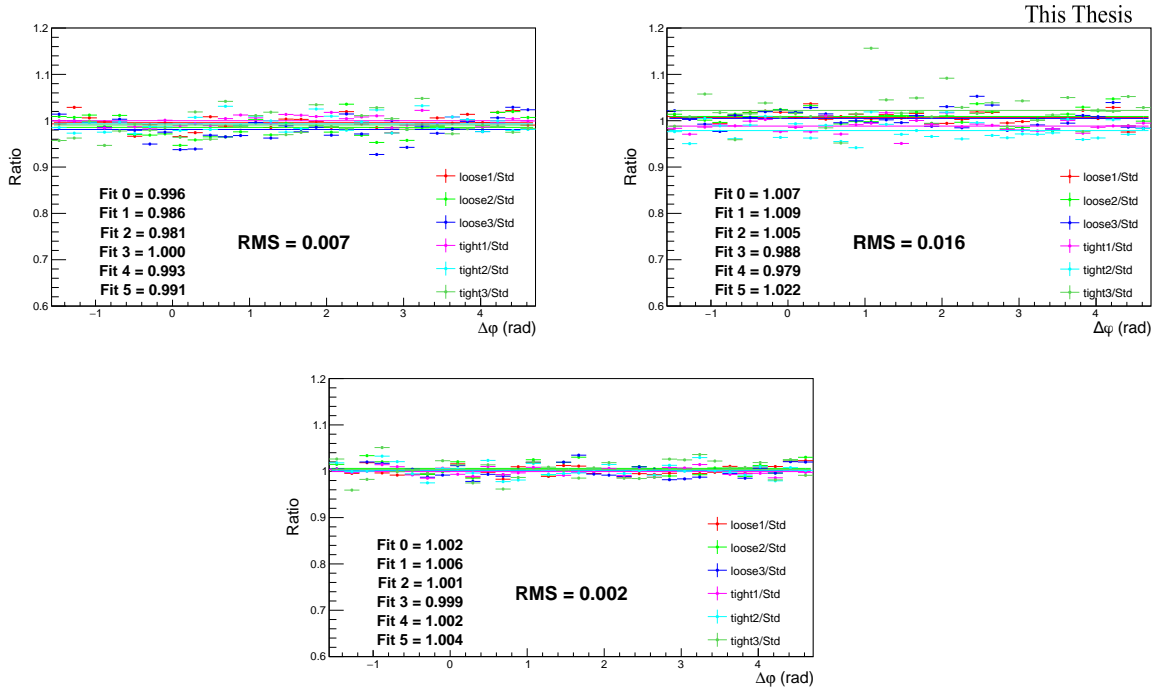


Figure 5.13: Ratios of azimuthal correlations between D^0 mesons and charged particles obtained with alternate D-meson cut sets over those obtained with standard selection with $p_T(\text{trigger})$ 3-5 (top-left), 5-8 (top-right), 8-16 (bottom) GeV/c and $p_T(\text{assoc}) > 0.3$ GeV/c.

5.1. Systematic studies

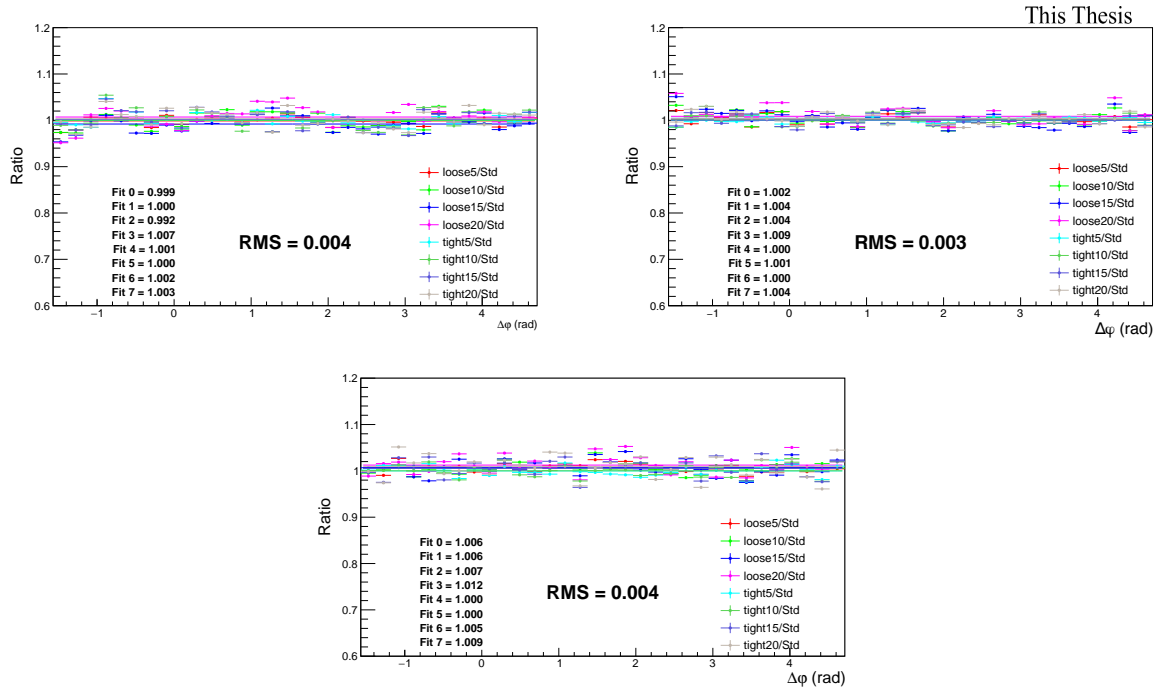


Figure 5.14: Ratios of azimuthal correlations between D^+ mesons and charged particles obtained with alternate D-meson cut sets over those obtained with standard selection with $p_T(\text{trigger})$ 3-5 (top-left), 5-8 (top-right), 8-16 (bottom) GeV/c and $p_T(\text{assoc}) > 0.3$ GeV/c.

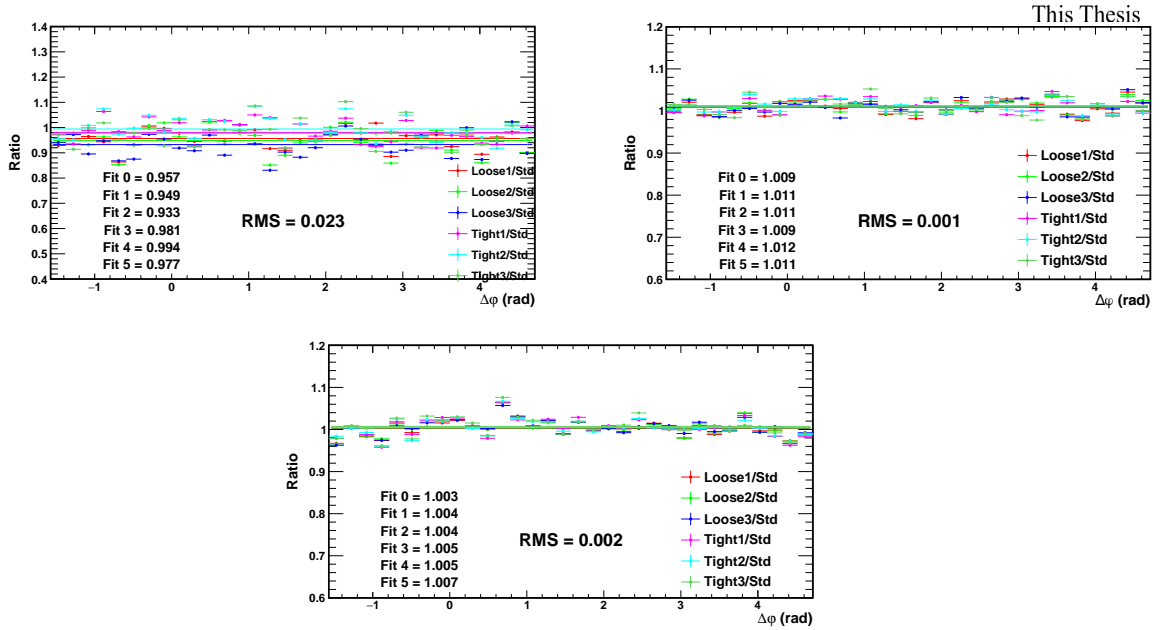


Figure 5.15: Ratios of azimuthal correlations between D^{*+} mesons and charged particles obtained with alternate D-meson cut sets over those obtained with standard selection with $p_T(\text{trigger})$ 3-5 (top-left), 5-8 (top-right), 8-16 (bottom) GeV/c and $p_T(\text{assoc}) > 0.3$ GeV/c.

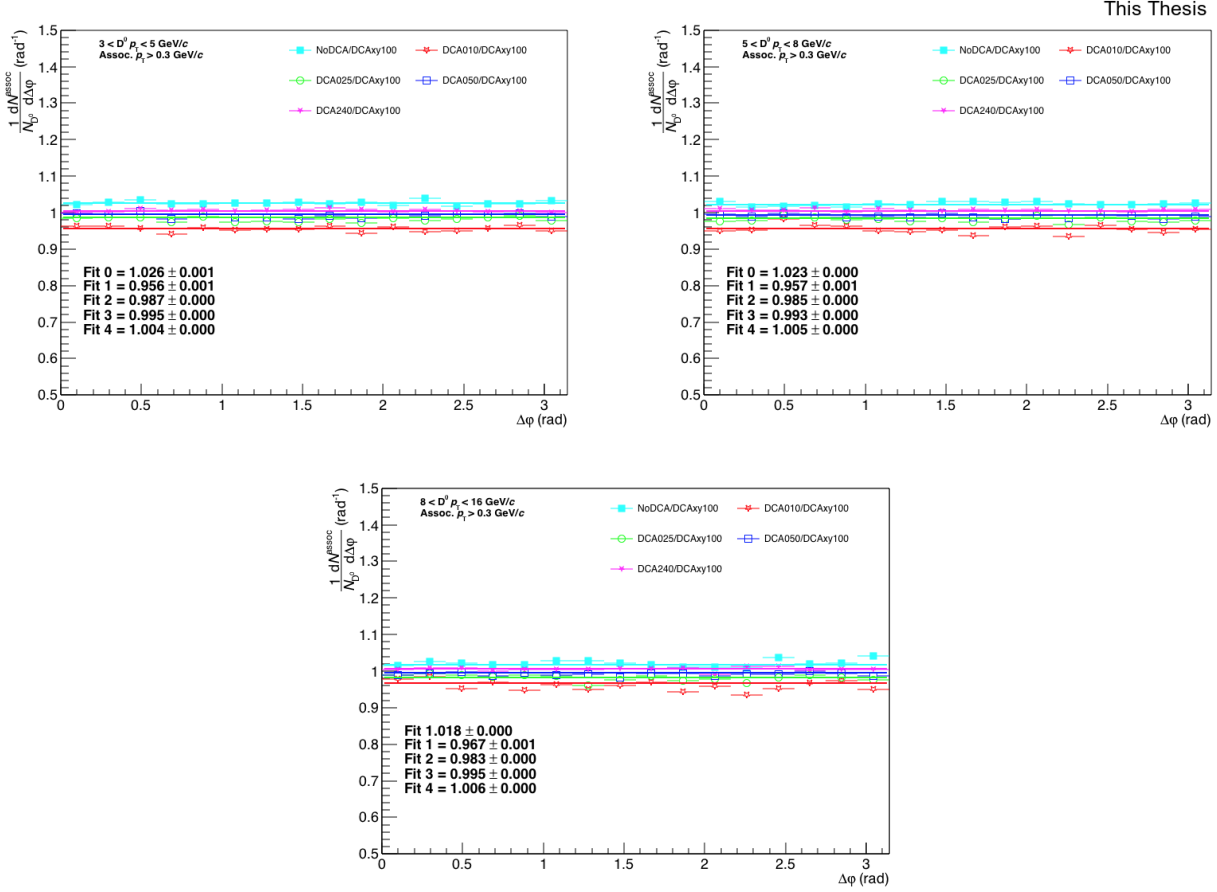


Figure 5.16: Ratios of two-particle azimuthal correlations between D^0 mesons and charged particles obtained with alternate DCA cut over those obtained with standard DCA cut with $p_T(\text{trigger})$ 3-5 (top-left), 5-8 (top-right), 8-16 (bottom) GeV/c and $p_T(\text{assoc}) > 0.3$ GeV/c.

by varying the templates and the f_{prompt} assumption is considered, and a value of the systematics defined as the envelope spread divided by $\sqrt{3}$ is taken as systematic uncertainty. This uncertainty is assumed uncorrelated among the different $\Delta\varphi$ points.

5.1.6 Uncertainty on secondary track contamination

The number of primary and secondary tracks which are accepted from the DCA cut is determined for different values of the DCA selection, and the correlation distributions for the various cases are evaluated. The variation is done by taking different DCA_{xy} values (i.e, 0.1, 0.25, 0.5, 1.0, 2.4 cm and without any DCA cut). From this figure, this is obvious that we are accepting more secondary tracks with the loosening of the DCA_{xy} value. The ratios of correlation distributions between D mesons and charged particles obtained with respect to a loose DCA_{xy} 1 cm for other DCA_{xy} selections after purity correction is shown in figure 5.16. The plots show a flat trend along the $\Delta\varphi$ axis and the maximum uncertainty is 3%.

5.1.7 Uncertainty on correction for the bias on the b to D decay topology

The evaluation of this systematic uncertainty is already explained earlier. For each of the few data points close to the centre of the near-side peak, which are affected by the bias, a bilateral and symmetric uncertainty of amplitude $|C(\Delta\varphi)_{\text{corr}} - C(\Delta\varphi)_{\text{raw}}|/\sqrt{12}$ is assigned.

5.1.8 Overall uncertainty

The systematic uncertainties originated from the above mentioned sources are evaluated for three different $p_{\text{T}}(\text{D})$ regions 3-5, 5-8 and 8-16 GeV/ c with $p_{\text{T}}(\text{assoc}) > 0.3, > 1, 0.3 - 1$ GeV/ c . The plots are shown with only one associated p_{T} region, for rest of the p_{T} region systematic uncertainties are evaluated and listed in tables 5.1, 5.2 and 5.3 for D^0 , D^+ and D^{*+} mesons respectively.

Sources	pp (D^0)								
Associate p_{T}	>1.0 GeV/ c			>0.3 GeV/ c			0.3 -1.0 GeV/ c		
$p_{\text{T}}(\text{D})$ (GeV/ c)	3-5	5-8	8-16	3-5	5-8	8-16	3-5	5-8	8-16
Yield Extraction	1%	1%	1%	1%	1%	1%	1%	1%	1%
Background Subtraction	2%	2%	2%	2%	2%	2%	2%	2%	2%
Cut Variation	1%	2%	1%	1%	2%	1%	1%	2%	1%
Tracking Efficiency	3.5%	3.5%	3.5%	3.5%	3.5%	3.5%	3.5%	3.5%	3.5%
Track Purity Sample	3%	3%	3%	3%	3%	3%	4%	4%	4%

Table 5.1: Systematic table for D^0 .

Sources	pp (D^+)								
Associate p_{T}	>1.0 GeV/ c			>0.3 GeV/ c			0.3 -1.0 GeV/ c		
$p_{\text{T}}(\text{D})$ (GeV/ c)	3-5	5-8	8-16	3-5	5-8	8-16	3-5	5-8	8-16
Yield Extraction	1%	1%	1%	1%	1%	1%	1%	1%	1%
Background Subtraction	1%	1%	1%	1%	1%	1%	1%	1%	1%
Cut Variation	1%	1%	1%	1%	1%	1%	1%	1%	1%
Tracking Efficiency	3%	3%	3%	3%	3%	3%	4%	4%	4%
Track Purity Sample	3%	3%	3%	3%	3%	3%	4%	4%	4%

Table 5.2: Systematic table for D^+ .

Sources	pp (D^{*+})								
Associate p_{T}	>1.0 GeV/ c			>0.3 GeV/ c			0.3 -1.0 GeV/ c		
$p_{\text{T}}(\text{D})$ (GeV/ c)	3-5	5-8	8-16	3-5	5-8	8-16	3-5	5-8	8-16
Yield Extraction	3%	3%	3%	2%	2%	2%	2%	2%	2%
Background Subtraction	2%	1%	2%	1%	1%	1%	1%	1%	1%
Cut Variation	2%	1%	1%	2%	1%	1%	2.5%	1%	1%
Tracking Efficiency	3%	4%	4%	3%	3%	3%	3%	3%	3%
Track Purity Sample	3%	3%	3%	3%	3%	3%	4%	4%	4%

Table 5.3: Systematic table for D^{*+} .

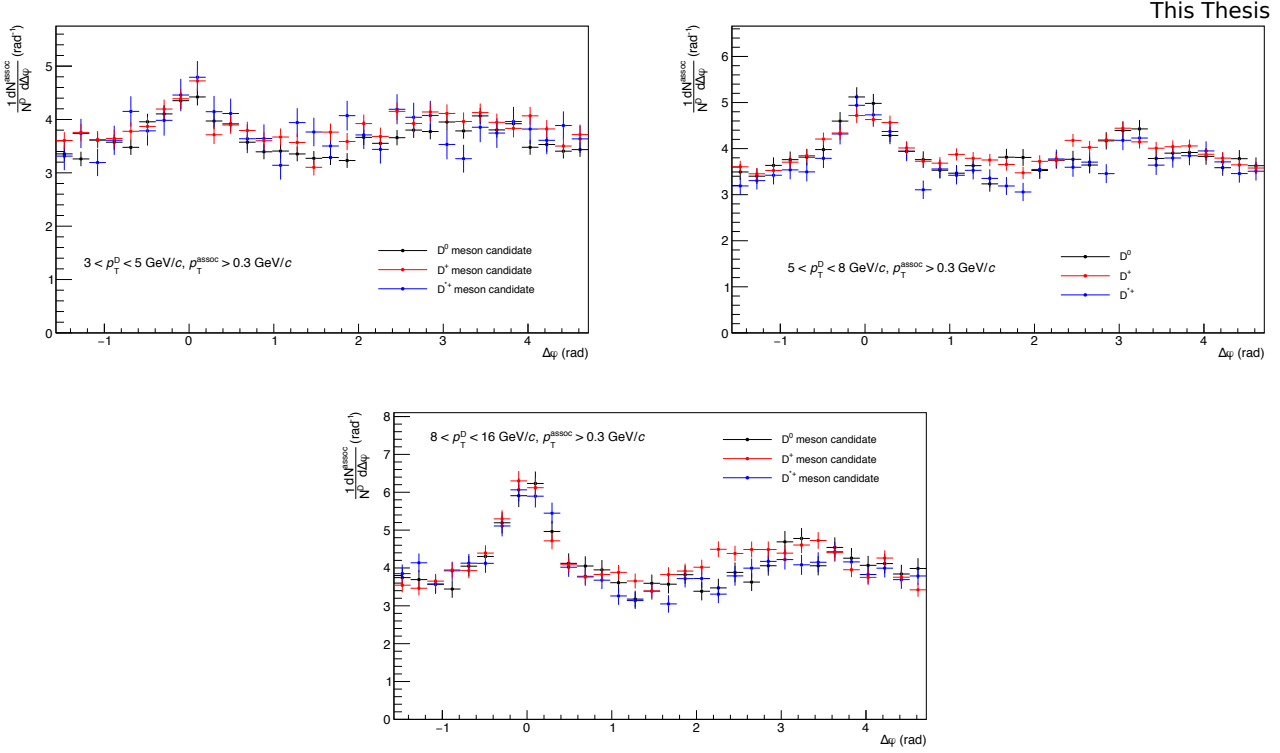


Figure 5.17: Comparison of azimuthal correlation distributions between D mesons (D^0 , D^+ and D^{*+}) and charged particles with D-meson p_T 3-5 GeV/ c , 5-8 GeV/ c and 8-16 GeV/ c and associated $p_T > 0.3$ GeV/ c .

5.2 Results

5.2.1 Comparison of results from D^0 , D^+ and D^{*+}

Figure 5.17 shows the comparison of correlation results D^0 , D^+ and D^{*+} for three different trigger p_T 3-5 GeV/ c , 5-8 GeV/ c and 8-16 GeV/ c and associated $p_T > 0.3$ GeV/ c . These results are shown before applying the feed-down subtraction and removal of secondary track contamination. As these corrections affect the correlation distributions in same way for the three D meson sample, figure 5.17 works as a way to check compatibility among the correlation distribution for three D mesons.

As shown in figure 5.17, the $\Delta\phi$ distributions for three D mesons shows an overall agreement, within the level of the uncertainties for all the kinematic ranges.

Given the compatibility of the observed D^0 , D^+ and D^{*+} azimuthal correlations within the statistical and systematic uncertainties as shown in figure 5.17, and considering that the differences found in the correlation distributions observed in Monte Carlo simulations based on Pythia6 (Perugia0, Perugia2010, Perugia2011 tunes) and Pythia8 are within the statistical uncertainties (though a slight near side hierarchy is present), a weighted average (equation 5.1) of the azimuthal correlation distributions of the three mesons is performed in order to reduce the overall uncertainties. The inverse of

5.2. Results

the sum in quadrature of the statistical uncertainty and of the systematic uncertainty uncorrelated among the three D mesons is used as weight.

$$\langle \frac{1}{N_D} \frac{dN_{assoc}}{dp_T} \rangle_{Dmesons} = \frac{\sum_{i=meson} w_i \frac{1}{N_D} \frac{dN_{assoc}}{d\varphi}}{\sum_{i=meson} w_i}; w_i = \frac{1}{\sigma_{i,stat}^2 + \sigma_{i,uncorr.syst.}^2} \quad (5.1)$$

The statistical uncertainty and the uncertainty on the yield extraction on the average are then recalculated using the formula:

$$\sigma^2 = \frac{\sum_{i=meson} w_i \sigma_i^2}{\sum_{i=meson} w_i} \quad (5.2)$$

which, for $\sigma_i^2 = 1/w_i$, coincides with the standard formula giving the uncertainty on a weighted average. The contribution to the average systematic uncertainty for those uncertainty sources not included in the weight definition, is evaluated via error propagation on the formula of the weighted average (equation 5.1), resulting in equation 5.3 and 5.4 for sources considered uncorrelated and correlated among the mesons. In particular, the uncertainties on the associated track reconstruction efficiency, on the contamination from secondary tracks, on the feed-down subtraction, and that resulting from the Monte Carlo closure test are considered fully correlated among the mesons, while those deriving from the yield extraction, the background subtraction and on the D meson reconstruction and selection efficiency are treated as uncorrelated.

$$\sigma^2 = \frac{\sum_{i=meson} w_i^2 \sigma_i^2}{(\sum_{i=meson} w_i)^2} \quad (5.3)$$

$$\sigma = \frac{\sum_{i=meson} w_i \sigma_i}{\sum_{i=meson} w_i} \quad (5.4)$$

Figure 5.18 shows the average of D^0 , D^+ and D^{*+} azimuthal correlations in the D meson p_T ranges $3 < p_T < 5$ GeV/ c , $5 < p_T < 8$ GeV/ c and $8 < p_T < 16$ GeV/ c with associated tracks with $p_T > 0.3$ GeV/ c , $p_T > 1$ GeV/ c and $0.3 < p_T < 1$ GeV/ c . The fit function is composed of two Gaussian functions with mean fixed at 0 and π and a baseline, whose values are fixed to the weighted average of the 8 lower points in the correlation distribution.

Despite being evaluated in the full 2π range, the range of final results is reduced to $[0, \pi]$ radians, reflecting the points outside that range over the value of 0. This allows to reduce the impact of statistical fluctuations on the data points (supposing equal statistics for a pair of symmetric bins, after the reflection the relative statistical uncertainty for the resulting bin is reduced by a factor $1/\sqrt{2}$).

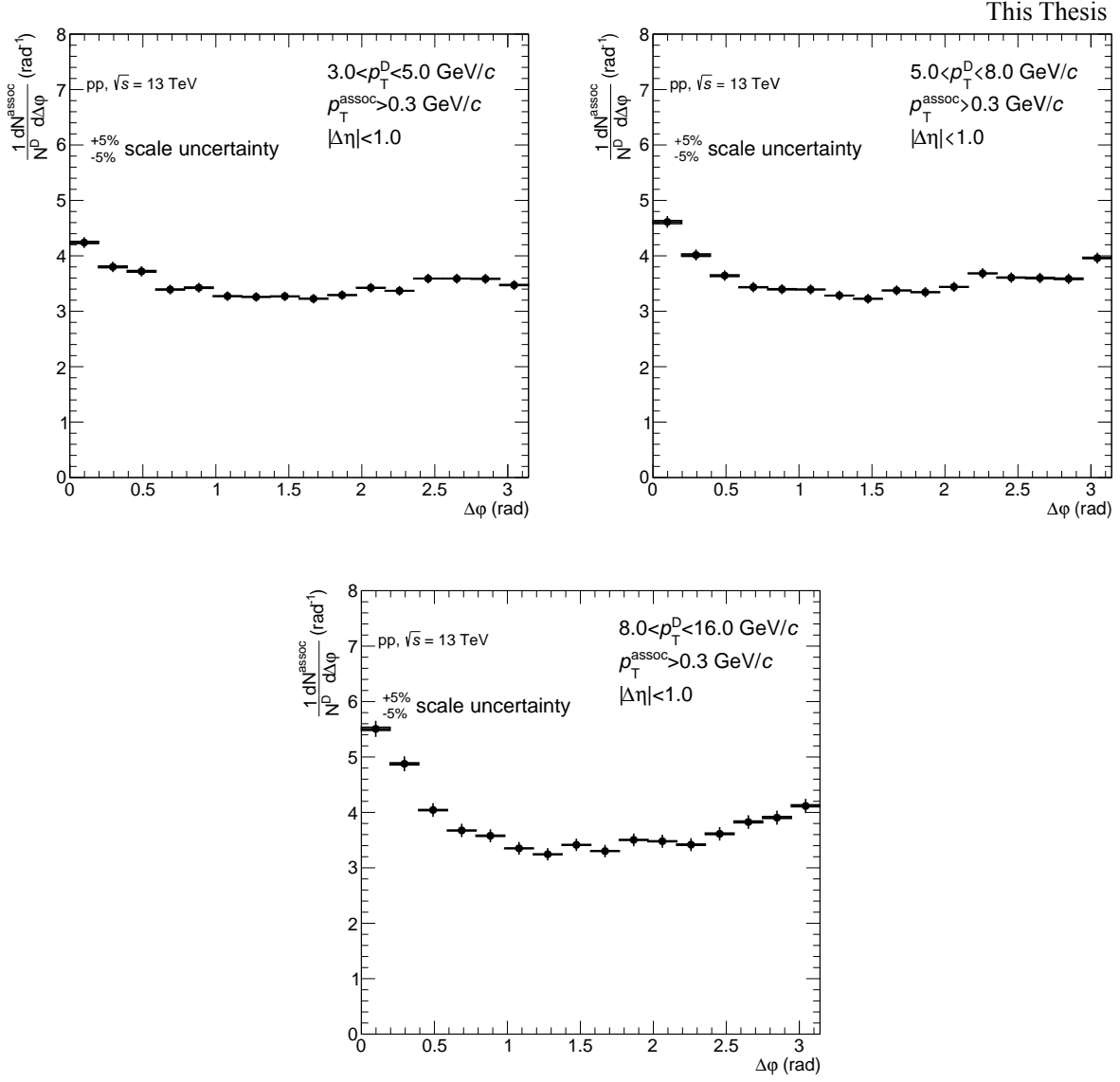


Figure 5.18: Average of D^0 , D^+ and D^{*+} azimuthal correlations, from analysis on the data sample, for the different D p_T bins 3-5, 5-8, 8-16 GeV/c and associated $p_T > 0.3 \text{ GeV}/c$.

5.2.2 Fitting of correlation spectra and fit observables

The properties of the azimuthal correlation distribution are quantified by fitting the distribution with a function composed of two Gaussian functions, modelling the near and the away side peaks, and a constant term describing the baseline given in equation 5.5. The mean of the Gaussian are fixed at $\Delta\varphi = 0$ and $\Delta\varphi = \pi$. To accomplish the 2π periodicity of the $\Delta\varphi$ variable, the Gaussian functions are “duplicated” with mean at $\Delta\varphi = 2\pi$ and $\Delta\varphi = -\pi$.

$$f(\Delta\varphi) = c + \frac{Y_{NS}}{\sqrt{2\pi}\sigma_{NS}} e^{-\frac{(\Delta\varphi - \mu_{NS})^2}{2\sigma_{NS}^2}} + \frac{Y_{AS}}{\sqrt{2\pi}\sigma_{AS}} e^{-\frac{(\Delta\varphi - \mu_{AS})^2}{2\sigma_{AS}^2}} \quad (5.5)$$

An example of the results from the fit is shown in Figure 5.19. From the fit results, we find the values of near-side and away-side yields and widths from the integral and sigma of the Gaussian functions respectively. Calculation of correlation baseline is done on basis of the “physical” minimum estimation which is quite faithful against the statistical fluctuations. Because of larger statistical fluctuations present in data results and no such fluctuations in MC results, different procedure to estimate best physical minimum is considered. Estimation of the baseline systematic uncertainty has been done by calculation of minimum of the azimuthal correlation distribution for MC (considering two lowest values) and average on the transverse region in case of data. So for the data, baseline uncertainty is calculated as the average of the 8 points lying in the so-called “transverse region” (for the 2π plot ranges), i.e. the interval $\frac{\pi}{4} < |\Delta\varphi| < \frac{\pi}{2}$.

The near-side observables give information on the multiplicity and angular spread of the tracks from the fragmentation of the charm jet which gave birth to the D-meson trigger. At first order, instead, the away-side observables are related to the hadronization of the charm parton produced in the opposite direction (though the presence of NLO processes for charm production breaks the full validity of this assumption). The baseline value is a rough indicator of the underlying event multiplicity, though below the baseline level also charm and beauty-related pairs are contained (especially in cases of NLO production for the heavy quarks).

The evaluation of the systematics is performed as follows:

- The fits are repeated by changing the range of the transverse region in which the baseline is evaluated.
- In addition, $\Delta\varphi$ correlation points are shifted to the upper and lower bounds of their uncorrelated systematic boxes, and refitted.
- The fits are also repeated by moving the baseline value from its default value (i.e. with the

This Thesis

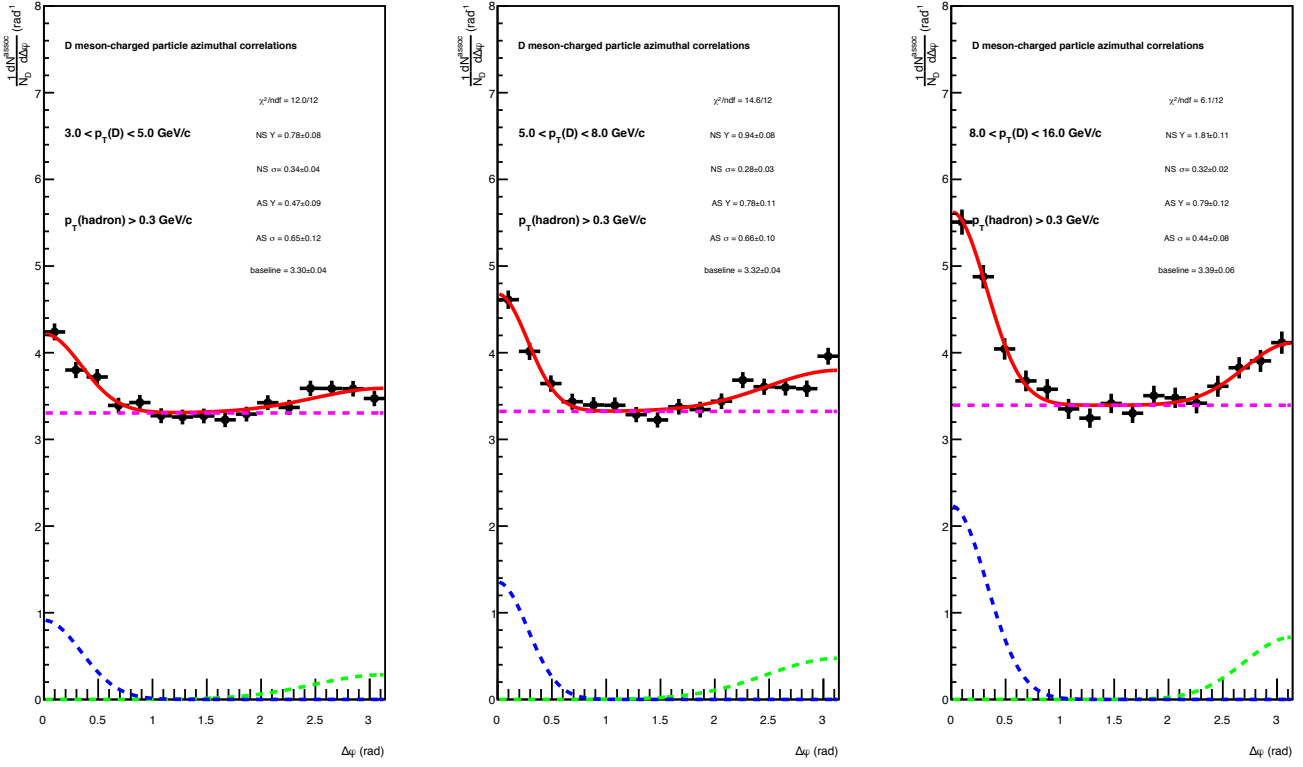


Figure 5.19: Example of fit to azimuthal correlation distributions and baseline estimation.

default transverse region) on top and on bottom of its statistic uncertainty. This helps to account, though in a systematic uncertainty, for the statistical uncertainty on the baseline position (since in the fit the baseline is constrained, and its error is not propagated to the other observables).

- The envelope between (i) the RMS of the relative variations of the parameters between the fit outcomes defined in the first two points, and (ii) the relative variations of the parameters from the fit outcomes defined in the third point, is considered as systematic uncertainty for the near-side and away-side widths.
- For the estimation of the baseline and of the near side associated yield, that value is added in quadrature with the correlated systematics in the correlation plot. In case of the near side width this is not the case, since it is not affected by the different normalization.

$$\sigma^{syst} = \sqrt{(Max(\Delta par^{ped.mode}, \Delta par^{\Delta point}))^2 + (\sigma_{syst}^{corr})^2} \quad (5.6)$$

Figures 5.20, 5.21, 5.22, 5.23, 5.24 present the near-side associated yield, width, away-side asso-

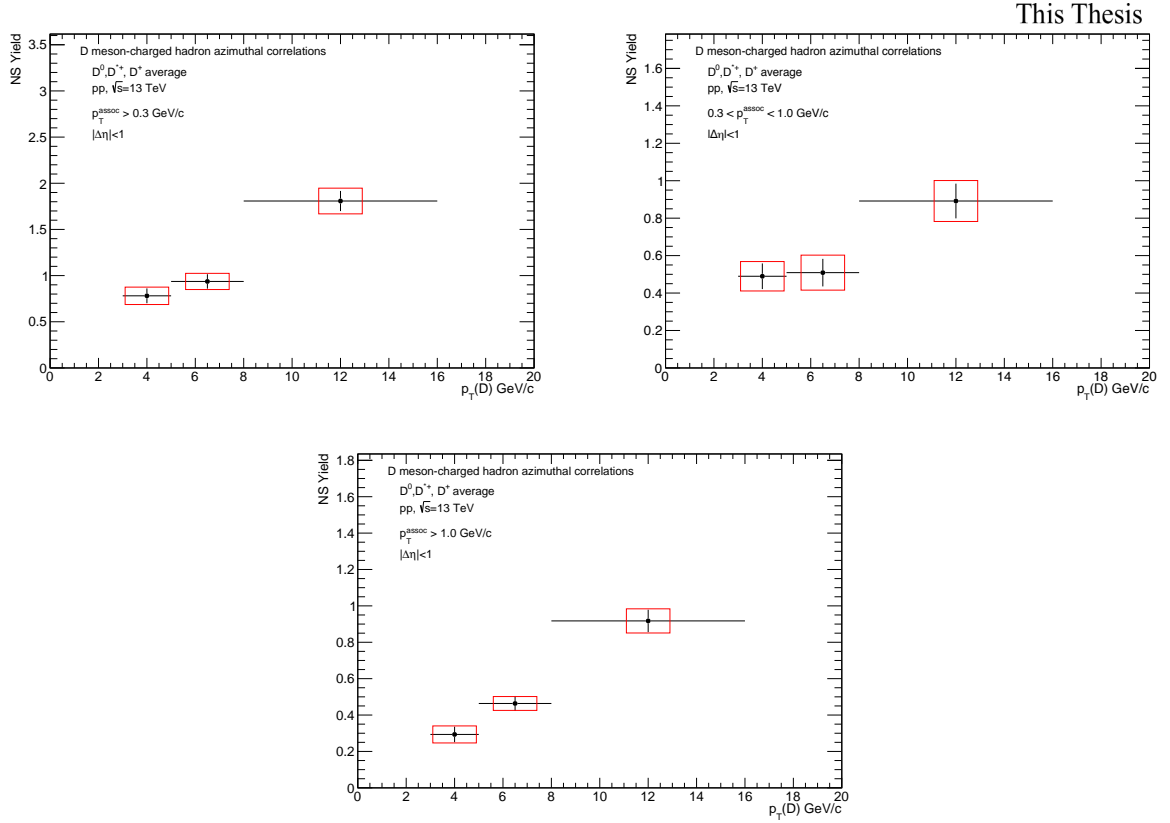


Figure 5.20: Near-side yield $p_T(D)$ trend for the D-meson average, extracted from fit to the azimuthal correlation distributions, for all the analyzed kinematic ranges of associated track p_T .

ciated yield, width (the sigma of the Gaussian part of the fit functions) and the height of the baseline respectively, for the average correlation distributions, in the kinematic ranges studied in the analysis.

5.2.3 Final results

Comparison with pp $\sqrt{s}=7$ TeV and pPb $\sqrt{s_{NN}}=5.02$ TeV results

The baseline subtracted correlation plots for average D^0 , D^+ D^{*+} is compared among three cases i.e. pp 7 TeV, pp 13 TeV and pPb 5.02 TeV and shown in figure 5.25. Figure 5.26 shows the comparison plots for near-side yield and width. The figures show that the results are similar within uncertainties revealing the fact that there is similar charm-jet properties for three different collision systems.

Comparison with models

A comparison of average correlation distributions (baseline subtracted) between D meson and charged particles in the pp collisions at $\sqrt{s}=13$ TeV is shown in figure 5.27 with the expectations from Monte-Carlo simulations (Pythia6-Perugia0, Pythia6-Perugia2010, Pythia6-Perugia2011 and Pythia8). The

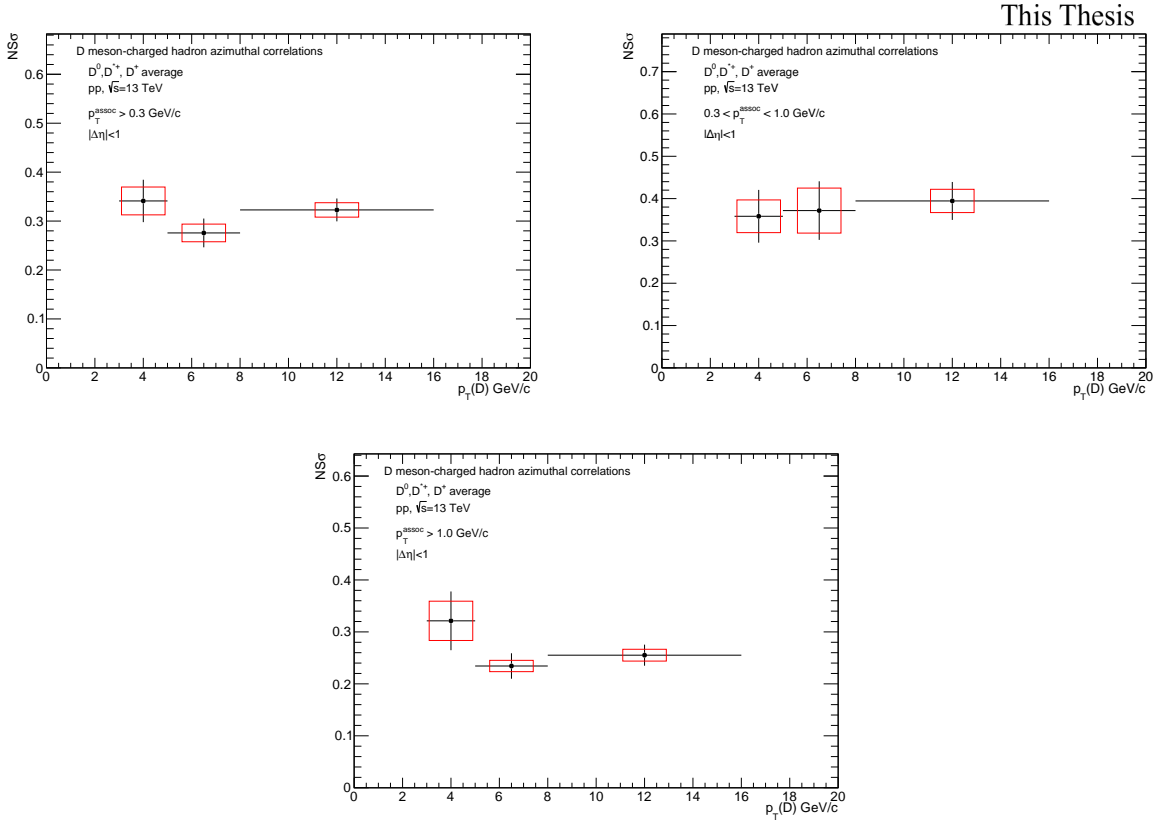


Figure 5.21: Near-side sigma $p_T(D)$ trend for the D-meson average, extracted from fit to the azimuthal correlation distributions, for all the analyzed kinematic ranges of associated track p_T .

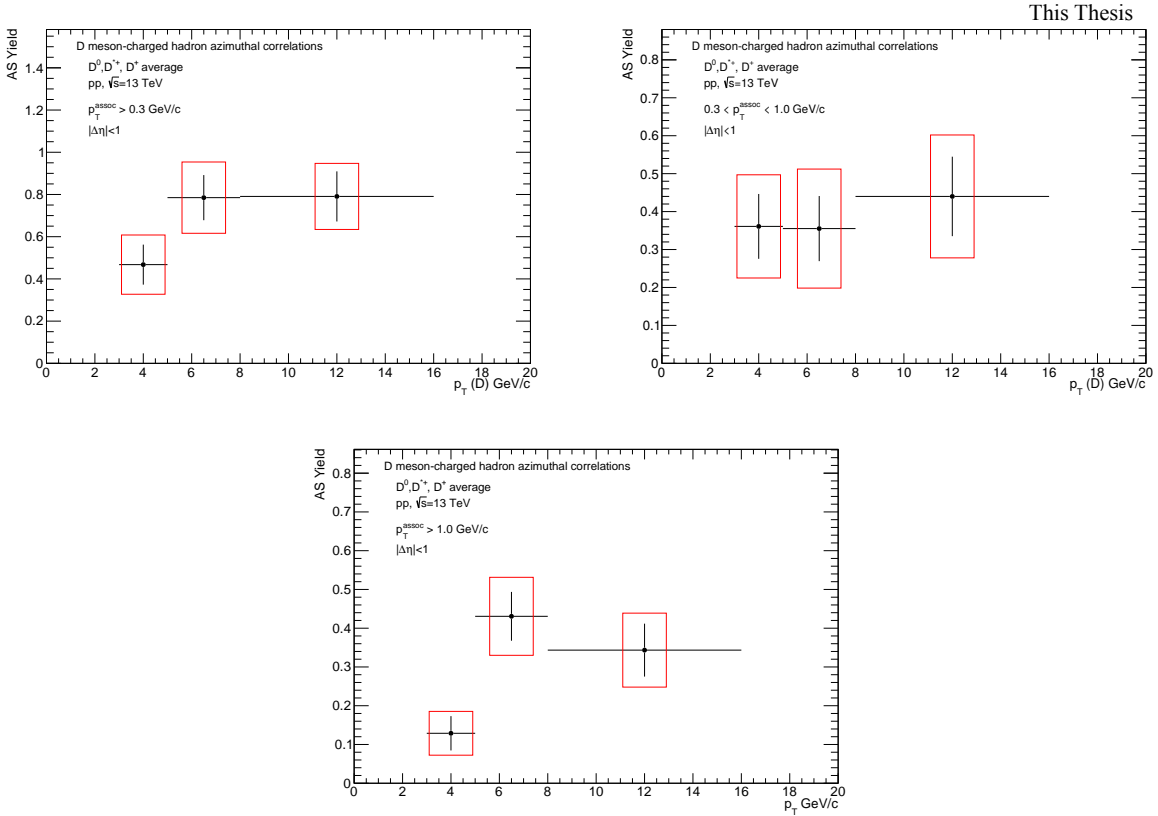


Figure 5.22: Away-side yield $p_T(D)$ trend for the D-meson average, extracted from fit to the azimuthal correlation distributions, for all the analyzed kinematic ranges of associated track p_T .

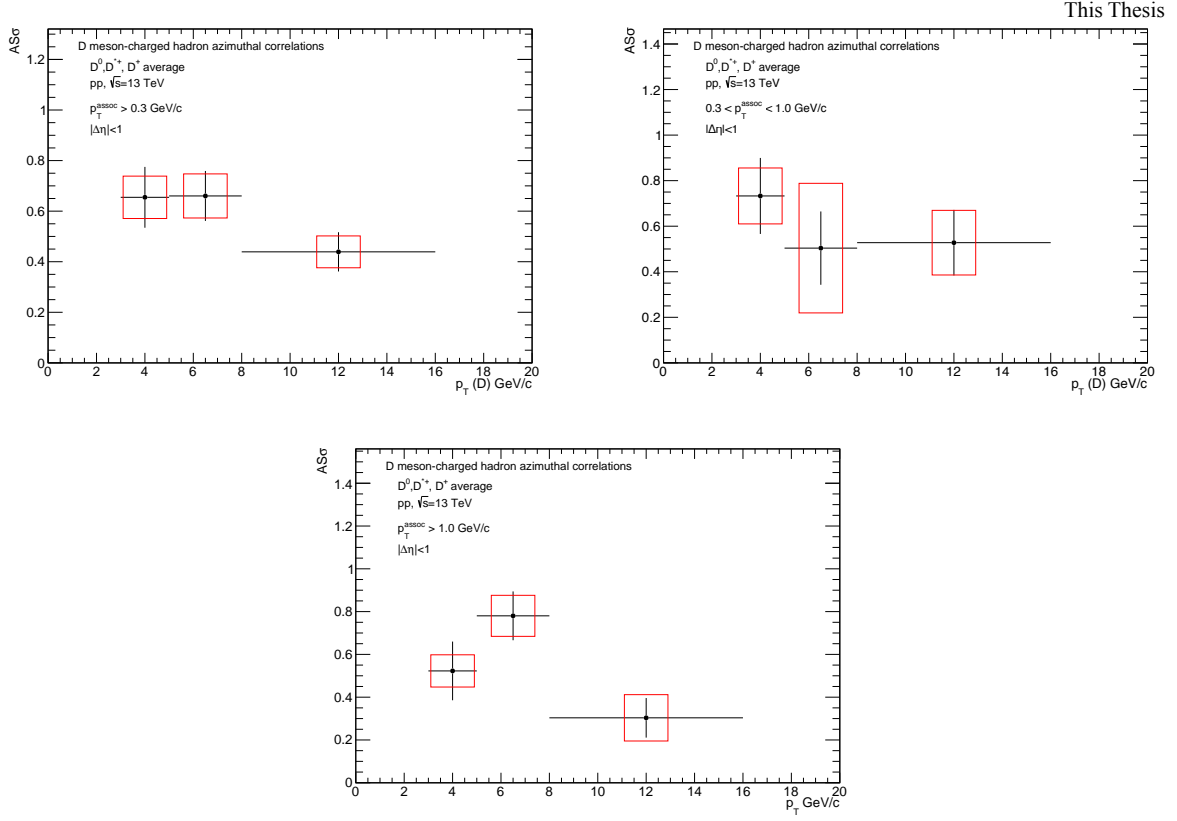


Figure 5.23: Away-side sigma $p_T(D)$ trend for the D-meson average, extracted from fit to the azimuthal correlation distributions, for all the analyzed kinematic ranges of associated track p_T .

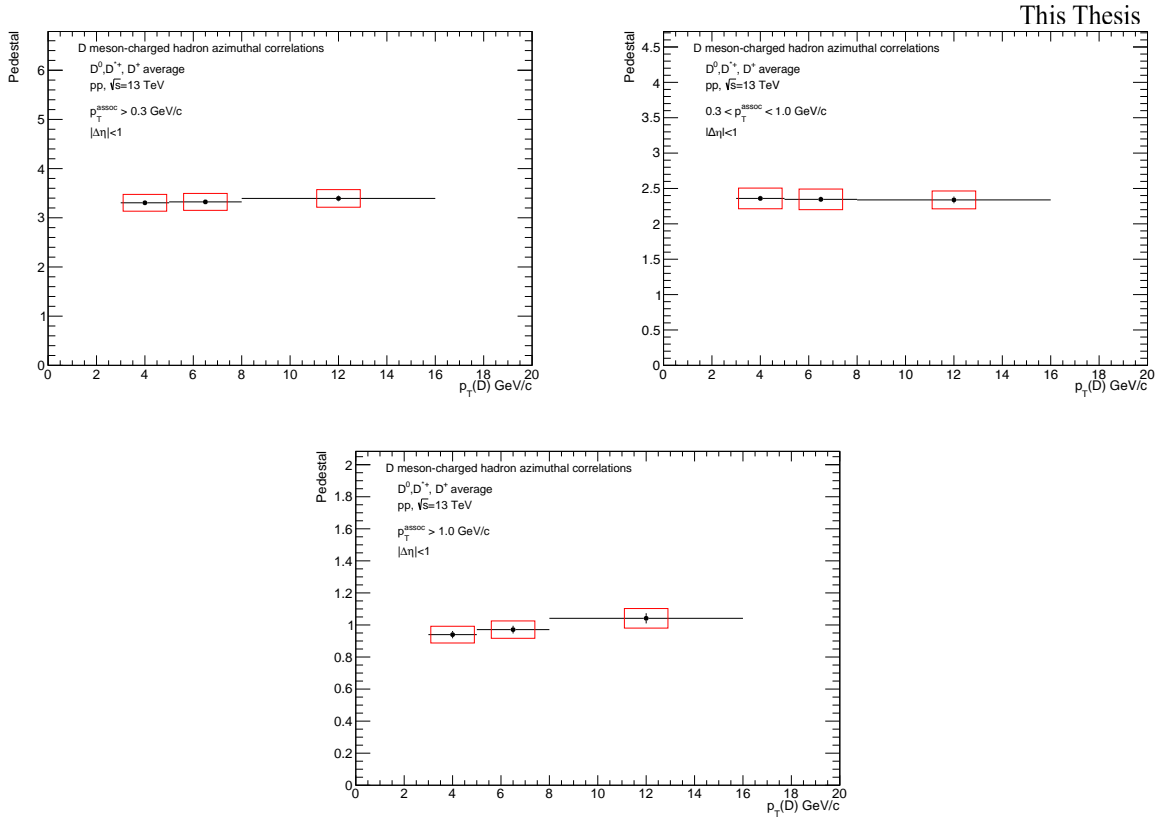


Figure 5.24: Baseline height for the D-meson average, extracted from fit to the azimuthal correlation distributions, for all the analyzed kinematic ranges of associated track p_T .

This Thesis

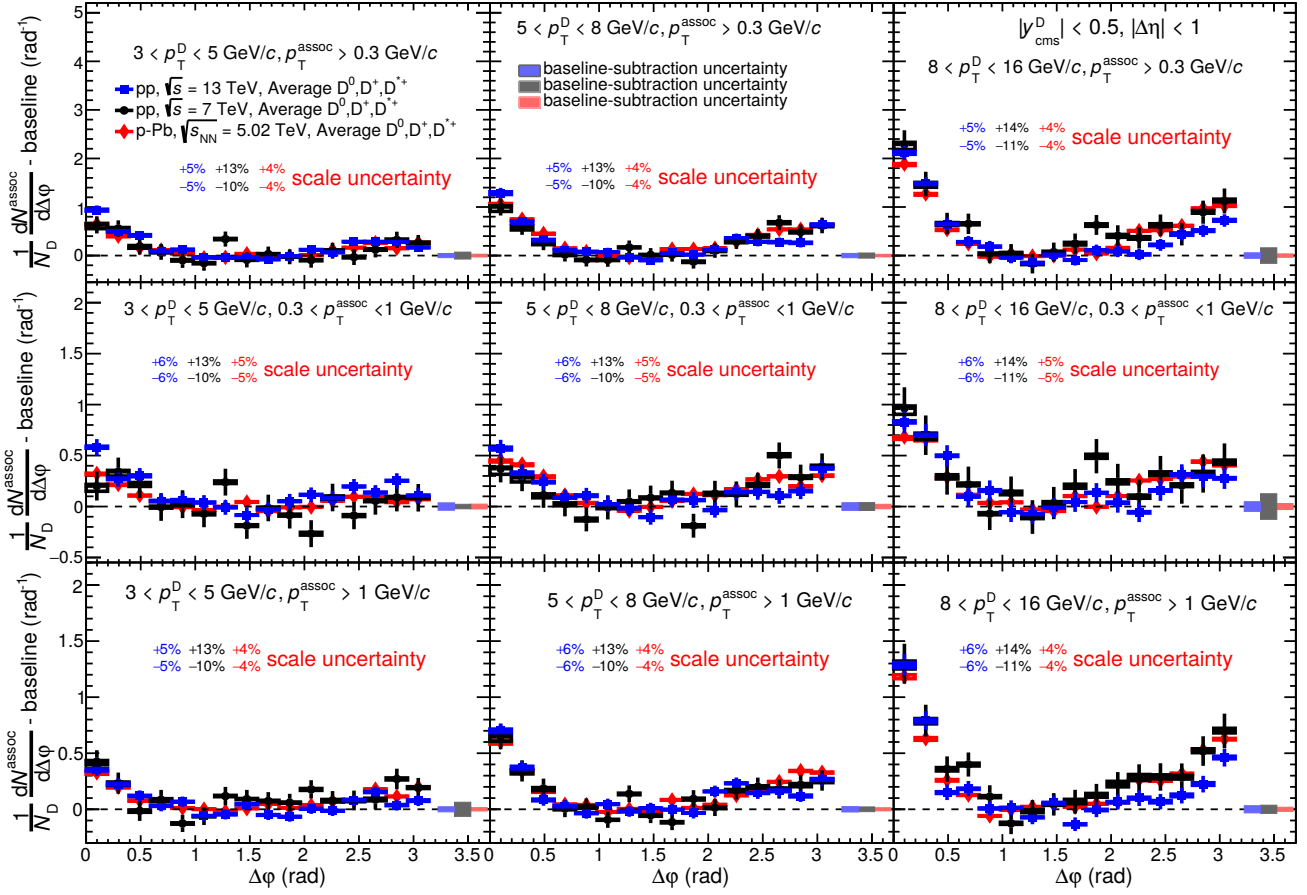


Figure 5.25: Two-particle azimuthal correlations between D mesons and charged particles: comparison among pp 7 TeV, 13 TeV and pPb 5.02 TeV data.

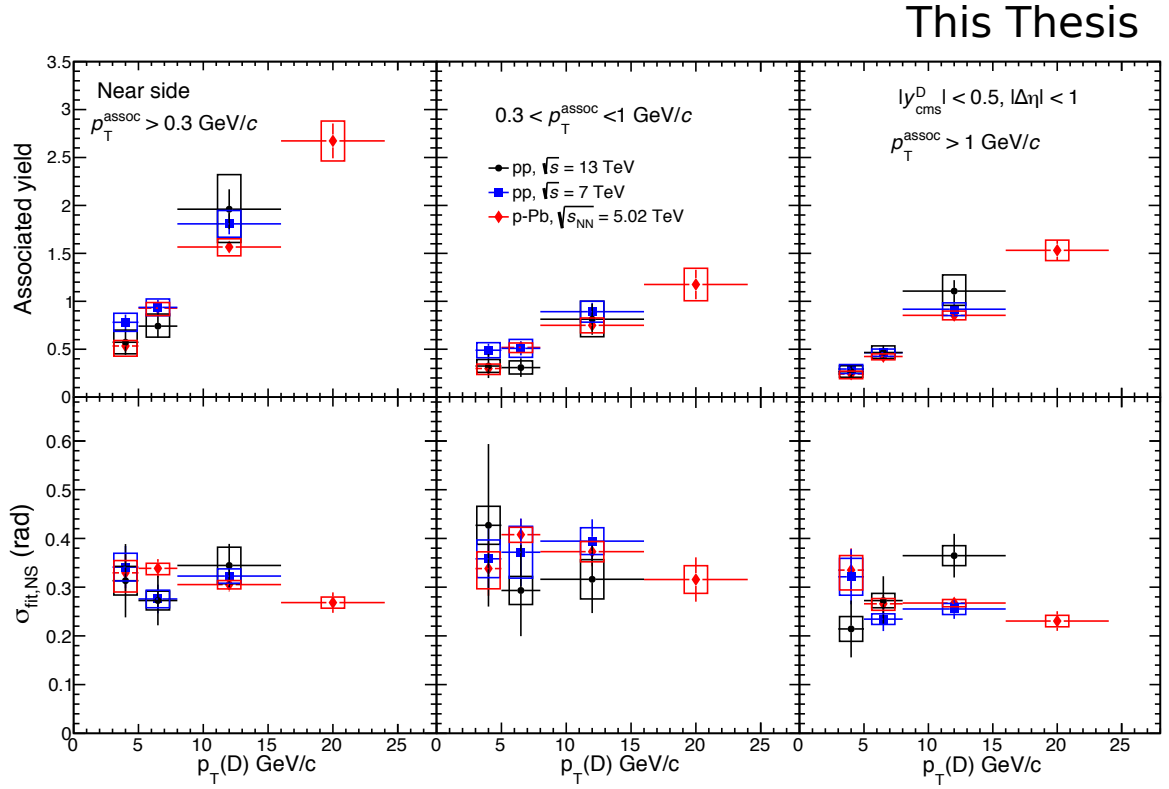


Figure 5.26: Near-side physical observables: comparison among pp 7 TeV, 13 TeV and pPb 5.02 TeV data.

shape of the correlation distributions is well reproduced by all the models, together with their p_T trend and with the evolution of the correlation peaks.

Figures 5.28 and 5.29 show the same comparison for the fit observables (peak yields and widths for near-side and away-side, respectively), for all the addressed p_T ranges.

This Thesis

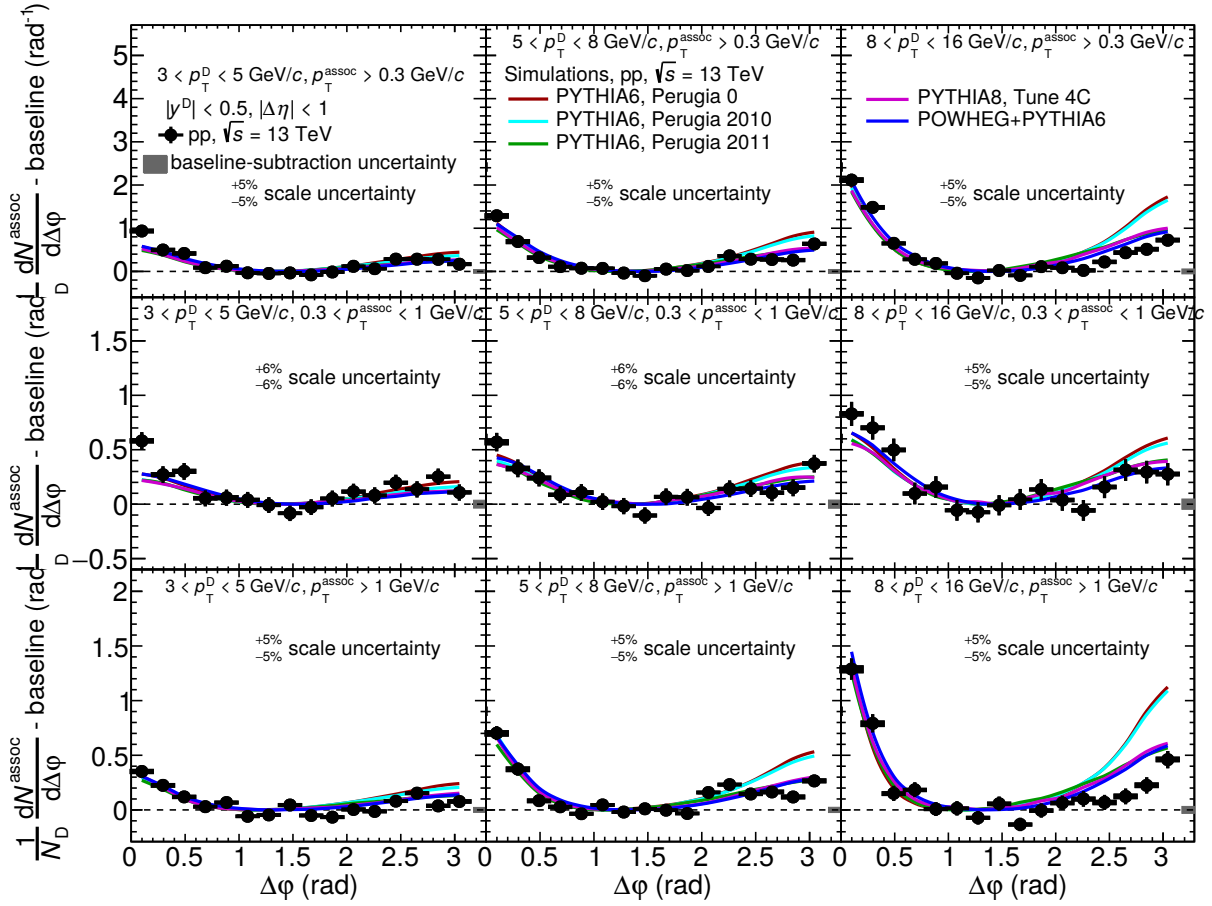


Figure 5.27: Two particle azimuthal correlations between D mesons and charged particles : comparison of pp 13 TeV data with different Monte-Carlo models.

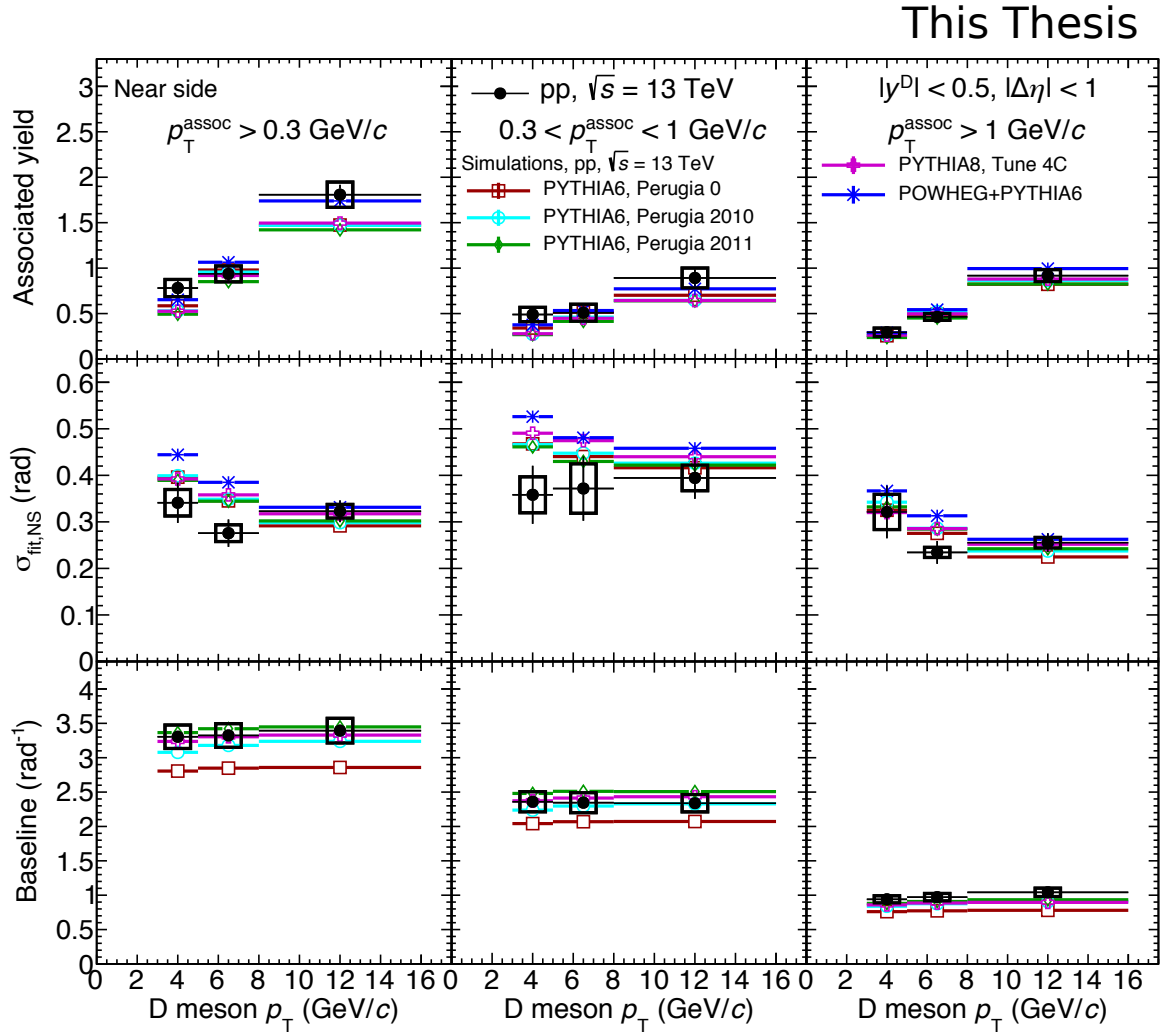


Figure 5.28: Near-side physical observables : comparison of pp 13 TeV data with different Monte-Carlo models.

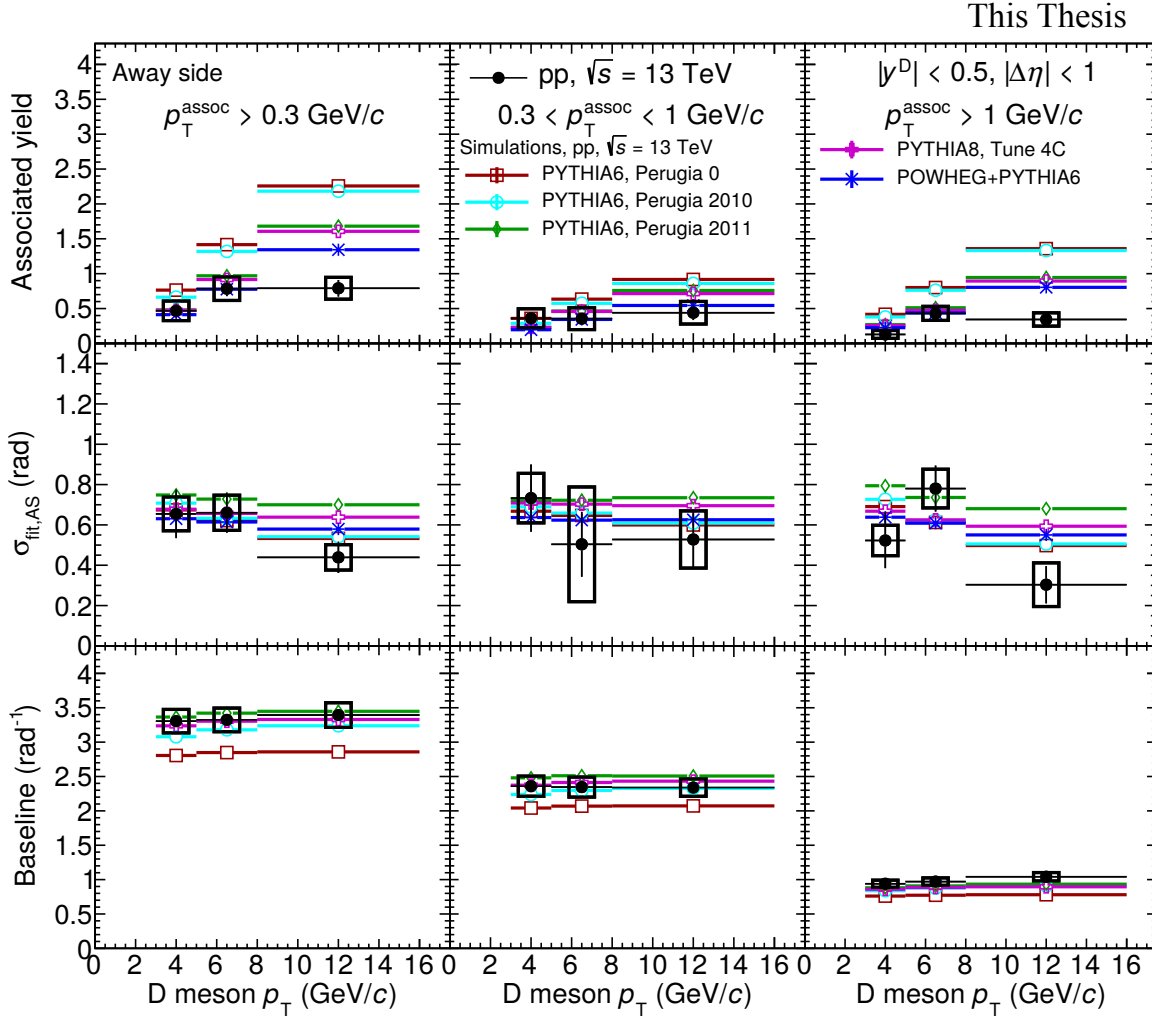


Figure 5.29: Away-side physical observables : comparison of pp 13 TeV data with different Monte-Carlo models.

Chapter 6

Study of small systems with hydro-based simulated events

In this chapter, we present the results of analysis of simulated pp and pPb events, generated by the EPOS3 Monte-Carlo event generator. Aiming to understand the anomalous particle production mechanism in high-multiplicity events of these small systems at the LHC energies, as already discussed, the generated events from the hydro-based event generator was analysed in terms of several observables as a function of multiplicity and matched with existing data.

6.1 High multiplicity events of small systems: An experimental review

6.1.1 pp collisions

Recent LHC results in small systems provide some anomalous features in particle production which lead us to study the high-multiplicity events in pp and pPb collisions and explain the possible reason of signals which resembles the formation of the hydrodynamic medium in heavy-ion collisions. The most important signature of “collectivity” in small systems is the “ridge”-like structure in long-range two-particle azimuthal correlations. It was first reported in pp collisions at $\sqrt{s} = 7$ TeV by CMS collaboration [90]. The two-particle angular correlation function is defined by the per-trigger associated yields of charged particles obtained from $\Delta\eta, \Delta\varphi$ distribution (where $\Delta\eta$ and $\Delta\varphi$ are the differences in the pseudo-rapidity (η) and azimuthal angle (φ) of the two particles) and is given by:

$$\frac{1}{N_{trig}} \frac{d^2 N_{assoc}}{d\Delta\eta d\Delta\varphi} = B(0, 0) \times \frac{S(\Delta\eta, \Delta\varphi)}{B(\Delta\eta, \Delta\varphi)} \quad (6.1)$$

where N_{trig} is the number of trigger particles in the specified $p_T^{trigger}$ range.

The function $S(\Delta\eta, \Delta\varphi)$ is the differential measure of per-trigger distribution of associated hadrons in the same-event, i.e.,

$$S(\Delta\eta, \Delta\varphi) = \frac{1}{N_{trig}} \frac{d^2 N_{same}^{assoc}}{d\Delta\eta d\Delta\varphi} \quad (6.2)$$

The background distribution function $B(\Delta\eta, \Delta\varphi)$ is defined as:

$$B(\Delta\eta, \Delta\varphi) = \frac{d^2 N^{mixed}}{d\Delta\eta d\Delta\varphi} \quad (6.3)$$

where N^{mixed} is the number of mixed event pairs.

The factor $B(0,0)$ in equation. 6.1 is used to normalize the mixed-event correlation function such that it is unity at $(\Delta\eta, \Delta\varphi)=(0,0)$.

The correlation measurement is done in the range of $\Delta\varphi = -\pi/2$ to $3\pi/2$. The near-side (NS) correlation peak is formed in the range $\Delta\varphi = -\pi/2$ to $\pi/2$ representing the trigger and associated particles in the same side of the jet, while the away-side (AS) correlation peak is formed in the range $\Delta\varphi = \pi/2$ to $3\pi/2$ representing the trigger and associated particles from two opposite sides of the jet.

Depending on the selection of $|\Delta\eta|$ region, the correlation distributions are categorized by “short-range” ($|\Delta\eta| \approx 0$) and “long-range” ($|\Delta\eta| \gg 0$) correlations. The back-to-back short-range jet correlation gets smeared due to fragmentation process and medium effects which affects the away-side peak. In long-range correlation, the away-side structure comes due to momentum conservation and other effects while the near-side structure is attributed to the medium formation. In this case, a “ridge” structure is occurred in small $|\Delta\varphi|$ and wide $|\Delta\eta|$ region, which is basically a soft particle (low p_T) phenomena. The “ridge” structure is found in CuCu [167] and AuAu [167, 168, 169] collisions at RHIC energies and PbPb collisions [63, 64] at LHC energies. The hydrodynamic collective flow of a strongly interacting and expanding medium [66, 67, 68] is expected to be responsible for the “ridge”-like structure in the relativistic heavy ion systems.

Figure 6.1 shows the near-side ridge-like structure in long-range two particle azimuthal correlations for high multiplicity pp events at $\sqrt{s} = 7$ TeV with two different transverse momentum ranges $p_T > 0.1$ GeV/c and $1 < p_T < 3$ GeV/c. It is clear from the figure that the ridge structure is visible

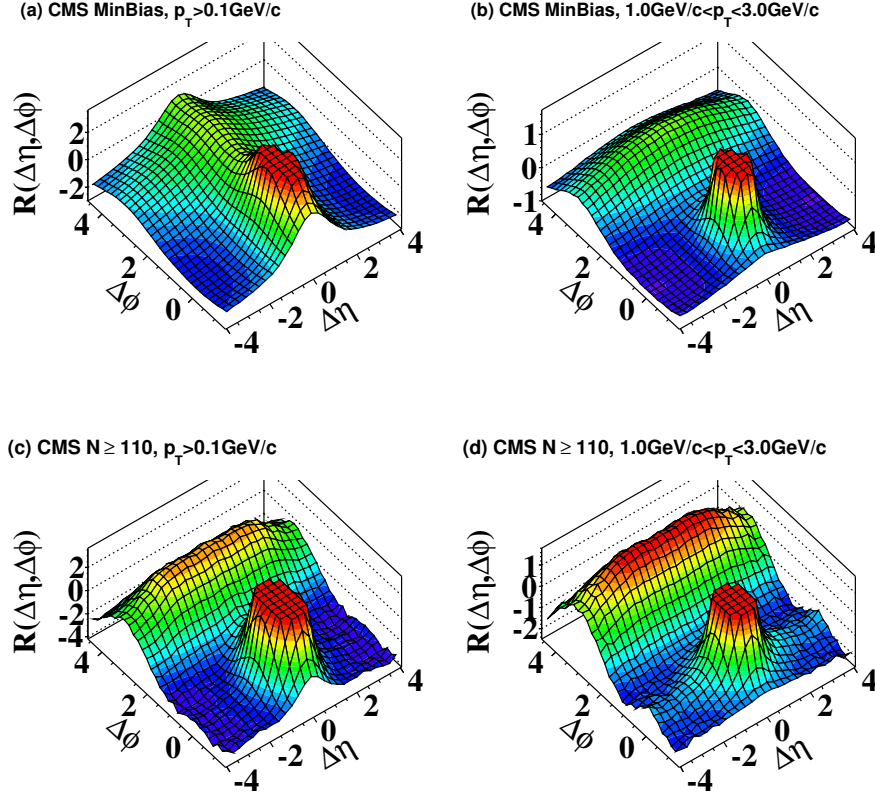


Figure 6.1: Two-particle azimuthal correlations as a function of $\Delta\eta$, $\Delta\phi$ in pp collisions at $\sqrt{s} = 7$ TeV: minimum bias events (upper panel), high multiplicity events (lower panel) [90].

only at a region of intermediate p_T i.e. $1 < p_T < 3$ GeV/c and high multiplicity events i.e $N \geq 110$.

Same study has been done for pp $\sqrt{s} = 13$ TeV by CMS collaboration [91]. In figure 6.2, the long-range near-side associated yield has been shown as a function of p_T (fig. 6.2(a)) and multiplicity (fig. 6.2(b)). It is clear from the figure that the yield peaks at $1 < p_T < 2$ GeV/c for multiplicity ≥ 105 (≥ 110 for pp 7 TeV) for both the centre-of-mass energies. From the multiplicity dependence of of near-side associated yield, it is shown that the yield value is consistent with zero (determined by ZYAM method) for low multiplicity events. After multiplicity ≥ 40 , the yield value increases with almost linear trend revealing the presence of ridge-like correlations. The gluon saturation model [170] as well as the hydrodynamic models describe the data qualitatively, however fails to explain quantitatively. In this thesis, we will show results of EPOS3 hydrodynamic model which describe the inclusive charged particle p_T spectra both qualitatively and quantitatively, but fails to describe other observables qualitatively.

The Fourier harmonics of azimuthal anisotropy, i.e., the elliptic flow (v_2) and triangular flow (v_3) are obtained from the two-particle long-range azimuthal correlations and these help to strengthen the claim of hydrodynamic origin of the long-range correlations. Some experimental studies have

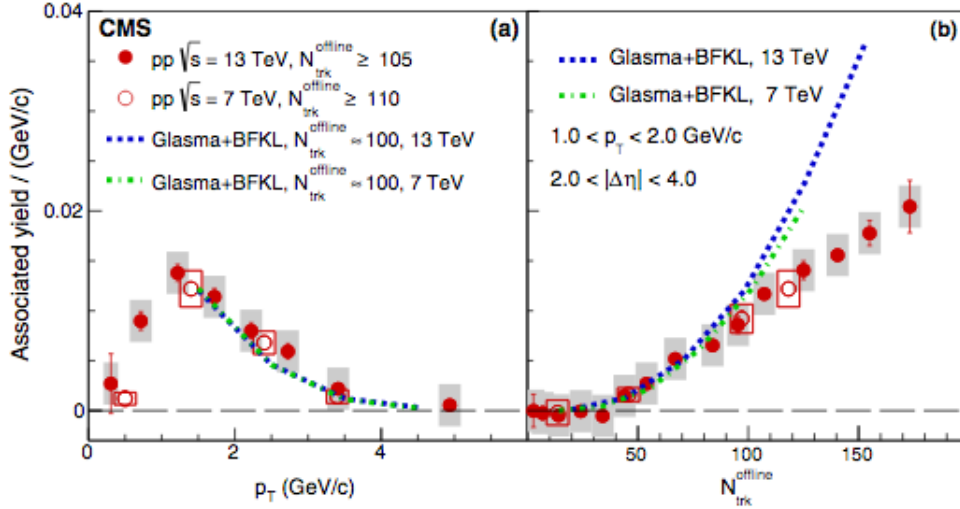


Figure 6.2: Near-side long-range associated yield as a function of (a) transverse momentum, (b) multiplicity for pp $\sqrt{s}=7$ TeV and 13 TeV measured by CMS experiment [91]. Curves represent the predictions of the gluon saturation model [170].

been done for both pp $\sqrt{s} = 7$ TeV and 13 TeV to extract elliptic flow coefficient v_2 for all charged particles, its p_T dependence [95] and mass ordering of $v_2(p_T)$ for identified charged particles [92].

The CMS experiment has extracted the v_2^{sub} and v_3^{sub} values from two- and multi-particle correlations of identified and inclusive charged particles for different multiplicity classes in pp collisions at $\sqrt{s} = 5, 7$ and 13 TeV. These Fourier harmonics from long-range azimuthal correlations are subtracted from the contribution of short-range correlations. Figure 6.4 shows the multiplicity dependence of v_2^{sub} and v_3^{sub} values in pp collisions compared with pPb and PbPb collisions at $\sqrt{s_{NN}} = 5$ and 2.76 TeV respectively. From the figure, it is clear that both v_2^{sub} and v_3^{sub} values in pp collisions follow similar trend as in pPb and PbPb collisions. Though v_2^{sub} values for pp collisions are smaller than the pPb and PbPb collisions, v_3^{sub} values for all three collision systems are comparable.

Some experimental studies have been done for both pp $\sqrt{s} = 7$ TeV and 13 TeV to extract elliptic flow coefficient v_2 of charged particles, its p_T dependence [95]. The mass ordering of $v_2(p_T)$ of identified charged particles [92] also confirms the formation of collective medium.

Figure 6.3 shows similar v_2 values for inclusive charged particles, K_s^0 and $\Lambda/\bar{\Lambda}$ across most of the p_T region within statistical uncertainties while there is a clear difference in v_2 among different species for high multiplicity events [92]. The v_2 for identified particles are consistently below the inclusive charged particle which reveals stronger azimuthal anisotropy for lighter particles as the inclusive charged particles are mostly consisted with pions. The similar trend has been found from RHIC data for heavy-ion collisions [171, 172].

Along with the azimuthal anisotropy, the collective behaviour in pp collisions are also found

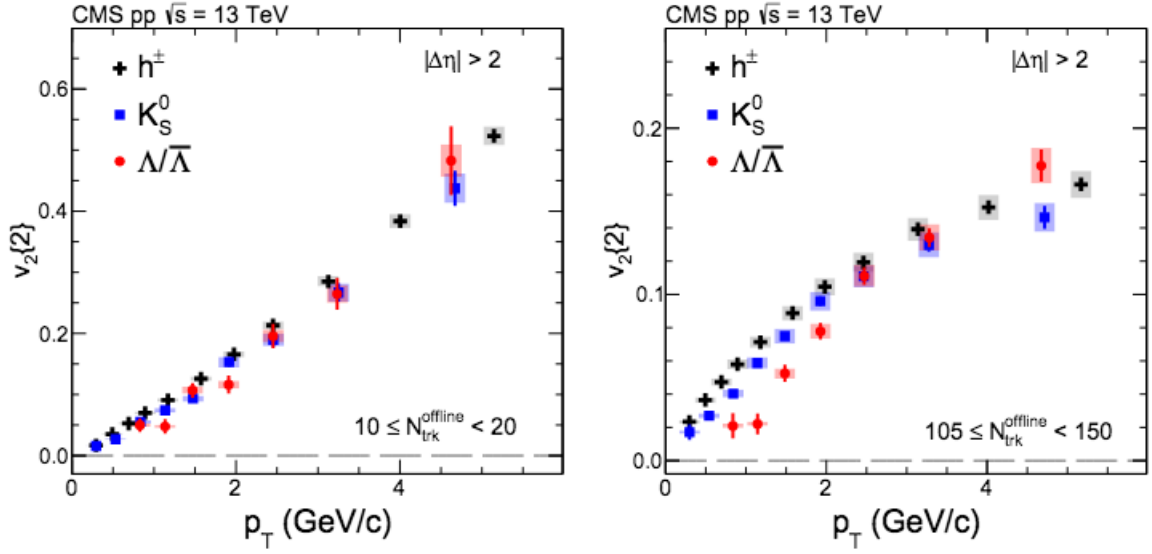


Figure 6.3: The elliptic flow measurement of inclusive charged particles, K_s^0 and $\Lambda/\bar{\Lambda}$ as a function of transverse momentum for pp $\sqrt{s} = 13$ TeV measured by CMS experiment [92].

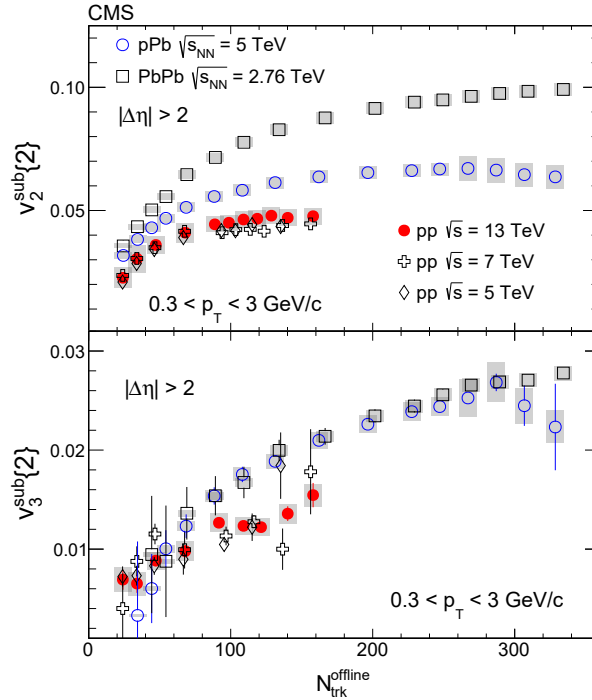


Figure 6.4: The $v_2^{sub}\{2\}$ and $v_3^{sub}\{2\}$ of charged particles as a function of charged particle multiplicity $N_{trk}^{offline}$ in pp collisions at $\sqrt{s} = 5, 7$ and 13 TeV, pPb collisions at $\sqrt{s_{NN}} = 5$ TeV, and PbPb collisions $\sqrt{s_{NN}} = 2.76$ TeV, after correcting for back-to-back jet correlations estimated from low-multiplicity data [92].

in terms of strong transverse radial flow extracted from the identified charged particle yields by hydrodynamics-motivated Boltzmann - Gibbs blast-wave (BGBW) model [97]. This model does not include a full hydrodynamic calculation and assumes instantaneous freeze-out of all the particle species at a kinetic freeze-out temperature (T_{kin}) and with common transverse radial flow velocity ($\langle\beta\rangle$) from the freeze-out surface of a locally thermalized system, expanding with a common velocity field. A brief description of this model is given in section 6.3.2.

The p_T spectra of the RHIC heavy ions data [173, 174] is successfully described by BGBW model and the parameters T_{kin} and $\langle\beta\rangle$ have been extracted by the simultaneous fit to the p_T spectra of pions, kaons and protons for a p_T -range up to 1.2 GeV/ c . A centrality and energy dependence study has been performed [174] for AuAu collisions that reveals that the $\langle\beta\rangle$ increases and the T_{kin} decreases with both the centrality and the centre-of-mass energy of collisions. Though the fitting of transverse mass spectra of pions, kaons and protons with a thermal model from central heavy-ion collisions data at fixed-target experiments at SPS energies - 200 A GeV SS and 158 A GeV PbPb provided evidence of collective transverse flow [175], the multiplicity dependent study of pp data at $\sqrt{s} = 200$ GeV at RHIC analysis could not find any appreciable values of T_{kin} and $\langle\beta\rangle$ through the blast-wave analysis.

The CMS experiment has measured p_T -spectra [176] of pions (π^\pm), kaons (K^\pm), and protons (p and \bar{p}) over the rapidity range $|y| < 1$ for the pp collisions at $\sqrt{s} = 0.9, 2.76$ and 7 TeV with different multiplicity classes, in the pseudorapidity interval, $|\eta| < 2.4$. The analysis has been performed on the p_T - ranges 0.1 to 1.2 GeV/ c for π^\pm , 0.2 to 1.050 GeV/ c for K^\pm and 0.35 - 1.7 GeV/ c for p and \bar{p} . The analysis [96] of the multiplicity dependent identified particle spectra data extracted values for β and T_{kin} compared with those for AA and pA data, as shown in figure 6.5.

The simultaneous fits with the BGBW description to the transverse momentum spectra of π^\pm , K^\pm and $p(\bar{p})$ in high multiplicity pp events at $\sqrt{s} = 0.9, 2.76$ and 7 TeV at LHC gives appreciable values of T_{kin} and β indicating the formation of collective medium in high-multiplicity events in pp collisions at LHC energies. We can find a similar trend of T_{kin} and β as a function of multiplicity to that for the heavy-ion collisions where the formation of thermalized partonic medium is established.

One of the most commonly measured parameter is $T_{effective}$, the inverse slope parameter obtained from fitting the transverse mass (m_T) spectra by equation:

$$\frac{dN}{m_T dm_T} = C \exp\left(-\frac{m_T}{T_{effective}}\right) \quad (6.4)$$

Increase in the inverse slope parameter with mass m for pions (π^\pm), kaons (K^\pm), and protons (p and \bar{p}), already observed in heavy-ion collisions [177, 175], attributes to the collective transverse flow

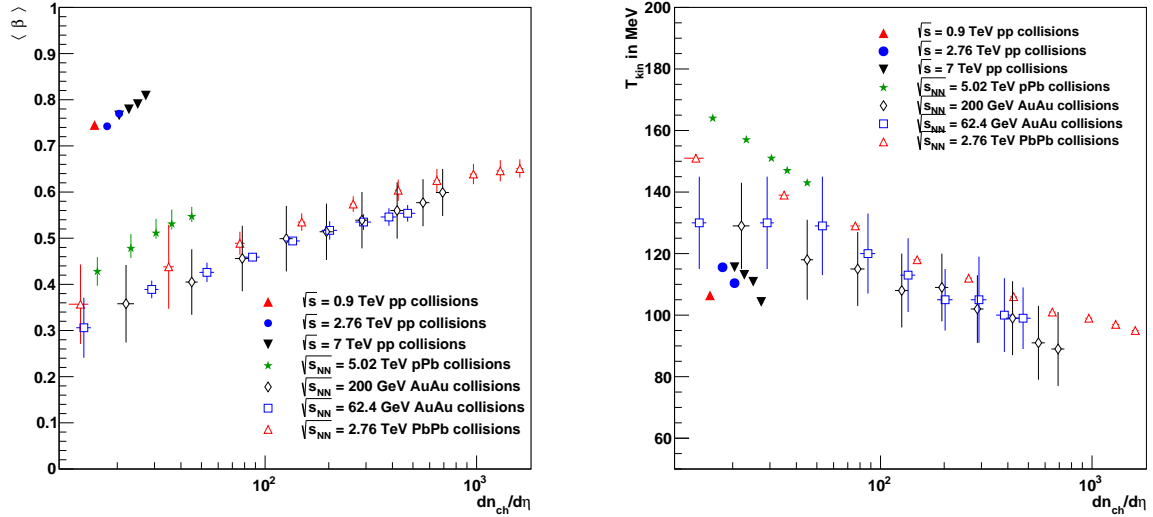


Figure 6.5: The \sqrt{s} and centrality ($dn_{ch}/d\eta$) dependence of mean transverse radial velocity ($\langle \beta \rangle$) and kinetic-freezeout temperature (T_{kin}), as obtained by simultaneous fits in the BGBW framework to the published spectra of π^\pm , K^\pm and $p(\bar{p})$ in pp collisions at LHC is compared with results from similar analysis for AuAu collisions at RHIC [174], PbPb and pPb collisions at LHC energies [96].

of the medium formed in the collision. The same increasing trend is found in high multiplicity pp collisions at $\sqrt{s} = 7$ TeV as shown in figure 6.6.

6.1.2 pPb collisions

Similar to pp collisions, the collective natures are found in pPb collisions also reported by LHC [179, 180]. The long-range ridge-like structures are found for high multiplicity or most central events in the intermediate p_T range.

Figure 6.7 shows the comparison of near-side long range associated yield of pp, pPb and PbPb systems for different centre-of-mass energies in $1 < p_T < 2$ GeV/c as a function of multiplicity. Here also, the ridge-like correlation is visible for all the three systems at multiplicity ≥ 40 . For a given multiplicity, the yield in pp collisions is around 10% and 25% of those observed in PbPb and pPb collisions respectively revealing a strong system-size dependence.

The ALICE experiment has reported the results of double-ridge structure (both in near and away side) in pPb collisions [94] as shown in figure 6.8. To remove the contribution of correlation from jets, the low multiplicity correlation distributions are subtracted from high multiplicity distributions. In this figure, the two dimensional correlation distributions are shown by considering identified trigger particle and inclusive associated charged particles in intermediate p_T range. By fitting the one-

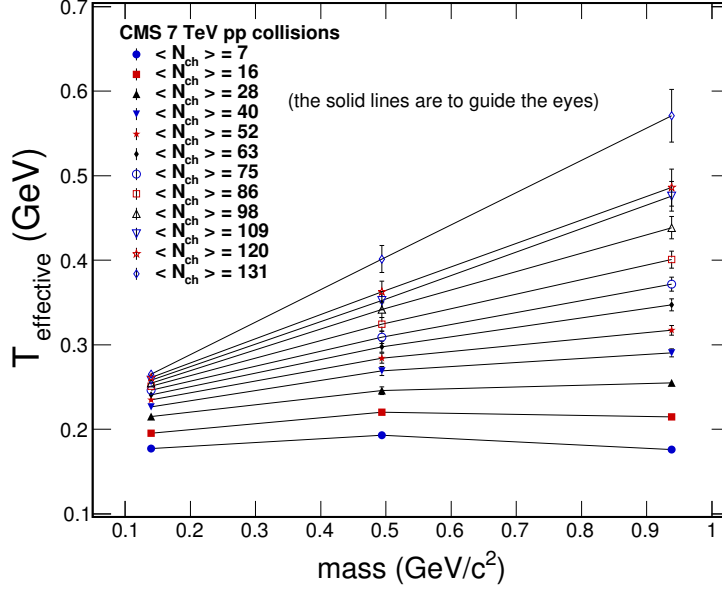


Figure 6.6: The inverse slope parameter $T_{effective}$ as a function of mass of identified particles ($m_{\pi^\pm} = 0.14$, $m_{K^\pm} = 0.495$, $m_{p(\bar{p})} = 0.938 \text{ GeV}/c^2$) as obtained from the measured transverse momentum spectra from non-single diffractive events of pp collisions as measured by the CMS experiment [176] at $\sqrt{s} = 7 \text{ TeV}$. $\langle N_{ch} \rangle$ is the mean multiplicity of the charged particles. The lines in the figure are drawn connecting the points just to guide the eyes. The figure has been published in Ref. [178].

dimensional $\Delta\varphi$ projection of correlation spectra, the elliptic flow v_2 is obtained as shown in figure 6.9 where the mass ordering is visible similar to that found in PbPb collisions [181]. The elliptic and triangular flow pattern is observed for charged particles in pAu, dAu and $^3\text{HeAu}$ at $\sqrt{s_{NN}}=200 \text{ GeV}$ [182] which is reported to be well described by hydrodynamic models which includes the formation of a short-lived QGP droplet.

Another important signature of QGP formed by heavy-ion collisions is studied by taking identified charged particle ratio which has been reported by ALICE for pPb collisions also [183]. Figure 6.10 shows the particles ratios K/π , p/π and Λ/K_s^0 from pPb $\sqrt{s_{NN}} = 5.02 \text{ TeV}$ as a function of p_T for most central and peripheral collisions. Results are compared with PbPb collisions at $\sqrt{s_{NN}} = 2.76 \text{ TeV}$ [184, 185] and a qualitative agreement is found on the enhancement of particle ratios at intermediate p_T . A similar enhancement of p/π ratio is observed in RHIC energies [186].

The different features of collectivity found in high multiplicity / most central pp and pPb collisions in LHC energies, lead us to study the multiplicity dependent pp collisions further, more specifically, to focus on the high-multiplicity or most central events pp and pPb collisions to understand the origin of collectivity in small systems.

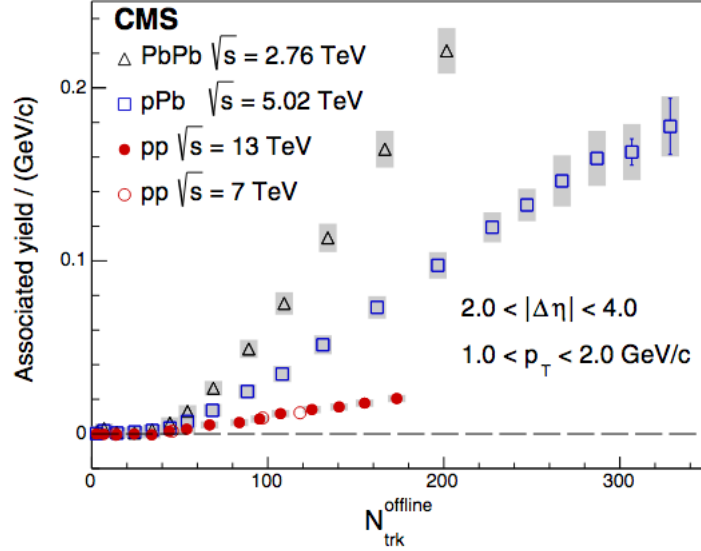


Figure 6.7: Near-side long-range associated yield as a function of multiplicity for pp $\sqrt{s}=7$ TeV and 13 TeV, pPb $\sqrt{s_{NN}}=5.02$ TeV and PbPb $\sqrt{s_{NN}}=2.76$ TeV data measured by CMS experiment [91].

6.2 Event generation with EPOS3

“EPOS” stands for **E**nergy conserving quantum mechanical approach, on an basis of **P**artons, parton ladders, strings, **O**ff-shell remnants and **S**plitting of parton ladders. This model works on the parton-based Gribov-Regge theory [187]. A detail technical description on the parameters used in this model can be found in [188]. In this model, an individual parton scattering, known as “pomeron”, gives rise to a parton ladder which is considered as a longitudinal colour field of “flux-tube” and carries the transverse momentum of the hard scattering. The parton ladders consist of hard perturbative QCD (pQCD) scatterings along with initial-state and final-state parton emission. The flux tubes are expanded and fragmented into string segment of quark-antiquark pairs. In the case of many elementary parton-parton hard scatterings in a collision, a large number of flux tubes are formed leading to a high local string-segment density, and subsequently high multiplicity of the collisional event. In the hydrodynamic EPOS3 model, the high local string-segment density, above a critical value, constitutes the bulk matter or a medium. The string segments that do not have enough energy to escape from the bulk matter form the “core” which gets thermalized and undergoes (3+1D) viscous hydrodynamical evolution with a lattice-QCD-complied crossover equation of state. The hydrodynamical evolution is followed by particle production via the Cooper-Frye mechanism. After that, the hadronic evolution takes place and the “soft” (low- p_T) hadrons freeze out. The string segments from outside the bulk matter form the “corona”. The string segments in the “corona” hadronize via the Schwinger mechanism and escape as “high”- p_T jet hadrons. The string segments

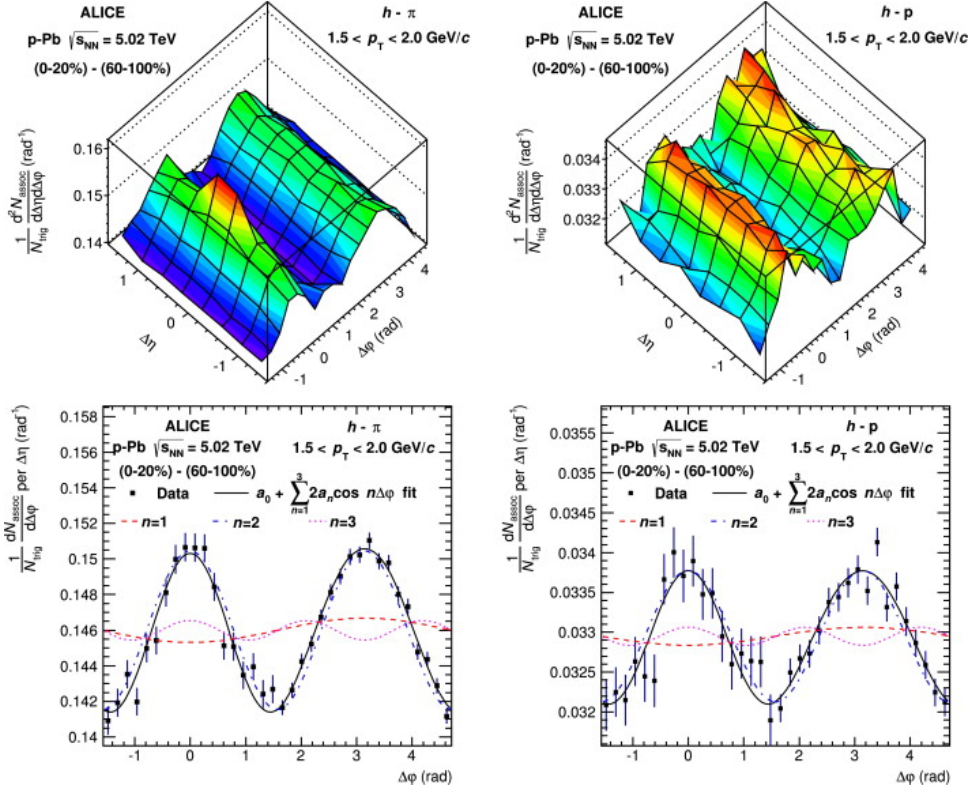


Figure 6.8: Top panels: The $(\Delta\eta, \Delta\phi)$ correlation distribution of $h-\pi$ (left) and $h-p$ (right) of pPb collisions at $\sqrt{s_{\text{NN}}} = 5.02$ TeV measured by ALICE. Bottom panels: $\Delta\phi$ projections of top panels [94].

carrying enough energy to escape the bulk matter constitute the “semi-hard” or intermediate- p_T particles. These segments, while escaping the bulk matter, pick up quarks or antiquarks from within the bulk matter, and the intermediate- p_T hadrons thus produced in this process inherit the properties of the bulk matter. After hadronization, the hadron-hadron re-scattering is modeled via ultra-relativistic quantum molecular dynamics (UrQMD).

Using EPOS3.107 code, we have generated 40 million minimum-bias events in pp collisions at $\sqrt{s} = 7$ and 13 TeV and 10 million minimum-bias events in pPb collisions at $\sqrt{s_{\text{NN}}} = 5.02$ TeV with and without implementing hydrodynamics. Suitable subsamples of different multiplicity and centrality classes and different kinematic cuts are selected from the simulated minimum-bias event samples.

6.3 Analysis in pp collisions

We have reproduced the inclusive charged-particle p_T spectra for pp $\sqrt{s} = 7$ TeV [189] and 13 TeV [190] with EPOS3 hydro events as shown in figure 6.11. From the figure it is clear that data is well described by EPOS3 model. We use the same event sample for further differential study. The analysis in pp collisions is performed in terms of experimental observables that exhibit the flow-like

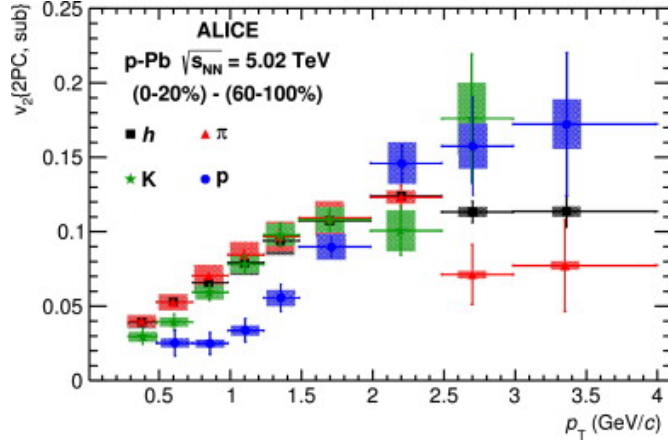


Figure 6.9: Elliptic flow v_2 as a function of transverse momentum for pPb $\sqrt{s_{NN}}=5.02$ TeV measured by ALICE [94].

behaviour in high-multiplicity events, namely,

- Long-range two-particle azimuthal correlations among charged particles.
- Blast-wave description of identified charged particle yield.
- Mean transverse momentum ($\langle p_T \rangle$) as a function of mean charged particle multiplicity ($\langle N_{ch} \rangle$).
- Inverse slope parameter of transverse mass (m_T) distribution.

6.3.1 Long-range two-particle azimuthal correlations

The ridge-like two-particle long-range angular correlation is found to be an important signal of collectivity in small systems, as already discussed. In models, using “flux-tube+hydro” approach [182], a qualitative agreement is found with data. In spite of the successes of the hydrodynamic approach in qualitative description, a quantitative comparison with the data is essential, particularly to access how the hydrodynamic description, implemented in EPOS, works better than the non-hydrodynamic models [191, 192] including the reasonably well understood particle production mechanism in the pQCD inspired multi-parton interaction (MPI) model, like the one implemented in PYTHIA Monte Carlo Code [157].

The analysis tool for two-particle azimuthal correlations is already discussed in chapter 4. The per-trigger associated yields of charged particles obtained from $(\Delta\eta, \Delta\varphi)$ distribution (where $\Delta\eta$ and $\Delta\varphi$ are the differences in the pseudo-rapidity (η) and azimuthal angle (φ) of the two particles) and is given in equation 6.1.

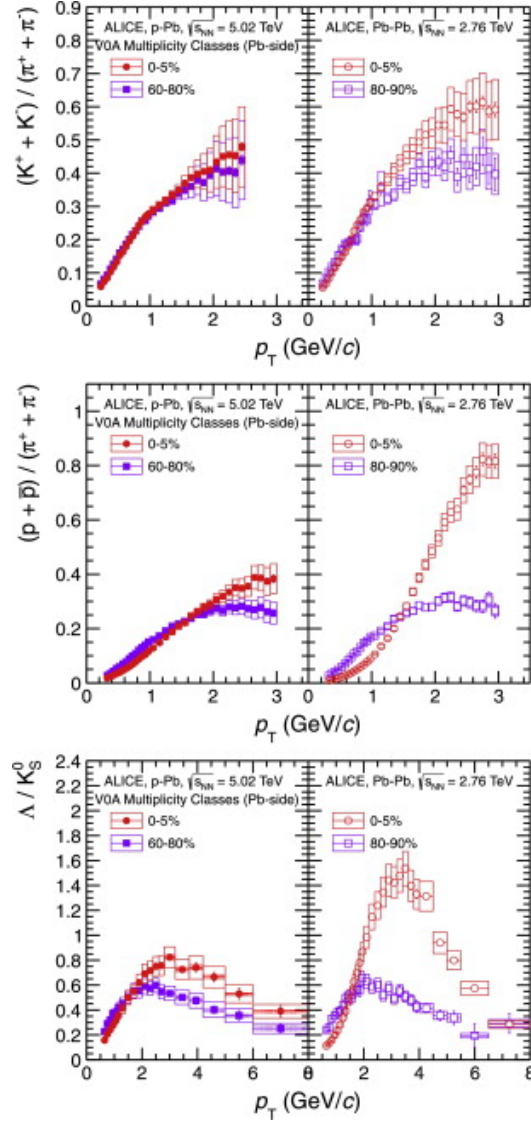


Figure 6.10: Identified charged particle ratios K/π (top), p/π (middle) and Λ/K_s^0 (bottom) for pPb and PbPb collisions with $\sqrt{s_{NN}} = 5.02$ TeV and 2.76 TeV respectively for most central and peripheral event classes [183].

The two-particle azimuthal correlations study helps us to extract several sources of correlations in multiparticle production, depending on the studied ranges of $|\Delta\eta|$ and the p_T for the trigger and the associated particles. In the context of the present study, the correlated emission of particles from collective medium can be extracted by studying the long-range ($|\Delta\eta| \gg 0$) two-particle azimuthal angle correlations. In relativistic heavy-ion collisions, the long-range two-particle azimuthal angle correlations are attributed to the formation of collective medium [167, 167, 168, 169, 63, 64]. The correlated pair yields per trigger with small $|\Delta\varphi|$ over a wide range of $|\Delta\eta|$ (long-range), result a “ridge” structure in the constructed correlation functions. The analysis [91] of LHC pp data in terms of correlated yields as a function $|\Delta\varphi|$ reveals that the “ridge”- structure becomes prominent in pp collisions with increasing multiplicity of events. It is the near-side ($|\Delta\varphi| \sim 0$) long-range correla-

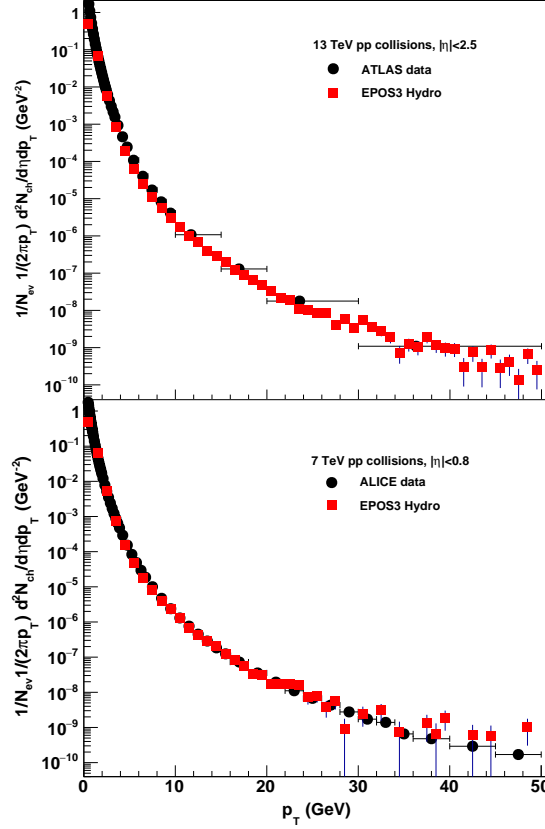


Figure 6.11: Inclusive charged particles p_T spectra from generated minimum-bias events of pp collisions at $\sqrt{s}=7$ and 13 TeV from the EPOS3 event generator, with hydrodynamic calculations, are compared with data, as measured by the ALICE [189] (lower panel) and ATLAS [190] (upper panel).

tions, that are of particular interest for the present study of quantitative comparison of data and the hydrodynamic simulation of multi-particle production in high-multiplicity pp events.

The long-range two-particle angular correlations of the charged particles have been constructed in simulated events, keeping the kinematic cuts and multiplicity classes similar as chosen for analysis of the data at reference [91] for $\sqrt{s} = 7$ and 13 TeV. As expected from a hydrodynamic code of particle production like the EPOS3-hydro, the long-range two-particle azimuthal correlations of charged particles show a prominent ridge-like structure for high-multiplicity events, while such structure is absent in low-multiplicity events. In figure 6.12 we have shown representative plots of two-particle correlation function for $1 < p_T^{\text{trigger}}, p_T^{\text{associated}} < 2$ GeV/ c with unidentified charge particle as trigger, for the hydrodynamic-EPOS3 generated pp collisions at $\sqrt{s} = 7$ TeV for events of multiplicity-classes $N_{ch} > 110$ and $N_{ch} < 35$, after removing the short-range jet-like correlations. The per trigger associated yield, for high-multiplicity event class, in different p_T -intervals, for both the non-hydrodynamic and hydrodynamic EPOS3 generated pp collisions at $\sqrt{s} = 7$ and 13 TeV are projected onto $\Delta\varphi$ and

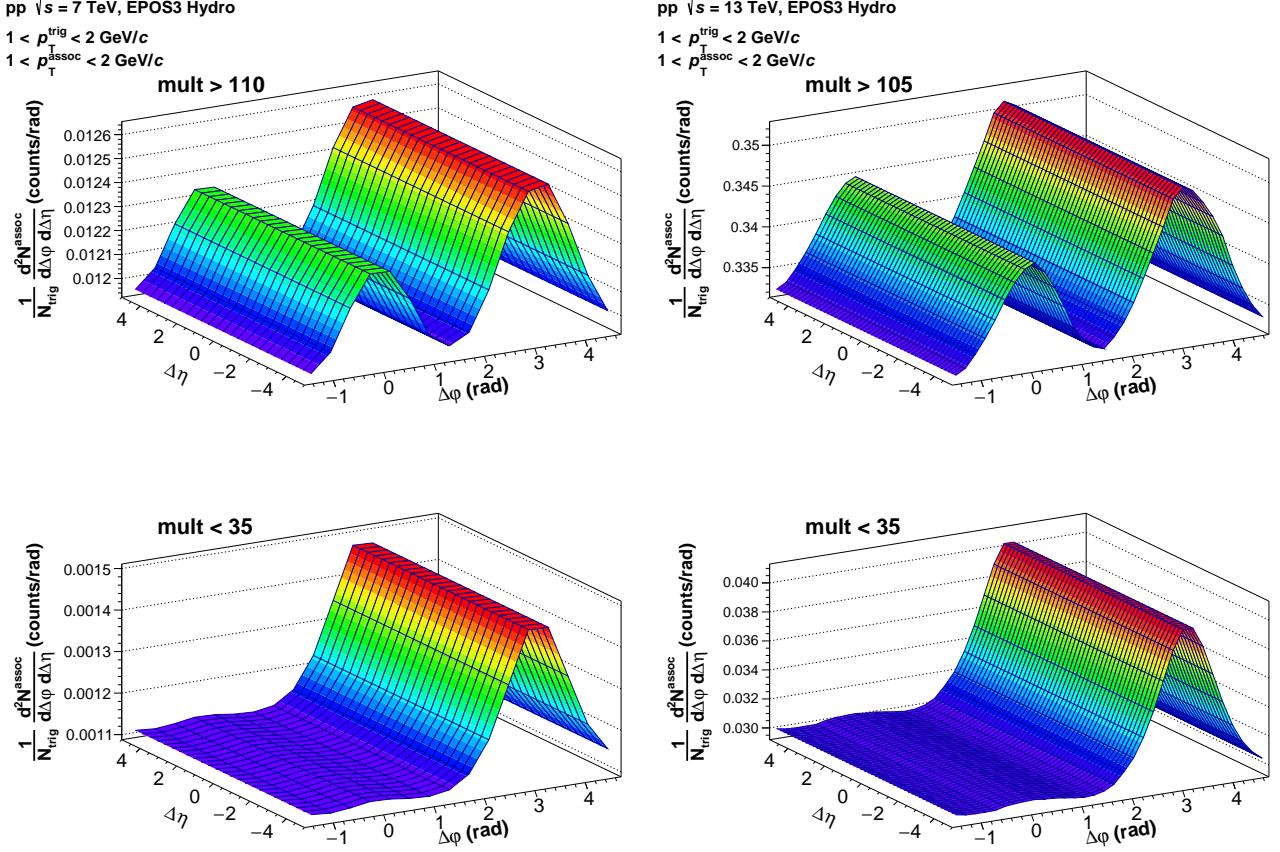


Figure 6.12: Two particle $\Delta\eta, \Delta\phi$ charge particle correlation function for $1 < p_T^{\text{trigger}}, p_T^{\text{associated}} < 2$ GeV/c with unidentified charged particle as trigger, for the hydrodynamic-EPOS3 generated pp collisions at $\sqrt{s} = 7$ TeV (left column) and 13 TeV (right column) for events of multiplicity-class $N_{ch} > 110$ (upper panel) and $N_{ch} < 35$ (lower panel). The short-range correlations have been suppressed for clear presentation of the long-range correlations

shown in the figure 6.13, to compare the data in the same kinematic ranges.

The appearance of ridge-like structure in long-range two-particle angular correlations of charged particles in the high-multiplicity EPOS3-hydro generated pp events at $\sqrt{s} = 7$ and 13 TeV reflects the collective property, that is expected in a hydrodynamic model of particle production. The correlated yields of high-multiplicity event class as a function of $\Delta\phi$ for different p_T intervals in the simulated events reveals similar feature as observed in data i.e., the ridge-like structure is most prominent in the 1-2 GeV/c p_T -range and in the highest-multiplicity events and gradually decreases with increasing p_T . Nevertheless, as it is clear in the figure 6.13, for the most prominent p_T -range of 1-2 GeV/c, the EPOS3 events overestimate the correlated yields as compared to the data.

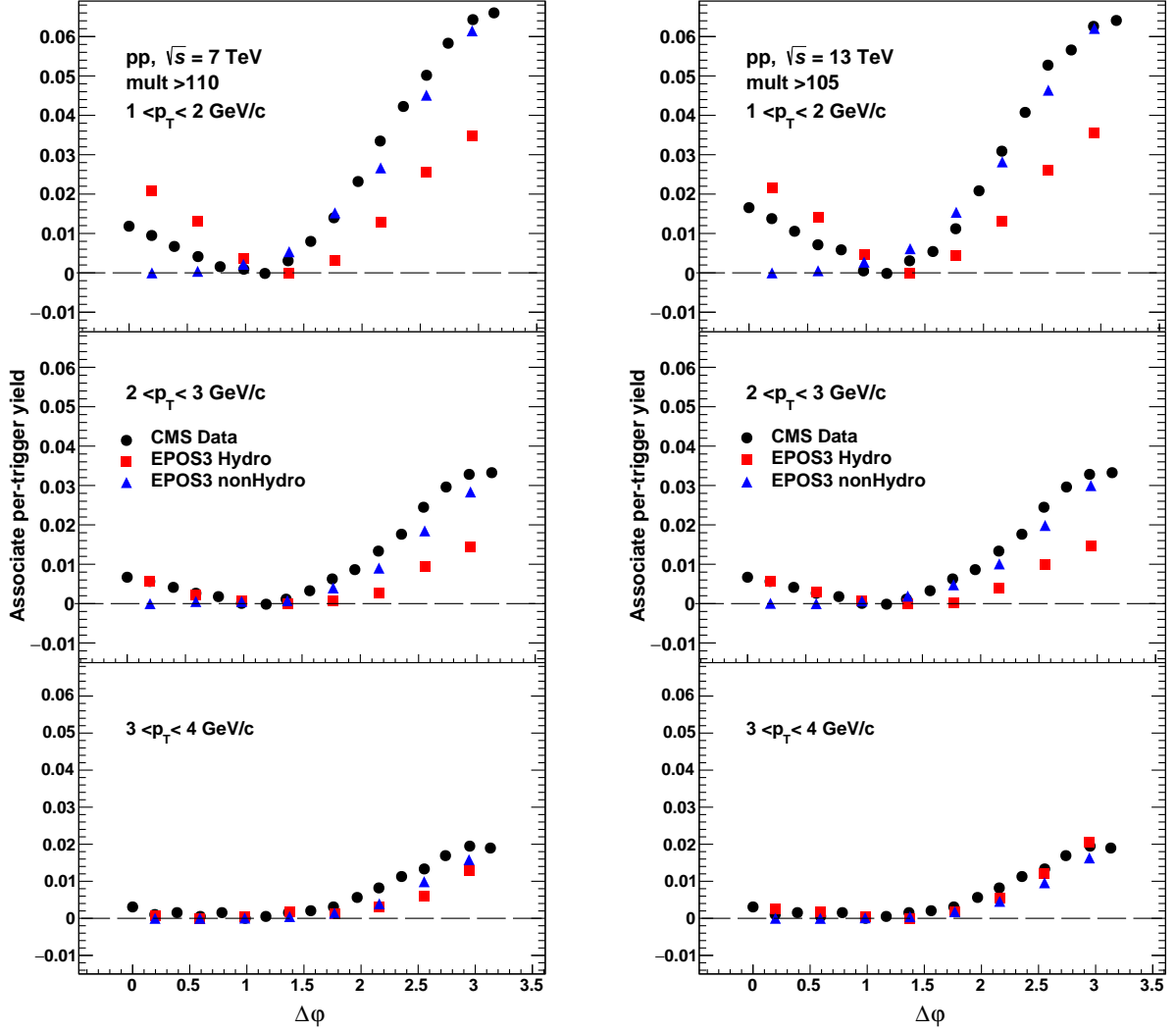


Figure 6.13: One dimensional $\Delta\phi$ projection for high-multiplicity events for the region of ridge-like correlations obtained from the long-range two-particle azimuthal correlations of charged particles, averaged over $2 < |\Delta\eta| < 4$, for $1 < p_T^{\text{trigger}}, p_T^{\text{associated}} < 2 \text{ GeV}/c$, $2 < p_T^{\text{trigger}}, p_T^{\text{associated}} < 3 \text{ GeV}/c$ and $3 < p_T^{\text{trigger}}, p_T^{\text{associated}} < 4 \text{ GeV}/c$ from the data and the EPOS3 generated events of pp collisions at $\sqrt{s} = 7$ [90] and 13 TeV [91].

6.3.2 Blast-wave description of identified charged particle yield

To study the collective transverse radial flow in pp collisions, we have followed a hydrodynamic-motivated Boltzmann-Gibbs blast-wave (BGBW) model [97], which is already well-established in heavy-ion collisions. This model considers the produced particles to be in locally thermalized state inside the system, which expands collectively with a common velocity field. The model does not include hydrodynamic evolution but considers that the system undergoes an instantaneous common freeze-out at a kinetic freeze-out temperature (T_{kin}) and a transverse radial flow velocity (β) at the freeze-out surface. The BGBW, thoroughly used in analyzing the relativistic heavy-ion collisions data, revealed [96] transverse radial flow for high-multiplicity pp collisions [176] data, also.

Assuming the hard-sphere particle source of uniform density, the transverse momentum spectra, in the BGBW model, is given by,

$$\frac{dN}{p_T dp_T} \propto \int_0^R r dr m_T \mathbf{I}_0 \left(\frac{p_T \sinh \rho}{T_{kin}} \right) \mathbf{K}_1 \left(\frac{m_T \cosh \rho}{T_{kin}} \right) \quad (6.5)$$

where $\rho = \tanh^{-1} \beta$, \mathbf{I}_0 and \mathbf{K}_1 are modified Bessel functions.

The flow velocity profile is given by,

$$\beta = \beta_s \left(\frac{r}{R} \right)^n \quad (6.6)$$

where β_s is the surface velocity and r/R is the relative radial position in the thermal source. The average transverse flow velocity, $\langle \beta \rangle$ is given by, $\langle \beta \rangle = \frac{2}{(2+n)} \beta_s$.

The EPOS3 generated pp events following hydrodynamics are expected to exhibit the radial flow. Thus, using the BGBW formalism, we have compared the radial flow parameters quantitatively for the EPOS3 generated events and the data. The Chi-square (χ^2) test has been used to ensure goodness of fit while obtaining the fit-parameters, the kinetic freeze-out temperature and the radial flow velocity, from the data spectra as well as from the EPOS3 generated spectra. In this analysis, we keep lower p_T - cut at 0.475 GeV/c for spectra of all the species. At the higher side, the p_T -range is limited to $p_T < 2$ GeV/c or less, depending on the availability of the data.

We calculate R for different event classes with different $\langle N_{ch} \rangle$ in $|\eta| < 2.4$ in this study, from the relation, $R(\langle N_{ch} \rangle) = a \cdot \langle N_{ch} \rangle^{1/3}$ where $a = 0.597 \pm 0.009(stat.) \pm 0.057(syst.)$ fm at 0.9 TeV and $a = 0.612 \pm 0.007(stat.) \pm 0.068(syst.)$ fm, as parameterized [176] by the CMS experiment from the measurement of radius of source of emission as a function of average charged particle multiplicity for pp collisions at $\sqrt{s} = 7$ TeV. The BGBW fit parameters are available [96] for different multiplicity classes of pp collisions at $\sqrt{s} = 7$ TeV [176]. We fit the blast-wave function to the p_T spectra for different sets of data for $\sqrt{s} = 13$ TeV [193], keeping the kinetic freeze-out temperature (T_{kin}), the radial flow velocity (β_s) and the exponent (n) of the flow velocity profile free to produce the best possible simultaneous or combined fits to the data, in terms of χ^2/ndf , using the MINUTE program in the ROOT analysis framework.

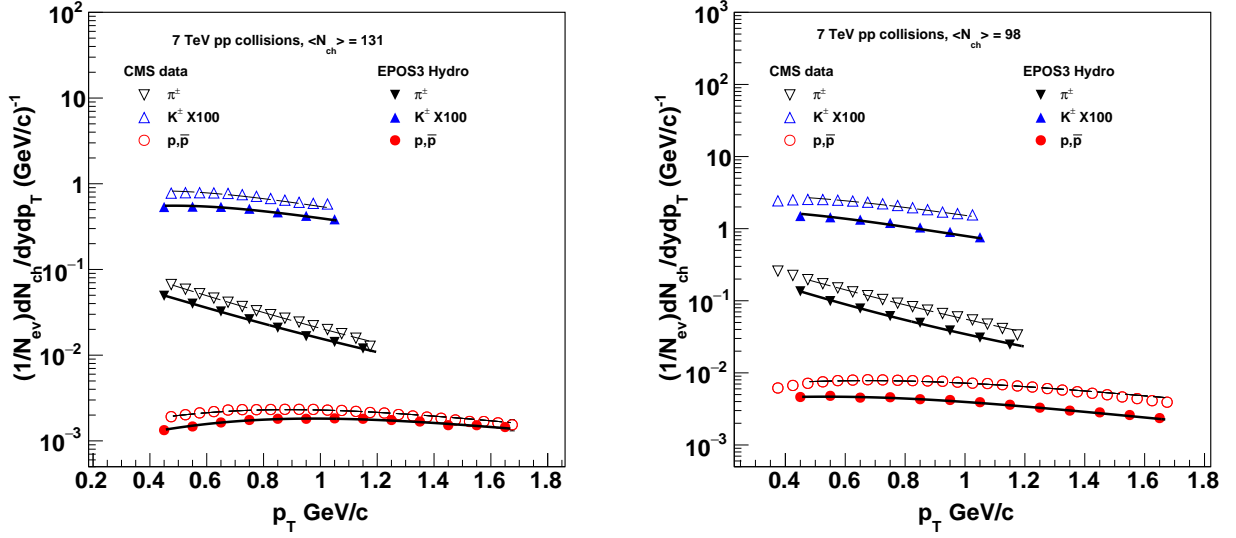


Figure 6.14: The transverse momentum spectra for π^\pm , K^\pm , $p(\bar{p})$ as measured by the CMS experiment [176] at LHC for the event-class of average multiplicity = 131 and 98 in pp -collisions at $\sqrt{s} = 7$ TeV, along with BG-blast-wave fits (solid lines). The uncorrelated statistical and systematic uncertainties have been added in quadrature.

The figure 6.14 contains representative plots where BGBW fits to the spectra data of identified particles from pp collisions at 7 TeV for the event-classes of average multiplicity = 98 and 131, respectively, are shown along with the fits to the simulated spectra, obtained from the respective class of simulated events.

$\sqrt{s}(\text{TeV})$	$\langle N_{ch} \rangle$	$T_{kin}(\text{MeV})$	$\langle \beta \rangle$	n	$\chi^2/n.d.f$
7	98	115.57 ± 0.11	0.766 ± 0.004	0.540 ± 0.006	1.02
7	109	113.09 ± 0.12	0.779 ± 0.004	0.503 ± 0.006	0.61
7	120	110.84 ± 0.15	0.790 ± 0.004	0.480 ± 0.006	0.34
7	131	104.29 ± 0.15	0.809 ± 0.005	0.436 ± 0.005	0.44
13	108	140.80 ± 0.022	0.723 ± 0.005	0.58 ± 0.01	1.65
13	119	129.31 ± 0.019	0.778 ± 0.002	0.56 ± 0.011	0.86
13	130	128.29 ± 0.019	0.763 ± 0.004	0.50 ± 0.009	1.18
13	141	119.77 ± 0.016	0.764 ± 0.004	0.48 ± 0.01	1.40
13	151	112.84 ± 0.016	0.783 ± 0.004	0.44 ± 0.011	1.44
13	162	102.67 ± 0.017	0.826 ± 0.003	0.36 ± 0.007	0.93

Table 6.1: T_{kin} , $\langle \beta \rangle$ and n , the parameters of the the BGBW, obtained from the simultaneous fit to the published [176, 193] spectra of π^\pm , K^\pm and $p(\bar{p})$ and respective $\chi^2/n.d.f$ for pp collisions at $\sqrt{s} = 7$ and 13 TeV for different event classes depending on average multiplicity, $\langle N_{ch} \rangle$, in the range $|\eta| < 2.4$.

The fit parameters, the kinetic freeze-out temperature (T_{kin}), the average radial flow velocity ($\langle \beta \rangle$) at the freeze-out surface, and the exponent (n) as obtained by simultaneous fit of identified particle spectra by BGBW have been tabulated for different classes of high-multiplicity pp events and

for $\sqrt{s} = 7$ and 13 TeV, along with respective $\chi^2/n.d.f$ in table 6.1. The table includes parameters for those event classes which fit reasonably with the BW function. The table 6.2 presents similar results for the EPOS3-hydro model generated events.

The figure 6.14 as well as the tables 6.1 and 6.2 show that the data and the EPOS3-hydro generated events are not matching quantitatively, in terms of the BW-parameters, except for very high multiplicity classes of average multiplicity = 151 and 162 in pp collisions at $\sqrt{s} = 13$ TeV.

$\sqrt{s}(TeV)$	$\langle N_{ch} \rangle$	$T_{kin}(MeV)$	$\langle \beta \rangle$	n	$\chi^2/n.d.f$
7	98	106.10 ± 0.015	0.768 ± 0.0003	0.59 ± 0.001	30.83
7	109	105.91 ± 0.008	0.808 ± 0.001	0.46 ± 0.005	1.51
7	120	103.30 ± 0.01	0.813 ± 0.002	0.45 ± 0.003	1.59
7	131	103.02 ± 0.02	0.829 ± 0.002	0.39 ± 0.004	0.52
13	108	142.00 ± 0.002	0.749 ± 0.001	0.63 ± 0.01	7.54
13	119	142.00 ± 0.0019	0.774 ± 0.005	0.50 ± 0.002	0.86
13	130	141.96 ± 0.006	0.774 ± 0.008	0.45 ± 0.009	1.16
13	141	127.98 ± 0.016	0.797 ± 0.001	0.44 ± 0.004	1.31
13	151	112.90 ± 0.01	0.814 ± 0.006	0.43 ± 0.004	0.96
13	162	100.52 ± 0.015	0.815 ± 0.007	0.42 ± 0.007	1.43

Table 6.2: T_{kin} , $\langle \beta \rangle$ and n , the parameters of the the BGBW, obtained from the simultaneous fit to the spectra obtained from simulated EPOS events for π^\pm , K^\pm and $p(\bar{p})$ and respective $\chi^2/n.d.f$ for pp collisions at $\sqrt{s} = 7$ and 13 TeV for different event classes depending on average multiplicity, $\langle N_{ch} \rangle$, in the range $|\eta| < 2.4$.

6.3.3 Mean transverse momentum ($\langle p_T \rangle$) as a function of charged particle multiplicity (N_{ch})

The $\langle p_T \rangle$ of charged particles as a function of N_{ch} , in the pseudorapidity range $|\eta| < 0.3$ and with the transverse momentum, p_T up to 10 GeV/c, has been measured by ALICE at the LHC [194] and it was reported that data of pp collisions at $\sqrt{s} = 7$ TeV is well described by the pQCD-inspired multiple parton interaction (MPI) model with colour reconnection, as implemented in PYTHIA code. We have calculated these observables, in the the same kinematic ranges used by ALICE, for the events generated with both the hydro and non-hydro EPOS3 simulations.

The ATLAS experiment has studied [190] the same for pp collisions at $\sqrt{s} = 13$ TeV with different kinematic ranges, $|\eta| < 2.4$ and $p_T > 0.5$ GeV/c. We repeat the same analysis according the kinematic cuts used for the ATLAS data. The results for both pp $\sqrt{s} = 7$ and 13 TeV are depicted

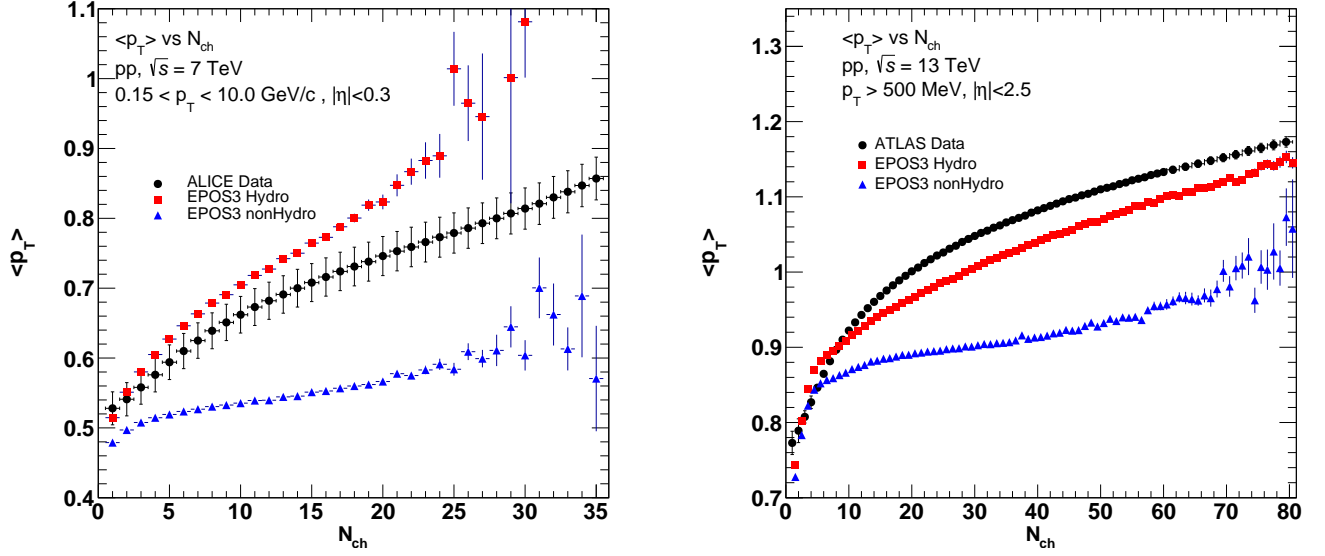


Figure 6.15: Average transverse momentum, $\langle p_T \rangle$, as a function of charged particle multiplicity, N_{ch} , as measured by ALICE and ATLAS [194, 190] in pp collisions at $\sqrt{s} = 7$ and 13 TeV respectively, compared with the simulated events from EPOS3 event generator, with and without Hydro calculations.

in the plots, along with the data in Fig. 6.15. As is clear from this figure, the EPOS3 code, with or without hydrodynamics, cannot describe the ALICE as well as ATLAS measurements of $\langle p_T \rangle$ as a function of N_{ch} .

It is noted that both the ALICE and the ATLAS data includes particles of p_T , much higher than the p_T -range of the “soft” particles produced from the “core” or the bulk collective medium as considered in the EPOS hydrodynamic code. In view of this, to compare the data with “soft” particles only, we choose the CMS data on identified p_T -spectra from events with different multiplicity ranges.

The CMS experiment has measured p_T -spectra of π^\pm , K^\pm , $p(\bar{p})$ over the rapidity, ($y = (1/2)\ln \frac{E+p_L}{E-p_L}$) range $|y| < 1$ for the pp collisions at $\sqrt{s} = 7$ and 13 TeV $|\eta| < 2.4$. The measured p_T - ranges for the measured identified particles in the pp collisions at both the energies, 7 TeV [176] and 13 TeV [193] are 0.1 to 1.2 GeV/c for π^\pm , 0.2 to 1.050 GeV/c for K^\pm and 0.35 - 1.7 GeV/c for p and \bar{p} . The measured p_T -ranges fall within the p_T - range of EPOS3 for particles originating from hydrodynamic bulk medium.

We compute $\langle p_T \rangle$ from the CMS data on identified charged particle spectra for different event classes from pp collisions at $\sqrt{s} = 7$ [176] and 13 [176] TeV. It is clear from figure 6.16 that for for pp $\sqrt{s} = 7$ TeV, the majority of soft particles (pion) shows a mismatch between data and simulated

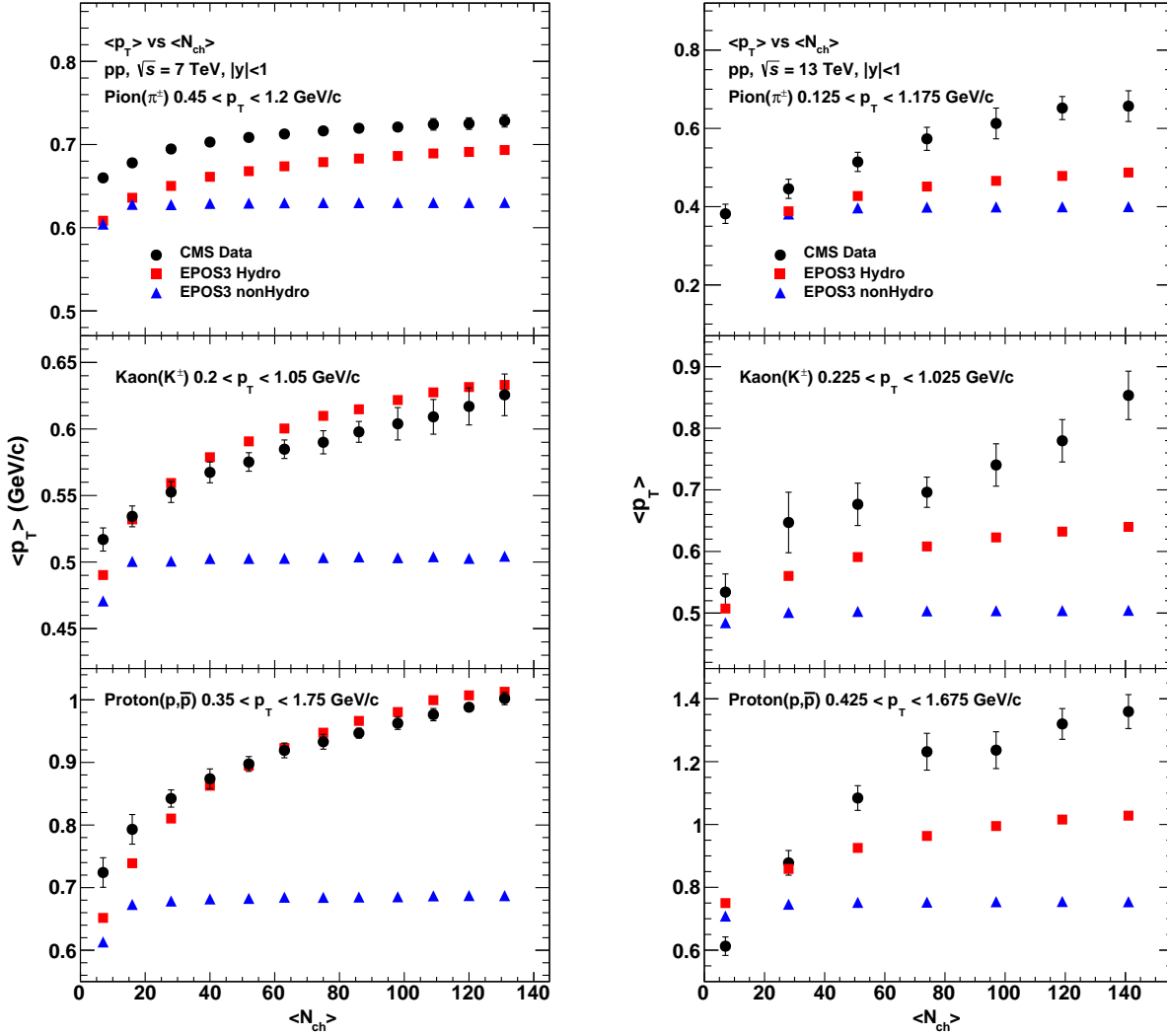


Figure 6.16: Average transverse momentum, $\langle p_T \rangle$, as a function of mean charged particle multiplicity, $\langle N_{ch} \rangle$, for the identified charged particles in pp collisions at $\sqrt{s} = 7$ and 13 TeV. The CMS data [176, 193], have been compared with simulated events using EPOS3 event generator with and without hydrodynamics.

events, while for $\sqrt{s} = 7$ TeV this disagreement is occurring for all the three identified charged particles.

6.3.4 Inverse slope parameter of transverse mass (m_T) distribution

The slope of transverse mass m_T -spectra of identified particle provides information on the temperature of a medium, if formed, from where the particles are produced, and the effect of transverse expansion of the medium. We have obtained the m_T spectra of identified charged particle for different high-multiplicity classes of pp events at $\sqrt{s} = 7$ and 13 TeV from the p_T -spectra measured [176, 193] by the CMS experiments using the relation, $m_T = (m^2 + p_T^2)^{1/2}$.

The m_T -spectra are fitted, in the range corresponding to low- p_T , with the exponential function:

$$\frac{dN}{m_T dm_T} = C \cdot \exp\left(-\frac{m_T}{T_{effective}}\right) \quad (6.7)$$

where $T_{effective}$, the inverse slope parameter, contains the effect due to the transverse expansion of the system. The increase in the inverse slope parameter, $T_{effective}$ for identified particles (π^\pm , K^\pm , p and \bar{p}), is attributed to the collective transverse flow of the medium formed in the collision. The increase in inverse slope parameters has also been observed in heavy-ion collisions [175, 177] as well as the high-multiplicity event classes of pPb collisions at $\sqrt{s_{NN}} = 5.02$ TeV [195].

We fit the m_T - spectra of identified particles in the overlapped range ($0.475 < p_T < 1.025$) of p_T - spectra at $\sqrt{s} = 7$ and 13 TeV, obtained from the data [176, 193] as well as from the EPOS3-hydro simulation for the high-multiplicity event classes. The inverse slope parameters, obtained from the best fit of the spectra, in terms of χ^2/ndf , using the MINUTE program in the ROOT analysis framework are presented in figure 6.17 for some representative high-multiplicity event-classes.

From the figures 6.17, it is clear that while the EPOS3-hydro high-multiplicity pp events exhibit mass ordering of inverse slope parameter of the m_T - distributions but deviate largely from the ones obtained from the measured spectra.

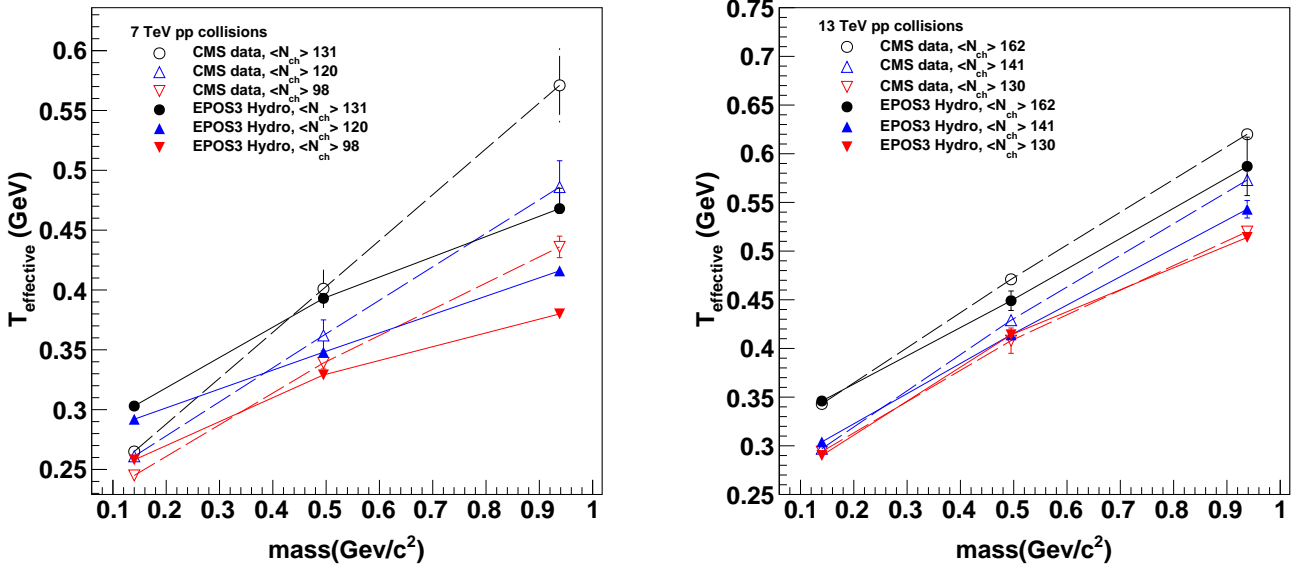


Figure 6.17: The mass ordering of the inverse slope parameter $T_{effective}$ of identified particles ($m_{\pi^\pm} = 0.14$, $m_{K^\pm} = 0.495$, $m_{p(\bar{p})} = 0.938$ GeV/c^2) as measured by the CMS experiment at $\sqrt{s} = 7$ TeV [176] and 13 TeV [193], for a few event classes of high-multiplicity, is compared with those obtained from EPOS3-hydro simulated events. The $\langle N_{ch} \rangle$ is the mean multiplicity of the charged particles of respective event-class.

6.4 Analysis in pPb collisions

In pPb collisions at $\sqrt{s_{NN}} = 5.02$ TeV, we have studied some basic observables like p_T spectra of identified particles, mean p_T as a function of charged particle multiplicity, inverse slope parameter of transverse mass (m_T) and compared those with available experimental results. We have extended the study to centrality dependent long-range two-particle azimuthal correlations between charged particles as well as D mesons and charged particles, for which no experimental results are available till now.

6.4.1 Centrality dependent invariant yields of identified charged particles

The invariant yield spectra of identified (π^\pm , K^\pm , $p(\bar{p})$) charged particles has been obtained for different centrality classes using EPOS3 generated events for pPb collisions at $\sqrt{s_{NN}} = 5.02$ TeV. Results are compared with the same measured by ALICE [196] as shown in figure 6.18. From this figure, it is clear that there is no larger deviation from data to EPOS3, specially for the most central collisions.

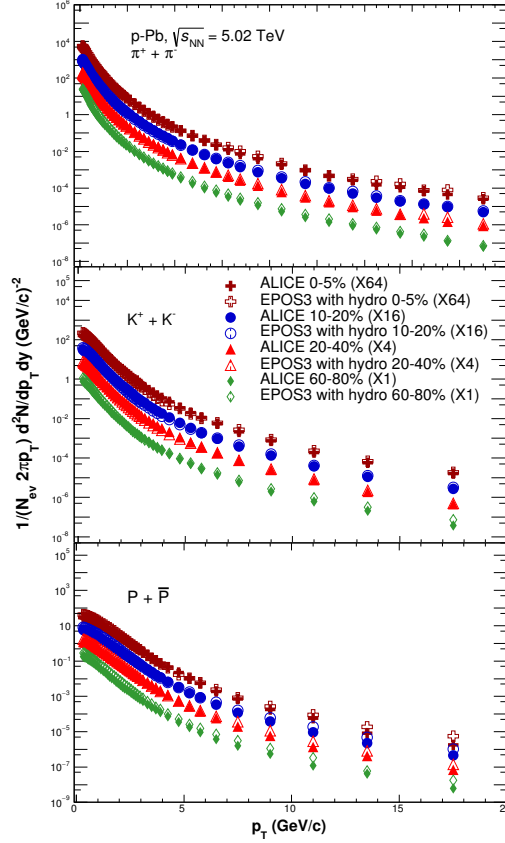


Figure 6.18: Centrality dependent invariant yields of identified charged particles in pPb collisions at $\sqrt{s_{NN}} = 5.02$ TeV, measured by ALICE [196] compared with the simulated events from the EPOS3 event generator with Hydro calculations.

6.4.2 Mean transverse momentum ($\langle p_T \rangle$) as a function of charged particle multiplicity

Similar to pp collisions at $\sqrt{s} = 7$ TeV, The $\langle p_T \rangle$ of charged particles as a function of charged particle multiplicity (N_{ch}), in the pseudorapidity range $|\eta| < 0.3$ and with the transverse momentum, p_T up to 10 GeV/c, has been measured by ALICE at the LHC [194] in pPb collisions at $\sqrt{s_{NN}} = 5.02$ TeV. We have calculated these observables, in the the same kinematic ranges used by ALICE, for the events generated with both the hydro and non-hydro EPOS3 simulations and the results are shown in figure 6.19 which indicate a good agreement between EPOS3 and experimental results.

We have also compared the data with “soft” particles only, obtained from CMS results on identified ($\pi^\pm, K^\pm, p(\bar{p})$) p_T -spectra from events with different multiplicity classes [195]. We compute $\langle p_T \rangle$ from the p_T spectra of identified particles and compare it with that obtained from EPOS3 hydro-based simulated events as a function of mean charged particle multiplicity ($\langle p_T \rangle$). The results are shown in figure 6.20 and indicate a good agreement between data and EPOS3.

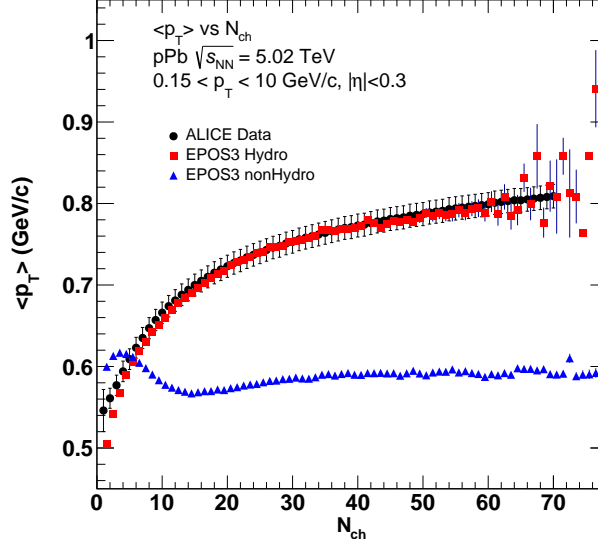


Figure 6.19: Average transverse momentum, $\langle p_T \rangle$, as a function of charged particle multiplicity, N_{ch} , as measured by ALICE [194] in pPb collisions at $\sqrt{s_{NN}} = 5.02$ TeV respectively, compared with the simulated events from EPOS3 event generator, with and without Hydro calculations.

6.4.3 Inverse slope parameter of transverse mass (m_T) spectra

Similar to pp collisions as described in 6.3.4, the slopes of transverse mass (m_T) spectra of identified particles have been obtained in different multiplicity class in pPb collisions at $\sqrt{s_{NN}} = 5.02$ TeV from CMS experiment [195]. Same thing has been repeated for EPOS3 generated events with hydro calculations. The inverse slope parameters, obtained from the best fit of the spectra, in terms of χ^2/ndf , using the MINUTE program in the ROOT analysis framework are presented in figure 6.21 for some representative high-multiplicity event-classes.

From the figures 6.21, it is clear that while the EPOS3-hydro high-multiplicity pPb events exhibit mass ordering of inverse slope parameter of the m_T - distributions and also very close to the ones obtained from the measured spectra.

6.4.4 Long-range two-particle azimuthal correlations

As discussed in section 6.3.1, the same analysis tool has been used for the centrality dependent pPb analysis at $\sqrt{s_{NN}} = 5.02$ TeV. First we construct the long-range two-particle azimuthal correlations between the charged particles with four different centrality bins (0 – 20%, 20 – 40%, 40 – 60%, 60 – 100%) and three different p_T regions (1-2, 2-3, 3-4 GeV/c) considering $2 < |\Delta\eta| < 4$ using EPOS3 hydro-based simulated events. The per-trigger associated particle yields as a function of $\Delta\varphi$ and subtracted by $Yield|_{\Delta\varphi=1.0}$ are shown in figure 6.22 (left). It is observed from the figure, the centrality dependence of correlated yields from the simulated events, show similar features observed by CMS

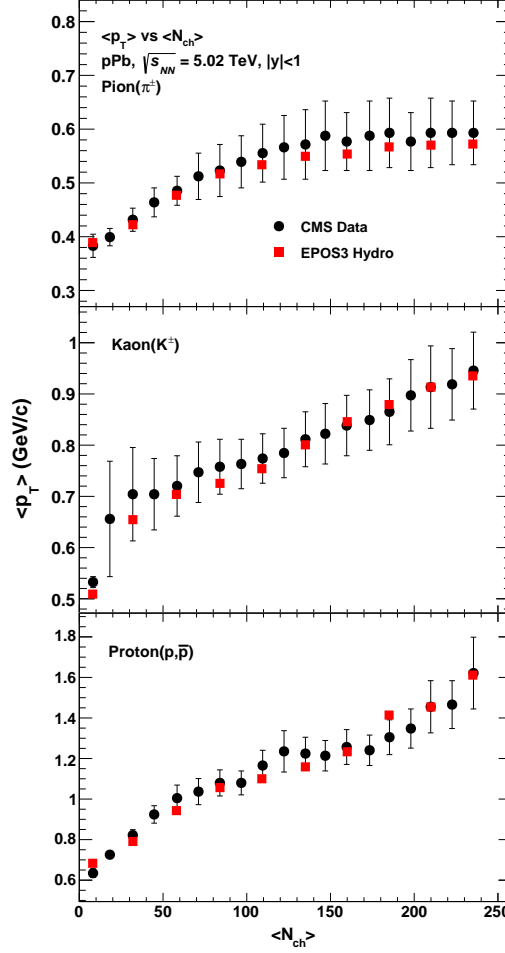


Figure 6.20: Average transverse momentum, $\langle p_T \rangle$, as a function of mean charged particle multiplicity, $\langle N_{ch} \rangle$, as measured by CMS [195] in pPb collisions at $\sqrt{s_{NN}} = 5.02$ TeV respectively, compared with the simulated events from EPOS3 event generator, with Hydro calculations.

[83], i.e., the ridge-like structure is most prominent in $1 < p_T < 2$ GeV/c for the most central collisions and gradually decreases with increasing p_T .

Next, the long-range two-particle azimuthal correlations are constructed between D-mesons and charged particles with the simulated events considering the same centrality classes, p_T intervals, $|\Delta\eta|$ range. The per-trigger correlated yields as a function of $\Delta\varphi$ are shown in figure 6.22 (right). As observed from the figure, the correlated yields from simulated events, for the considered p_T intervals do not exhibit the same feature as obtained from the correlations between charged particles. The absence of the ridge-like structure in the “low” p_T -range seems consistent in view of the production of the heavy-quarks and their non-interaction with the thermalized bulk-matter in the EPOS3 framework.

ALICE has measured a significant positive D-meson v_2 with $2 < p_T < 6$ GeV/c range, in 30 - 50 % centrality class of PbPb collisions at $\sqrt{s_{NN}} = 2.76$ TeV [197]. This motivates us to study the long-range two-particle azimuthal correlations between D mesons and charged particles with

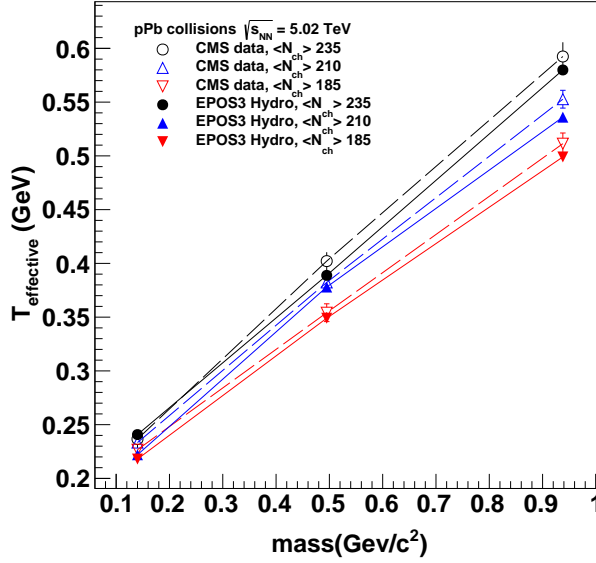


Figure 6.21: The mass ordering of the inverse slope parameter $T_{effective}$ of identified particles ($m_{\pi^\pm} = 0.14$, $m_{K^\pm} = 0.495$, $m_{p(\bar{p})} = 0.938 \text{ GeV}/c^2$) as measured by the CMS experiment in pPb collisions at $\sqrt{s_{NN}} = 5.02 \text{ TeV}$ [195], for a few event classes of high-multiplicity, is compared with those obtained from EPOS3-hydro simulated events. The $\langle N_{ch} \rangle$ is the mean multiplicity of the charged particles of respective event-class.

an intermediate- p_T range. Thus, we have constructed the correlations with $3 < p_T^{trigg} < 5 \text{ GeV}/c$, $1 < p_T^{assoc} < 3 \text{ GeV}/c$ and $2 < |\Delta\eta| < 4$ as shown in figure 6.23. A clear ridge-like structure is observed in the figure for the most-central pPb collisions at $\sqrt{s_{NN}} = 5.02 \text{ TeV}$ revealing the collective properties of D mesons in intermediate p_T range.

According to the EPOS3 hydrodynamic model, high-multiplicity events are generated from large number of flux tubes created in many initial parton-parton scatterings in an event. A large number of flux-tubes breaks to form a medium of high string-segment density. The low- p_T final state particles come from the thermalized bulk-matter created with low energy string-segments. The semi-hard particles, like the D-mesons in the intermediate p_T -range, having enough energy to escape the bulk-matter, hadronize by picking-up quark or antiquark from the bulk-matter. The D-mesons in this intermediate p_T -range, thus carry the collective property of the bulk-matter, as reflected in the ridge-like structure in two-particle angular correlations between the D-mesons in this p_T range and charged particles in low- p_T range.

For identifying the source of the collectivity of the D mesons in EPOS framework, therefore, we investigate the simulated events further. We select two different classes of D mesons according to the production mechanisms: 1) “soft” particles originating from the “core” or the plasma and 2) particles from semi-hard string fragmentation. We calculate the invariant yields of D mesons separately from

6.4. Analysis in pPb collisions

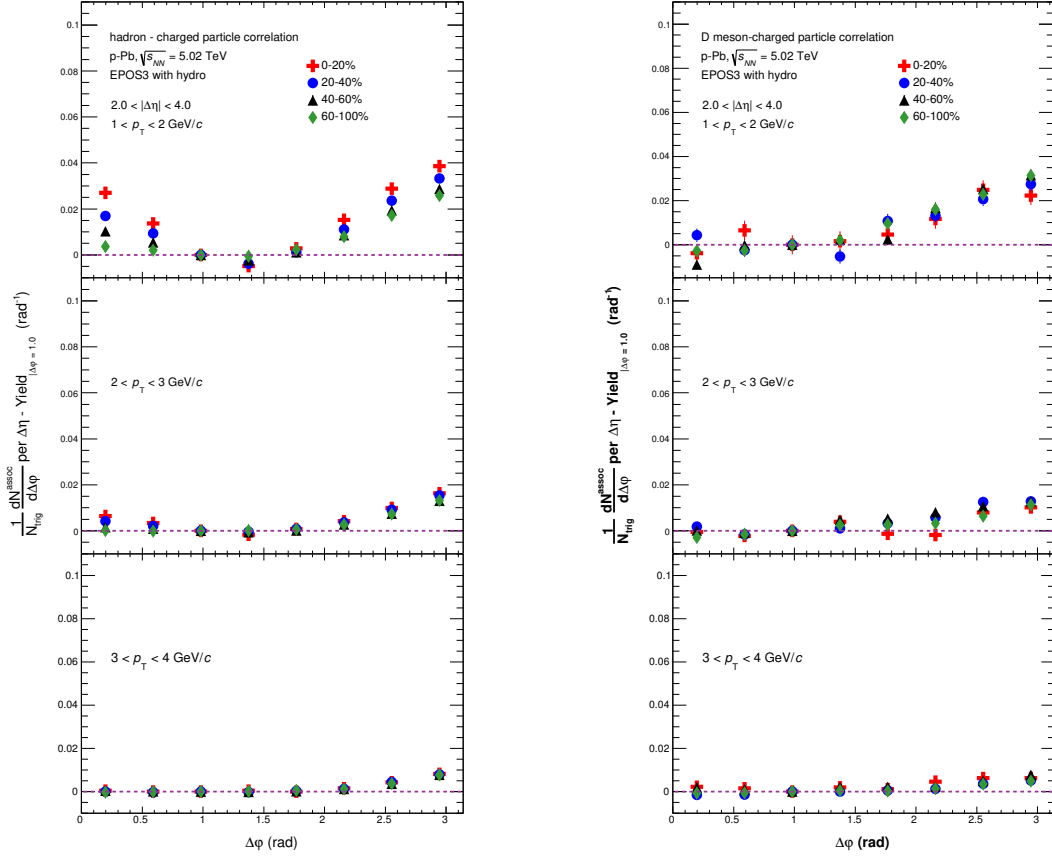


Figure 6.22: Centrality dependent correlated yield as a function $\Delta\varphi$, as obtained from the long-range two-particle azimuthal correlations between charged particle (left) and between D mesons and charged particles (right), for EPOS3 generated pPb collisions at $\sqrt{s_{NN}} = 5.02$ TeV in different ranges of $p_T^{trigger}$ and p_T^{assoc} .

two different selected classes. From figure 6.24, it has been observed that the D-meson yield from (semi-)hard string fragmentation (non-plasma source) dominate largely the same from the plasma source in EPOS3 hydrodynamic framework.

In the figure 6.25, we compare the centrality dependent per-trigger associated yield from the two sources as a function $\Delta\varphi$ and subtracted by the $Yield|_{\Delta\varphi=1.0}$, as obtained from the long-range two-particle azimuthal correlations of D-mesons and charged particles, averaged over $2 < |\Delta\eta| < 4$, for $3 < p_T^{trigger} < 5$ GeV/c and $1 < p_T^{associated} < 3$ GeV/c for the EPOS3-hydro generated events in pPb collisions at $\sqrt{s_{NN}} = 5.02$ TeV. It becomes clear from the figure 6.25, correlated pair yields per trigger, suggests that major contribution to the observed ridge-like structure comes from the D mesons produced in the bulk-matter or the “plasma”.

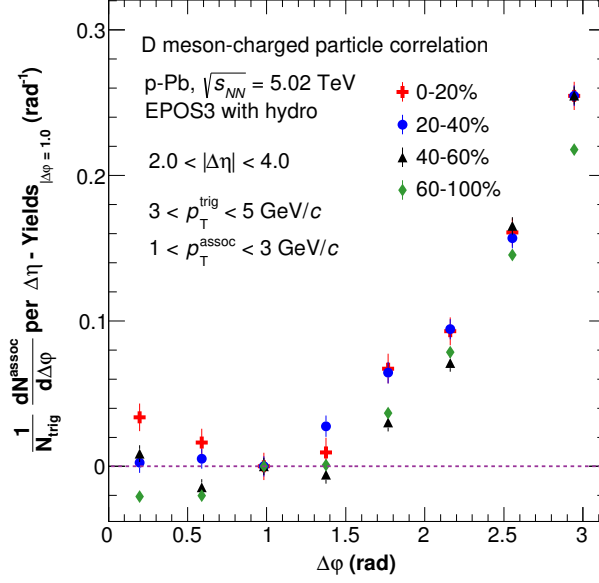


Figure 6.23: Centrality dependent correlated yield, as obtained from the long-range two-particle azimuthal correlations of D-mesons and charged particles, averaged over $2 < |\Delta\eta| < 4$, for $3 < p_T^{trigg} < 5$ GeV/c and $1 < p_T^{assoc} < 3$ GeV/c, for the hydrodynamic-EPOS3 generated pPb collisions at $\sqrt{s_{NN}} = 5.02$ TeV.

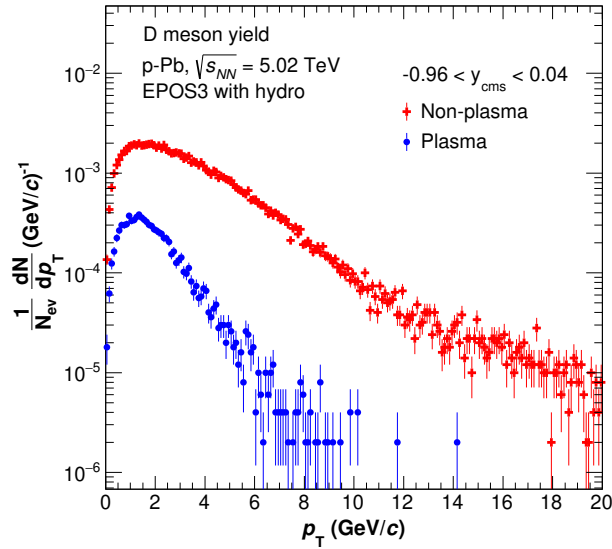


Figure 6.24: Invariant yield of EPOS3 generated D-mesons from two different sources, plasma and non-plasma.

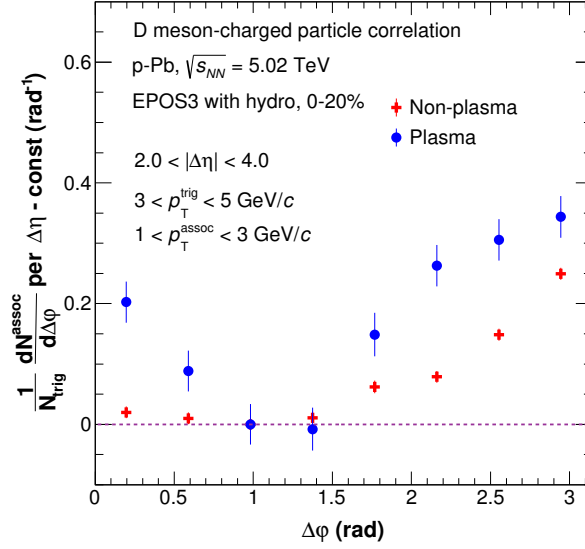


Figure 6.25: Correlated yield, as obtained from the long-range two-particle azimuthal correlations of D-mesons and charged particles, averaged over $2 < |\Delta\eta| < 4$, for $3 < p_T^{trig} < 5$ GeV/c and $1 < p_T^{assoc} < 3$ GeV/c, for the hydrodynamic-EPOS3 generated pPb collisions with 0-20% centrality events at $\sqrt{s_{NN}} = 5.02$ TeV.

Chapter 7

Summary and Outlook

In this chapter, we summarize the work presented in this thesis followed by brief discussions on future perspective.

7.1 Azimuthal correlations between D mesons and charged particles in pp collisions at $\sqrt{s} = 13$ TeV measured by ALICE

7.1.1 Summary and conclusion

This thesis has presented the first ALICE measurement of two-particle azimuthal correlations between D mesons and charged particles with minimum-bias events of pp collisions at $\sqrt{s} = 13$ TeV, the highest available energy at the LHC till date. The analysis has been performed by considering the D meson (D^0, D^+, D^{*+}) as “trigger” particles in three different p_T^D region: 3-5, 5-8, 8-16 GeV/ c and the primary charged particles as “associated” particles in three different p_T^{assoc} region: > 0.3 , 1.0, 0.3-1.0 GeV/ c . The correlation distributions as a function of $\Delta\varphi$ shows similarity for all the three D mesons within uncertainty, that helps us obtaining the final results, with improved statistical precision, by averaging the results from three types of D mesons. The correlation properties, i.e, the near-side and away-side peak yields and the widths are extracted by fitting the final correlation distributions with two gaussian and a constant term. The near-side yield and width gives the multiplicity and angular spread of the tracks from the fragmentation of the charm jet. The away-side observables are related to the hadronization of the charm quark produced in the opposite direction (though the presence of NLO processes for charm production affects both the yields and width of the away-side peak). The baseline value is a rough indicator of the underlying event multiplicity,

though below the baseline level also charm and beauty-related pairs are contained (especially in cases of NLO production for the heavy quarks). The near-side peak associated yield shows an increasing trend with D-meson p_T while the width of the near-side peak does not show any clear p_T dependence with the current level of uncertainty. For the away-side peaks, the poor statistical precision on the fit parameters does not allow the quantification of physical observables and their p_T dependence.

The results have been compared with several Monte-Carlo event generators like PYTHIA6 (Perugia0, 2010, 2011), PYTHIA8 and POWHEG+PYTHIA6. For near-side peaks, all the event generators are found to agree with data within uncertainties, but for away-side peaks, PYTHIA8 and POWHEG+PYTHIA6 shows closeness to data.

The correlation distributions and the near-side peak properties obtained from the pp collisions at $\sqrt{s} = 13$ TeV are compared with same analysis performed on pp collisions at $\sqrt{s} = 7$ TeV and pPb collisions $\sqrt{s_{NN}} = 5.02$ TeV. The results show similarity among the three systems within uncertainties indicating similar charm-jet properties for pp and pPb collisions for the given centre-of-mass energies.

7.1.2 Outlook

This analysis may be repeated with the pp data at $\sqrt{s} = 13$ TeV from the 2017 and 2018 LHC run. The merged up results from the pp run containing the data with three years: 2016, 2017 and 2018 will provide a better precision to the correlation spectra and will allow us to extent this study to higher p_T^D and p_T^{assoc} regions. Also, with the merging of data, one will be able to quantify the away-side fit parameters properly.

Having larger sample of statistics, we can divide this analysis into several multiplicity classes to carry out a multiplicity-dependent study, focussing on the high-multiplicity pp events. The multiplicity dependence study on the correlation properties will also help us to investigate if the charm-jet properties and the charm production mechanisms get modified due to in-medium effect, if any, in high-multiplicity pp events.

The correlation analysis can be performed in pp collision at 13 TeV by considering the heavy-flavour decay electrons as trigger and primary charged hadrons as associated particles. These two complementary studies will help in better understanding of heavy-quark production mechanisms and the jet properties containing heavy-flavour hadrons.

7.2 Simulation studies with hydro-based event generator EPOS3 for high-multiplicity events of pp and pPb collisions at LHC energies

7.2.1 Summary and conclusion

We have presented a simulation based study for pp and pPb collisions in LHC energies using EPOS3 event generator in which 3+1D viscous hydrodynamics is implemented. The hydrodynamics based models provide a framework to study the collective properties of the medium (if formed) in search of the origin of the anomalous features of particle production mechanisms in small systems. We summarize the results in the following sections.

pp collisions

In the context of several collective signatures of particle productions in pp collisions at LHC energies, we have done the analysis with simulated pp events at $\sqrt{s} = 7$ and 13 TeV from EPOS3 event generator. The quantitative comparisons are made with the particle production data in high-multiplicity pp events for better understanding of the experimental signals.

We have done the multiplicity dependent study of the long-range two-particle angular correlations between charged particles with the events generated from EPOS3 model. The EPOS3-hydro generated high-multiplicity events exhibits the “ridge-like” structure, that is most prominent in the 1 to 2 GeV/c p_T range and decreases gradually with increasing p_T -interval. The diminishing trend of correlated yields with the increasing p_T -interval is similar to that is observed in data. However, the EPOS3 events overestimate the correlated yields in the p_T range 1-2 GeV/c.

The kinetic freeze-out temperature (T_{kin}) and a transverse radial flow velocity (β) at the freeze-out surface as obtained from the blast-wave fits to the identified particle spectra for high-multiplicity event classes of EPOS3-simulated events, do not match those parameters for the data.

The mean transverse momentum as a function of charged particle multiplicity, for both inclusive and identified charged particles from EPOS3 generated events, in different kinematic ranges, vary widely from those measured by different experiments at the LHC.

The inverse slope parameters obtained by exponential fits to the transverse mass spectra of EPOS3 generated events, exhibits mass-ordering as expected in hydrodynamic model of particle production, but the values of the fit parameters do not agree with those obtained from the data.

This data-driven study reveals that though the EPOS3 hydrodynamic model may describes the na-

ture of some of the average bulk features quite reasonably, reflecting collective properties of particle production in the high-multiplicity pp events at LHC energies, it cannot match the data quantitatively. The quantitative mismatches in BW-fitting, the $\langle N_{ch} \rangle$ dependence of $\langle p_T \rangle$ and the inverse slope parameters of m_T spectra - all these reflect mismatch at the fundamental stage. In this context, it can be noted that some of the non-hydrodynamic models of particle productions also qualitatively match certain bulk collective features of high-multiplicity pp events. In an alternate approach, in the IP-Glasma model, based on colour glass condensate (CGC), followed by the Lund string fragmentation algorithm of PYTHIA, with further tuning of the p_T -smearing fragmentation parameter in the default PYTHIA, the particle mass dependence of $\langle p_T \rangle$ and the p_T dependence of v_2 for pp collisions could be qualitatively reproduced [191]. The ALICE measurement of $\langle p_T \rangle$ of the charged particles as a function of $\langle N_{ch} \rangle$, including particle of p_T up to 10 GeV/c from pp collisions at 7 TeV, could be well reproduced [194] by invoking Colour Reconnection mechanism in PYTHIA (while EPOS3 remain far away from the data). The MPI model, however, cannot explain [178] the dependence of $\langle p_T \rangle$ on $\langle N_{ch} \rangle$ or does not provide alternate explanations to other important features of particle production in high-multiplicity events pp collisions at 7 TeV when the p_T -range is restricted to the range of interest for studying the hydrodynamic collectivity. The results of our analysis are consistent with the ALICE measurements [198] of pseudo-rapidity and transverse-momentum distributions of charged particles produced in 13 TeV pp collisions which could not be well described by either the PYTHIA or the EPOS Monte Carlo Generators. Similarly, no other particle production model, hydrodynamic or non-hydrodynamic, could quantitatively match the collective features of the high-multiplicity pp data. We, thus, conclude that the observed anomaly in particle production in high-multiplicity pp events at the LHC still remains uniquely unresolved.

pPb collisions

In the studies of pPb collisions at $\sqrt{s_{NN}} = 5.02$ TeV, we have done a few basic analysis, namely, centrality dependant invariant yield of identified particles ($\pi^\pm, K^\pm, p(\bar{p})$), mean transverse momentum as a function of charged particle multiplicity, inverse slope parameter from the transverse mass spectra of identified particles ($\pi^\pm, K^\pm, p(\bar{p})$) using EPOS3 event generator. We have compared the results with available experimental data considering same kinematic conditions. The results show good agreement between data and EPOS3.

We extended the study to the two-particle azimuthal correlations in long range ($2 < \Delta\eta < 4$). First, we have constructed the correlations between charged particles in different centrality region (0 – 20%, 20 – 40%, 40 – 60%, 60 – 100%), considering p_T ranges 1-2, 2-3, 3-4 GeV/c with EPOS3-

hydro generated events. The “ridge”-like structures are prominent in the most central collisions for p_T interval 1-2 GeV/c and gradually decreases with increasing p_T . This feature is similar to that found in CMS experiment [83]. Next, we have done the similar analysis between D mesons and charged particles considering the same centrality bins and p_T intervals with the simulated events. It has been observed that, the “ridge”-like structures do not appear here due the non-implementation of interaction between heavy-quarks and thermalized bulk matter in the present version of EPOS3 code.

However, this study on the two-particle angular correlations between D-mesons and charged particles in the intermediate p_T -range for trigger ($3 < p_T^{trigger} < 5$ GeV/c) and low- p_T range for associated particles ($1 < p_T^{assoc} < 3$ GeV/c), using the EPOS3 generated events clearly shows a prominent ridge-like structure in most central events of pPb collisions. The high-multiplicity events in EPOS3 hydrodynamic model, are generated from large number of flux tubes which are created through many of the initial parton-parton scatterings in an event. A large number of flux-tubes breaks to form a medium of high string-segment density. The low- p_T final state particles come from the thermalized bulk-matter created with low energy string-segments. The semi-hard particles, like the D-mesons in the intermediate p_T -range ($3 < p_T^{trigger} < 5$ GeV/c), having enough energy to escape the bulk-matter, hadronize by picking-up quark or antiquark from the bulk-matter. The D-mesons in this intermediate p_T -range, thus carry the collective property of the bulk-matter, as reflected in the ridge-like structure in two-particle angular correlations between the D-mesons in intermediate- p_T range and charged particles in low- p_T range. The study has been further extended classifying the two sources of D mesons: “plasma” and “non-plasma” and it has been observed that, the major contribution to the observed ridge-like structure indeed comes from the D mesons produced in the bulk-matter or the “plasma”.

This study addresses the particular issue of formation of collective medium in high-multiplicity ultra-relativistic pPb collisions and its response to the heavy-flavour particles. It is interesting to note that the collective behaviour of the intermediate- p_T D mesons from the EPOS3 generated pPb events at $\sqrt{s_{NN}} = 5.02$ TeV is consistent with results from several studies on D mesons in the similar p_T -range of PbPb collisions data in LHC energies [199, 200].

Considering observed collective properties of D mesons in the intermediate- p_T range, in relativistic heavy-ion collisions and several similarities in features of particle production mechanisms from the data of pPb and PbPb collisions, the prediction of collective behaviour of intermediate- p_T D-mesons in the EPOS3 generated high-multiplicity pPb events at $\sqrt{s_{NN}} = 5.02$ TeV, appears reliable.

7.2.2 Outlook

As revealed by the studies presented in this thesis, though the hydro-like features in high-multiplicity pPb data can be well reproduced by the EPOS3 generated events, in general, those observed in the high-multiplicity pp events couldn't yet be quantitatively explained with the EPOS3 event generator. The observation thus invites further tuning or modification of the EPOS3 event generator. This points to the scope of further improvement on hydrodynamic evolution or any other physics processes, the way they are implemented in the code, for pp collisions. It may be noted that several hydrodynamic [201, 202, 203] and non-hydrodynamic [191, 192] models can describe the observed features of particle production in high-multiplicity pp events qualitatively, but there does not exist any model, hydrodynamic or non-hydrodynamic, that satisfactory explain quantitatively the of majority of the observed features of high-multiplicity pp events, leaving the scope for further studies wide open.

Bibliography

- [1] J. C. Collins and M. J. Perry, *Superdense Matter: Neutrons Or Asymptotically Free Quarks?*, *Phys. Rev. Lett.* **34** (1975) 1353.
- [2] E. V. Shuryak, *Theory of Hadronic Plasma*, *Sov. Phys. JETP* **47** (1978) 212.
- [3] E. V. Shuryak, *Quark-Gluon Plasma and Hadronic Production of Leptons, Photons and Psions*, *Phys. Lett.* **78B** (1978) 150.
- [4] E. V. Shuryak, *Quantum Chromodynamics and the Theory of Superdense Matter*, *Phys. Rept.* **61** (1980) 71.
- [5] D. Teaney, J. Lauret and E. V. Shuryak, *Flow at the sps and rhic as a quark-gluon plasma signature*, *Phys. Rev. Lett.* **86** (2001) 4783.
- [6] PHENIX collaboration, *Formation of dense partonic matter in relativistic nucleus-nucleus collisions at RHIC: Experimental evaluation by the PHENIX collaboration*, *Nucl. Phys.* **A757** (2005) 184 [[nucl-ex/0410003](#)].
- [7] B. B. Back et al., *The PHOBOS perspective on discoveries at RHIC*, *Nucl. Phys.* **A757** (2005) 28 [[nucl-ex/0410022](#)].
- [8] BRAHMS collaboration, *Quark gluon plasma and color glass condensate at RHIC? The Perspective from the BRAHMS experiment*, *Nucl. Phys.* **A757** (2005) 1 [[nucl-ex/0410020](#)].
- [9] STAR collaboration, *Global Λ hyperon polarization in nuclear collisions: evidence for the most vortical fluid*, *Nature* **548** (2017) 62 [[1701.06657](#)].
- [10] S. Weinberg, *The Making of the standard model*, *Eur. Phys. J.* **C34** (2004) 5 [[hep-ph/0401010](#)].
- [11] https://en.wikipedia.org/wiki/Standard_Model.

- [12] P. W. Higgs, *Broken symmetries and the masses of gauge bosons*, *Phys. Rev. Lett.* **13** (1964) 508.
- [13] M. E. Peskin and D. V. Schroeder, *An Introduction to quantum field theory*. Addison-Wesley, Reading, USA, 1995.
- [14] A. Deur, S. J. Brodsky and G. F. de Teramond, *The QCD Running Coupling*, *Prog. Part. Nucl. Phys.* **90** (2016) 1 [[1604.08082](#)].
- [15] PARTICLE DATA GROUP collaboration, *Review of particle physics*, *Phys. Rev. D* **98** (2018) 030001.
- [16] R. Hagedorn, *Hadronic matter near the boiling point*, *Nuovo Cim.* **A56** (1968) 1027.
- [17] G. Baym and S. A. Chin, *Can a Neutron Star Be a Giant MIT Bag?*, *Phys. Lett.* **62B** (1976) 241.
- [18] B. A. Freedman and L. D. McLerran, *Fermions and Gauge Vector Mesons at Finite Temperature and Density. 3. The Ground State Energy of a Relativistic Quark Gas*, *Phys. Rev.* **D16** (1977) 1169.
- [19] G. Chapline and M. Nauenberg, *Asymptotic Freedom and the Baryon-Quark Phase Transition*, *Phys. Rev.* **D16** (1977) 450.
- [20] G. Aarts, *Introductory lectures on lattice QCD at nonzero baryon number*, *J. Phys. Conf. Ser.* **706** (2016) 022004 [[1512.05145](#)].
- [21] Z. Fodor and S. D. Katz, *Lattice determination of the critical point of QCD at finite T and μ* , *JHEP* **03** (2002) 014 [[hep-lat/0106002](#)].
- [22] Z. Fodor and S. D. Katz, *Critical point of QCD at finite T and μ , lattice results for physical quark masses*, *JHEP* **04** (2004) 050 [[hep-lat/0402006](#)].
- [23] M. A. Stephanov, K. Rajagopal and E. V. Shuryak, *Event-by-event fluctuations in heavy ion collisions and the QCD critical point*, *Phys. Rev.* **D60** (1999) 114028 [[hep-ph/9903292](#)].
- [24] B. Müller, J. Schukraft and B. Wyslouch, *First results from $pb+pb$ collisions at the lhc*, *Annual Review of Nuclear and Particle Science* **62** (2012) 361 [<https://doi.org/10.1146/annurev-nucl-102711-094910>].

- [25] ALICE collaboration, *Centrality dependence of the charged-particle multiplicity density at midrapidity in Pb-Pb collisions at $\sqrt{s_{\text{NN}}} = 5.02$ TeV*, *Phys. Rev. Lett.* **116** (2016) 222302 [[1512.06104](#)].
- [26] CMS collaboration, *Jet properties in PbPb and pp collisions at $\sqrt{s_{\text{NN}}} = 5.02$ TeV*, *JHEP* **05** (2018) 006 [[1803.00042](#)].
- [27] Y. Aoki, G. Endrodi, Z. Fodor, S. D. Katz and K. K. Szabo, *The Order of the quantum chromodynamics transition predicted by the standard model of particle physics*, *Nature* **443** (2006) 675 [[hep-lat/0611014](#)].
- [28] A. Masayuki and Y. Koichi, *Chiral restoration at finite density and temperature*, *Nuclear Physics A* **504** (1989) 668 .
- [29] F. Karsch and M. Lutgemeier, *Deconfinement and chiral symmetry restoration in an $SU(3)$ gauge theory with adjoint fermions*, *Nucl. Phys.* **B550** (1999) 449 [[hep-lat/9812023](#)].
- [30] M. A. Halasz, A. D. Jackson, R. E. Shrock, M. A. Stephanov and J. J. M. Verbaarschot, *Phase diagram of qcd*, *Phys. Rev. D* **58** (1998) 096007.
- [31] T. A. Collaboration, G. Aad, E. Abat, J. Abdallah, A. A. Abdelalim, A. Abdesselam et al., *The ATLAS experiment at the CERN large hadron collider*, *Journal of Instrumentation* **3** (2008) S08003.
- [32] T. C. Collaboration, S. Chatrchyan, G. Hmayakyan, V. Khachatryan, A. M. Sirunyan, W. Adam et al., *The CMS experiment at the CERN LHC*, *Journal of Instrumentation* **3** (2008) S08004.
- [33] T. L. Collaboration, A. A. Alves, L. M. A. Filho, A. F. Barbosa, I. Bediaga, G. Cernicchiaro et al., *The LHCb detector at the LHC*, *Journal of Instrumentation* **3** (2008) S08005.
- [34] ALICE collaboration, *ALICE: Physics performance report, volume I*, *J. Phys.* **G30** (2004) 1517.
- [35] P. Senger, *The compressed baryonic matter experiment at FAIR in darmstadt*, *Journal of Physics G: Nuclear and Particle Physics* **30** (2004) S1087.
- [36] B. Friman, C. Hohne, J. Knoll, S. Leupold, J. Randrup, R. Rapp et al., *The CBM physics book: Compressed baryonic matter in laboratory experiments*, *Lect. Notes Phys.* **814** (2011) pp.1.

- [37] <https://u.osu.edu/vishnu/2014/08/06/sketch-of-relativistic-heavy-ion-collisions/>.
- [38] C. Y. Wong, *Introduction to high-energy heavy ion collisions*. 1995.
- [39] P. B. Arnold, G. D. Moore and L. G. Yaffe, *Photon emission from quark gluon plasma: Complete leading order results*, *JHEP* **12** (2001) 009 [[hep-ph/0111107](#)].
- [40] P. Aurenche, F. Gelis and H. Zaraket, *KLN theorem, magnetic mass, and thermal photon production*, *Phys. Rev.* **D61** (2000) 116001 [[hep-ph/9911367](#)].
- [41] R. Chatterjee, L. Bhattacharya and D. K. Srivastava, *Electromagnetic probes*, *Lect. Notes Phys.* **785** (2010) 219 [[0901.3610](#)].
- [42] J. Alam, B. Sinha and S. Raha, *Electromagnetic probes of quark gluon plasma*, *Phys. Rept.* **273** (1996) 243.
- [43] J. Alam, S. Sarkar, P. Roy, T. Hatsuda and B. Sinha, *Thermal photons and lepton pairs from quark gluon plasma and hot hadronic matter*, *Annals Phys.* **286** (2001) 159 [[hep-ph/9909267](#)].
- [44] K. Kajantie, J. I. Kapusta, L. D. McLerran and A. Mekjian, *Dilepton Emission and the QCD Phase Transition in Ultrarelativistic Nuclear Collisions*, *Phys. Rev.* **D34** (1986) 2746.
- [45] L. D. McLerran and T. Toimela, *Photon and Dilepton Emission from the Quark - Gluon Plasma: Some General Considerations*, *Phys. Rev.* **D31** (1985) 545.
- [46] R. Rapp and J. Wambach, *Chiral symmetry restoration and dileptons in relativistic heavy ion collisions*, *Adv. Nucl. Phys.* **25** (2000) 1 [[hep-ph/9909229](#)].
- [47] H. A. Weldon, *Reformulation of finite temperature dilepton production*, *Phys. Rev.* **D42** (1990) 2384.
- [48] ALICE collaboration, *Suppression of Charged Particle Production at Large Transverse Momentum in Central Pb-Pb Collisions at $\sqrt{s_{NN}} = 2.76$ TeV*, *Phys. Lett.* **B696** (2011) 30 [[1012.1004](#)].
- [49] CMS collaboration, *Study of high- p_T charged particle suppression in PbPb compared to pp collisions at $\sqrt{s_{NN}} = 2.76$ TeV*, *Eur. Phys. J.* **C72** (2012) 1945 [[1202.2554](#)].
- [50] X.-N. Wang and M. Gyulassy, *Gluon shadowing and jet quenching in $A + A$ collisions at $s^{*}(1/2) = 200$ -GeV*, *Phys. Rev. Lett.* **68** (1992) 1480.

- [51] STAR collaboration, *Experimental and theoretical challenges in the search for the quark gluon plasma: The STAR Collaboration's critical assessment of the evidence from RHIC collisions*, *Nucl. Phys.* **A757** (2005) 102 [[nucl-ex/0501009](#)].
- [52] M. Gyulassy and M. Plumer, *Jet Quenching in Dense Matter*, *Phys. Lett.* **B243** (1990) 432.
- [53] M. Gyulassy and L. McLerran, *New forms of QCD matter discovered at RHIC*, *Nucl. Phys.* **A750** (2005) 30 [[nucl-th/0405013](#)].
- [54] CMS collaboration, *Observation and studies of jet quenching in PbPb collisions at nucleon-nucleon center-of-mass energy = 2.76 TeV*, *Phys. Rev.* **C84** (2011) 024906 [[1102.1957](#)].
- [55] STAR collaboration, *Distributions of charged hadrons associated with high transverse momentum particles in pp and Au + Au collisions at $s(NN)^{1/2} = 200$ -GeV*, *Phys. Rev. Lett.* **95** (2005) 152301 [[nucl-ex/0501016](#)].
- [56] D. d'Enterria and B. Betz, *High- $p(T)$ hadron suppression and jet quenching*, *Lect. Notes Phys.* **785** (2010) 285.
- [57] M. Cacciari, G. P. Salam and G. Soyez, *The anti- k_t jet clustering algorithm*, *JHEP* **04** (2008) 063 [[0802.1189](#)].
- [58] ALICE collaboration, *In-Medium Energy Loss and Correlations in Pb-Pb Collisions at $\sqrt{s_{NN}} = 2.76$ TeV*, *AIP Conf. Proc.* **1422** (2012) 209 [[1109.6208](#)].
- [59] A. M. Poskanzer and S. A. Voloshin, *Methods for analyzing anisotropic flow in relativistic nuclear collisions*, *Phys. Rev.* **C58** (1998) 1671 [[nucl-ex/9805001](#)].
- [60] S. A. Voloshin, A. M. Poskanzer and R. Snellings, *Collective phenomena in non-central nuclear collisions*, *Landolt-Bornstein* **23** (2010) 293 [[0809.2949](#)].
- [61] J.-Y. Ollitrault, *Anisotropy as a signature of transverse collective flow*, *Phys. Rev.* **D46** (1992) 229.
- [62] P. F. Kolb and U. W. Heinz, *Hydrodynamic description of ultrarelativistic heavy ion collisions*, [nucl-th/0305084](#).
- [63] ALICE collaboration, *Elliptic flow of charged particles in Pb-Pb collisions at 2.76 TeV*, *Phys. Rev. Lett.* **105** (2010) 252302 [[1011.3914](#)].

- [64] CMS collaboration, *Long-range and short-range dihadron angular correlations in central PbPb collisions at a nucleon-nucleon center of mass energy of 2.76 TeV*, *JHEP* **07** (2011) 076 [[1105.2438](#)].
- [65] G.-Y. Qin, *Anisotropic Flow and Jet Quenching in Relativistic Nuclear Collisions*, *Int. J. Mod. Phys. E* **24** (2015) 1530001 [[1502.02554](#)].
- [66] J.-Y. Ollitrault, *Anisotropy as a signature of transverse collective flow*, *Phys. Rev. D* **46** (1992) 229.
- [67] U. Heinz and R. Snellings, *Collective flow and viscosity in relativistic heavy-ion collisions*, *Ann. Rev. Nucl. Part. Sci.* **63** (2013) 123 [[1301.2826](#)].
- [68] C. Gale, S. Jeon and B. Schenke, *Hydrodynamic Modeling of Heavy-Ion Collisions*, *Int. J. Mod. Phys. A* **28** (2013) 1340011 [[1301.5893](#)].
- [69] R. Rapp and H. van Hees, *Heavy Quarks in the Quark-Gluon Plasma*, in *Quark-gluon plasma 4*, pp. 111–206, 2010, [0903.1096](#), [DOI](#).
- [70] W. Buchmuller and S. H. H. Tye, *Quarkonia and Quantum Chromodynamics*, *Phys. Rev. D* **24** (1981) 132.
- [71] G. S. Bali, *QCD forces and heavy quark bound states*, *Phys. Rept.* **343** (2001) 1 [[hep-ph/0001312](#)].
- [72] P. L. Cho and A. K. Leibovich, *Color octet quarkonia production. 2.*, *Phys. Rev. D* **53** (1996) 6203 [[hep-ph/9511315](#)].
- [73] P. L. Cho and A. K. Leibovich, *Color octet quarkonia production*, *Phys. Rev. D* **53** (1996) 150 [[hep-ph/9505329](#)].
- [74] T. Matsui and H. Satz, *J/ψ Suppression by Quark-Gluon Plasma Formation*, *Phys. Lett. B* **178** (1986) 416.
- [75] K. J. Eskola, H. Paukkunen and C. A. Salgado, *EPS09: A New Generation of NLO and LO Nuclear Parton Distribution Functions*, *JHEP* **04** (2009) 065 [[0902.4154](#)].
- [76] M. Hirai, S. Kumano and T. H. Nagai, *Determination of nuclear parton distribution functions and their uncertainties in next-to-leading order*, *Phys. Rev. C* **76** (2007) 065207 [[0709.3038](#)].

- [77] J. W. Cronin, H. J. Frisch, M. J. Shochet, J. P. Boymond, P. A. Piroué and R. L. Sumner, *Production of hadrons at large transverse momentum at 200, 300, and 400 gev*, *Phys. Rev. D* **11** (1975) 3105.
- [78] J. W. Cronin, H. J. Frisch, M. J. Shochet, J. P. Boymond, P. A. Piroué and R. L. Sumner, *Production of hadrons with large transverse momentum at 200 and 300 gev*, *Phys. Rev. Lett.* **31** (1973) 1426.
- [79] Y. Zhang, G. Fai, G. Papp, G. G. Barnaföldi and P. Lévai, *High- p_T pion and kaon production in relativistic nuclear collisions*, *Phys. Rev. C* **65** (2002) 034903.
- [80] Z.-B. Kang, J.-W. Qiu and W. Vogelsang, *Low-mass lepton pair production at large transverse momentum*, *Phys. Rev. D* **79** (2009) 054007 [[0811.3662](#)].
- [81] Z.-B. Kang, I. Vitev and H. Xing, *Nuclear modification of high transverse momentum particle production in $p+A$ collisions at RHIC and LHC*, *Phys. Lett. B* **718** (2012) 482 [[1209.6030](#)].
- [82] ALICE collaboration, *Transverse momentum distribution and nuclear modification factor of charged particles in p -Pb collisions at $\sqrt{s_{NN}} = 5.02$ TeV*, *Phys. Rev. Lett.* **110** (2013) 082302 [[1210.4520](#)].
- [83] CMS collaboration, *Observation of long-range near-side angular correlations in proton-lead collisions at the LHC*, *Phys. Lett. B* **718** (2013) 795 [[1210.5482](#)].
- [84] ALICE collaboration, *Long-range angular correlations on the near and away side in p -Pb collisions at $\sqrt{s_{NN}} = 5.02$ TeV*, *Phys. Lett. B* **719** (2013) 29 [[1212.2001](#)].
- [85] ALICE collaboration, *Long-range angular correlations of π , K and p in p -Pb collisions at $\sqrt{s_{NN}} = 5.02$ TeV*, *Phys. Lett. B* **726** (2013) 164 [[1307.3237](#)].
- [86] PHENIX COLLABORATION collaboration, *Nuclear effects on hadron production in $d + Au$ collisions at $\sqrt{s_{NN}} = 200$ gev revealed by comparison with $p + p$ data*, *Phys. Rev. C* **74** (2006) 024904.
- [87] O. Nachtmann, *Pomeron physics and QCD*, in *Proceedings, Ringberg Workshop on New Trends in HERA Physics 2003: Ringberg Castle, Tegernsee, Germany, September 28-October 3, 2003*, pp. 253–267, 2004, [hep-ph/0312279](#), DOI.
- [88] A. Buckley et al., *General-purpose event generators for LHC physics*, *Phys. Rept.* **504** (2011) 145 [[1101.2599](#)].

- [89] J. M. Katzy, *QCD Monte-Carlo model tunes for the LHC*, *Progress in Particle and Nuclear Physics* **73** (2013) 141.
- [90] CMS collaboration, *Observation of Long-Range Near-Side Angular Correlations in Proton-Proton Collisions at the LHC*, *JHEP* **09** (2010) 091 [[1009.4122](#)].
- [91] CMS COLLABORATION collaboration, *Measurement of long-range near-side two-particle angular correlations in pp collisions at $\sqrt{s} = 13$ TeV*, *Phys. Rev. Lett.* **116** (2016) 172302.
- [92] CMS collaboration, *Evidence for collectivity in pp collisions at the LHC*, *Phys. Lett.* **B765** (2017) 193 [[1606.06198](#)].
- [93] ATLAS collaboration, *Observation of Long-Range Elliptic Azimuthal Anisotropies in $\sqrt{s} = 13$ and 2.76 TeV pp Collisions with the ATLAS Detector*, *Phys. Rev. Lett.* **116** (2016) 172301 [[1509.04776](#)].
- [94] ALICE collaboration, *Long-range angular correlations of π , K and p in p-Pb collisions at $\sqrt{s_{NN}} = 5.02$ TeV*, *Phys. Lett.* **B726** (2013) 164 [[1307.3237](#)].
- [95] ATLAS COLLABORATION collaboration, *Observation of long-range elliptic azimuthal anisotropies in $\sqrt{s} = 13$ and 2.76 tev pp collisions with the atlas detector*, *Phys. Rev. Lett.* **116** (2016) 172301.
- [96] P. Ghosh, S. Muhuri, J. K. Nayak and R. Varma, *Indication of transverse radial flow in high-multiplicity proton-proton collisions at the Large Hadron Collider*, *J. Phys.* **G41** (2014) 035106 [[1402.6813](#)].
- [97] E. Schnedermann, J. Sollfrank and U. Heinz, *Thermal phenomenology of hadrons from 200a gev s+s collisions*, *Phys. Rev. C* **48** (1993) 2462.
- [98] D. d'Enterria, *Jet quenching*, *Landolt-Bornstein* **23** (2010) 471 [[0902.2011](#)].
- [99] R. Abir, U. Jamil, M. G. Mustafa and D. K. Srivastava, *Heavy quark energy loss and D-mesons in RHIC and LHC energies*, *Phys. Lett.* **B715** (2012) 183 [[1203.5221](#)].
- [100] R. Baier, Y. L. Dokshitzer, A. H. Mueller, S. Peigne and D. Schiff, *Radiative energy loss of high-energy quarks and gluons in a finite volume quark - gluon plasma*, *Nucl. Phys.* **B483** (1997) 291 [[hep-ph/9607355](#)].
- [101] M. Gyulassy, P. Levai and I. Vitev, *Jet quenching in thin quark gluon plasmas. 1. Formalism*, *Nucl. Phys.* **B571** (2000) 197 [[hep-ph/9907461](#)].

- [102] M. Gyulassy, P. Levai and I. Vitev, *NonAbelian energy loss at finite opacity*, *Phys. Rev. Lett.* **85** (2000) 5535 [[nucl-th/0005032](#)].
- [103] M. Gyulassy, P. Levai and I. Vitev, *Reaction operator approach to nonAbelian energy loss*, *Nucl. Phys.* **B594** (2001) 371 [[nucl-th/0006010](#)].
- [104] S. Cao, G.-Y. Qin and S. A. Bass, *Heavy-quark dynamics and hadronization in ultrarelativistic heavy-ion collisions: Collisional versus radiative energy loss*, *Phys. Rev. C* **88** (2013) 044907.
- [105] Y. L. Dokshitzer and D. E. Kharzeev, *Heavy quark colorimetry of QCD matter*, *Phys. Lett.* **B519** (2001) 199 [[hep-ph/0106202](#)].
- [106] R. Perez Ramos, V. Mathieu and M.-A. Sanchis-Lozano, *Heavy quark flavour dependence of multiparticle production in QCD jets*, *JHEP* **08** (2010) 047 [[1005.1582](#)].
- [107] H. Pereira Da Costa, *Early times and thermalization in heavy ion collisions: A Summary of experimental results for photons, light vector mesons, open and hidden heavy flavors*, *Nucl. Phys.* **A830** (2009) 883C [[0908.3178](#)].
- [108] STAR collaboration, *Measurement of D -meson azimuthal anisotropy in Au + Au 200 GeV collisions at RHIC*, *Nucl. Phys.* **A956** (2016) 256 [[1601.00743](#)].
- [109] ALICE collaboration, *Suppression of high transverse momentum D mesons in central Pb-Pb collisions at $\sqrt{s_{NN}} = 2.76$ TeV*, *JHEP* **09** (2012) 112 [[1203.2160](#)].
- [110] ALICE collaboration, *D-meson azimuthal anisotropy in midcentral Pb-Pb collisions at $\sqrt{s_{NN}} = 5.02$ TeV*, *Phys. Rev. Lett.* **120** (2018) 102301 [[1707.01005](#)].
- [111] PHENIX COLLABORATION collaboration, *Azimuthal correlations of electrons from heavy-flavor decay with hadrons in p+p and au+au collisions at $\sqrt{s_{NN}} = 200$ gev*, *Phys. Rev. C* **83** (2011) 044912.
- [112] S. Cao, G.-Y. Qin and S. A. Bass, *Modeling of heavy-flavor pair correlations in au-au collisions at 200a gev at the bnl relativistic heavy ion collider*, *Phys. Rev. C* **92** (2015) 054909.
- [113] ALICE collaboration, *D-meson production in p-Pb collisions at $\sqrt{s_{NN}} = 5.02$ TeV and in pp collisions at $\sqrt{s} = 7$ TeV*, *Phys. Rev.* **C94** (2016) 054908 [[1605.07569](#)].
- [114] ALICE collaboration, *Measurement of electrons from heavy-flavour hadron decays in p-Pb collisions at $\sqrt{s_{NN}} = 5.02$ TeV*, *Phys. Lett.* **B754** (2016) 81 [[1509.07491](#)].

- [115] ALICE collaboration, *Recent results from the ALICE experiment on open heavy flavours in hadronic collisions at the LHC*, in *Proceedings, 52nd International Winter Meeting on Nuclear Physics (Bormio 2014): Bormio, Italy, January 27-31, 2014*, 2014, [1405.4723](#).
- [116] ALICE collaboration, *Measurement of azimuthal correlations of D mesons and charged particles in pp collisions at $\sqrt{s} = 7$ TeV and p-Pb collisions at $\sqrt{s_{NN}} = 5.02$ TeV*, *Eur. Phys. J. C* **77** (2017) 245 [[1605.06963](#)].
- [117] M. Cacciari, S. Frixione, N. Houdeau, M. L. Mangano, P. Nason and G. Ridolfi, *Theoretical predictions for charm and bottom production at the LHC*, *JHEP* **10** (2012) 137 [[1205.6344](#)].
- [118] B. A. Kniehl, G. Kramer, I. Schienbein and H. Spiesberger, *Inclusive Charmed-Meson Production at the CERN LHC*, *Eur. Phys. J. C* **72** (2012) 2082 [[1202.0439](#)].
- [119] ALICE collaboration, *Measurement of charm production at central rapidity in proton-proton collisions at $\sqrt{s} = 2.76$ TeV*, *JHEP* **07** (2012) 191 [[1205.4007](#)].
- [120] ALICE collaboration, *Measurement of charm production at central rapidity in proton-proton collisions at $\sqrt{s} = 7$ TeV*, *JHEP* **01** (2012) 128 [[1111.1553](#)].
- [121] ALICE collaboration, *Measurement of D-meson production in pp collisions with ALICE at the LHC*, *Springer Proc. Phys.* **203** (2018) 415 [[1705.05147](#)].
- [122] ALICE collaboration, *D-meson production in proton-proton collisions with ALICE at the LHC*, *Nucl. Part. Phys. Proc.* **294-296** (2018) 32 [[1802.09256](#)].
- [123] ALICE collaboration, *Measurement of the production of charm jets tagged with D^0 mesons in pp collisions at $\sqrt{s} = 7$ TeV*, [1905.02510](#).
- [124] LHCb collaboration, *Observation of double charm production involving open charm in pp collisions at $\sqrt{s} = 7$ TeV*, *JHEP* **06** (2012) 141 [[1205.0975](#)].
- [125] ATLAS collaboration, *Measurement of $D^{*+/-}$ meson production in jets from pp collisions at $\sqrt{s} = 7$ TeV with the ATLAS detector*, *Phys. Rev.* **D85** (2012) 052005 [[1112.4432](#)].
- [126] STAR collaboration, *Measurement of the Bottom contribution to non-photonuclear electron production in p + p collisions at $\sqrt{s} = 200$ GeV*, *Phys. Rev. Lett.* **105** (2010) 202301 [[1007.1200](#)].
- [127] ALICE collaboration, *Beauty production in pp collisions at $\sqrt{s} = 2.76$ TeV measured via semi-electronic decays*, *Phys. Lett. B* **738** (2014) 97 [[1405.4144](#)].

- [128] R. Voss and A. Breskin, eds., *The CERN Large Hadron Collider, accelerator and experiments*. 2009.
- [129] G. Antchev, P. Aspell, I. Atanasov, V. Avati, V. Berardi, M. Berretti et al., *The totem detector at lhc*, *Nuclear Instruments and Methods in Physics Research Section A: Accelerators, Spectrometers, Detectors and Associated Equipment* **617** (2010) 62 .
- [130] A. Tricomi, O. Adriani, L. Bonechi, M. Bongi, G. Castellini, R. D'Alessandro et al., *The lhcf experiment at the lhc: Physics goals and status*, *Nuclear Physics B - Proceedings Supplements* **196** (2009) 30 .
- [131] O. Frasciello, *Wake Fields and Impedance Calculations of LHC Collimators' Real Structures*. 07, 2016.
- [132] T. A. Collaboration, K. Aamodt, A. A. Quintana, R. Achenbach, S. Acounis, D. Adamová et al., *The ALICE experiment at the CERN LHC*, *Journal of Instrumentation* **3** (2008) S08002.
- [133] ALICE collaboration, *ALICE technical design report of the inner tracking system (ITS)*, .
- [134] ALICE collaboration, *ALICE: Technical design report of the time projection chamber*, .
- [135] ALICE COLLABORATION collaboration, *ALICE Time-Of-Flight system (TOF): Technical Design Report*, Technical Design Report ALICE. CERN, Geneva, 2000.
- [136] ALICE COLLABORATION collaboration, P. Cortese, *ALICE transition-radiation detector: Technical Design Report*, Technical Design Report ALICE. CERN, Geneva, 2001.
- [137] ALICE collaboration, *ALICE technical design report of the photon spectrometer (PHOS)*, .
- [138] T. Cormier, C. W. Fabjan, L. Riccati and H. de Groot, *ALICE electromagnetic calorimeter: addendum to the ALICE technical proposal*, Tech. Rep. CERN-LHCC-2006-014, CERN, Geneva, Mar, 2006.
- [139] ALICE collaboration, *ALICE technical design report: Detector for high momentum PID*, .
- [140] A. Fernández, E. Gámez, G. Herrera, R. López, I. León-Monzón, M. Martínez et al., *Acorde a cosmic ray detector for alice*, *Nuclear Instruments and Methods in Physics Research Section A: Accelerators, Spectrometers, Detectors and Associated Equipment* **572** (2007) 102 .
- [141] ALICE collaboration, *ALICE technical design report of the dimuon forward spectrometer*, .

- [142] ALICE COLLABORATION collaboration, M. Gallio, W. Klempt, L. Leistam, J. De Groot and J. Schükraft, *ALICE Zero-Degree Calorimeter (ZDC): Technical Design Report*, Technical Design Report ALICE. CERN, Geneva, 1999.
- [143] ALICE collaboration, *ALICE technical design report: Photon multiplicity detector (PMD)*, .
- [144] ALICE collaboration, *ALICE technical design report on forward detectors: FMD, T0 and V0*, .
- [145] A. collaboration, *Alignment of the ALICE inner tracking system with cosmic-ray tracks*, *Journal of Instrumentation* **5** (2010) P03003.
- [146] K. Røed, K. Ullaland, H. Helstrup and T. Natås, *Single event upsets in sram fpga based readout electronics for the time projection chamber in the alice experiment*, .
- [147] W. Blum, L. Rolandi and W. Riegler, *Particle detection with drift chambers*, Particle Acceleration and Detection. 2008, [10.1007/978-3-540-76684-1](https://doi.org/10.1007/978-3-540-76684-1).
- [148] ALICE collaboration, *Performance of the ALICE VZERO system*, *JINST* **8** (2013) P10016 [[1306.3130](https://arxiv.org/abs/1306.3130)].
- [149] V. Balagura, *Notes on van der Meer Scan for Absolute Luminosity Measurement*, *Nucl. Instrum. Meth.* **A654** (2011) 634 [[1103.1129](https://arxiv.org/abs/1103.1129)].
- [150] W. Carena, P. Van de Vyvre, F. Carena, S. Chapeland, V. Chibante Barroso, F. Costa et al., *ALICE DAQ and ECS User's Guide*, Tech. Rep. ALICE-INT-2005-015. CERN-ALICE-INT-2005-015, CERN, Geneva, 2005.
- [151] ALICE COLLABORATION collaboration, *The ALICE trigger electronics*, .
- [152] R. Bramm, T. Kollegger, C. Loizides and R. Stock, *The Physics of ALICE HLT trigger modes*, [hep-ex/0212050](https://arxiv.org/abs/hep-ex/0212050).
- [153] <http://alien.web.cern.ch/>.
- [154] <http://alice-offline.web.cern.ch/>.
- [155] <http://root.cern.ch>.
- [156] P. Z. Skands, *Tuning Monte Carlo Generators: The Perugia Tunes*, *Phys. Rev.* **D82** (2010) 074018 [[1005.3457](https://arxiv.org/abs/1005.3457)].

- [157] T. Sjostrand, S. Mrenna and P. Z. Skands, *A Brief Introduction to PYTHIA 8.1*, *Comput. Phys. Commun.* **178** (2008) 852 [[0710.3820](#)].
- [158] X.-N. Wang and M. Gyulassy, *hijing: A monte carlo model for multiple jet production in pp, pA, and AA collisions*, *Phys. Rev. D* **44** (1991) 3501.
- [159] R. Brun, R. Hagelberg, M. Hansroul and J. C. Lassalle, *Geant: Simulation Program for Particle Physics Experiments. User Guide and Reference Manual*, .
- [160] GEANT4 collaboration, *GEANT4: A Simulation toolkit*, *Nucl. Instrum. Meth.* **A506** (2003) 250.
- [161] A. Fasso et al., *The Physics models of FLUKA: Status and recent developments*, eConf **C0303241** (2003) MOMT005 [[hep-ph/0306267](#)].
- [162] R. Frühwirth, *Application of kalman filtering to track and vertex fitting*, *Nuclear Instruments and Methods in Physics Research Section A: Accelerators, Spectrometers, Detectors and Associated Equipment* **262** (1987) 444 .
- [163] E. Wolin and L. Ho, *Covariance matrices for track fitting with the kalman filter*, *Nuclear Instruments and Methods in Physics Research Section A: Accelerators, Spectrometers, Detectors and Associated Equipment* **329** (1993) 493 .
- [164] ALICE collaboration, *Measurement of azimuthal correlations of D mesons and charged particles in pp collisions at $\sqrt{s} = 7$ TeV and p-Pb collisions at $\sqrt{s_{NN}} = 5.02$ TeV*, *Eur. Phys. J.* **C77** (2017) 245 [[1605.06963](#)].
- [165] M. Ivanov, K. Safarik, Y. Belikov and J. Bracinik, *TPC tracking and particle identification in high-density environment*, *arXiv e-prints* (2003) physics/0306108 [[physics/0306108](#)].
- [166] M. Cacciari, M. Greco and P. Nason, *The $P(T)$ spectrum in heavy flavor hadroproduction*, *JHEP* **05** (1998) 007 [[hep-ph/9803400](#)].
- [167] PHOBOS collaboration, *System size dependence of cluster properties from two-particle angular correlations in Cu+Cu and Au+Au collisions at $s(NN)^{1/2} = 200$ -GeV*, *Phys. Rev.* **C81** (2010) 024904 [[0812.1172](#)].
- [168] STAR COLLABORATION collaboration, *Distributions of charged hadrons associated with high transverse momentum particles in pp and Au + Au collisions at $\sqrt{s_{NN}} = 200$ GeV*, *Phys. Rev. Lett.* **95** (2005) 152301.

- [169] STAR collaboration, *Long range rapidity correlations and jet production in high energy nuclear collisions*, *Phys. Rev.* **C80** (2009) 064912 [[0909.0191](#)].
- [170] K. Dusling, P. Tribedy and R. Venugopalan, *Energy dependence of the ridge in high multiplicity proton-proton collisions*, *Phys. Rev. D* **93** (2016) 014034.
- [171] STAR COLLABORATION collaboration, *Mass, quark-number, and $\sqrt{s_{NN}}$ dependence of the second and fourth flow harmonics in ultrarelativistic nucleus-nucleus collisions*, *Phys. Rev. C* **75** (2007) 054906.
- [172] PHENIX COLLABORATION collaboration, *Deviation from quark number scaling of the anisotropy parameter v_2 of pions, kaons, and protons in Au + Au collisions at $\sqrt{s_{NN}} = 200$ gev*, *Phys. Rev. C* **85** (2012) 064914.
- [173] STAR collaboration, *Identified particle distributions in pp and Au+Au collisions at $s(NN)^{1/2} = 200$ GeV*, *Phys. Rev. Lett.* **92** (2004) 112301 [[nucl-ex/0310004](#)].
- [174] STAR collaboration, *Systematic Measurements of Identified Particle Spectra in pp, d^+ Au and Au+Au Collisions from STAR*, *Phys. Rev.* **C79** (2009) 034909 [[0808.2041](#)].
- [175] THE NA44 COLLABORATION collaboration, *Collective expansion in high energy heavy ion collisions*, *Phys. Rev. Lett.* **78** (1997) 2080.
- [176] CMS collaboration, *Study of the inclusive production of charged pions, kaons, and protons in pp collisions at $\sqrt{s} = 0.9, 2.76, \text{ and } 7$ TeV*, *Eur. Phys. J.* **C72** (2012) 2164 [[1207.4724](#)].
- [177] N. Xu, *Study of bulk properties at high energy nuclear collisions—the search for the partonic equation of state at rhic*, *Progress in Particle and Nuclear Physics* **53** (2004) 165 .
- [178] S. Kar, S. Choudhury, S. Muhuri and P. Ghosh, *Multiple parton interactions and production of charged particles up to the intermediate- p_T range in high-multiplicity pp events at the lhc*, *Phys. Rev. D* **95** (2017) 014016.
- [179] LHCb collaboration, *Measurements of long-range near-side angular correlations in $\sqrt{s_{NN}} = 5$ TeV proton-lead collisions in the forward region*, *Phys. Lett.* **B762** (2016) 473 [[1512.00439](#)].
- [180] S. Chatrchyan, V. Khachatryan, A. Sirunyan, A. Tumasyan, W. Adam, E. Aguilo et al., *Observation of long-range, near-side angular correlations in ppb collisions at the lhc*, *Physics Letters B* **718** (2013) 795 .

- [181] ALICE collaboration, *Anisotropic flow of charged hadrons, pions and (anti-)protons measured at high transverse momentum in Pb-Pb collisions at $\sqrt{s_{NN}}=2.76$ TeV*, *Phys. Lett. B* **719** (2013) 18 [[1205.5761](#)].
- [182] PHENIX collaboration, *Creating small circular, elliptical, and triangular droplets of quark-gluon plasma*, *Nature Phys.* **15** (2019) 214 [[1805.02973](#)].
- [183] ALICE collaboration, *Multiplicity Dependence of Pion, Kaon, Proton and Lambda Production in p-Pb Collisions at $\sqrt{s_{NN}} = 5.02$ TeV*, *Phys. Lett. B* **728** (2014) 25 [[1307.6796](#)].
- [184] ALICE collaboration, *Centrality dependence of π , K, p production in Pb-Pb collisions at $\sqrt{s_{NN}} = 2.76$ TeV*, *Phys. Rev. C* **88** (2013) 044910 [[1303.0737](#)].
- [185] ALICE collaboration, *K_S^0 and Λ production in Pb-Pb collisions at $\sqrt{s_{NN}} = 2.76$ TeV*, *Phys. Rev. Lett.* **111** (2013) 222301 [[1307.5530](#)].
- [186] PHENIX COLLABORATION collaboration, *Spectra and ratios of identified particles in au+au and d+au collisions at $\sqrt{s_{NN}} = 200$ gev*, *Phys. Rev. C* **88** (2013) 024906.
- [187] K. Werner, F.-M. Liu and T. Pierog, *Parton ladder splitting and the rapidity dependence of transverse momentum spectra in deuteron-gold collisions at the bnl relativistic heavy ion collider*, *Phys. Rev. C* **74** (2006) 044902.
- [188] H. J. Drescher, M. Hladik, S. Ostapchenko, T. Pierog and K. Werner, *Parton based Gribov-Regge theory*, *Phys. Rept.* **350** (2001) 93 [[hep-ph/0007198](#)].
- [189] ALICE collaboration, *Energy Dependence of the Transverse Momentum Distributions of Charged Particles in pp Collisions Measured by ALICE*, *Eur. Phys. J. C* **73** (2013) 2662 [[1307.1093](#)].
- [190] ATLAS collaboration, *Charged-particle distributions in $\sqrt{s} = 13$ TeV pp interactions measured with the ATLAS detector at the LHC*, *Phys. Lett. B* **758** (2016) 67 [[1602.01633](#)].
- [191] B. Schenke, S. Schlichting, P. Tribedy and R. Venugopalan, *Mass ordering of spectra from fragmentation of saturated gluon states in high-multiplicity proton-proton collisions*, *Phys. Rev. Lett.* **117** (2016) 162301.
- [192] K. Dusling, W. Li and B. Schenke, *Novel collective phenomena in high-energy proton-proton and proton-nucleus collisions*, *Int. J. Mod. Phys. E* **25** (2016) 1630002 [[1509.07939](#)].

- [193] CMS collaboration, *Measurement of charged pion, kaon, and proton production in proton-proton collisions at $\sqrt{s} = 13$ TeV*, *Phys. Rev.* **D96** (2017) 112003 [[1706.10194](#)].
- [194] ALICE collaboration, *Multiplicity dependence of the average transverse momentum in pp, p-Pb, and Pb-Pb collisions at the LHC*, *Phys. Lett.* **B727** (2013) 371 [[1307.1094](#)].
- [195] CMS collaboration, *Study of the Production of Charged Pions, Kaons, and Protons in pPb Collisions at $\sqrt{s_{NN}} = 5.02$ TeV*, *Eur. Phys. J.* **C74** (2014) 2847 [[1307.3442](#)].
- [196] ALICE collaboration, *Multiplicity dependence of charged pion, kaon, and (anti)proton production at large transverse momentum in p-Pb collisions at $\sqrt{s_{NN}} = 5.02$ TeV*, *Phys. Lett.* **B760** (2016) 720 [[1601.03658](#)].
- [197] ALICE collaboration, *D meson elliptic flow in non-central Pb-Pb collisions at $\sqrt{s_{NN}} = 2.76$ TeV*, *Phys. Rev. Lett.* **111** (2013) 102301 [[1305.2707](#)].
- [198] ALICE collaboration, *Pseudorapidity and transverse-momentum distributions of charged particles in proton-proton collisions at $\sqrt{s} = 13$ TeV*, *Phys. Lett.* **B753** (2016) 319 [[1509.08734](#)].
- [199] ALICE collaboration, *Transverse momentum dependence of D-meson production in Pb-Pb collisions at $\sqrt{s_{NN}} = 2.76$ TeV*, *JHEP* **03** (2016) 081 [[1509.06888](#)].
- [200] CMS collaboration, *Measurement of prompt D^0 meson azimuthal anisotropy in Pb-Pb collisions at $\sqrt{s_{NN}} = 5.02$ TeV*, *Phys. Rev. Lett.* **120** (2018) 202301 [[1708.03497](#)].
- [201] K. Werner, I. Karpenko and T. Pierog, *“ridge” in proton-proton scattering at 7 tev*, *Phys. Rev. Lett.* **106** (2011) 122004.
- [202] C. Shen, J.-F. m. c. Paquet, G. S. Denicol, S. Jeon and C. Gale, *Collectivity and electromagnetic radiation in small systems*, *Phys. Rev. C* **95** (2017) 014906.
- [203] R. D. Weller and P. Romatschke, *One fluid to rule them all: viscous hydrodynamic description of event-by-event central p+p, p+Pb and Pb+Pb collisions at $\sqrt{s} = 5.02$ TeV*, *Phys. Lett.* **B774** (2017) 351 [[1701.07145](#)].